Meena D. Lysko

Measurement and Models of Solar Irradiance

Doctoral thesis
for the degree of doctor scientiarum

Trondheim, August 2006

Norwegian University of Science and Technology
Faculty of Natural Sciences and Technology
Department of Physics

NTNU
Innovation and Creativity

NTNU
Norwegian University of Science and Technology

Doctoral thesis
for the degree of doctor scientiarum

Faculty of Natural Sciences and Technology
Department of Physics

ISBN 82-471-8070-7 (printed version)
ISBN 82-471-8069-3 (electronic version)
ISSN 1503-8181

Doctoral theses at NTNU, 2006:152

Printed by NTNU-trykk

This thesis is dedicated to my grandfather, Mr Raghubir Mudna.

You gave me a dream. I am proud to hold a part of its reality.

Contents

Acknowledgements

Never underestimate the experience and knowledge of the learned.

This work is a result of collaboration between the Departments of Physics at the Norwegian University of Science and Technology and the University of Kwazulu-Natal, South Africa.

Most importantly, I thank my scientific advisor Professor Jørgen Løvseth for his wisdom, time, patience, guidance and valued positive criticisms throughout this work. For me, he has always been a pillar of strength, encouragement and support.

I would also like to thank:

* Professor Berit Kjeldstad for her role as co-advisor and for the encouraging words throughout this work.

* Asbjørn Fjellvikås from the Electronic Workshop for his help with the instrument's electronics and front-end control software. I appreciate our frequent discussions on the intrument's performance and challenges. I also thank Jan Frode Jæger for his help in building the filter.

* Arnolf Bjølstad from the Mechanical Workshop for his expertise. His enthusiasm and important suggestions translated the instrument's drawings into reality. I thank all the staff at the workshop for machining and assembling the parts, as well as for always accomodating my numerous other requests.

* Guri Eggan from the International Office. Her help and advice to a foreign student is highly appreciated. Also Gudrun Gresman, Inger Kosberg and other personnel from the faculty who have always either sorted out or advised me on the administrative necessities. I thank Oddbjørn Grandum for his help with the Solar Platform and for his kind assistance with PC troubles.

* All at the University of Kwazulu-Natal who have contributed to the success of this work. In particular, Professor Ahmed Bawa for pioneering the joint collaboration and for his continuous encouragement. Also Professor Ramesh Bharuthram, Professor Michael McPherson and Professor Sadha Pillay for their critical help during my work in South Africa. I also thank the staff from the Academic Instrumentation Unit for their speedy and professional help whenever I requested it.

This acknowledgement would not be complete without the mention of my family and friends for their patience, continous encouragement and support. I am indebted to the Aasen's, the Løvseth's and the Pilipenko's. This work could not be completed if it was not for the love of my dear Dad, Mum, darling Daughter and my treasured Husband. My Dad's inspiration and my maestro of a husband are my backbone. I love you all.

Preface

Solar radiation is the main driving force for the Earth's weather and climate. It is also the prime source for renewable energy technologies. Solar energy technologies can satisfy the current energy demand and at the same time reduce anthropogenic greenhouse gas emissions. It follows from scientific and engineering research within the field that accurate terrestrial solar radiation data and derived models can improve the detection of long-term climate change, the validation of Earth radiation budget estimates, and the deployment of solar energy systems. But, accurate assessment of solar energy at the Earth's surface is difficult due to spatial, temporal and angular variability. These variations emphasise the need for localised solar radiation measurements and models.

In light of the above, this work has aimed at improving the quality of radiation data at two specific locations; one in Trondheim, Norway and the other in Durban, South Africa. This has entailed the development of an automatic data logging system, and frequent radiometer calibrations with traceability to the World Radiometric Reference. In addition, a radiometer called the Direct-Diffuse Solar Radiometer has been developed for the mapping of sky radiance. Supplementary work has been done to re-affirm the need for quality ground-based data.

The work done is twofold, the first on the measurements of solar irradiance and the second on the implementation of solar radiation models. So, the presentation of the work is divided into two parts. Chapters 1 to 5 are included in Part A under the heading "Measurement of Solar Irradiance". Chapters 6 is given in Part B, "Data Modelling".

Chapter 1 describes the concept of solar irradiance, discusses the components of solar radiation and introduces the radiometers in common use for the measurements of solar irradiance. Motivations for the development of the Direct-Diffuse Solar Radiometer are also included.

Chapter 2 describes the radiation mapping at the two sites, with particular emphasis on methods implemented for higher accuracy sampling, data reliability and continuity.

Regular radiometer calibration is necessary to ensure the data quality. Therefore the methodology for and results from calibration of the site radiometers are given in *Chapter 3*.

The acquired direct and global data for the sites are presented in *Chapter 4*. Diurnal 1-minute variations are discussed along with estimates of monthly and annual trends, with particular emphasis on atmospheric transmittance and the clearness index.

The last chapter in Part A, i.e. *Chapter 5,* presents the work done on the Direct-Diffuse Solar Radiometer (DDSR-1B). The instrument is designed for measuring sky irradiance as well as direct solar irradiance. The DDSR-1B is a prototype ground based instrument which is mounted on a remotely controlled solar tracker/sky positioner. The Chapter discusses the DDSR-1B's design, control, calibration and field tests in detail.

Chapter 6 in Part B considers 2 available software products that can generate estimates of direct normal solar irradiances for any ground location. This chapter also concludes the work for this thesis by re-emphasising the need for localised solar radiation measurements and models.

Finally, Chapter 7 collects the major conclusions given through the course of this text.

Part A: Measurement of Solar Irradiance

All of South Africa's energy demands would be met if 0.1% of the solar radiation on its land was converted to useful energy.

Chapter 1
Introduction to Solar Irradiance

This chapter defines solar radiation, discusses motivations for measurements of the components of solar irradiance and introduces radiometers that are currently in use.

1.1. Solar Radiation

Solar radiation is a general term that, in this book stands, for the electromagnetic radiation emitted by the sun. The total amount of solar radiation received at normal incidence at the top of the earth's atmosphere, at the mean sun-earth distance, is referred to as the Total Solar Irradiance (TSI) or extraterrestrial solar irradiance. The TSI varies over time, albeit by a small amount, and its magnitude and variations directly or indirectly affects many atmospheric and biological processes on earth. Since November 1978 a complete set of TSI measurements from various space borne radiometers is available, yielding a time series of 26 years. FIGURE 1.1 shows the measured time series, consisting of mean daily values plotted from the composite data set version d30_60_040 from PMOD/WRC and with reference to Fröhlich et al. in [10., 1998][1] and Fröhlich in [12., 2003]. For the duration of this test, 17 November 1978 to 20 April 2004, the absolute minimum and maximum daily TSI were 1362Wm^{-2} and 1368Wm^{-2}, respectively. Following the work of Gueymard in [15., 2004] an estimate of the mean TSI for the above period is made. Applying a 27-day smoothing filter (with missing data substituted with the mean of the data for the last day before and the first day after the observed gap), the maximum and minimum values become 1367.1Wm^{-2} and 1364.8Wm^{-2}, respectively, yielding a mean value of 1365.9±1.4Wm^{-2}.

In general a long-term average of the TSI is given the term 'solar constant' and is used in most applications instead of the TSI. The World Meteorological Organisation (WMO) has recommended a solar constant of 1367Wm^{-2} according to Fröhlich et al. in [9., 1986]. A more recent

1. In this dissertation, references are placed in square brackets. The first entry gives the cross-reference number which is found at the end of the relevant chapter and the second gives the publication year.

standardisation in [2., 2000], by the American Society for Testing and Materials (ASTM), gives the solar constant as 1366.1Wm^{-2}.

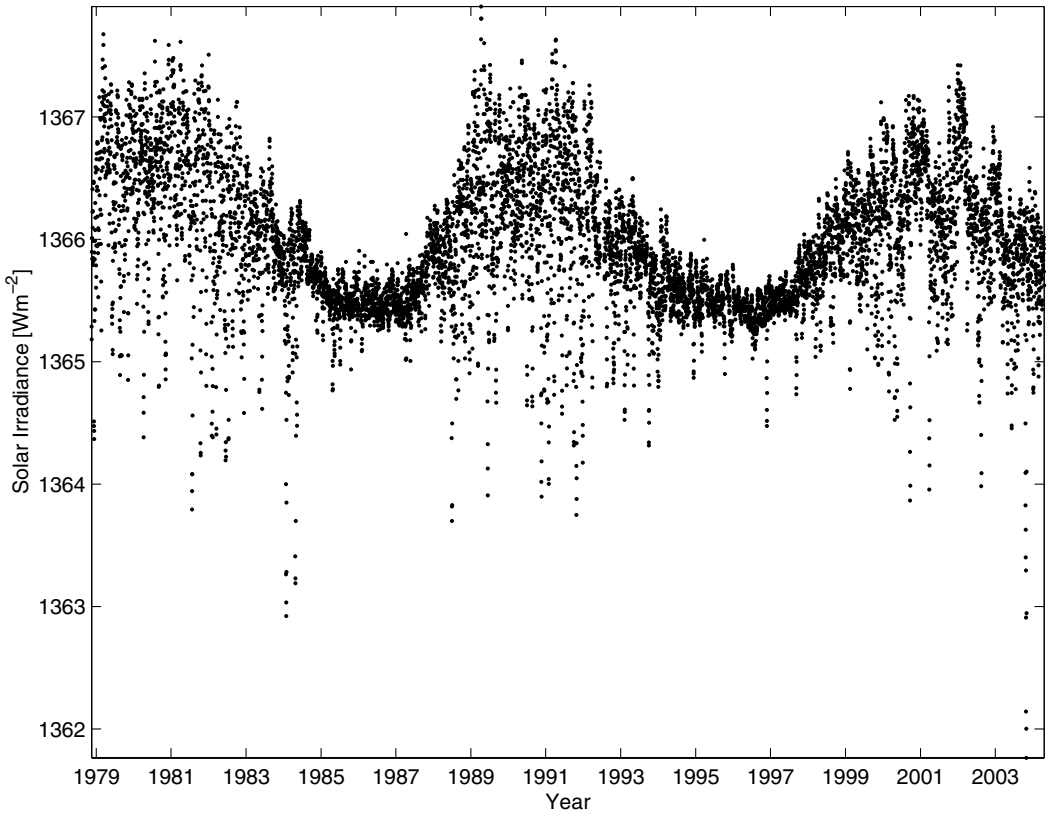

FIGURE 1.1
Daily TSI for the period 17/11/1978-20/04/2004. Plotted with dataset version d30_60_040 from PMOD/WRC, Davos, Switzerland and with the acknowledgement of unpublished data from the VIRGO Experiment on the cooperative ESA/NASA Mission SoHO and with references to [10., 1998] and [12., 2003].

The value of 1365.9Wm^{-2} as calculated from the most recent data set from PMOD/WRC is 1.1Wm^{-2} less than the WMO recommendation and 0.2Wm^{-2} less than the ASTM value. However, TSI measurements have an inherent absolute uncertainty of at least 0.1% or 1.4Wm^{-2}. This is shown by Gueymard in [15., 2004]. So it can be argued that the above differences are insignificant. For the purposes of this thesis, unless stated otherwise, the WMO recommendation of:

$$S_c = 1367 Wm^{-2} \tag{1}$$

is used.

The solar constant is related to the extraterrestrial solar spectral irradiance E_λ by:

$$S_c = \int_0^\infty E_\lambda d\lambda \tag{2}$$

The spectral distribution of the extraterrestrial solar radiation is shown in FIGURE 1.2 and is based on the spectrum given by Gueymard in [15., 2004]. It is evident that over 97% of the total solar energy lies between 300nm to 2500nm. The solar energy confined to this spectral region is often referred to as short-wave solar radiation, and the integrated energy (over the same region) is referred to as broadband or total solar radiation.

Since the distance between the sun and earth varies during the year, the value of the solar radiation flux, S_o outside the atmosphere is in general different from S_c. Applying an eccentricity correction factor for the Earth's orbit, with R_o as the mean sun-earth distance and R the sun-earth distance at the given moment in time:

$$E_o = \left(\frac{R_o}{R}\right)^2 \approx 1 + 0.033\cos(2\pi d_n/365), \tag{3}$$

it follows that:

$$S_o = E_o \cdot S_c \tag{4}$$

The eccentricity approximation in equation (3):

$$1 + 0.033\cos(2\pi d_n/365), \tag{5}$$

where d_n is the day number of the year, is used by Duffie et al. in [7., 1980]. Expressions with greater accuracy in E_o are available. For instance Spencer, in [35., 1971], gives the eccentricity in terms of a Fourier series type expansion.

Not all the extraterrestrial solar radiation penetrates through the atmosphere to the Earth's surface. Part of it is scattered and/or absorbed by the atmospheric constituents such as ozone, water vapour, aerosol, and clouds). A typical spectral distribution of the radiation reaching the Earth's surface is shown by the lower curve of FIGURE 1.2.

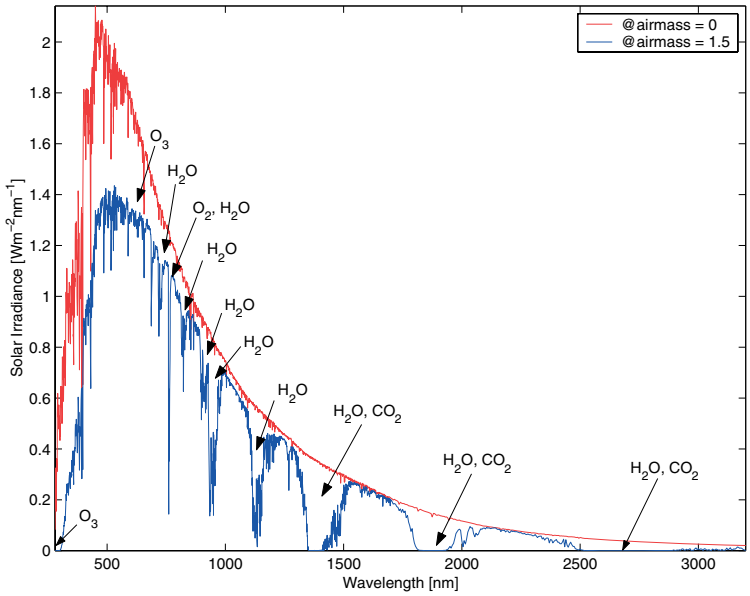

FIGURE 1.2
Spectral distribution of solar radiation at airmass zero at the top of the atmosphere (upper curve), and a typical distribution of that which reaches the earth's surface (at airmass 1.5). The extraterrestrial data series is taken from ASTM G173-03 [15.] and that for the surface data from E-490-00 [14.].

The spectra for shortwave solar radiation is well documented in literature on atmospheric physics; for example Salby in [33., 1996] and Kondratyev in [23., 1969], to name but two sources. High-altitude atmospheric ozone is mainly responsible for almost complete attenuation of the extraterrestrial solar radiation below 300nm. Water vapour is mainly responsible for the several strong bands of absorption in the infrared region, i.e wavelengths greater than 800nm. In fact, the absorption bands of water vapour and carbon dioxide strips off almost all the solar radiation above 2500nm. It thereby follows that the *solar radiation at sea level has a spectral window from about 300nm to 2500nm*, with inherent attenuation along its path from outside the atmosphere, due to Rayleigh and Mie scatterers and due to atmospheric absorbers.

1.2. Components of Solar Radiation

Solar radiation is redistributed as it traverses the Earth's atmosphere. It is therefore necessary to look at the radiation according to its distribution. The distribution is illustrated in FIGURE 1.3.

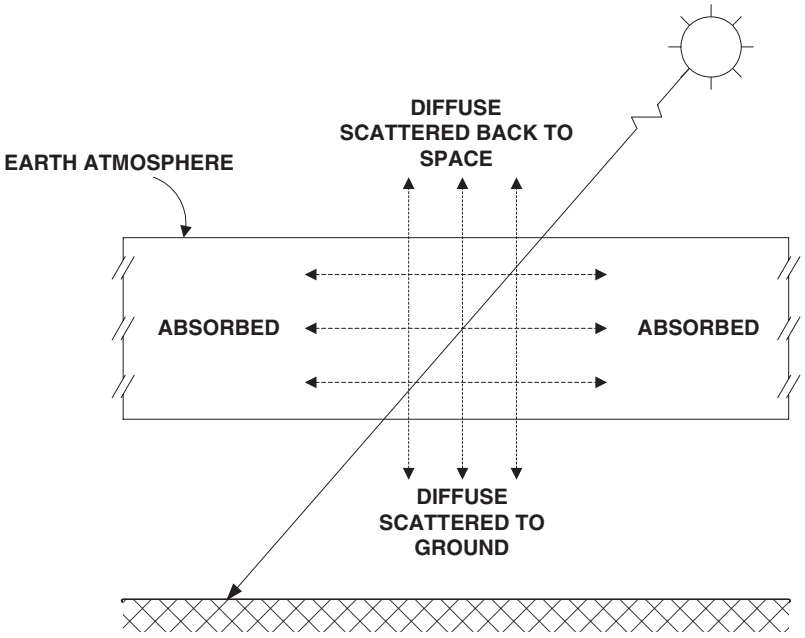

FIGURE 1.3
The distribution of direct, diffuse, and absorbed solar radiation as illustrated by Iqbal in [20., 1983].

1.2.1. Direct Solar Radiation

The solar radiation arriving on the ground, directly in line from the solar disk is called *direct or beam radiation*.

Kondratyev in [23., 1969] derives an expression for the total direct radiation S_m at the Earth's surface level in the case when the atmospheric mass in the direction of the sun is m[1].

$$S_m = \int_0^{\infty} S_{o,\lambda} \cdot p_\lambda{}^m \cdot d\lambda \tag{6}$$

Here $S_{o,\lambda}$ is the monochromatic solar radiant flux outside the atmosphere, and p_λ is the atmospheric transparency coefficient for radiation at wavelength λ.

A solution to equation (6) requires prior knowledge of the input parameters for each particular wavelength. In the case of the real atmosphere a theoretical estimate of the direct component is further complicated by the temporal and spatial variability of the atmospheric transparency. If a factor T_m, which is the integral transparency coefficient over the whole spectrum, is introduced, equation (6) becomes:

$$S_m = (T_m)^m \cdot \int_0^\infty S_{o,\lambda} d\lambda = (T_m)^m \cdot S_o, \tag{7}$$

with S_o as defined in equation (4).

It is clear from equation (7) that observational data S_m from radiometric measurements would permit a quantitative characterisation of the atmospheric transparency for the observational site.

1.2.2. Diffuse Solar Radiation

Due to the scattering of radiant energy in the atmosphere, the short-wave solar radiation reaching the Earth's surface is not only direct solar but also scattered or *diffuse radiation*.

In a clear sky, the magnitude of diffuse solar radiation is dependant upon solar height, atmospheric transparency, and the albedo of the underlying surface. The presence of clouds greatly influences the diffuse magnitude. Kondratyev discusses the theoretical calculations of diffuse radiation without and with the influence of clouds in [23., 1969]. In either case, the theoretical calculation is complicated, and like with the direct component,

1. The atmospheric mass m is a dimensionless quantity indicating by how many times the optical thickness in the direction of the sun exceeds the optical thickness in the direction of the vertical. With radiation attenuation by a mass factor a_λ along a path ds with air density ρ the atmospheric mass in the direction of the sun is $m = \frac{\int a_\lambda \rho ds}{\int a_\lambda \rho dh}$, where dh is the optical thickness in the vertical direction.

is further complicated by temporal and spatial variability; which again suggests that in order to be able to employ analytical models it is necessary to measure/evaluate a number of parameters. Also, models do require verification. All of the above requires true observations.

Most of the measured and numerically calculated diffuse solar radiation data are for the horizontal surface. However, because of the anisotropic distribution of solar radiance over the sky hemisphere, the horizontal surface rarely receives the maximum input of solar energy. It is hereby evident that efficient solar systems require a prior knowledge of the anisotropic distribution, which is possible with true observations or empirical approximations that are validated by true observations.

It also follows that the true observations $L(\theta,\phi)$ of sky radiance would allow its integration for a total flux of diffuse radiance $F_{diffuse}$ representing incidence from all zenith angles θ and azimuth angles ϕ over the hemisphere of the sky i.e.:

$$F_{diffuse} = \int_0^{2\pi}\int_0^{\pi/2} L(\theta,\phi)\sin\theta\cos\theta d\theta d\phi \tag{8}$$

1.2.3. Global Solar Radiation

The total solar radiation is termed *global solar radiation*; and is the sum of the direct and diffuse solar radiation. In the case of a horizontal surface the total radiation F^H_{Global} is the sum of the vertical component of the direct beam S_m and the diffuse horizontal radiation $F^H_{Diffuse}$:

$$F^H_{Global} = S_m\cos\theta_z + F^H_{Diffuse}, \tag{9}$$

where θ_z is the angle between the direct beam and the normal to surface.

A ratio K_T of the global radiation incident on a horizontal surface to the horizontal component of the extraterrestrial radiation, i.e:

$$K_T = \frac{F^H_{Global}}{S_o\cos\theta_z}, \tag{10}$$

gives an indication of the solar climate at a particular location and is called the clearness parameter.

1.3. Solar Radiometry

Radiometry is the basic tool to attain solar radiation data. The pyrheliometer, mounted on a solar tracker, is used in the measurements of direct solar irradiance. The pyranometer is used for measurements of global solar irradiance. A common technique for the measurements of diffuse solar irradiance is a pyranometer equipped with a shadow band that shields off the direct sun beam.

1.3.1. Radiometer Sensors

Thermal-type radiation sensors are employed by most of the specialised companies (for example Eplab, Kipp & Zonen and EKO). These convert the heating effect of solar radiation into an electrical signal. Amongst the thermal-type sensors, thermopiles are the most used. A description and working principle of radiometer sensors can be found in most handbooks on solar radiation, including [20., 1983].

Recent radiometer designs (for example the EKO MS-092 digital sunshine sensor described by Winans in [39., 2002]) use pyroelectric elements that generate a voltage only when a change of temperature is detected. The pyroelectric detector is discussed in detail in Chapter 5 (see page 127).

1.3.2. The Pyrheliometer

Absolute pyrheliometers and reference standard pyrheliometers are used as references in solar radiometer calibrations, whilst routine measurements of direct normal irradiance are taken by field pyrheliometers.

1.3.2.1. View-Limiting Geometry

A description of, and specification for a pyrheliometer's view-limiting geometry is given by the WMO in [40., 1997]. A brief discussion follows,

and greater detail is given in Chapter 5: Direct-Diffuse Solar Radiometer-1B, Section 5.3.1, “View Limits,” on page 100.

All pyrheliometers should be narrow angled so as to measure only the radiation from the sun, which represents a full angle of about 0.53^{o}. However, pyrheliometers with small apertures require special attention so as to avoid the instabilities associated with pointing accuracy. Major, in [24., 1995], has shown that if the pointing error is larger than the slope angle, the irradiance of the pyrheliometric sensor decreases rapidly with increasing mispointing. However, large slope angles would let in a greater amount of circumsolar radiation.

Circumsolar radiation is a result of small angle forward scattering of solar radiation by atmospheric particles whose dimensions are comparable to the wavelengths scattered. Ångström et al. in [1., 1966] have shown the influence of circumsolar radiation on pyrheliometric measurements. The WMO’s view-limiting specifications for pyrheliometers means that a narrow annulus of sky is, inevitably, also measured. However, as is shown by Jeys et al. in [21., 1975], the solar aureole has little effect on the direct beam intensity measured by Eplab’s normal incidence pyrheliometers for cloudless conditions. Still, the effect of the solar aureole under cloudy conditions is significant.

The work by Ångström and others have lead to the WMO recommendation of a full view angle of 5^{o}, and a slope angle of 1^{o}. This means that all pyrheliometers following the WMO standard effectively measures a solar aureole component between 0.25^{o} and 1^{o}.

1.3.2.2. Solar Tracking

A pyrheliometer is mounted on a solar tracker in order to maintain normal solar incidence. One of the most commonly used commercial solar trackers is the Eplab model ST. This tracker has a specified pointing accuracy of $\pm 0.25^{o}$ but requires frequent manual adjustments for declination and the equation of time in order to keep the pyrheliometer aligned to the sun.

Automatic solar trackers have increased in popularity. Automatic solar trackers such as EKO's STR, BRUSAG's INTRA and Eplab's SMT-3 have a pointing accuracy of 0.1^{o} or less due to active solar position feedback sensors.

1.3.2.3. Absolute and Reference Pyrheliometers

The World Standard Group of pyrheliometers, responsible for the World Radiometric Reference (see section 3.1 on page 48), are absolute cavity pyrheliometers. An absolute cavity pyrheliometer, as given by the WMO in [40., 1997], is a primary standard since it can be used to define the scale of total irradiance without resorting to reference sources or radiators. A description and operating principle of the Eplab Model HF absolute cavity pyrheliometer are given in section 3.3.2 on page 51.

Reference pyrheliometers are secondary standard pyrheliometers, whose instrument constant is obtained through calibration against an absolute pyrheliometer. The Ångström compensation pyrheliometer, described by Iqbal in [20., 1983], is an example of a reference pyrheliometer.

1.3.2.4. Field Pyrheliometers

Field pyrheliometers are secondary instruments that are calibrated against the reference pyrheliometers (see section 3.4 on page 57).

The Eppley Normal Incidence Pyrheliometer (NIP) is amongst one of the commonly used field pyrheliometers. These field instruments are sealed at the viewing end by a glass window to allow continuous operation; under all weather conditions. The Eppley NIP uses a 1-mm thick Infrasil II (water-free fused silica) window which has spectral transmittance from $260nm$ to $2700nm$ (specified here for a minimum of 80% transmittance through a 1-cm-thick sample) [19., 1998]. The low-end complete cutoff is at about $200nm$. The infrared is completely cutoff above $4300nm$.

The collimating tube, down to the receiver, is 203mm in length. This, together with a front aperture radius of 10.3mm and receiver radius of 4mm, gives the following viewing angles:

$$Slope\ Angle = 1.78^{o} \tag{11}$$

$$Limit\ Angle = 4.03^{o}$$

$$Opening\ \frac{1}{2}\ Angle = 2.9^{o}$$

The above geometrical dimensions are for the Eppley NIP 18653 given by Major in [25., 1999]. In comparison with the Eppley absolute cavity HF 18748 (which is similar in construction to most absolute cavities), the NIP 18653 effectively receives an additional 1^{o} of circumsolar radiation. The extra aureole in the NIP will lead to variability about the absolute cavity value. An estimated variability of ±0.1%, under the assumption of clear skies, is quoted by Thacher et al. in [38., 200].

The Eppley NIP's receiver is a multijunction thermopile coated with 3M Flat Black for maximum radiation absorption. Use of the absorber, the window and the above mentioned view-limits results in NIP sensitivity to the spectral content of the solar irradiance. However the cavity radiometers, used to calibrate the NIP, has no window and a near unity absorbing light trap. As a result, changes in the spectrum of light are measured equally well, and infrared light beyond the NIP window cutoff is also measured. It thereby follows that the calibration factor of the NIP would vary under different atmospheric turbidity conditions. Thacher et al. therefore suggest a total NIP spectral uncertainty of ±0.3%. This total estimate covers the effects of field of view, window spectral transmission, and absorber spectral reflectance.

Sensor temperature is another factor affecting a field pyrheliometer's accuracy. For the NIP, Eplab uses a thermal compensation circuit to confine the thermopile temperature variability to ±1% over the interval of $-20^{o}C$ to $+40^{o}C$.

With all of the mentioned calibration transfer uncertainties and additional factors such as the previously mentioned tracking error, the NIP's minimum cumulative uncertainty (which is the root sum of squares of uncertainties) can, according to Thacher et al. in [38., 2000], be ±0.5% (i.e at the 95% confidence level). This is within the WMO specification of ±0.9% for the one minute totals from a high quality pyrheliometer.

1.3.3. The Pyranometer

Routine measurements of global solar irradiance are taken by pyranometers that are placed horizontally flat. This gives the detector a full view of the sky dome and so accepts radiation from all directions within the dome.

A description of common pyranometers, for example the Eppley Precision Spectral Pyranometer (PSP), may be found in literature such as [32.], [20.], and [9.]. The discussion to follow pertains to the pyranometer's sources of error; the knowledge of which is necessary to review the instrument's calibration results and routine observational data.

1.3.3.1. Directional Error

It is known that the sensor surface of the typical thermopile pyranometers are not lambertian and hence the sensors do not have perfect cosine responses. According to Haeffelin et al. in [17., 2001], pyranometer data errors of up to 10% at low solar elevations may be attributed to the cosine response problem. Work by Stoffel et al., described in [36., 1999], suggests that the pyranometer data can be considerably improved by using responsivities that are a function of zenith angle. The functionality can be investigated in a laboratory with the aid of a cosine test bench. Beaubien in [4., 1998], Michalsky et al. in [28., 1995] and Philipona et al. in [31., 1993] report on their laboratory test benches that are used to investigate the directional response of pyranometers.

The sensitivity of a pyranometer also depends on the angle of azimuth. Nast, in [30., 1983], has tested the dependence of the sensitivity by rotating the pyranometer and keeping the incident angle at a constant value of 80^{o}. As reported by Nast, the typical difference between the highest and the lowest sensitivity that resulted from this test is 7% for the Eppley PSP under observation. Nast explains that the azimuth error is probably caused by a mismatch between the instrument's sensor plane and spirit level. Radiometric levelling could correct the problem, but this may not be true if the sensor surface is not uniform.

It is evidenced by Michalsky et al. in [26., 1999] that the measurements of global downward solar irradiance as the sum of the direct and diffuse

components of downwelling solar irradiance greatly alleviate the directional response problem.

1.3.3.2. Pyranometer Zero Offset

The domes of pyranometers are used to protect the sensor and reduce the effects of convection. However, the dome influences the radiation balance between the sensor and the target. This is, for example, shown in the expression derived by Ji et al. in [22., 2000] (based on a simplified, but illustrative energy balance model for the Eppley PSP):

$$F^{H}_{Global} = \left(\frac{1-\rho_d}{\varepsilon_s} + \rho_d\right) k\alpha\Delta V + \varepsilon_d(\sigma T_s^4 - \sigma T_d^4) + \tau(\sigma T_s^4 - L) \tag{12}$$

where:

ρ_d is the longwave reflectance off the dome,

$\varepsilon_s, \varepsilon_d$ are the sensor and dome longwave emittances, respectively,

k is the thermal conductivity of the thermopile,

α is the thermopile constant,

ΔV is the output voltage of the thermopile,

σ is the Stefan-Boltzmann constant,

T_s, T_d are the sensor and dome temperatures, respectively,

τ is the longwave transmittance, and

F^{H}_{Global}, L are respectively the ambient shortwave and longwave irradiances.

The first term on the right hand side of equation (12) is the output of a PSP. The remaining two terms are responsible for the pyranometer's zero-offset and cannot be calibrated off with present calibration techniques.

The second term is considered as the thermal dome effect in pyranometers and can cause an underestimation of the downwelling irradiance exceeding $10 Wm^{-2}$. This is verified in research reports by Ji et al. [22., 2000], Bush et al. [5., 2000] and others. The third term is due to the influence of the ambient longwave radiation and is usually small.

A pyranometer's instantaneous zero-offset may be measured by total shading of the glass hemispheres and the resulting output voltage may be used as the correction factor for unshaded measurements. Gulbrandsen, in [16., 1978], has shown that the difference between corrected and uncorrected global irradiance measured on 12 March 1975, with solar azimuth of 64^{o}, was $10.6 Wm^{-2}$. Unfortunately, pyranometer zero-offset is variable and depends on factors like wind speed, cloud cover and turbidity.

Global Radiation may be measured indirectly so as to eliminate the offset errors caused by heating and cooling. This entails the measurement of the diffuse component with a shaded pyranometer and the measurement of the direct component with a pyrheliometer, and then summing the record as justified in equation (9) (see section 1.3.4 and section 3.5). In the past this has been a laborious process, but with automation the method can give high precision measurements.

1.3.3.3. Pyranometer Time Response

There is suggestion by Shen et al. in [34., 1992] that pyranometers have multiple time constants, caused by the inertia of the sensor, the net infra-red radiation between the inner dome and sensor, and a change in the temperature of the housing. Nast in [30., 1983] has shown that an Eppley PSP under test required a 1-second to decay exponentially to 2% of the initial exposed irradiance once the light source was switched off and a further 9-seconds to reach 0.05% of the initial signal.

The pyranometer's total response time to irradiance change defines the minimal sampling time for measurements on the accuracy of the instrument. In addition, the response time has to be considered during calibration of the pyranometer (see section 3.5 on page 58).

A software correction for instantaneous radiation readings tainted by errors that are due to the inherent thermal response is proposed by Suehrcke

et al. in [37., 1990]. The errors usually balance out when the individual instantaneous radiation measurements are integrated over sufficiently long time periods, but in the study of instantaneous solar radiation measurements moments of rapid radiation changes would result in errors due to the time response of the instrument.

1.3.4. Diffuse Radiometers

When the global horizontal solar radiation F^H_{Global} is measured by a pyranometer and direct normal radiation S_m is measured by a pyrheliometer, the total diffuse horizontal irradiance $F^H_{Diffuse}$ can be found by rearranging equation (9) to give:

$$F^H_{Diffuse} = F^H_{Global} - S_m \cos\theta_z \tag{13}$$

Observation of the diffuse component by means of equation (13) suggests that measurement errors, as reviewed for the pyrheliometer in section 1.3.2 and more especially for the pyranometer in section 1.3.3, are superimposed.

A more conventional approach to measurements of diffuse horizontal solar irradiance is by means of a pyranometer that is suitably shaded from the direct component. The output thence represents a hemispherical integration of the sky radiance incident on the pyranometer's flat horizontal surface. This is seen from equation (13) by setting the direct component $S_m = 0$. Still, the inaccuracies associated with pyranometer measurements are inferred.

The above mentioned hemispheric integration does not quantify the angular distribution of sky radiance; the knowledge of which is essential in applications of solar energy involving inclined planar surfaces. For measurements of the angular distribution a sky-scanning radiometer is required, but may not be as readily available as the commercial pyranometers and pyrheliometers.

1.3.4.1. Diffuse Measurements by Shaded Pyranometers

It is a prevalence to measure diffuse solar irradiance by shielding a pyranometer from the direct solar beam with a shade ring or shadowband mount. This kind of shading apparatus inevitably screens a portion of the sky and the resulting measurements then require theoretical corrections that are based on the inherent geometry and sky conditions. The need for such corrections have been addressed by Batlles et al. in [3., 1995] and others.

Work by Michalsky et al., described in [27., 1986], has led to a microprocessor-based rotating shadowband radiometer. Besides the inaccuracies associated with the silicon sensor the authors have devised an instrument that measures the diffuse component as well as the global and direct components. In addition, a real-time correction is made for the amount of diffuse screening by the shadowband without the need for theoretical calculations. The diffuse correction is astutely determined from the difference between the total horizontal and the average of measurements made with the shadowband at $\pm 6^{o}$ in hour angle from the sun. The instrument does not, however, measure the angular distribution of diffuse radiance.

1.3.4.2. Diffuse Measurements by Sky Scanners

The angular distribution of diffuse radiance may be monitored by using multiple pyranometers mounted at different angles of azimuth and zenith. An example of a multiple pyranometer method is discussed by Faiman et al. in [8., 1992]. The method involves measuring the global radiation received on four different, but fixed, surfaces with a set of Eppley PSP's and the extraction of the beam and diffuse components with a reconstruction algorithm. The extraction is based on the assumption of an isotropic distribution of the diffuse component over the sky. Further, as indicated by Nast in [30., 1983], some pyranometers are sensitive to tilting because of the changes in convective flow inside the instruments' hemispheres. There is also the concern of pyranometer induced errors as discussed in section 1.3.3. Systems with a multiple set of pyranometers can be bulky and expensive.

In light of the above Hämäläinen et al., in [18., 1985], have proposed a compact multipyranometer. The instrument consists of 25 sensors mounted

on a metal hemisphere with a reference sensor in the lower part of the metal hemisphere. The sensors are temperature transducers. In principle, the difference between an irradiated sensor and the reference sensor is proportional to the total insolated energy over the integration period. Computation of the direct irradiance and diffuse radiance distribution is not trivial. Besides the complexity in the retrieval algorithm, the instrument's array of sensors may require temperature corrections for better accuracies. The pertinent drawback is that the instrument does not measure the sky radiance distribution directly.

The EKO: Sky Scanner MS-300 developed by Nakamura et al. and described in [29., 1991] is an example of, and may be the only existent commercial instrument for the determination of the angular distribution of sky radiance. The instrument was specifically developed for the measurement of sky luminance distribution, and remodeled for sky radiance monitoring. The sensor for the sky radiance is a pyroelectric and its measuring range is from 0 to $300 Wm^{-2}sr^{-1}$. The half aperture angle and slope angle of the collimator are 5.5^{o} and 1^{o}, respectively. The instrument measures the spatial distribution of the radiance by scanning a total of 145 points on the sky vault.

Another sky scanning radiometer is described by Coombes et al. in [6., 1982]. This is a research oriented instrument which measures short and total wave radiation over the hemispherical sky dome. Scanning is by way of a mirror which directs sun and sky radiation onto the detector. The detector system involves a pyroelectric detector and a chopper, and a temperature monitoring/regulating feature. The sky viewing directions are such that neighbouring sky frames either only just overlap or do not quite overlap and is based on the radiometer's 14^{o} full field of view angle.

A spectroradiometer, the Grandum-Løvseth Periscope, has been developed at NTNU. A full account of this instrument is given in [13., 1997]. The instrument records spectral distributions of the direct solar radiation and spectral and angular distributions of the diffuse radiation. Radiation is collected by a movable collimator- mirror system. The spectral range is gained by three monochromators.

The motivations for the need of a radiometer capable of diffuse radiance measurements have incited part of the work reported in this dissertation. The Direct Diffuse Solar Radiometer-1B has been designed and developed with the purpose of measuring direct irradiance, and angular circumsolar and sky distributions. Like the sky-scanning radiometers discussed above, this radiometer is controlled by a microcontroller. A complete discussion on the developed instrument is given in Chapter 5.

1.4. Chapter Summary

This chapter has defined the solar radiation impinging the top of the earth's atmosphere, discussed its spectral content and given the components of solar radiation arising from its redistribution in traverse through the earth's atmosphere. Various radiometers have been reviewed for measuring the different components, with focus on the necessities for instrument development and data collection with regards to the angular distribution of diffuse radiance.

1.5. References

1. Ångström A., Rodhe B., *Pyrheliometric Measurements with Special Regard to the Circumsolar Sky Radiation*, Tellus XVIII, 1, 1966.
2. ASTM, *Standard Solar Constant Zero Air Mass Solar Spectral Irradiance Tables*, Standard E490-00, American Society for Testing and Materials, West Conshohocken, P.A., 2000.
3. Batlles F. J., Olmo F. J., Alados-ArboledasBatt L., *On Shadowband Correction Methods for Diffuse Irradiance Measurements*, Solar Energy, Vol. 57, No. 6, pp. 433-443, December 1996.
4. Beaubien D.J., Bisberg A., Beaubien A.F., *Investigations in Pyranometer Design*, Journal of Atmospheric and Oceanic Technology, Vol. 15, pp. 677-686, June 1998.
5. Bush B.C., Valero P.J.F., Simpson A.S., *Characterization of Thermal Effects in Pyranometers: A Data Correction Algorithm for Improved Measurement of Surface Insolation*, Journal of Atmospheric and Oceanic Technology, Vol. 17, pp. 165-175, February 2000.
6. Coombes C. A., Harrison A.W., *An Automatic All Sky Scanning Radiometer*, Can. J. Phys., 60, pp. 919-925, 1982.
7. Duffie J.A., Beckman W.A., *Solar Engineering of Thermal Processes*, John Wiley & Sons, Inc., USA, 1980.

8. Faiman D., Feuermann D., Ibbetson P, Zemel A., *A Multipyranometer Instrument for Obtaining the Solar Beam and Diffuse Components, and the Irradiance on Inclined Planes*, Solar Energy, Vol. 48, No. 4, pp. 253-259, 1992.
9. Fröhlich C., Julius L., *World Climate Research Programme: Revised Instruction Manual on Radiation Instruments and Measurements*, WCRP Publications Series No. 7, WMO/TD-No.149, October 1986.
10. Fröhlich C., Lean J., 1998, *The Suns Total Irradiance: Cycles, Trends and Related Climate Change Uncertainties since 1978*, Geophys.Res.Let., 25, pp. 4377-4380, 1998 (up to version 8).
11. Fröhlich C., *Observations of Irradiance Variations*, Space Science Reviews 00, pp. 1–10, 2000.
12. Fröhlich C., *Solar Irradiance Variability*, in: Chapter 2 of Geophysical Monograph Series, 111, American Geophysical Union, in press 2003
13. Grandum O., *Et automatisk målesystem for kartlegging av vinkel- og spektralfordeling av direkte og diffus solstråling*, PhD dissertation submitted to the Faculty of Physics, Informatics and Mathematics, Norwegian University of Science and Technology, Trondheim, Norway (in Norwegian), 1997.
14. Gueymard C., Myers D., Emery K., *Proposed Reference Irradiance Spectra for Solar Energy Systems Testing*, Solar Energy, Vol. 73, Issue 6, pp. 443-467, December 2002.
15. Gueymard C.A., *The Sun's Total and Spectral Irradiance for Solar Energy Applications and Solar Radiation Models*, Solar Energy, 76, pp. 423-453, 2004.
16. Gulbrandsen A., *On the Use of Pyranometers in the Study of Spectral Solar Radiation and Atmospheric Aerosols*, Journal of Applied Meteorology, Vol. 17, pp. 899-904, June 1978.
17. Haeffelin M., Kato S., Smith A.M., Rutledge C.K., Charlock T.P., Mahan J.R., *Determination of the Thermal Offset of the Eppley Precision Spectral Pyranometer*, Applied Optics, Vol. 40, No. 4, pp. 472-484, February 2001.
18. Hämäläinen M., Nurkkanen P., Slåen T., *A Multisensor Pyranometer for Determination of the Direct Component and Angular Distribution of Solar Radiation*, Solar Energy, Vol. 35, No. 6, pp. 511-525, 1985.
19. Heraeus, *Heraeus Windows*, http://www.fused-silica.com/uploads/100004_PDF/100010.doc, August 1998.
20. Iqbal M., *An Introduction to Solar Radiation*, Academic Press Canada, 1983.
21. Jeys T.H., Vant-Hull L.L., T*he Contribution of the Solar Aureole to the Measurements of Pyrheliometers*, Solar Energy, Vol. 18, pp. 343-348, 1976.
22. Ji Q., Tsay S., *On the Dome Effect of Eppley Pyrgeometers and Pyranometers*, Geophysical Research Letters, Vol. 27, No. 7, pp. 971-974, April 2000.
23. Kondratyev K.YA., *Radiation in the Atmosphere*, International Geophysics series, Vol. 12, 1969.
24. Major G., *On the Pointing Error of Pyrheliometers*, Material prepared for the BSRN discussion held in Davos, Switzerland, October 1995.

25. Major G., *The Role of Geometry amongst the Standard Pyrheliometers*, Quarterly Journal of the Hungarian Meteorological Service, 2, pp. 77-84, 1999.
26. Michalsky J., Dutton E., Rubes M., Nelson D., Stoffel T., Wesley M., Splitt M., DeLuisi J., *Optical Measurement of Surface Shortwave Irradiance using Current Instrumentation*, Journal of Atmospheric and Oceanic Technology, Vol. 16, pp. 55-69, January 1999.
27. Michalsky J.J., Berndt J. L., Schuster G. J., *A Microprocessor-Based Rotating Shadowband Radiometer*, Solar Energy, Vol. 36, No. 5, pp. 465-470, 1986.
28. Michalsky J.J., Harrison L.C., Berkheiser W.E., *Cosine Response Characteristics of Some Radiometric and Photometric Sensors*, Solar Energy, Vol. 54, No.6, pp. 397-402, 1995.
29. Nakamura H., Oki M., Koga Y., *New Sky Scanner for the Measurement of Sky Luminance Distribution*. Proceedings of the 22nd Session of the CIE 1(1), Melbourne, pp. 61–62, 1991.
30. Nast P.M., *Measurements of the Accuracy of Pyranometers*, Solar Energy, Vol. 31, No.3, pp. 279-282, 1983.
31. Philipona R., Heimo A., Hoegger B., *Investigations of Solar Radiation Detectors Using a Laboratory Test Facility for Solar Radiation Meteorological Instruments*, Solar Energy, Vol. 51, No. 2, pp. 159-163, 1993.
32. Robinson N, *Solar Radiation*, Elsevier Publishing Company, 1966.
33. Salby M.L., *Fundamentals of Atmospheric Physics*, International Geophysics series, Vol. 61, 1996.
34. Shen B., Robinson A.M., *Measurement and Analysis of the Step Response of Pyranometers Requiring Second-Order Correction*, Solar Energy, Vol. 49, No. 4, pp. 309-313, 1992.
35. Spencer J.W., *Fourier Series Representation of the Position of the Sun*, Search 2 (5), 172, 1971.
36. Stoffel T.L., Reda I., Myers D.R., Renne D., Wilcox S.W., Treadwell J., *Current Issues in Terrestrial Solar Radiation Instrumentation for Energy, Climate and Space Applications*, NREL/CP-560-27094, October 1999.
37. Suehrcke H., Ling C.P., McCormick P.G., *The Dynamic Response of Instruments Measuring Instantaneous Solar Radiation*, Solar Energy, Vol. 44, No. 3, pp. 145-148, 1990.
38. Thacher P.D., William E. B., King D.L., *Investigation of Factors Influencing the Accuracy of Pyrheliometer Calibrations*, Technical Reports about PV Modules and Arrays, Sandia National Laboratories, Albuquerque, April 2000.
39. Winans L.J., *Sunshine sensor testing for ASOS Product Improvement*, Sixth Symposium on Integrated Observing Systems, Orlando, FL, 2002.
40. WMO-No.8, *Guide to Meteorological Instruments and Methods of Observation*, Secretariat of the World Meteor. Org., Geneva, Switzerland, 1997

Chapter 2

Radiation Mapping

This chapter discusses the solar radiation mapping, global and direct, for sites at UKZN and NTNU. A detailed description of the data-acquiring system at UKZN (partially copied at NTNU and soon at the Mangosuthu Technikon, South Africa and the Eduardo Mondlane University, Mozambique) is given.

2.1. Introduction

There is an international call for high quality solar irradiance data. Networks, such as the Global Atmosphere Watch (GAW) and the Baseline Radiation Network (BSRN) have set up mapping sites about the globe. Measurements from stations associated with GAW and the BSRN, as well as from independent sites, are critical to numerous applications (some of which are discussed in Chapter 1).

The international network with standardised observations use reliable pyranometers in the mapping of global solar irradiance. A normal incidence pyrheliometer may be present at most of the sites for the acquisition of direct solar irradiance. Data acquisition (DAQ) frequency, reliability and accuracy impact on the data quality. Data storage and transfer are an integral part of the DAQ system. DAQ system implementation of data processing, validation and quality-control are essential for the highest possible quality and for the processing of the data into a form which is appropriate for the intended uses. Guidelines for measuring instruments, DAQ systems and the post processing of data for high accuracy are given in literature such as [7.] and [15.].

The independent sites at the UKZN and NTNU also provide high quality solar irradiance data. The UKZN, in collaboration with NTNU have set up SELFRAD, the Solar Energy Laboratory for Rural African Development. A division of SELFRAD is the Resource Measurement Unit that has a platform for instrument mounting and a resource measurement laboratory (RML) for data logging/publishing. The NTNU station has been designed for daily DAQ and to facilitate regional and National instrument calibrations.

2.2. The Observation Sites

The choice of location for a solar platform is critical. Some of the factors considered for the platform at NTNU and at UKZN are obstructions between the pyrheliometer and the sun, obstructions extending above the pyranometer horizon, limitation of noise from cabling between instruments and the data acquisition system, remote sources of electromagnetic interference, shadows of the direct sun onto the instruments and safe and easy access to the site for maintenance and experiments.

The solar platform at the UKZN is on the roof of the Physics building at the Durban-Westville Campus, South Africa on latitude S29^{o}49'2'' and longitude E30^{o}56'40''. The platform is 205m above the mean sea level. With its sub-tropic location, the UKZN site has a maximum solar altitude of 83.6^o in the mid-summer and correspondingly, 36.7^o in the mid-winter. FIGURE 2.1 gives the plot of the platform's viewed horizon and the transition of the solar azimuth and altitude angles through a year. The present viewed horizon is not higher than 3^o and is not along the sun's path. The site albedo due to natural ground cover is considered to be about 0.2[1], which is an average albedo between dry and green grass. However, UKZN is a mass of buildings, and is further surrounded by a suburban settlement. Thus the site's albedo may be influenced by the buildings' material. The platform itself is surrounded by corrugated roofing sheets which gives off an albedo of about 0.3.

NTNU's present solar platform is a galvanised-steel-gridded deck on the roof of Block E, the Natural Sciences building, Gløshaugen, Trondheim, Norway. The site is located at 63.5^o North and 10.5^o East, 72m above mean sea level. Instrumentation on the platform have a clear view of the natural horizon due Northeast-to-South-to-Northwest. The natural horizon due Northwest-to-North-to-Northeast is obscured by the building columns and ventilation shafts. A graph of the platform's viewed horizon is given in FIGURE 2.2. It is noted that the altitude of the viewed horizon is below 5.5^o. The viewed horizon gives at most one hour of sun obstruction. Due to NTNU's latitude, the ground albedo at NTNU varies significantly with season.

1. All albedo numbers are with reference to Iqbal in [11., 1983].

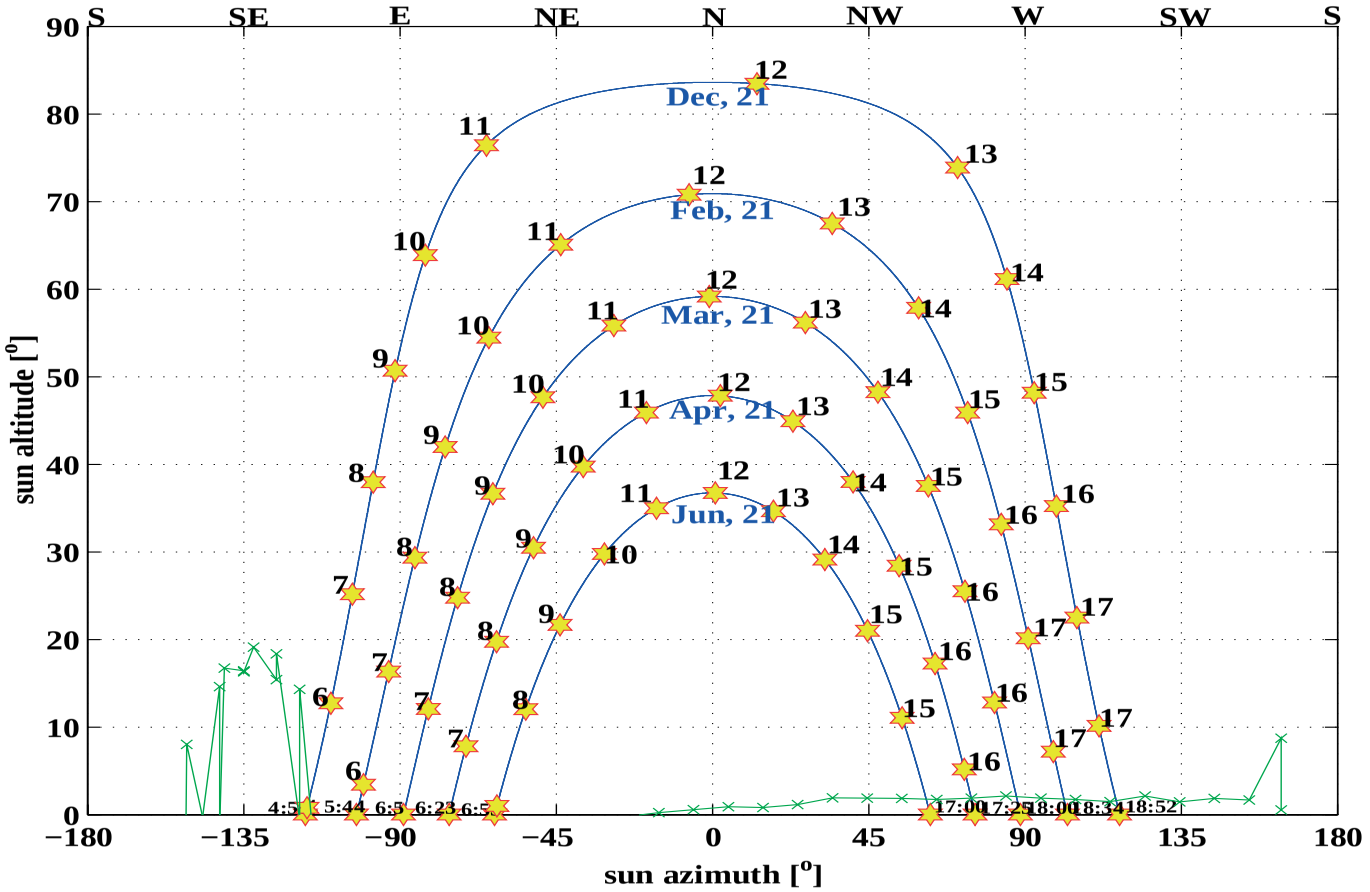

FIGURE 2.1
Horizon plot (x-) for UKZN's solar platform as a function of altitude. The sun's path over time of day is denoted by the curves along the selected months (¤-).

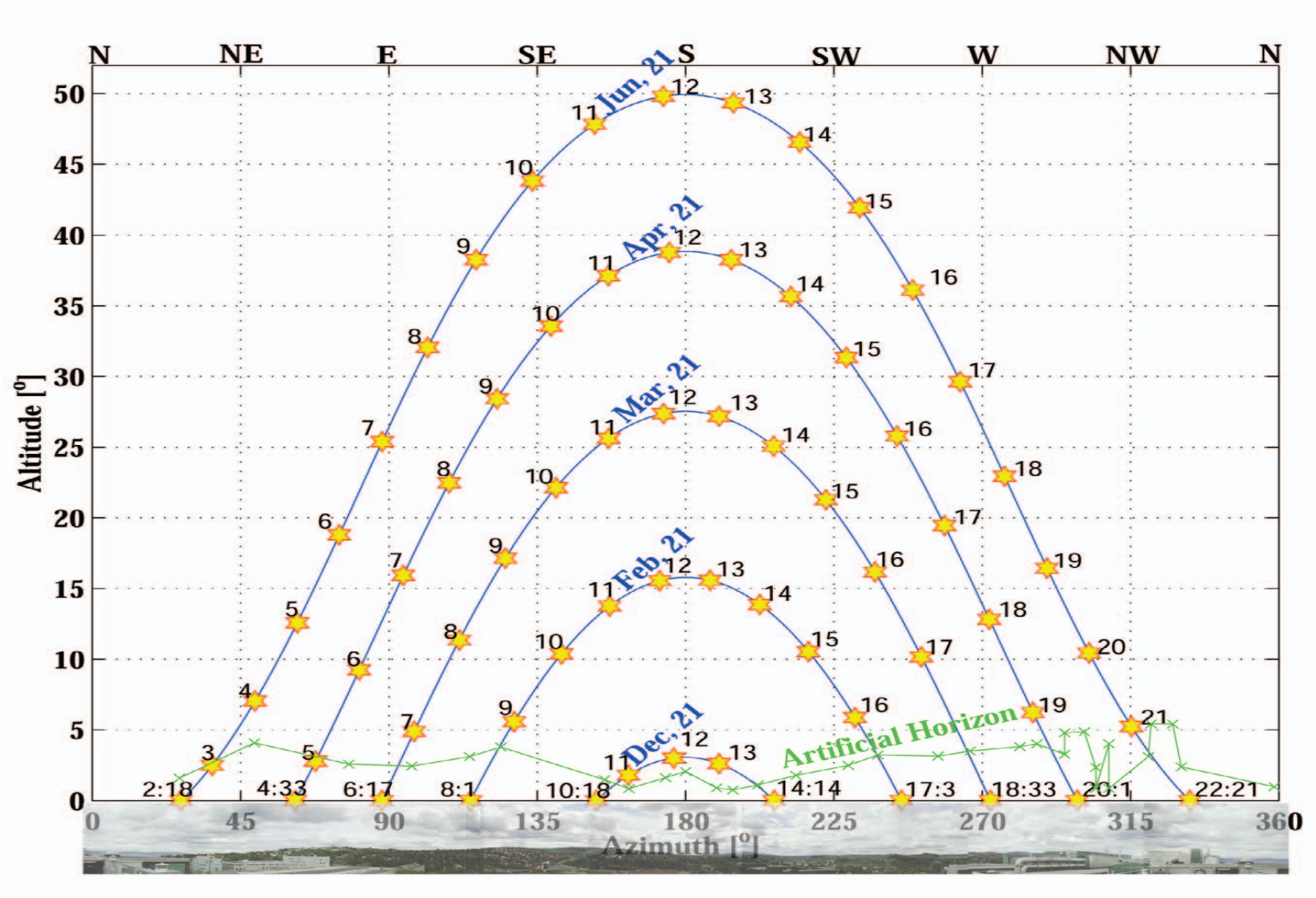

FIGURE 2.2
Horizon plot (x-) for NTNU's solar platform as a function of altitude. The sun's path over time of day is denoted by the curves along the selected months (¤-)

The ground is covered by snow during most of winter (2nd half of December, January and February), early spring (March) and occasionally in the months April, May, October and/or November. During the summer months (June, July and early August), the surrounding is mostly lush green. Golden leaves usually cover the ground in the autumn months. The albedo may thus be as high as 0.8 (newly fallen snow), or as low as 0.1 (bare ground at the onset of spring).

2.3. Site Radiometers

Measurements of direct solar irradiance at UKZN and NTNU are taken with Eppley normal incidence pyrheliometers (NIP). Global solar irradiance is mapped with Eppley precision spectral pyranometers (PSP). The PSPs at UKZN and NTNU are housed in Eppley ventilators, with the intention of reducing particle build-up on the instruments' dome and to downsize thermal offset. To keep in normal incidence to the sun, the NIP's are mounted on a solar tracker. UKZN and NTNU first used an electrically driven tracker (using a clock-based motor that makes one revolution every 24 hours) which requires frequent manual adjustments for declination and equation of time. The current trackers at both sites require minimal maintenance due to its autonomous operation.

2.3.1. Site Radiometers: UKZN

The mapping radiometers at UKZN are NIP#31127E6 and PSP#31234F3. They have been up and running since 1996. A second PSP is used for PSP on-field calibration.

2.3.2. Site Radiometers: NTNU

There are currently 2 mapping NIPs at NTNU. These are NIP#21132E6 and NIP#31856E6. The NIP#21132E6 was mounted on site at Lade in 1981 and then relocated to Gløshaugen in 2000. NIP#31856E6 was purchased from Eplab in 2000 and mounted on site at Gløshaugen in 2001.

There are currently 2 mapping PSPs at NTNU. These are PSP#16577F3 and PSP#33049F3. The PSP#16577F3 was mounted at the University of

Trondheim in 1977 and is now at Gløshaugen, since 2000. PSP#33049F3 was purchased from Eplab in 2000 and mounted on site at Gløshaugen in 2001.

2.4. Data Acquisition

This section describes the system used for acquiring, converting and saving the data received from the radiometers at both UKZN and NTNU.

2.4.1. Data Acquisition: UKZN

The data acquisition system at UKZN has been changed thrice since 1996. Not all the data is available due to lack of maintenance and/or power failures. A period of data from 1996 to 1997 is lost due to fatuous re-formatting of the system hard disk. Unfortunately all backup (at that time made on stiffy diskettes) have been misplaced. The current acquisition system at UKZN ensures real-time data backup to another PC and has a UPS system to monitor power failures and provide backup power for a limited time.

The following 3 sections give an overview of all three systems and discusses their disadvantages/advantages.

2.4.1.1. System1$_{UKZN}$ (June 1996 - August 1998)

A complete description of the first acquisition system developed for UKZN, referred to as System1$_{UKZN}$ (S1$_{UKZN}$) in this work, is given by Dhavraj in [3., 1998]. The gist here was an internal DAQ-card and software developed in the Quick Basic version 4.5 environment. The system summary is given in Table 2A and FIGURE 2.3 illustrates the system layout.

Dhavraj, in [3.], discusses the draw backs of such a system:

* a multitude of random PC-generated noise due to the unshielded PC-embedded DAQ-card.

* frequent monitoring of the calibration validity of the digital-to-

analog and analog-to-digital converters, leading to

* halts in data acquisition and thus loss in data,

* insufficient hard disk space meant off-loading data files.

For the period June 1996 to August 1998 just 15% of the acquired data is available and valid.

Table 2A: System Summary-$S1_{UKZN}$

DAQ	PC-74 LC board and PC-77 terminal board
Sampling Period	<0.01 second
Averaging Period	1 minute
Backup System	manual (to floppy)
Data Online	not available
Radiometers	NIP#31127E6, PSP#31234F3
Solar Tracker	ST-3

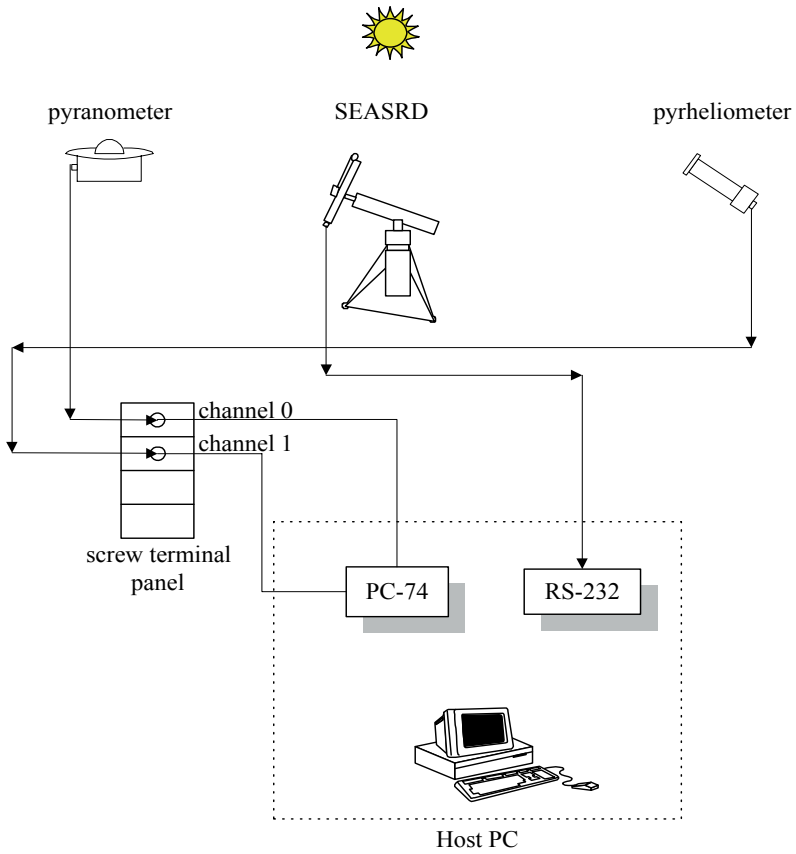

FIGURE 2.3
Schematic layout for $S1_{UKZN}$.

Table 2B: System Summary - $S2_{UKZN}$

DAQ	HP34970A Data Acquisition/Switch Unit with an HP349701A MUX.
Sampling Period	4 second
Averaging Period	1 minute
Backup System	automatic to floppy disk, CD, and local network.
Data Online	once a week using Apache
Radiometers	NIP#31127E6, PSP#31234F3, DDSR-1A
Solar Tracker	Eppley ST-3

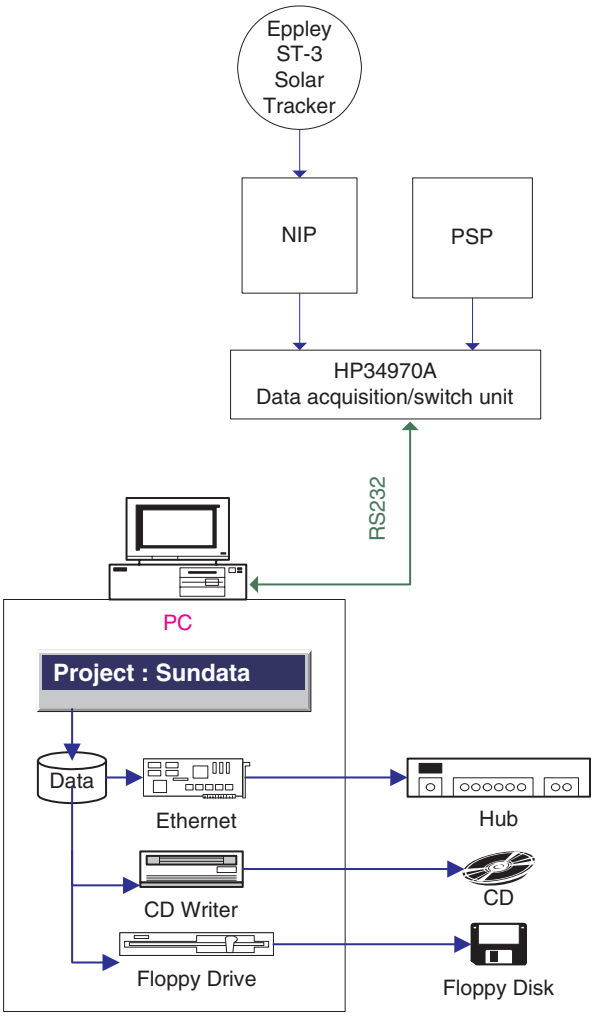

FIGURE 2.4
Schematic layout for $S2_{UKZN}$.

2.4.1.2. System2$_{UKZN}$ (August 1998-2001)

In the second system, System2$_{UKZN}$ (S2$_{UKZN}$), data from both the NIP and the PSP were acquired via the 'stand-alone' HP34970A data acquisition/switch unit and developed software, '*Project: Sundata.vbp*', under the visual basic environment. The system summary is given in Table 2B and FIGURE 2.4 illustrates the system layout.

Features:

* one minute averaged data read from the HP34970A unit and written to file,
* auto-calibration of the HP34970A to avoid unnecessary interruption to data acquisition,
* uninterruptability by view of multi-tasking,
* easily traceable subroutines and functions with the aid of forms and modules,
* timer interrupts for the time management of data collection from the HP34970A instrument.

Drawbacks:

* Automatic backup of files made once daily, but to floppy disk.
* Infrequent data copy to the network location. The DOS command file copied the data files to the network location *only once a week* to reduce application buildup.
* Acquisition with the PC-clock meant non-coherence with universal time.

2.4.1.3. System3$_{UKZN}$ (March 2001 to present)

Data from both the NIP and the PSP is currently acquired via the HP34970A data acquisition/switch unit, which is controlled by developed software in the Labview environment. Table 2C gives the system summary of System3$_{UKZN}$ (S3$_{UKZN}$) and FIGURE 2.5 gives a schematic overview of this system.:

Table 2CSystem Summary - S3$_{UKZN}$

DAQ	HP34970A Data Acquisition/Switch Unit with an HP349701A MUX.
Sampling Period	4 seconds
Averaging Period	1 minute
Backup System	automatic to a second PC, and local network.
Data Online	realtime (graphic + raw data with/without stats.)
Radiometers	NIP#31127E6, PSP#31234F3
Solar Tracker	Brusag: Intra (Automatic tracker)

There are two PCs in S3$_{UKZN}$. PC 1 serves as a backup for radiometer data from PC 2 and, at the same time, publishes data to the world wide web (www). One PC would have been sufficient for data acquisition and web publishing, but at the expense of a system that could run uninterrupted by time outs in checking for server access or by a secure environment, free from hacking.

PC 2 runs the ACQUIRE.vi which:

* acquires the radiometer data,
* calls on the external program, Dimension 4 to synchronise the PC clock to a timeserver, with reference to Chambers in [2., 1998].
* calls on Winzip to compress the data files,
* creates a jpeg file containing a ‘print-screen’ of the front panel for web publishing, and
* copies files over to PC 1’s root internet publishing directory.

Besides the software transition to the current system, three additional features have been included:

* An automatic solar tracker, INTRA, is used for the NIP mount instead of the 'manual' ST-3.
* two sky cams capture due west and due east sky conditions, hourly, and saves them as graphical files of jpeg format. The sky cams are controlled in PC 1 by the Supervision CAM software developed by Kirst in [12., 2002].
* an uninterruptable power supply (UPS) with 2 additional battery packs is used to supply power to all units for an hour upon mains power failure and then to systematically shut down the PCs'.

All published information are accessible at the Internet Resource Locator (URL):

http://www.phys.ntnu.no/~dhavraj/UDW/HTML/SELFRAD_MAIN.htm.

The one-minute averages are published in real-time for local comparisons. An image of the display screen (with site information and a scatter plot for each one-minute data) are published and refreshed each minute. The sky pictures are also published in real time. The one-minute data records for the day are compressed and put on-line at the end of each day. The data archive (from 1997 to present) is also available for downloading via the above URL.

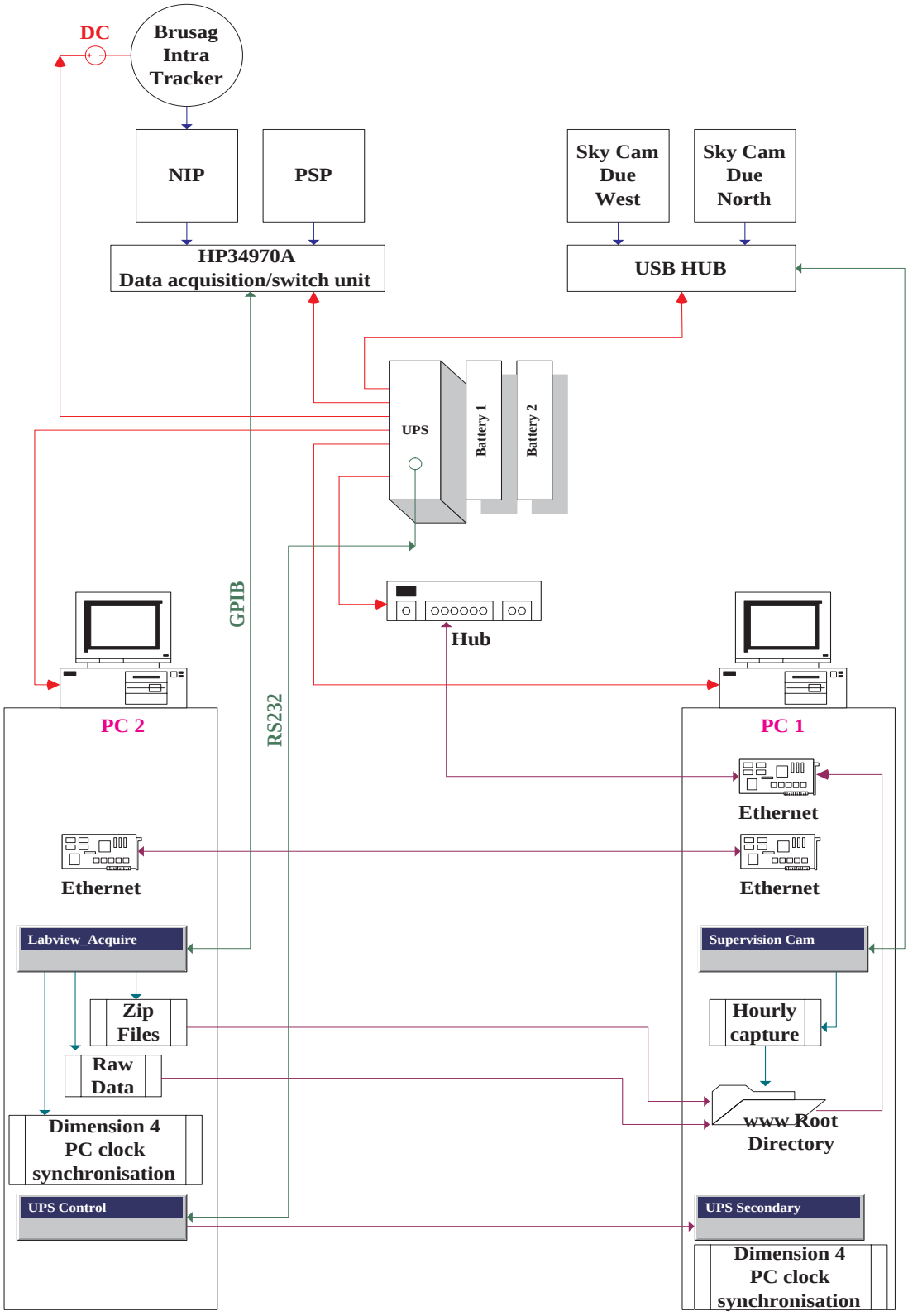

FIGURE 2.5
Schematic layout of the present data acquisition system, $S3_{UKZN}$ at UKZN.

2.4.2. Data Acquisition: NTNU

Since 1978 to present, the data acquisition system for NTNU has been changed three times. The first system, $System1_{NTNU}$ ($S1_{NTNU}$) was set up and run in the period 1978 to 1984. The second, $System2_{NTNU}$ ($S2_{NTNU}$) was set up and run in the period 1991 to 2001. The current set up, $System3_{NTNU}$ ($S3_{NTNU}$) has been in operation since 2001.

2.4.2.1. $System1_{NTNU}$ (1978-1984)

Brevik in [1.,1984] describes the acquisition system within the period 1978-1984. The schematic in FIGURE 2.6 illustrates the system and Table 2D gives a summary.

2.4.2.2. $System2_{NTNU}$ (1991-2001)

Amongst others, Grandum in [8., 1991] and Hveem in [10., 1998] give descriptions of $S2_{NTNU}$. The schematic in FIGURE 2.7 illustrates the system and Table 2E gives a summary.

2.4.2.3. $System3_{NTNU}$ (2001-present)

The current system at NTNU, Gloshaugen has been mapping data since 2001. The system is a replica of the current system at UKZN, except for the UPS, second PC and sky cameras. Sky cameras are not used as yet due to the cost/availability of weatherproof cameras. Instead of the second PC for web publishing, the logging PC's data directory is 'securely' shared with a user on the local area network (LAN) for data backup purposes.

Table 2D: System Summary - $S1_{NTNU}$

DAQ	HP9825A microcomputer with scanner and digital voltmeter
Sampling Period	* 20 minutes (up to Summer 1981) ¤ 10 seconds (up to Summer 1983) ø 3 seconds
Averaging Period	* single reading every 20 minutes (up to Summer 1981) ¤ 5 minutes (up to Summer 1983) ø 1 minute
Data Storage	automatic transfer to Digital/Vax 750 central computer
Data Backup	floppy discs, magnetic tape
Radiometers	Eppley NIP(1977), Eppley PSP
Solar Tracker	Eppley ST-1

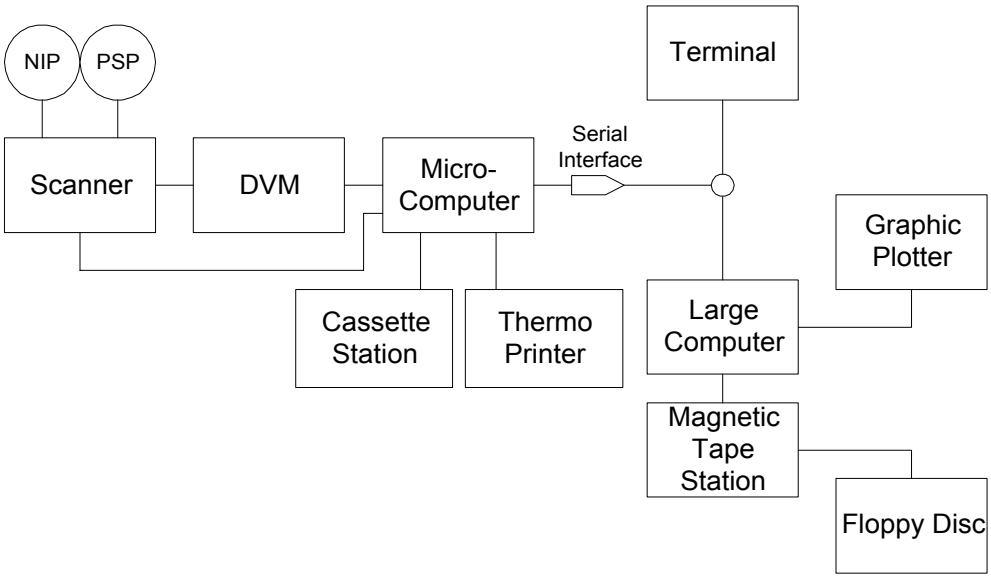

FIGURE 2.6
Schematic layout for $S1_{NTNU}$.

Table 2E: System Summary - $S2_{NTNU}$

DAQ	386Mhz PC (dos) with scanner and digital voltmeter
Sampling Period	5 seconds
Averaging Period	1 minute
Data Storage	monthly manual transfer to VAX
Data Backup	magnetic tape
Radiometers	Eppley NIP (#21132E6, 1981) Eppley PSP (#16577F3, 1977)
Solar Tracker	Eppley ST-1

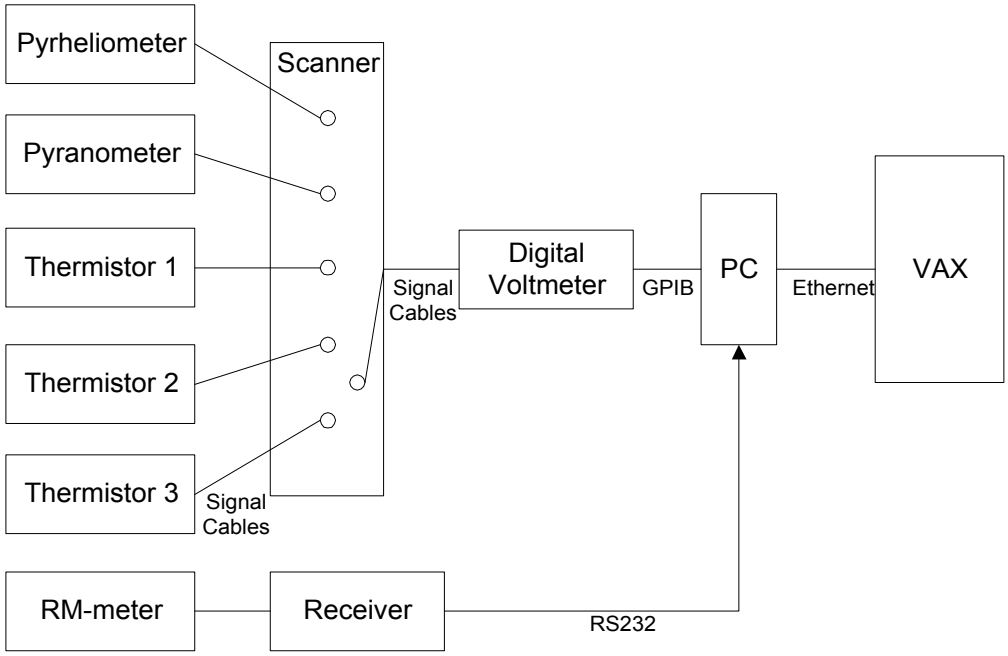

FIGURE 2.7
Schematic layout for $S2_{NTNU}$.

2.4.3. System Assessment

2.4.3.1. The Baseline Surface Radiation Network

The current data acquisition systems at UKZN and NTNU have been designed to meet the Baseline Surface Radiation Network (BSRN) recommendations, as given by McArthur in [13., 1998], on data acquisitioning. Table 2F gives the BSRN's recommendations and shows that the current systems, $S3_{UKZN}$ and $S3_{NTNU}$, meet (except for the sampling period) the BSRN set of recommendations. ***In addition, the $S3_{UKZN}$ makes data available to the world-wide web in real-time.***

Table 2F: System comparisons with BSRN requirements.

	BSRN Requirement	NTNU	UKZN
Sampling Period (sec)	1	4	4
Averaging Period (min)	1	1	1
Time Accuracy	1s	50ms*	50ms*
DAQ System** Accuracy	±0.01% or ±1μV	±0.009% or ±4μV***	±0.009% or ±4μV***
World-Wide Data Availa-bilty	transfer once every month	on request	real-time

* achieved by use of Dimension 4.

**% of reading or range error, whichever is greater.

*** a 40μV signal (~4.5Wm^{-2}) has a 10% error, an 8.8mV signal (~1000Wm^{-2}) has a 0.05% error.

2.4.3.2. Sampling Frequency

The DAQ sampling period is proposed by the response time of the radiometers. The Eppley radiometers have a response time of about 1-second. It may therefore be possible to collect 60 near independent samples within 1-minute. Continuous switching of the relays on the S3 DAQ multiplexer modules may result in a relay life of about 3½ years (assuming a relay lifetime of 100-million counts [9., 1997], and a 1-second switching period). Presently, the S3 DAQ systems take radiometer readings once every 4-seconds. This period extends the relay life to about 13-years. A

total of 15 samples are acquired for each 1-minute average record with the 4-second sampling period. If there is a sudden change from S_{mo} to 0 in direct radiation in the middle of the 1-minute period, the standard deviation estimate is approximately $S_{mo}/2$, independent of logging rate. The maximum error in the energy estimate by such a sudden change is $\pm S_{mo} \cdot (T_s/2)$ where T_s is the sampling period. For hourly values or daily values a sampling period of 4-second is fully adequate. But if one wants to study the power spectrum of the radiation, the highest frequency is $f = 1/(2T_s)$; and small T_s gives a higher Nyquist frequency.

An investigation into the data sampling speed has been made. The output from the NIPs and PSPs at NTNU were taken with a sampling frequency of around $1.6Hz$. The measuring equipment is a replica of $S3_{NTNU}$ to avoid disruptions to routine measurements. Data was collected for 19 days from the 15th of May 2004. Data from five of the 19 days have been considered for a representation of different sky conditions. The irradiance data from the NIP and PSP for each of the days are shown in the plots of FIGURE 2.8, together with the hourly wind speeds. The wind speeds are included for an indication of the rapidity of cloud movement on the partly cloudy days.

The analysis approach for any of the selected days are as follows:

i. a reference energy E_{Ref} for the day is calculated by integration of the observed irradiances (from sunrise to sunset) with respect to the corresponding sampling times,

ii. new irradiances and time arrays are generated by linear interpolation with a time step Δt, where Δt is the new sampling period.

iii. energies $E_{\Delta t}$ for the day are calculated by integration of the new irradiances with respect to the new time arrays,

iv. the relative energy difference $E_{diff} = \frac{|E_{ref} - E_{\Delta t}|}{E_{ref}} \times 100\%$ is calculated.

v. Procedures (ii) to (iv) are repeated for all the desired values of sampling period.

The results of the analysis, for sampling periods up to $60s$ are given in FIGURE 2.9(a) and FIGURE 2.9(b) for the direct and global irradiances, respectively. The energy differences increase with an increase in sampling period, as is expected. In addition, the slopes depend on the sky condition. The slopes for the clear sky days of the 30^{th} and 31^{st} of May are such that the relative energy differences are below 0.01% for all of the sampling periods. A $1-minute$ sampling period generates differences of up to 0.6% for PSP and 5% for the NIP (for the 17^{th} of May). However, the PSP energy differences at $4s$ are below 0.01% for all days. The same is true for the NIP except on the 19^{th} and 27^{th} of May. On these days the relative differences at $4s$ are below 0.03%. In absolute terms, the PSP daily energy estimates, sampled at a period of $4s$ gives a maximum uncertainty of $0.14Wh$ for the selected days. Likewise, the maximum uncertainty for the NIP is $0.28Wh$.

It is expected that the percentage of daily energy difference due to $S3_{NTNU}$'s sampling period of $4s$ should be no higher than 0.0003% for derivations from the NIPs and PSPs on clear sky days. This corresponds to daily energy uncertainties of less than $0.02Wh$. For partly cloudy sky days the energy differences are expected to be below 0.05%, corresponding to daily energy uncertainties of less than $1Wh$.

It is realised that the results from the few observation days for the above test do not represent all sky conditions and is only valid in the Trondheim region. It may also be concluded that the estimation of weather conditions and quality of data may be evaluated from high-speed sampling but is left for further investigation outside this dissertation.

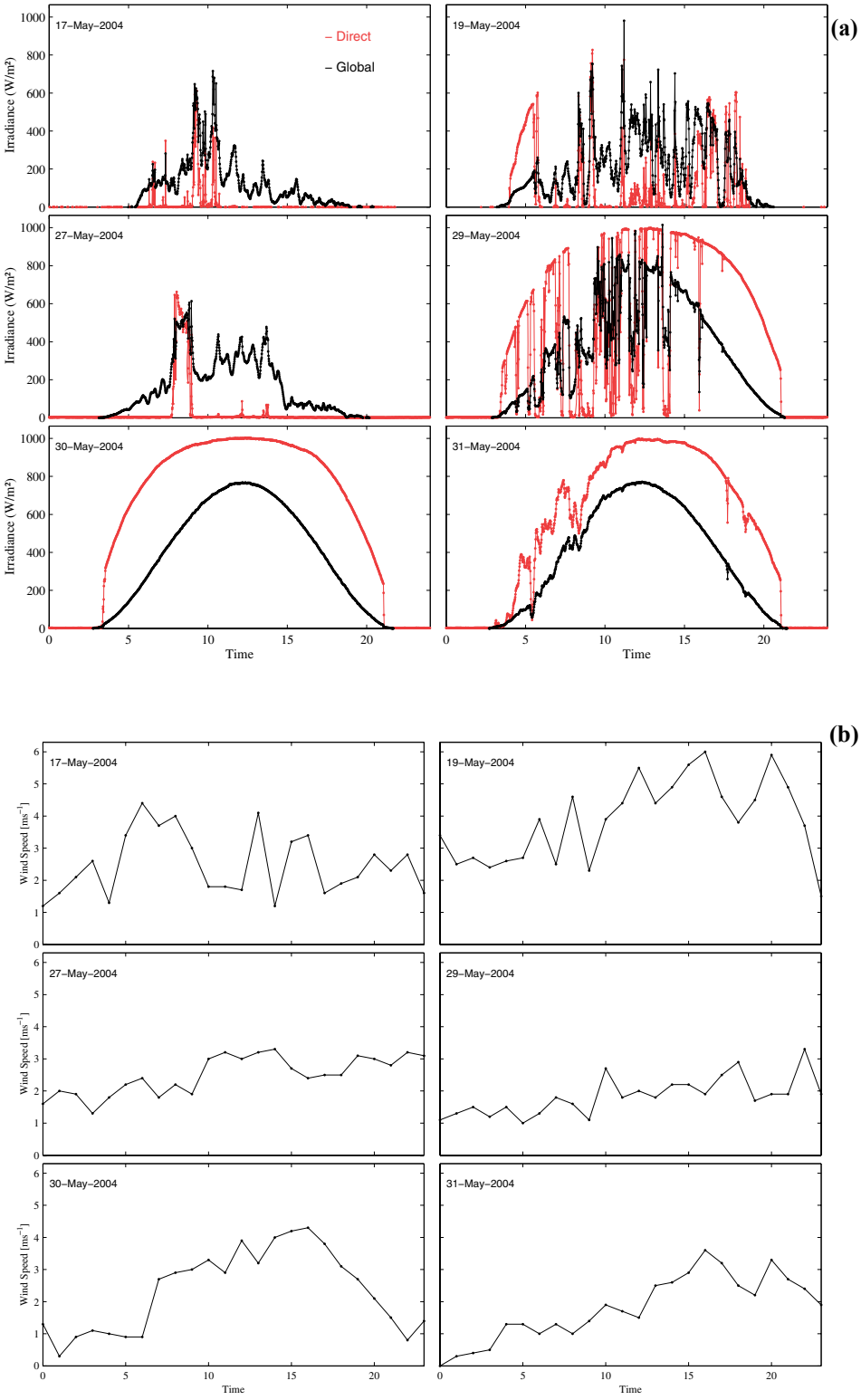

FIGURE 2.8
(a) Selected direct and global solar irradiance logs from the NIP and PSP at NTNU, sampled at $\sim 1.6Hz$. **(b)** Hourly wind speeds for Trondheim-Voll. © Klima, met.no.

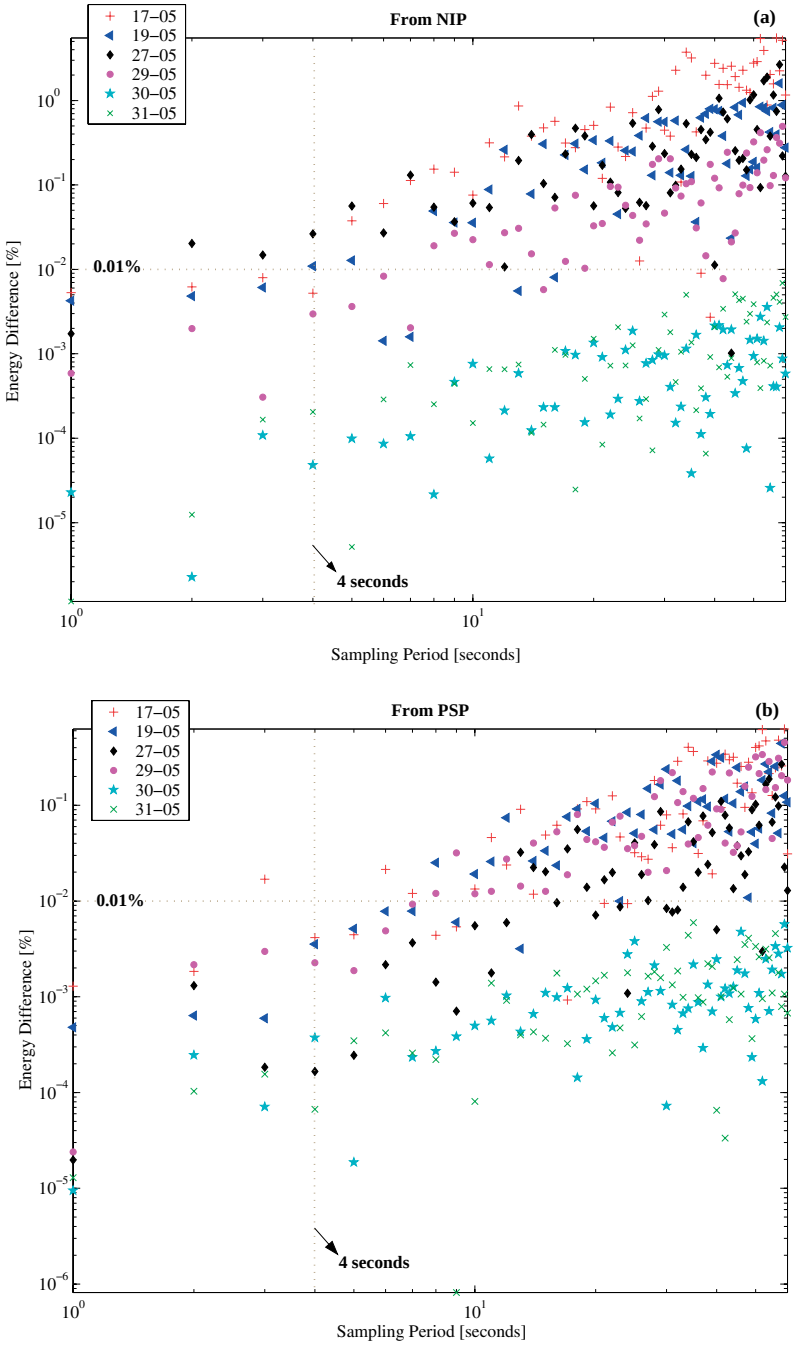

FIGURE 2.9
Estimated relative differences in the daily energy for variable sampling periods. The reference energy is the total energy calculated as an integration of each sampled irradiance with respect to its sampling time.

2.4.4. Automation

An efficient solar radiation data logging network depends on the level of automation. An annum status analysis for data collected at UKZN since 1996 has been made. All data for 1996 is lost, and validity of data for the proceeding years (i.e. 1997 to 2002) are 5%, 14%, 40%, 87%, 56% and 78% respectively. These are shown by the status maps of FIGURE 2.10(a) to FIGURE 2.10(f). There is a 100% validity since $S3_{UKZN}$ has been in operation (i.e. since March 19, 2002). Validity of data at UKZN is influenced by the frequency of instrument maintenance, power failures and data backup. A higher status has been achieved:

* on changing the NIP's ST-3 solar tracker mount to the Intra (automatic) tracker. There is now no occurrence of cable breakage or instrument misalignment.
* with a UPS system for power failure monitoring, backup power supply and systematic system shutdowns.
* with the incorporation of an automatic data backup system.
* with the incorporation of a secure LAN/WAN system for data transfer/publishing.

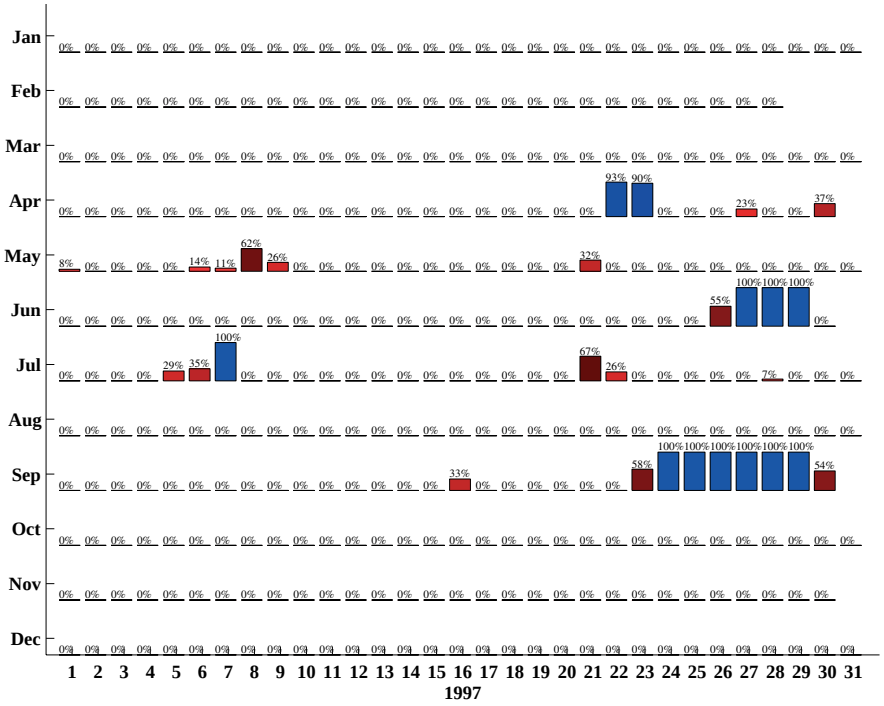

FIGURE 2.10(a)
Status of NIP data for UKZN in 1997.

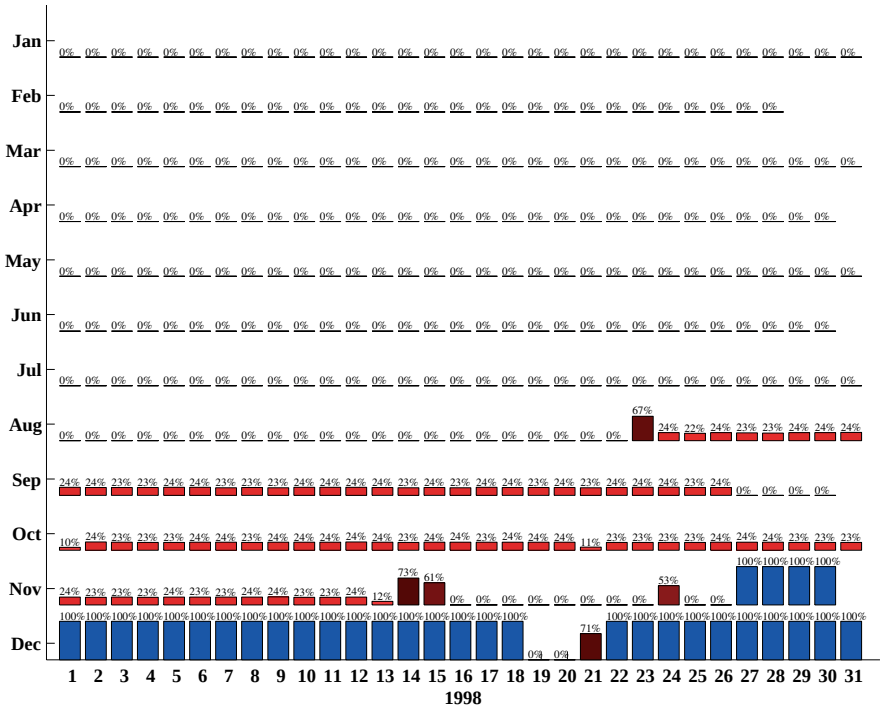

FIGURE 2.10(b)
Status of NIP data for UKZN in 1998.

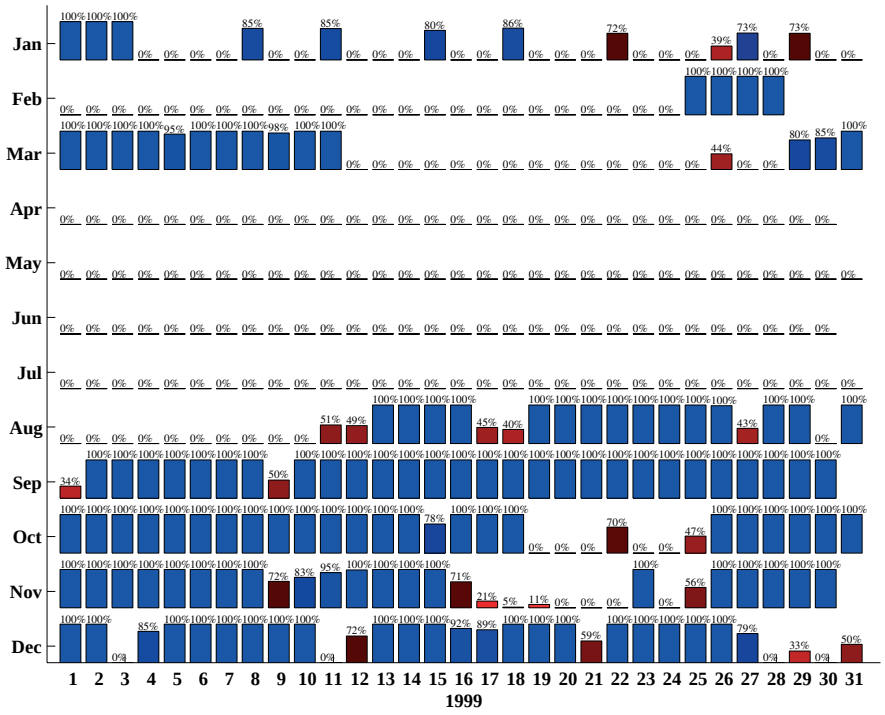

FIGURE 2.10(c)
Status of NIP data for UKZN in 1999.

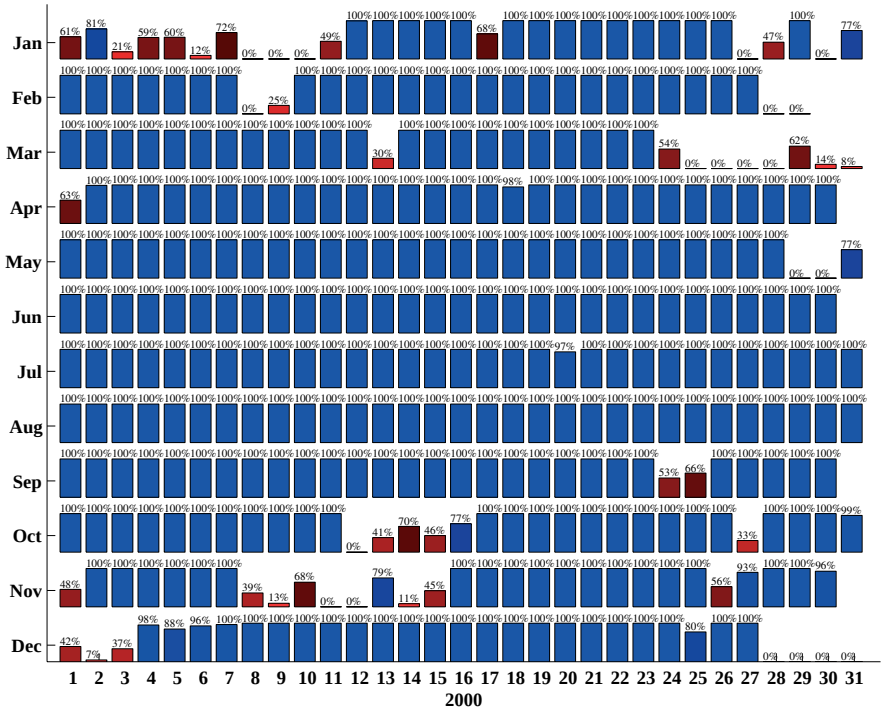

FIGURE 2.10(d)
Status of NIP data for UKZN in 2000.

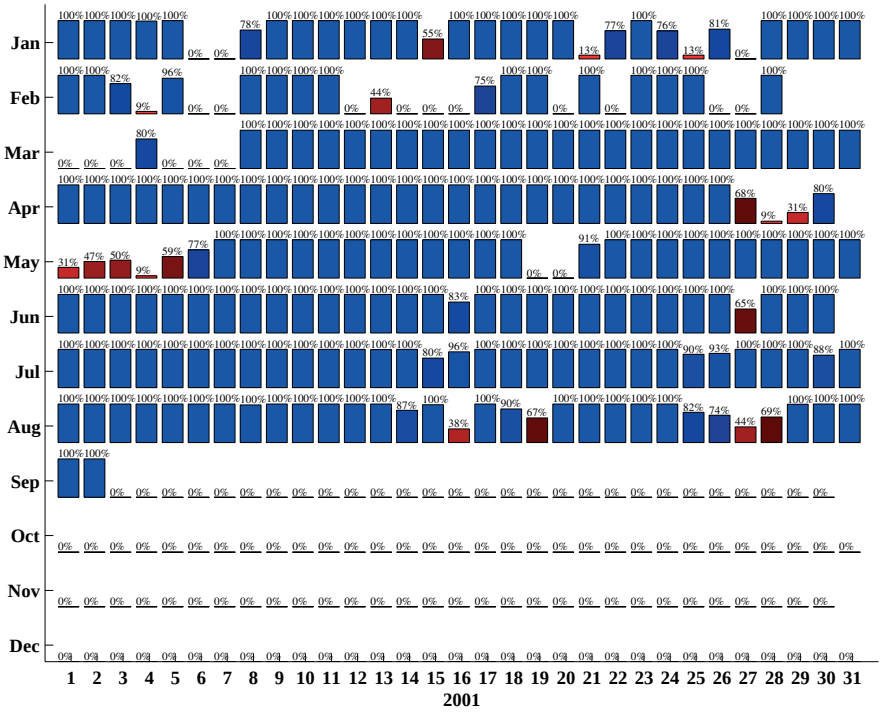

FIGURE 2.10(e)
Status of NIP data for UKZN in 2001.

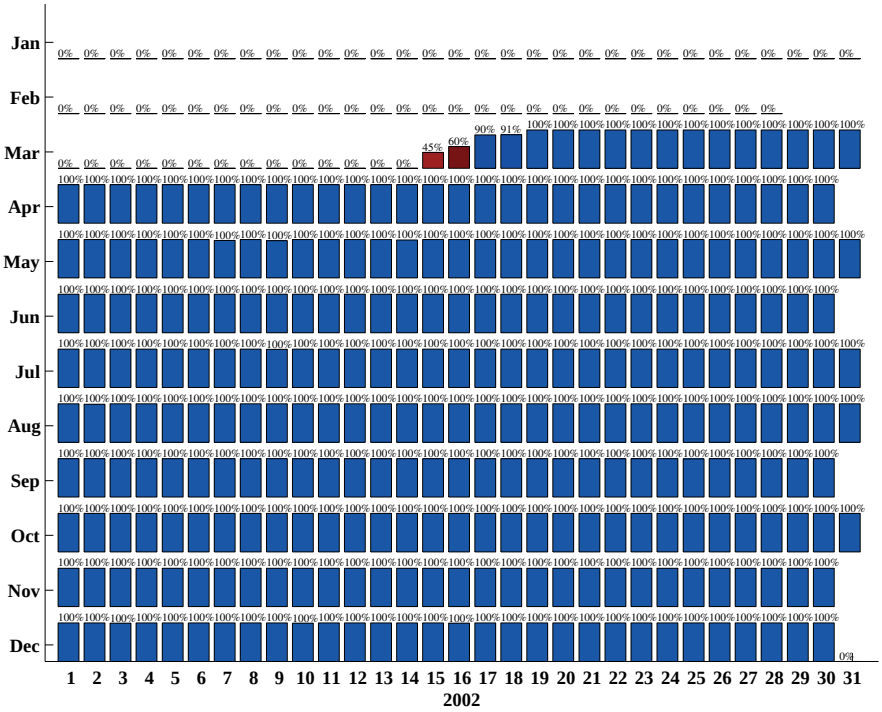

FIGURE 2.10(f)
Status of NIP data for UKZN in 2002.

2.5. Chapter Summary and Conclusions

Descriptions of the solar radiation mapping sites and the data acquisition systems at UKZN and NTNU have been given. It has been shown that a 4*s* sampling period is adequate to keep daily energy uncertainties below 1*Wh* and that system automation increases the status of data.

2.6. References

1. Brevik I., *Models of the Direct and Diffuse Solar Radiation*, Department of Physics, University of Tondheim, 1984
2. Chambers R., Dimension 4 Version 4.3, 1998
3. Dhavraj M.D., *The Setting Up and Calibration of Radiometers for the Measurements of Direct and Diffuse Solar Radiation at the University of Durban-Westville, UDW*, 1998
4. EPLAB, *Eppley Normal Incidence Pyrheliometer: Specifications*, (appendum to NIP SN31127E6), 1996

5. EPLAB, *Eppley Precision Pyranometer: Instrument Characteristics*, (appendum to PSP SN31234F3), 1996.
6. EPLAB, *Instruction Sheet for the Eppley Precision Pyranometer*, 1995
7. Fröhlich C., Julius L., *Revised Instruction Manual on Radiation Instruments and Measurements*, WMO/TD-No-149, WCRP Publications Series No. 7, Oct. 1986.
8. Grandum O., *Program maaling*, (developed software), Dept. of Physics, NTNU, 1991.
9. Hewlett Packard, *HP34970A Data Acquisition/Switch Unit: User's Guide*, 2nd ed. October 1997.
10. Hveem C., *Eksperimentelt Studuim av Forskjellige tidsserier for solstråling og analyse av variasjonsmønsteret*, Fysisk institutt, NTNU, 1998
11. Iqbal M., *An Introduction to Solar Radiation*, Academic Press, Canada, 1983.
12. Kirst P., *Supervision Cam*, Shareware, 2002
13. McArthur L.J.B., *BSRN Operations Manual version 1.0*, World Climate Research Programme, WMO/TD-No. 879, February 1998
14. Myers D.R., Stoffel T.L., Reda I., Wilcox S.M., Andreas A.M., *Recent Progress in Reducing the Uncertainty in and Improving Pyranometer Calibrations*, Journal of Solar Energy Engineering, Vol. 124, pp. 44-50, February 2002
15. Ohmura A. et al., *BSRN/WRCP: New Precision Radiometry for Climate Research*, American Meteorological Society, Vol. 79, No. 10, Oct. 1998.
16. WMO-No.8, *Guide to Meteorological Instruments and Methods of Observation*, Secretariat of the World Meteor. Org., Geneva, Switzerland, 1997

Chapter 3
Radiometer Calibration

Regular radiometer calibration is necessary to ensure data certainty/quality. The methodology for and results from calibration of the radiometers are given.

3.1. The World Radiometric Reference

The World Radiometric Reference (WRR) is a measurement standard representing the SI unit of solar irradiance and is obtained from the weighted mean of direct solar measurements from a diverse group of absolute cavity pyrheliometers. The World Meteorological Organisation (WMO) introduced the mandatory use of the WRR in 1979 and is in use since the 5th international pyrheliometer comparison in 1980. According to Fröhlich in [3., 1991], the WRR has an estimated accuracy of 0.3%.

An international pyrheliometer comparison (IPC) is held every five years to compare absolute radiometers from the Regional Radiation Centres. The comparison is made against a World Standard Group (WSG). These comparisons ensure world-wide irradiance measurement homogeneity since the WSG transfers the WRR, with the sun as the source, with a precision of less than 0.1%. The transfer mechanism of the WRR is given in section 3.2.

The WSG is maintained at the World Radiation Centre (WRC) in Davos, Switzerland. These instruments are pyrheliometers of primary standard type, meaning that they have a high characterisation quality, a cavity type receiver and an electrically calibrated heat flux meter (pyrheliometer classification is defined by the WMO in [8, 1997]). At the moment the WSG consists of 6 pyrheliometers: PMO-2, PMO-5, CROM-2L, PACRAD-3, TMI-67814 and HF-18748. These are indicated in the FIGURE 3.1.

The radiometers at UKZN and NTNU are traceable to the WRR by manufacture certification and by frequent calibrations against an absolute cavity pyrheliometer, the Eppley model HF31117 (see section 3.3).

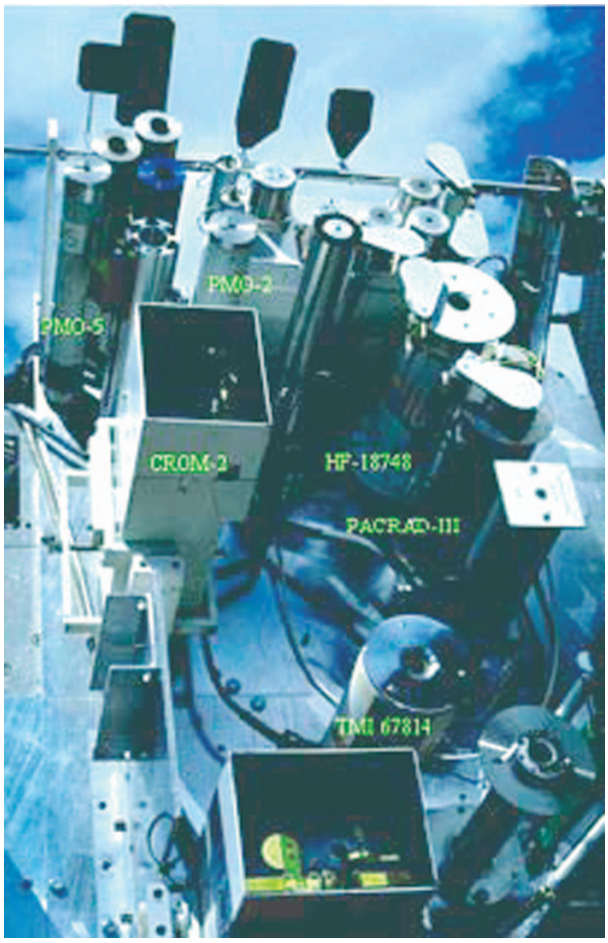

FIGURE 3.1
The current WSG of pyrheliometers on site at the PMOD/WRC.
By courtesy of PMOD/WRC, [10., 2004].

3.2. Transfer of the WRR

The irradiance (I) from a standard instrument, corrected to the WRR, is given by:

$$I|_{Instrument}^{WRR} = I_{Instrument} \times WRR_{Instrument}(IPC_m) \tag{14}$$

where the correction factor of the instrument, as achieved at the IPC number m[1], is given by the irradiance ratio:

$$WRR_{Instrument}(IPC_m) = \frac{I_{WRR}(IPC_m)}{I_{Instrument}(IPC_m)} \tag{15}$$

The WRR irradiance I_{WRR} at the IPC number m is given by equation (16). That is, $I_{WRR}(IPC_m)$ is the mean irradiance of the n-element WSG at the IPC_m; where the irradiance from each instrument of the WSG is corrected to the WRR of IPC_m.

$$I_{WRR}(IPC_m) = \left(\sum_n I|_{WSG}^{WRR}(n, IPC_m) \right) / n \tag{16}$$

The irradiance from instrument n, of the WSG at the IPC_m, corrected to the WRR is given by:

$$I|_{WSG}^{WRR}(n, IPC_m) = I_{WSG}(n, IPC_m) \times WRR_{WSG}(n, IPC_m) \tag{17}$$

The correction factor for each n of the instruments in the WSG is given by:

$$WRR_{WSG}(n, IPC_m) = \left\{ \frac{I_{WSG}(n, IPC_m) \times WRR_{WSG}(n, IPC_{m-1})}{\left(\sum_n I_{WSG}(n, IPC_m) \right) / n} \right\}^{-1} \tag{18}$$

1. The first m is $m=5$ (IPCv in 1980). IPC i (1959) to iv (1975) is not considered, as the WRR is based on the comparisons between 1970 and 1975.

3.3. Calibration of the Absolute Cavity, AHF31117

UKZN's Eppley model HF31117 absolute cavity pyrheliometer was granted permission to participate at the IPCix. The IPCix was held at the WRC/PMOD in the year 2000.

3.3.1. The IPC Protocol

The calibration protocol at the IPCix, as given by Rüedi in [11., 2001], were:

* Radiation Source:
  - direct solar and only a fraction of circumsolar radiation, with irradiances greater than $800 Wm^{-2}$.
* Meteorological Variables:
  - wind speed less than $2.5 ms^{-1}$,
  - greater than 8^{o} angular distance between clouds and sun.
  - the 500nm aerosol optical depth less than 0.12.
* Equipment:
  - the participating reference pyrheliometer; mounted on a solar tracker and kept aligned to the sun throughout the measurement runs.
  - all computer controlled systems synchronised to the timing of the IPC's measurement series.
  - DAQ system warm-up time of at least 30 minutes.

3.3.2. Description of AHF31117

A description of a model H-F cavity radiometer, such as the AHF31117, may be found in literature such as [2., 1998] and [5., 1992]. The description is repeated in part below since the AHF31117 is used to retrace the radiometers at NTNU and UKZN to the WRR periodically.

AHF31117 is a self-calibrating cavity pyrheliometer with an automatic operating system. A schematic diagram of the self-calibrating sensor is given in FIGURE 3.2. The sensor consists of a balanced, blackened cavity receiver pair attached to a double thermopile (indicated by TP in the figure).

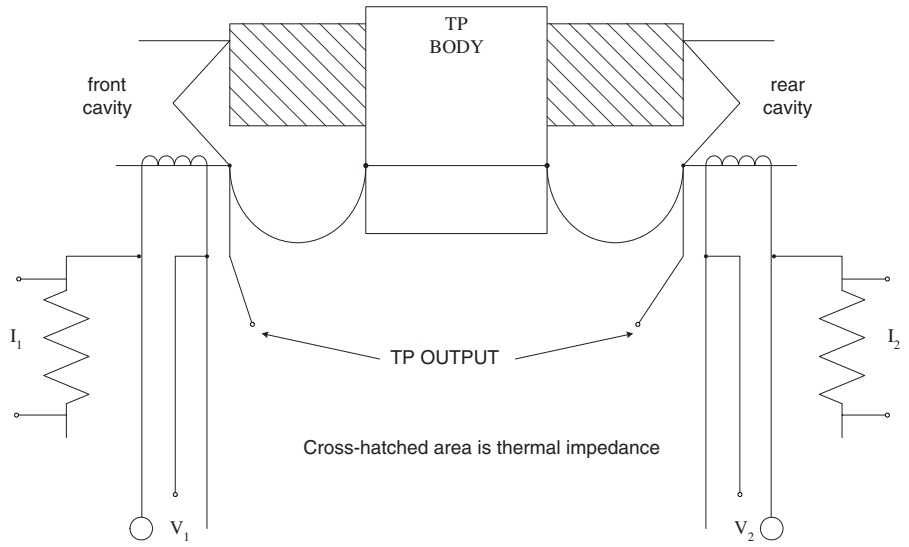

FIGURE 3.2
Schematic diagram of the Model H-F radiometer sensor. Courtesy of Hickey et al. in [6., 1977].

The thermopile pair is made up of copper on constantan junctions. The pair is arranged such that there are separate hot and cold junctions associated with each of the cavities. The hot junctions are in contact with the respective cavities and the cold junctions are on a common heat sunk base.

Each of the cavities (shown as front and rear in the diagram) is an inverted silver cone within a cylinder. The cone and the inside wall of the cylinder are coated with specular black paint. The cavities are fitted with heater windings which allow for absolute operation using an electrical substitution method, which relates the radiant power to electrical power. The front cavity views the direct solar beam by a 5^o full field of view and a slope angle of 0.8^o. The rear cavity views an ambient temperature blackbody. The assembled elements of the instrument are enclosed in a

tube, with an attached automatic shutter for shutting off the solar irradiance.

The operation of the radiometer, and the measurement of the required parameters is performed using a control unit. Some of the control functions are the setting of the calibration heater power level, activation of the calibration heater, selection of the signals to be measured and control of the shutter. The measured parameters include the thermopile signal, the heater voltage and the heater current which is measured as the voltage drop across a precision resistor. The instrument is normally operated in the passive mode, i.e. electrical calibrations are performed periodically during solar measurements while the instrument is temporarily shuttered. The electrical calibration is by the Primary Absolute Cavity Radiometer (PACRAD) mode. This means that the front heater is set to a fixed level close to the solar irradiance level. The thermopile output for the solar input and power input are sensed sequentially.

It is noted that operation of the AHF31117 is automatic. A description of a modified Eplab program which enables remote operation of the HF cavity radiometer, and allows for both NIP and PSP calibrations is given by Lysko in [9., 2003]. The program, AHF4AUX.BAS is a quick basic program. For the IPCix the instrument was controlled by software developed by Hickey (see [4., 2000]), such that the obtained series of direct solar irradiance S_m for each day could be submitted for a direct comparison with the WSG. Since the power calculation for the IPCix and general operation of the instrument is by the PACRAD Mode, the data reduction and equations for this mode is described below.

The power P_s which is assigned to the solar irradiance and which is effective in heating the front cavity during exposure is

$$P_s = S_m \, \alpha_c \, A \, \gamma \tag{19}$$

where S_m is the desired result, i.e. the solar irradiance, α_c is the absorptivity of the cavity, A is the area of the precision aperture, and γ is the stray light factor for the view tube.

The electrical power P_e is calculated from the measured voltage V_1 and measured current I_1

$$P_e = I_1 (V_1 - V_c) \tag{20}$$

where $V_c = I_1 R_c$, with R_c the lead correction resistance, is the voltage drop in the connection leads between the four wire connection points and the cavity heater.

The thermopile output signals, E_s and E_e, are proportional to the powers dissipated in the cavity, i.e.

$$\begin{aligned} E_s &= K_s P_s \\ E_e &= K_e P_e \end{aligned} \tag{21}$$

where the proportionality constants $K_s \neq K_e$ since there is a non equivalence L between radiant and electrical heating such that $K_e = L K_s$.

Combining terms, the solar irradiance is obtained:

$$S_m = \left(\frac{E_s}{E_e}\right) \left(\frac{P_e L}{\alpha_c A \gamma}\right). \tag{22}$$

The instrument's constants may be combined into a single correction factor, $C_f = \frac{L}{\alpha_c A \gamma}$, so that $S_m = \left(\frac{E_s}{E_e}\right) [C_f I_1 (V_1 - I_1 R_c)]$.

When the solar irradiance is stable over the measuring period, $E_e \approx E_s$ during the electrical calibration such that S_m reduces to:

$$S_m = C_f I_1 (V_1 - I_1 R_c) \tag{23}$$

The derivation of equation (23) assumes that temperature equilibrium has been achieved before the measurement period and that the radiative loss from the front cavity to the surroundings has been the same between measurements and calibration. It is therefore a preference to assure stable measuring conditions, for example that given by the IPC protocol for meteorological variables in section 3.3.1.

3.3.3. AHF31117 Results from the IPCix

Measurements from AHF31117 at the IPCix were taken in runs lasting 21 minutes with a basic cadence of 90 s. The run for the HF31117 started with the shutter closed, after 90 s the dark reading was acquired and the heater turned on until, at 180 s the voltage, current and thermopile were read. The heater was then turned off and the shutter opened. From 270 s onward the instrument was read every 90 s yielding 11 irradiance values per run. In this way a total of 91 irradiances were submitted for comparison with the WSG.

The first graph in FIGURE 3.3 are plots of the direct solar irradiance from the WSG and the AHF31117 from series of runs on the 27th of September 2000. The recorded direct solar irradiances are all above $850 Wm^{-2}$. According to Rüedi in [11., 2001], the optical depth at $500nm$ was below 0.07 during measurements between $11am$ and $1.30pm$ for this day, and remained below 0.09 for the subsequent measurements. The measurements were therefore in accordance with the IPC protocol (see section 3.3.1).

The lower graph in the FIGURE 3.3 are plots of the relative deviation of the AHF31117 from each of the WSG and gives an indication of AHF31117's stability during the runs. Without data omission the relative deviation is less than 0.5%. Further, the percentage relative deviation of AHF31117's calibration factor, as taken from the mean of the WSG irradiance measurements, is less than 0.4% except for one data point. This is shown graphically in FIGURE 3.4. The IPC required that the $\frac{WRR}{instrument}$ ratios be within 0.3% of the ratio median. Although the IPC final evaluation excluded 10 of the submitted measurements due to deviations outside the 0.3%, the standard deviation results in FIGURE 3.3 and FIGURE 3.4 suggest that the measurements from AHF31117 are reliable. The excluded deviations may be attributed to an alignment problem with the manual solar tracker for the AHF31117 and/or time incoherence.

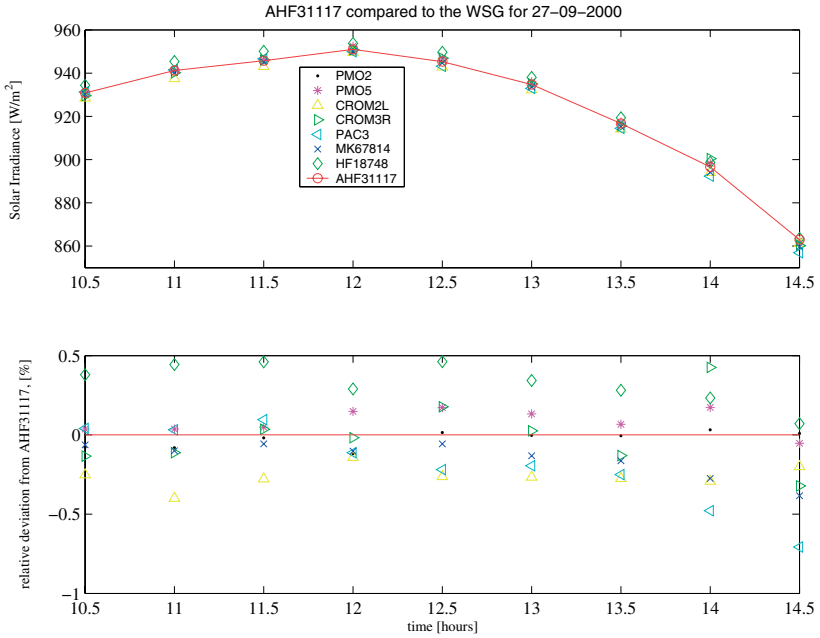

FIGURE 3.3
Plots of direct solar irradiance from the WSG and the AHF31117 from series of runs on the 27th September 2000 at the IPCix (top). Plots of the corresponding relative deviation of the AHF31117 from each of the WSG (bottom).

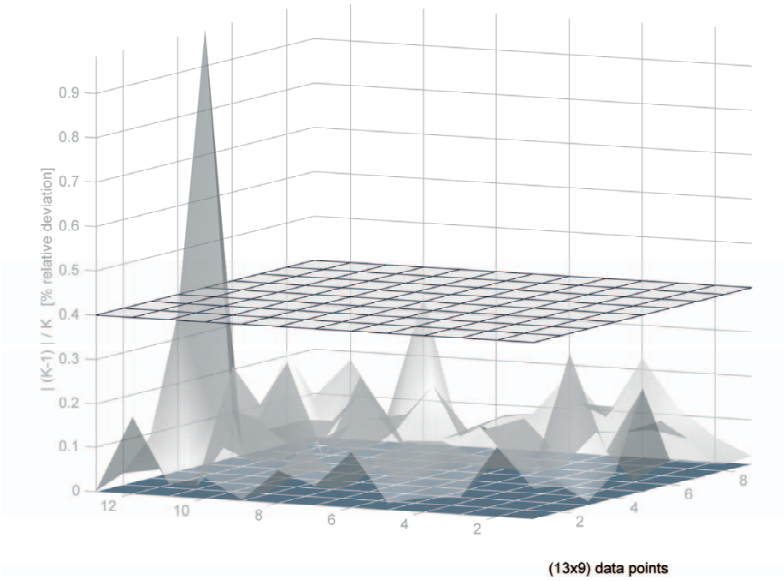

FIGURE 3.4
Relative deviation of AHF31117's calibration factor. The calibration factor (k_i) is taken as the ratio $\frac{WRR_i}{AHF31117_i}$, $i = 1, \ldots,$ number of data points. .

In AHF31117's final evaluation at the IPCix, given by Rüedi in [11., 2001]*, the ratio to the WRR is* 1.00035 ± 0.00058 *such that the instrument's new WRR is* 0.99965.

3.4. Calibration of NIPs at UKZN and NTNU

The field NIPs at UKZN and NTNU are calibrated by comparison with the AHF31117, using the sun as the source. The software program, AHF4AUX.BAS is used so that the calibration process is controlled remotely. The calibration is done in sessions. At the start of each session the AHF31117 self-calibrates. A single irradiance measurement is then taken every minute from the AHF31117 and the NIP under test and the data is stored for later comparisons.

One such calibration of the NIP at UKZN was made on the 6th and 7th of February 2001. First, the irradiance measurements from the AHF31117 was corrected to the WRR. Then, for each measurement the ratios of $\frac{AHF31117}{NIP}$ were computed. The median of the ratio for each session was also determined. Similar to the IPCix data selection criteria, the ratios which do not lie within 0.3% of the median were discarded. Finally the mean of the remaining ratios is the new calibration factor for the NIP. The selected data from the AHF31117 and the NIP is given graphically in FIGURE 3.5. *Based on the data, the NIP's new correction factor is* 0.9989 ± 0.0046.

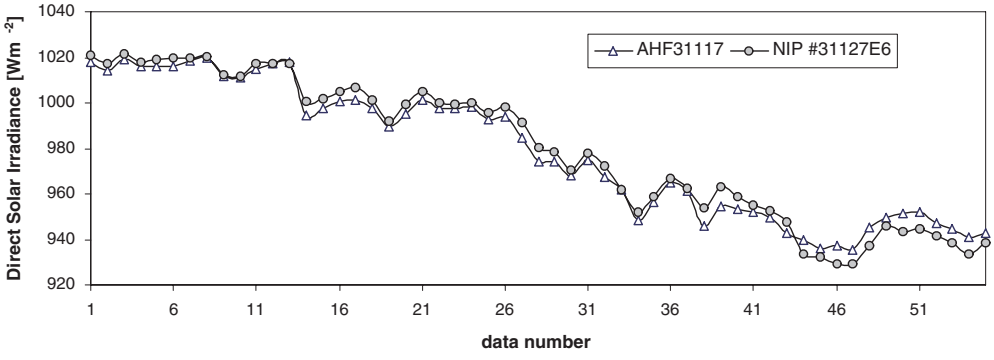

FIGURE 3.5
Direct solar irradiance data, from the 6th and 7th of February 2001, for calibration of the NIP at UKZN. The data from the AHF31117 is corrected to WRR.

Calibrations of the NIPs at NTNU are made using the procedure described above. The selected data for calibrations on the 10th of September 2002 is given graphically in FIGURE 3.6. *Based on the selected data, the new calibration factors for the NIP #21132E6 and NIP #31856E6 are* 1.050±0.002 *and* 1.005 ± 0.002*, respectively.*

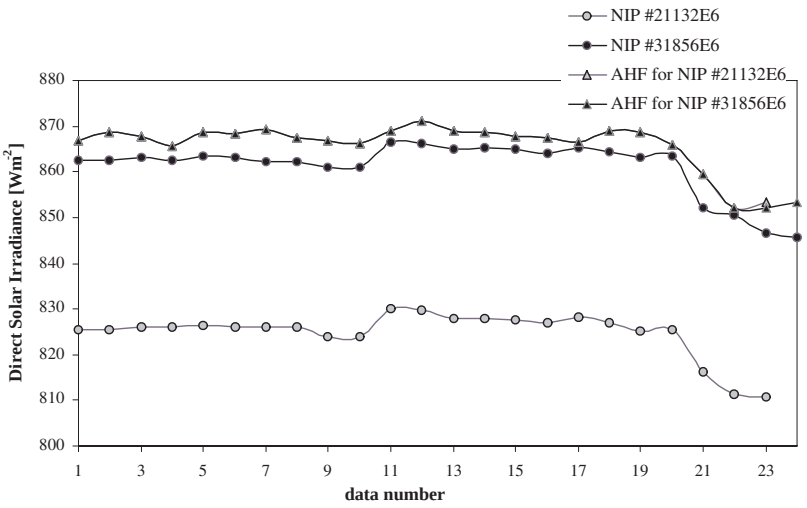

FIGURE 3.6
Direct solar irradiance data, from the 10th of September 2002, for calibration of the NIPs at NTNU. The data from the AHF31117 is corrected to WRR.

3.5. Calibration of PSPs at UKZN and NTNU

The conventional Sunshade method described by Iqbal in [7., 1983] is used to calibrate pyranometers at UKZN and NTNU. The direct solar irradiance from the pyranometer is compared to the direct solar irradiance from an NIP, which is calibrated against the AHF31117. This approach provides a trace to the WRR.

3.5.1. The Sunshade Method

The shading kit at UKZN is described by Dhavraj in [1., 1998]. The shading kit at NTNU is a quarter circular, 80cm radius (PSP sensor to disk length) rotatable arm with a slideable 8cm disk. A photograph of the kit in operation, with embossed illustration, is given in FIGURE 3.7. The

dimensions of the shading apparatus gives a 5.7^{o} aperture angle, making it comparable to the reference NIP's 5^{o} field of view.

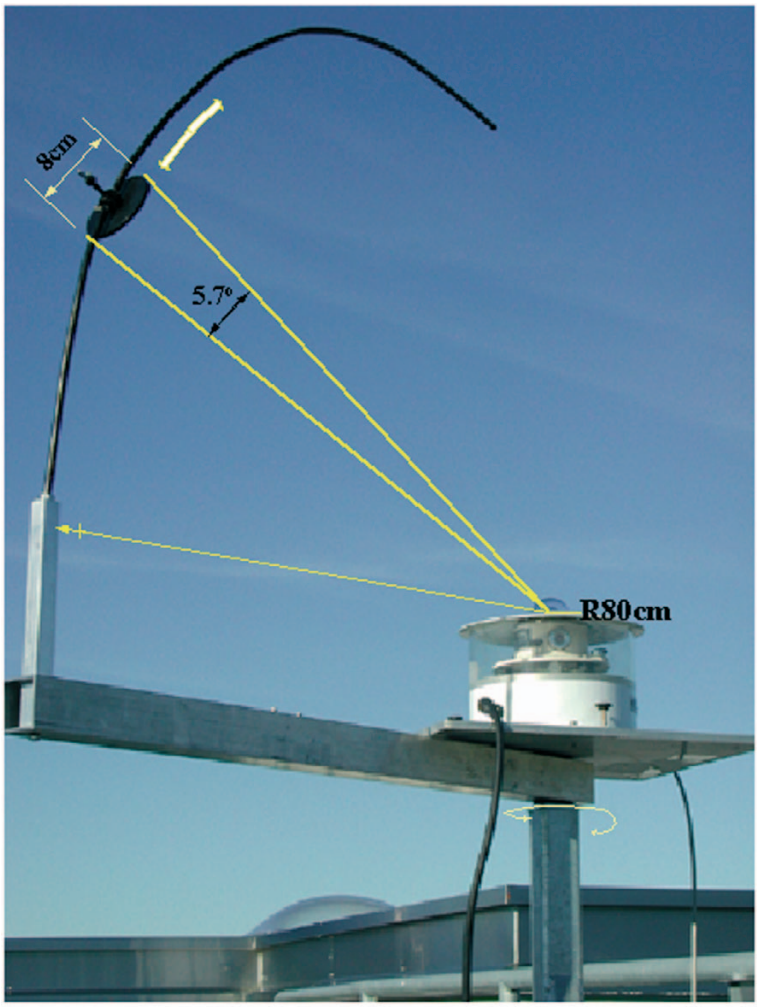

FIGURE 3.7
Illustration of the manual shading kit at NTNU. The kit is used for calibration of the pyranometers and maybe used for short-term diffuse measurements.

In this technique the test pyranometer is periodically shaded off by the shading disk for a diffuse measure and exposed to the beam radiation for a global measure. At the same time a reference NIP measures the direct solar irradiance. All quantities are in Wm^{-2}.

The test pyranometer calibration factor K for each period is then given by:

$$K = \frac{Direct_{NIP}}{Direct_{PSP}} = \frac{Direct_{NIP}}{(Global - Diffuse)_{PSP}} = \frac{NIP \cdot \cos\theta_z}{PSP_{exposed} - PSP_{shaded}} \tag{24}$$

An average of K over the entire calibration session is taken as the true new factor.

Alternatively, the pyranometer response R, in units V/Wm^{-2}, may be calculated if the pyranometer measurements are taken in volts and the NIP in Wm^{-2}:

$$R = \frac{Direct_{PSP}\big|_{Volts}}{Direct_{NIP}\big|_{Wm^{-2}}}. \tag{25}$$

3.5.2. PSP Calibration Results

Results from a calibration of the PSP at UKZN is given by Dhavraj in [1., 1998].

A calibration of the PSPs at NTNU was carried out on the 26th of September 2002 (Norwegian Autumn), at exactly past solar noon and 1 hour past solar noon respectively. This was a clear sky period with only occasional cloud disturbances. The shadow kit was manually adjusted so that the disk alternately shaded and exposed the pyranometer dome (and thus sensor) for durations of 5 minutes. Data from the instruments were retrieved using $S3_{NTNU}$ (see section 2.4.2.3). The available data were thus the 1-minute averages and corresponding standard deviations from the mean for the instruments. The reference is NIP#21132E6. This is traceable to the WRR according to Kirk in [8., 2002] and was re-calibrated (see section 3.4).

The calibration data for both PSPs were sifted. The 1-minute averages with standard deviations greater than 5% were excluded. The final data set from the 3 radiometers are shown by the plots in FIGURE 3.8(a) and FIGURE 3.8(b).

An indication of sky conditions and irradiance variations are shown in FIGURE 3.8(c) and FIGURE 3.8(d). These are curves of the percentage standard deviation of the 1-minute averages, taken from the 12 samples within the minute, for the sifted data set.

It is shown that during calibration of PSP #16577F3, the percentage maximum standard deviation for the 1-minute averages recorded for the PSP when shaded, PSP when exposed and NIP are 3.03%, 0.30% and 0.13% respectively. Likewise, for PSP #33049F3, the respective deviations are 2.34%, 0.55% and 0.28%. These low deviations suggest that the sky remained consistent during the measurements.

Table 3A tabulates the data used and results obtained for both PSPs. It follows that the PSPs' *new calibration factors* are:

PSP #16577F3: ***1.157 ± 0.001***

PSP #33049F3: ***0.998 ± 0.018*****,**

where the given uncertainties are the standard deviations in the mean of the calculated calibration factors.

The total uncertainty in the calibration of the PSPs is determined by the accuracy of the data logging system, transfer to the WRR, zenith angle computation (which is defined by time accuracy and the choice of algorithm), and the pyranometer inaccuracies. It is expected that the total uncertainty is less than 4%.

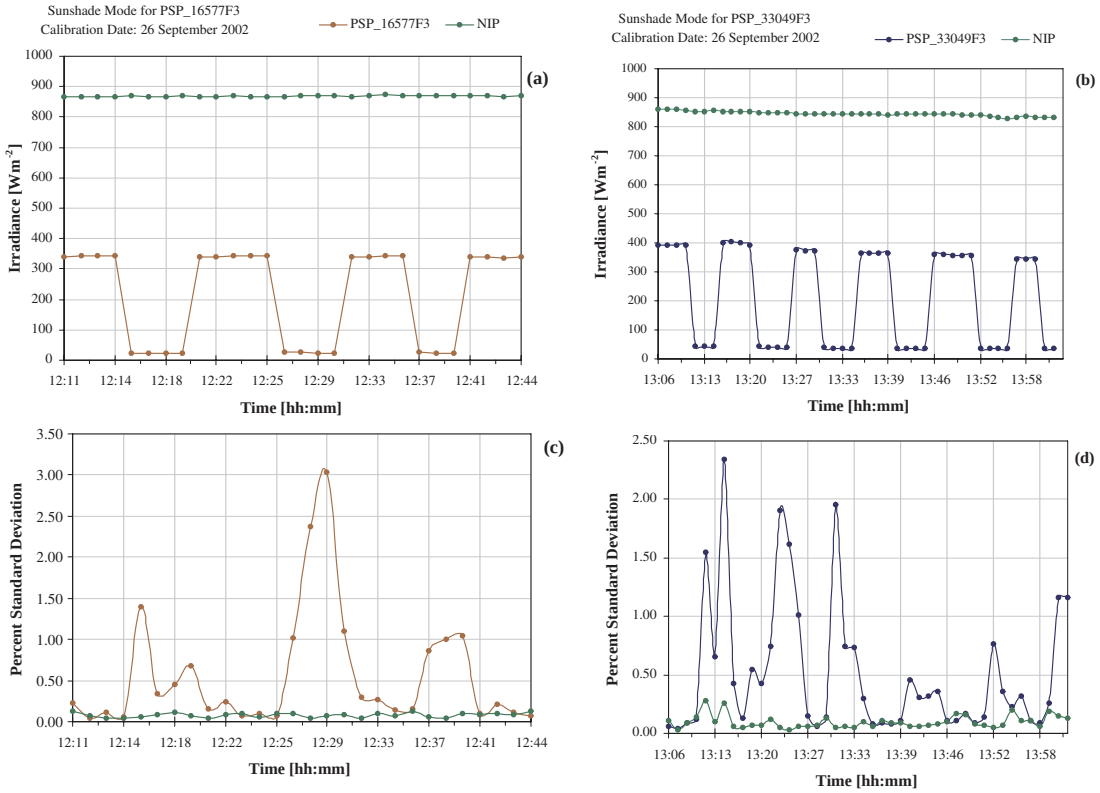

FIGURE 3.8
Data for the PSPs and NIP at NTNU in calibration of the PSPs. The % standard deviations in (c) and (d) suggest the sky condition during each observation.

Table 3A: Calibration numbers for PSP #16577F3 and PSP #33049F3

Pyranometer (Wm^{-2})		Pyrheliometer NIP #21132E6	Solar Zenith	NIP Direct	PSP Direct	K_PSP
Exposed (G_e)	Shaded (G_s)	I_b	θ_z (deg)	$I_b \cdot \cos\theta_z$	$G_e - G_s$	$\frac{I_b \cos\theta_z}{G_e - G_s}$
PSP #16577F3						
341.75	23.90	866.36	64.92	367.46	317.85	1.1561
342.2	25.15	866.52	64.97	366.83	317.05	1.1570
341.5	24.53	870.30	65.08	366.95	316.97	1.1577
average K_PSP #16577F3						1.1569
PSP #33049F3 (the newer PSP)						
393.25	44.20	859.01	65.83	351.88	349.05	1.0081
398.75	41.13	852.19	66.20	344.06	357.63	0.9621
374.67	37.88	844.05	66.57	335.79	336.79	0.9970
364.25	37.40	843.26	66.99	329.82	326.85	1.0091
357.60	36.35	842.37	67.49	322.65	321.25	1.0043
344.33	35.20	833.20	68.03	311.96	309.13	1.0092
average K_PSP #33049F3						0.9983

3.6. Calibration Validations

It is possible to validate the calibration factors for the NIPs and PSPs at NTNU by comparing the corrected data from each pair.

The pairs of direct and global data from four clear sky days in 2002 have been selected for validations of the calibration factors. The raw data from each instrument is given graphically in FIGURE 3.9. The data are not corrected, except that the irradiances are calculated from the instruments' original responsivities. The data is controlled in the comparison stage to exclude observations at solar heights below 7.5^{o} (see Figure 2.2 on page 26).

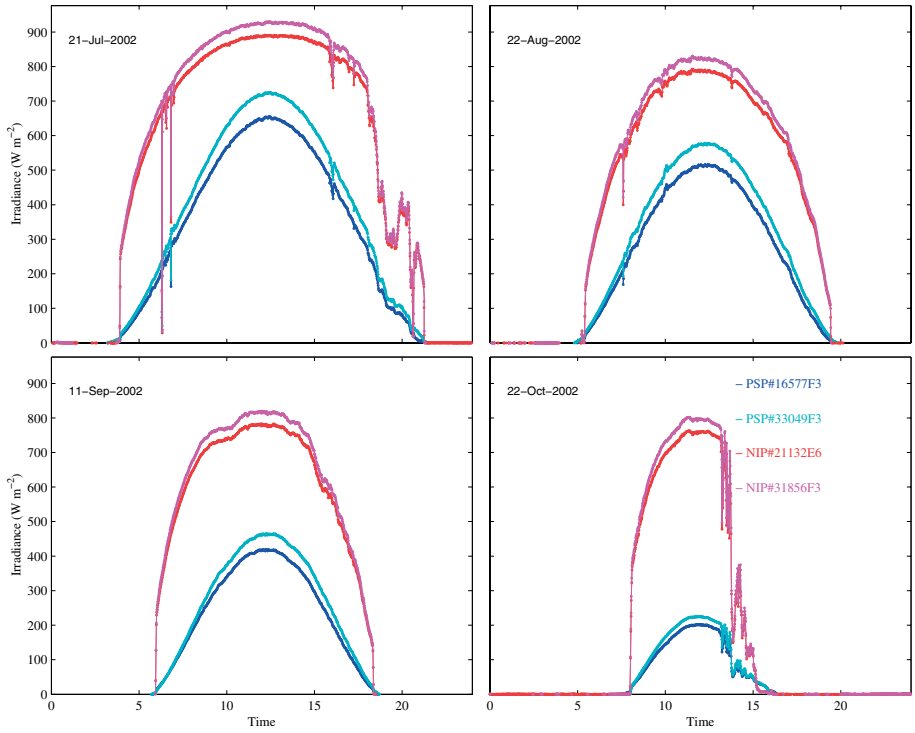

FIGURE 3.9
Clear sky observations from the NIPs and PSPs at NTNU for 4 clear sky days in 2000. The irradiances are calculated from the instruments' original responsivity; calibration factors are not included.

3.6.1. Calibration Validation: NIPs

The absolute irradiance differences between the two NIPs at NTNU for the selected days is given by the scatter plot in FIGURE 3.11. The original data are modified to incorporate the respective calibration factors.

From the 2705 observations, 92% of the irradiance differences are below $4 Wm^{-2}$ and correspond to a relative uncertainty of less than 0.9%. This is within the WMO uncertainty specification for high quality NIP's (see section 1.3.2.4, page 13). The higher absolute differences correspond to relative uncertainties below 2%, with the exception of 3 observations. The higher uncertainties in the 8% of observations may be attributed to deposits on either of the NIPs' windows in the interim to maintenance.

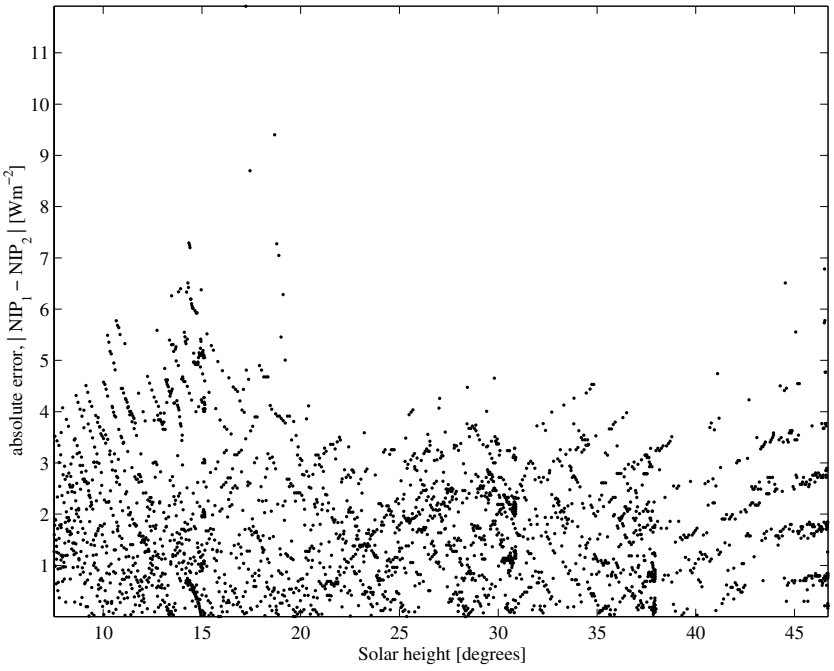

FIGURE 3.10
Scatter plots of absolute differences in direct solar irradiances from the 2 NIPs at NTNU for the clear sky observations given in FIGURE 3.9. The data from the NIPs are corrected by the calibration factors.

3.6.2. Validation: PSPs

The absolute irradiance differences between the two PSPs at NTNU for the selected days are given by the scatter plots in FIGURE 3.11. The original data are modified to incorporate the respective calibration factors.

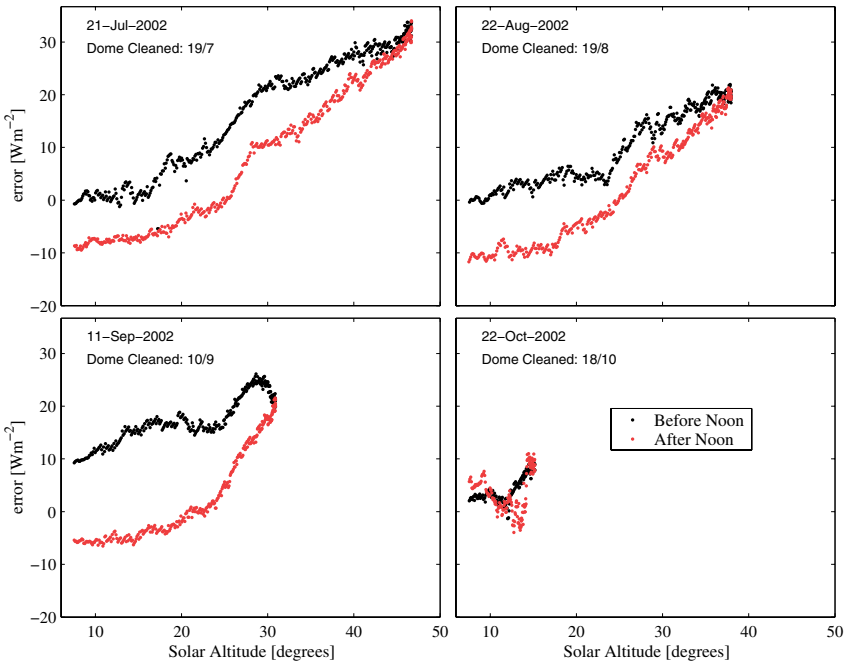

FIGURE 3.11
Scatter plots of differences in global solar irradiance from the 2 PSPs at NTNU for the selected clear sky days. The data from the PSPs are corrected by the calibration factors.

The maximum difference from the 4 day evaluations is $34 Wm^{-2}$. This corresponds to a 4.7% absolute deviation relative to the PSP #33049F3 minute average record of $724 Wm^{-2}$, which is between the 3% and 8% total uncertainty limits specified by WMO in [12., 1997] for high and good quality PSPs respectively.

The recorded differences may be attributed to directional and thermal factors mentioned in section 1.3.3 on page 14. It is evident from the plots that the irradiance differences between the two PSPs climbs with solar height to a maximum at solar noon, consistently. In addition, the polarity of error shows that PSP #16577F3 reads a higher irradiance before noon. The after noon errors switch polarity as indicated in the FIGURE 3.11. These indicate that deviations may be due to directional and temperature

responses. It is expected that corrections based on angular responses and day-time thermal offsets would reduce the uncertainties in calibrations of the PSPs.

3.7. Chapter Summary and Conclusions

Calibration procedures and results have been presented for the NIPs and PSPs at UKZN and NTNU. The calibrations are traced to the WRR and have been validated. The validations suggest that, with regular instrument maintenance, the total uncertainties in irradiances from the NIPs can be less than 0.9%. Likewise, it may be presumed that the uncertainties in global irradiances from the PSPs are less than 5%.

3.8. References

1. Dhavraj, *The Setting Up and Calibration of Radiometers for Measurements of Direct and Diffuse Solar Radiation at the University of Durban-Westville*, MSc. Thesis, Dept. of Physics, UDW, 1998.
2. Eplab, *Instruction and Information Manual for Model AHF Self-Calibrating Cavity Pyrheliometer and Model 409 Radiometer Control Unit*, The Eppley Laboratory, Inc., October 1998
3. Fröhlich C., *History of Solar Radiometry and the World Radiometric Reference*, Metrologia, 28, pp. 111-115, 1991.
4. Hickey J.R., *Program IPCHF117.BAS 09/20/2000 for Single Operation of AHF s/n 31117 at IPC*, Eplab, 2000.
5. Hickey J.R., Daniels D.B., Nelson D., *Automation of Cavity Pyrheliometer Operation for Routine Direct Solar Irradiance Measurements*, Proc. 1992 Annual Conference ASES, pp. 340-344, 1992.
6. Hickey J. R., Frieden R.G., Griffin F.J., Cone S.A., Maschoff R.H., Gniady J., *The Self-Calibrating Sensor of the Eclectic Satellite Pyrheliometer (ESP) Program*, Proc. 1977 Annual Conference ASES, pp. 15-1 - 15-4, 1977.
7. Iqbal M., *An Introduction to Solar Radiation*, Academic Press, Canada, 1983.
8. Kirk T., Communication by e-mail on traceability of NIP_21132E6, Eppley Lab, October 2002.
9. Lysko M.D., *Decode of AHF4AUX.BAS*, Lecture notes, NTNU, October 2003.
10. PMOD/WRC, *URL: http://www.pmodwrc.ch/pmod.php?topic=wrc*, 2004.
11. Rüedi I., *International Pyrheliometer Comparison IPC-IX: Results and Symposium*, Working Report No. 197, MeteoSwiss, Davos and Zürich, May 2001.
12. WMO-No.8, *Guide to Meteological Instruments and Methods of Observation*, Secretariat of the World Meteor. Org., Geneva, Switzerland, 1997.

Chapter 4

Presentation of Site Data

In this chapter some examples of daily records of direct and global solar irradiances measured at UKZN and NTNU are presented. In addition, evaluation of the measured global and direct solar irradiances is shown in the form of total power per month, transmission factors and irradiance frequency distributions with respect to solar height.

4.1. Introduction

The purpose of this chapter is to present the collected data and derived information from UKZN and NTNU. The selected daily records of direct normal and global irradiances give an indication of the expected levels for different radiation conditions. The month synopsis for each site may be used in the assessment of solar energy systems. The transmission factors for the direct normal, global horizontal and the diffuse horizontal irradiances may also be used to recover the estimates of the respective irradiances. Additionally, these factors may be used to provide a first estimate of the solar radiation climates for the sites. Greater detail in data characterization is provided by irradiance frequency distributions with respect to solar height. Such distributions are the basis of the Løvseth-Brevik Model, described in detail in [1.], and [8.].

4.2. Examples of Daily Records

Some examples of the daily records of direct and global solar irradiance, together with the calculated diffuse irradiance is shown. The examples have been selected for their illustration of different sky conditions and possible maintenance issues.

4.2.1. Examples of Daily Records at UKZN

A selection of 16 daily records of data from the site at UKZN are plotted against time of day and shown in FIGURE 4.1. The daily diffuse is included. Each record is numbered from 1 to 16.

Typically clear sky days are given by records 1, 2, 4, 5, 6, 8, and 9. On such days the sky is almost free of clouds in the direction of the sun during the solar day. The corresponding clearness parameters and direct ratios for these days are given by the plots in FIGURE 4.2.

A crude approach in checking the state of the pyranometer dome and pyrheliometer window is by comparing the irradiance transmission levels before and after solar noon for each of the clear sky days. The days represented by the records 1 and 2 are two consecutive winter days occurring in the middle of July 2003. The clearness parameters and direct ratios for the day in record 1 have respective relative absolute differences of less than 3% and 6% for the corresponding before and after noon solar heights above 27.4^{o}. The transmission results for the day in record 2 are similar. It follows, for these days, that the instruments may be considered as clean or homogeneously 'dusty'.

Regarding the recorded irradiances as true, there is a higher irradiance level on the second of the two consecutive days. The maximum value of the direct irradiance is about $123 Wm^{-2}$ higher on this day than on the preceding day. Likewise the global irradiance is about $52 Wm^{-2}$ higher. The large differences in irradiance levels for these consecutive days are due mainly to day to day variations of the extinction in the atmosphere. The same is true for the transmission factors from the 31^{st} of July 2003 (record 5). This can be seen by the corresponding transmission factor plots in FIGURE 4.2. The transmission factors for the 17^{th} of July 2003 are consistently lower than those for the 18^{th} of July 2003. Greatest transmission is on the 31^{st} of July 2003.

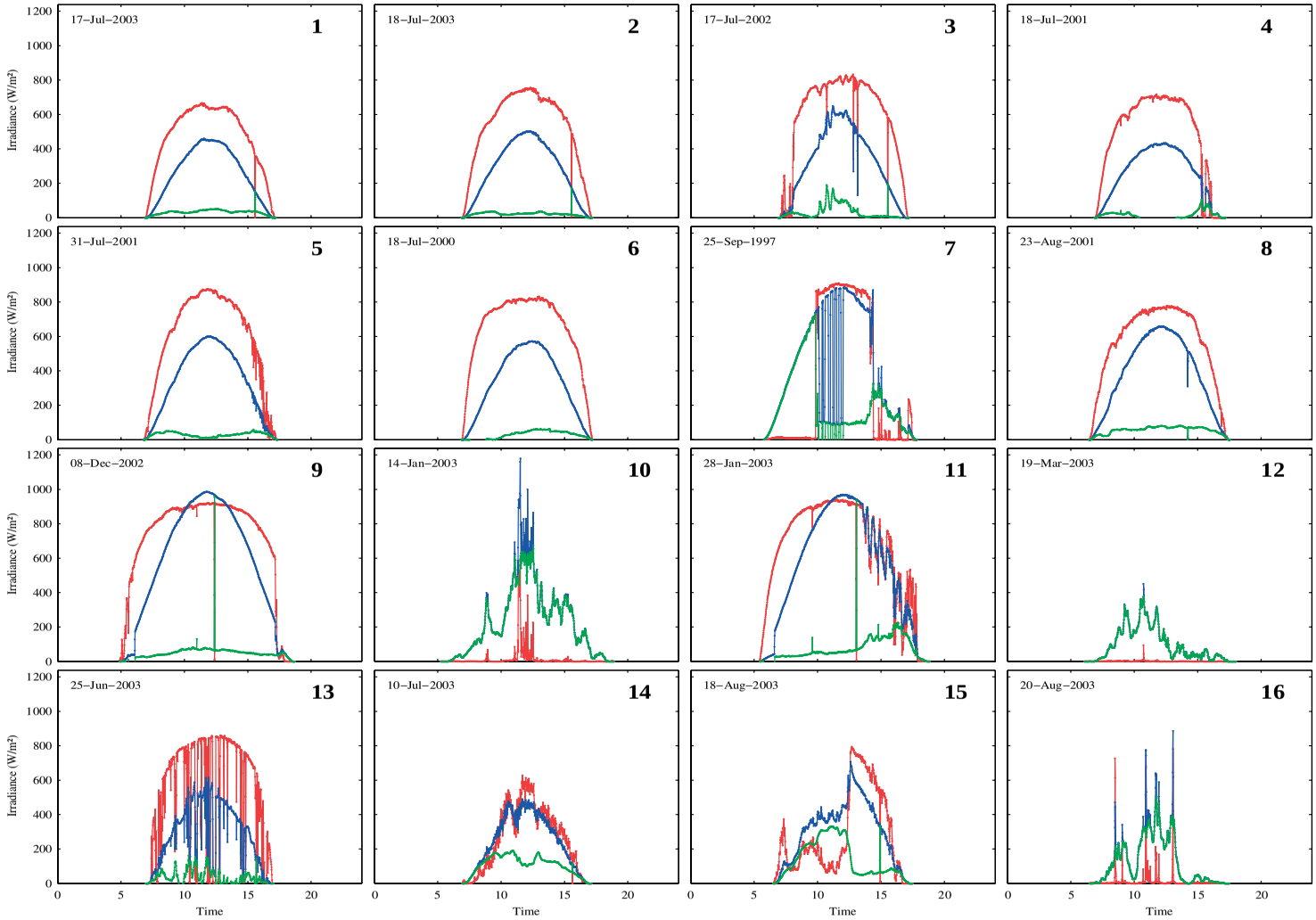

FIGURE 4.1
Sixteen records of direct normal (plotted in red) and global (plotted in blue) solar irradiance as a function of time of day for UKZN. The calculated horizontal diffuse (plotted in green) is also indicated.

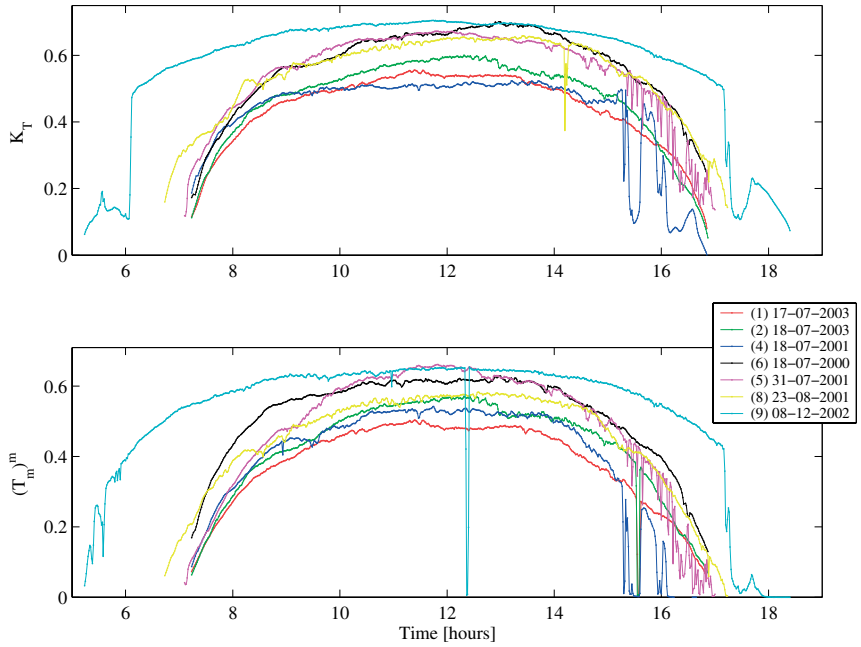

FIGURE 4.2
One-minute clearness parameters (K_T) and direct ratios (T) for the clear sky records in FIGURE 4.1. The record number is indicated in parenthesis in the legend.

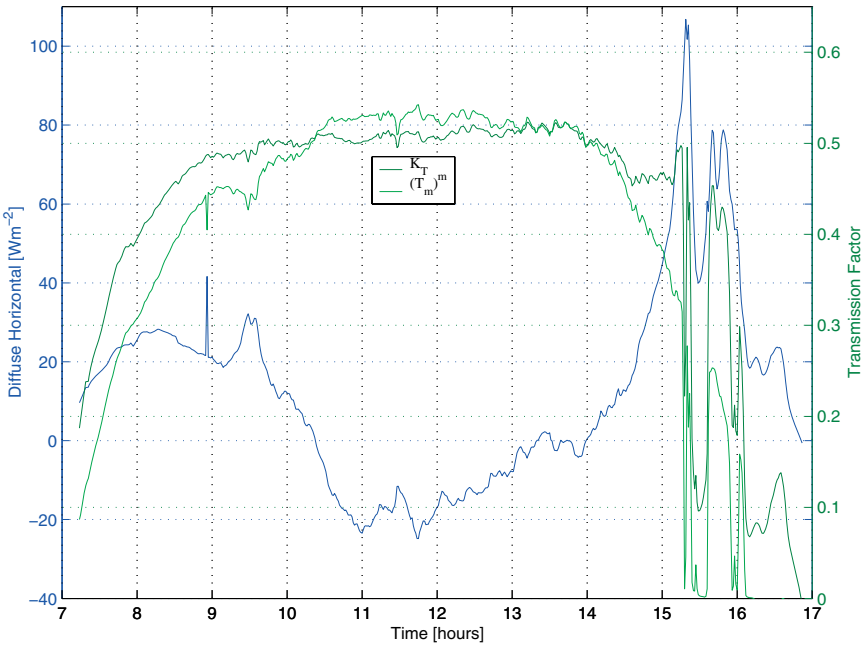

FIGURE 4.3
The calculated diffuse horizontal irradiance for the 18th July 2001 (day record 4 in FIGURE 4.1) against the time of day in blue. The plots in tones of green are the corresponding clearness parameters and direct ratios.

The clear days represented by the records 2 and 6 are on the same winter day but from two different years. Record 2 is from the year 2003 and record 6 is from the year 2000. The transmission factors for the day in record 2 are lower than for the day in record 6. There is a 10% difference at solar noon. Only a fraction of this difference can be related to the total extraterrestrial solar irradiance. The transmission parameters for the two days are evaluated with the corresponding total extraterrestrial solar irradiances (see section 1.1 on page 3) instead of the approximated extraterrestrial irradiances taken by equation (4). According to the dataset version d30_60_040 from PMOD/WRC, with references to Fröhlich et al. in [6., 1998] and Fröhlich in [7., 2003], the total solar irradiance for the two days are $1365.4622 Wm^{-2}$ and $1366.1545 Wm^{-2}$, respectively. This is a difference of 0.05%. It is therefore viable that the clear sky irradiances are only slightly lower for the day in record 2 in comparison to the day in record 6.

From the small and insignificant influence of the change in extraterrestrial irradiance it may be concluded that the differences in transmission factors for the days in records 2 and 6 are due to a greater amount of atmospheric extinction on the day represented by record 2 than on the day in record 6. But first the status of the instruments for the day in record 6 is checked as described before. It is found that the transparency coefficients for the day in record 6 have relative absolute differences of less than 5% for the corresponding before and after noon solar heights above 29^{o}. Records from the pyrheliometer on this day may therefore be viable. Data from the pyranometer may be questioned since the relative absolute differences in the clearness parameter are largely variable. So the large differences in these records (clear days of the same day number but from a different year) can be due to both dissimilar atmospheric extinctions and misread irradiances due to unclean instrument windows.

The day number in record 4 is the same as in records 2 and 6, but in the year 2001. The trend in the radiance plots suggest a clear sky day. From time $10h23$ to $14h01$ the calculated horizontal diffuse irradiances are negative. That is, the direct horizontal irradiances are higher than the corresponding global irradiances. At the same time, as shown in FIGURE 4.3, $(T_m)^m > K_T$. A possible explanation is that the observed global

irradiances for this day may be dubious. This can be if the pyranometer dome is unclean.

The day represented by the record 8 shows a dip in the global irradiance between 14*h*11 and 14*h*16 whilst the direct is less perturbed over this period. The dip in the global by the pyranometer observation may be due to disturbances from cleaning of the pyranometer dome. Another possibility is the 'bird factor'; an illustration of which is given by the picture in FIGURE 4.4.

FIGURE 4.4
A UKZN due west photogragh showing a bird pirched on the pyranometer. The picture was captured by the Creative Video Blaster Webcam 5.

It is typical that the level of the direct normal irradiances exceeds corresponding global horizontal irradiances at around solar noon for clear sky days in the summer months. The day in record 9 is an example. Also evident from this record is a delay in the global irradiance pick-up at sunrise in comparison with the direct normal irradiance pick-up. This is the case for most of the days in November, December and January. It is presumed that equipment on the sundeck obstructs the pyranometer's sunrise view during these days; when the day length is the longest. The

delay in global irradiance pick-up for the day in record 9 is approximately $1h15$.

All the days later than the 15th of March 2002 show a sudden drop in the direct solar irradiance for a single minute in the afternoons. This is clear from the days in records 1, 2, 3, 9, 11, 14 and 15. At the time of the drops the automatic solar tracker reaches its horizontal axis limit. So it pivots 180^{o} in the reverse azimuth direction and then realigns to the solar zenith. During this duration, of about 1-minute, the pyrheliometer is inevitably misaligned from the sun.

The day in record 7, the 25th of September 1997, illustrates three scenarios. The first is that the direct solar irradiance recorded between sunrise to $9h50$ is flawed. This deduction is made since the levels of the corresponding global irradiances suggest a clear sky so that all direct irradiances are expected to be, at most, higher than the global. However the direct irradiances are all below $15Wm^{-2}$. This is due to solar misalignment. The second scenario is the periodic drop in the global irradiances between $10h01$ and $12h02$. This is because the pyranometer is periodically shaded and exposed for calibration purposes (see “Calibration of PSPs at UKZN and NTNU” on page 58.). The last scenario illustrates the change from a clear sky day to a partly cloudy sky to overcast after $14h07$.

The fluctuations in the direct and global irradiances in the days represented by records 3 and 10 to 16 in FIGURE 4.1 are typical for overcast or partly cloudy days.

The fluctuations for the days in records 3, 11 and 13 are suggestive of intermittent sun cover by low level and widely scattered cumulus clouds.

The days represented by the records 10 and 16 show high peaks of global irradiances. The maximum for the day in record 10 is $1180Wm^{-2}$. This is higher than observed global irradiances from clear skies. The lower level on the clear days may be attributed to extinction caused by atmospheric aerosol. The clouds on days such as in records 10 and 16 are most likely the stratocumulus clouds and are associated with patches of clear and almost aerosol free sky. This would reduce atmospheric extinction and explains the higher global irradiances.

There is little or no direct solar irradiance on the day represented by record 12. This is due to the opaque and precipitable nimbostratus clouds. On occasions such as this the global and diffuse irradiances are the same.

The direct normal and global irradiances for the day represented by the record 14 are almost the same. This may be the case in the presence of the uniform, diffuse and translucent altostratus clouds.

The day represented by the record 15 is in winter, when the global irradiance levels are in general low. However, the direct irradiance is lower than the global for most of the day before noon. This can be due to irradiance scattering by high level cirrus clouds.

In summary, the UKZN is categorised as being part of the Kwazulu-Natal coast region. It's subtropical climate may explain the levels of observed solar irradiances. Relative humidity over the region is fairly high owing to the supply of moisture from the adjacent Indian Ocean. According to the City State of the Environment Report on Climate for the Durban Metropolitan Area given by [3., 1999], relative humidities can be close to 70% in the summer months and between 50% to 60% in the winter months. In conjunction with high temperatures, the atmosphere may be regarded as sultry, especially during the summer months and can explain the high global and lower direct irradiance levels during part of the day in record 9, for example. The spring and autumn months can have short periods of hot, dry conditions justifying the observed irradiances during, for example, the day represented by record 7. Precipitation in the Kwazulu-Natal coast region is expected mainly from October to April and particularly in the summer months (December, January and February) when there can be strong tropical thunderstorms almost daily in the afternoons. This can be interpreted from the direct and global solar irradiance observations at UKZN. Classic examples are most of the days in January 2003. For instance, the trend in irradiances on the 6^{th} and 16^{th} of January as shown in FIGURE 4.5. On these days the trend in global and direct irradiances before noon are suggestive of clear skies and high humidity. By $14h36$ on the 6^{th} the direct irradiance drops to null from a high of $833 Wm^{-2}$ at $13h53$. The irradiance levels for the rest of the day implies the possible presence of cumulonimbus clouds and a tropical thunderstorm, clearing out to cumulus clouds by $16h04$.

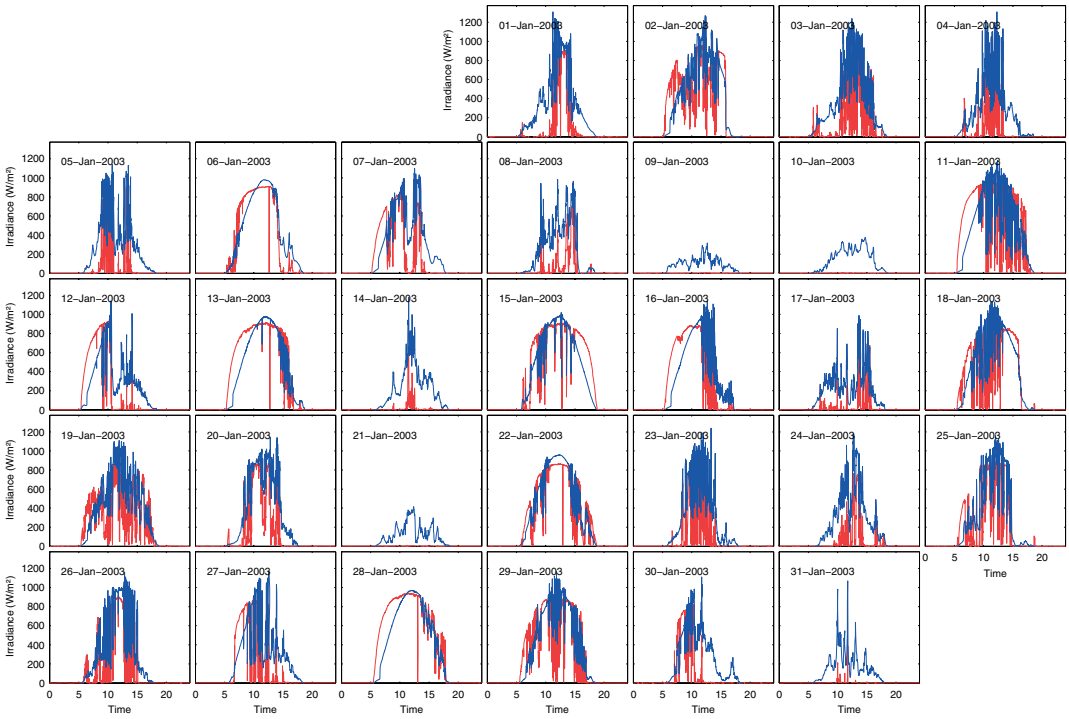

FIGURE 4.5
A calendar plot of direct and global solar irradiances recorded at UKZN for the days in January 2003.

The local land/sea breezes and topographically induced wind circulations should be considered when defining the distribution of solar radiation since they disperse or accumulate atmospheric components such as aerosols and air pollutants. For example, the mountain-plain winds transport pollutants released in the interior of Kwazulu-Natal towards the coast at night. By day the wind circulation reverses such that air pollutants from the coast are carried to the interior. There is a need for research into the influence of wind and particle dispersion on solar irradiance in the climatic regions of South Africa.

4.2.2. Examples of Daily Records at NTNU

Some examples of daily records of direct and calculated diffuse solar irradiance at NTNU are discussed by Brevik in [1., 1984]. An additional selection of 16 daily records of data from the site at NTNU are plotted against time of day and shown in FIGURE 4.6. The daily diffuse is included. Each record is numbered from 1 to 16.

The direct irradiances for the days represented by records 1 and 11 illustrate the effect of solar misalignment. The NIP tracker mount for these days was the 'manual' Eppley ST-3. Realignment of the tracker at $12h29$ for the day in record 1 and at $12h55$ for the day in record 11 resulted in irradiance jumps of 33% and 27%, respectively. The direct irradiant data before $8h25$ for the day in record 12 is also damped due to solar misalignment. The NIP for these data is mounted on the automatic tracker. The parameters of the tracker required re-configuration to avoid misalignment.

The days represented by records 1 to 6 are for the same day number, in mid-summer, but for the years 1996, 1997, 1998, 1999, 2002 and 2003, respectively. There are large differences in the levels of the time-corresponding irradiances. Aside from the solar misalignment, the day in record 1 has clear sky conditions for the first part of the day. The irradiance fluctuations for the days in records 2 and 6 suggest partly cloudy conditions with intermittent sun cover by cumulus clouds. The low global irradiances during the days in records 3 and 4, as well as the complete elimination of direct irradiances suggest that the sun is completely obscured for most of the solar day in these records. The day in record 5 shows a clear sky period between $08h43$ and $15h08$. Irradiance levels outside this period are influenced by intermittent cloud cover over the sun.

Records 7 and 9 give examples of clear sky days. The day in record 7 is in summer; the day in record 9 in winter. The differences in the maximum direct and global solar irradiances, and occurring at solar noon, are about $260 Wm^{-2}$ and $613 Wm^{-2}$, respectively. The clearness parameters on these days are 0.75 and 0.55, at solar noon. Likewise the transparency coefficients are 0.70 and 0.45. It follows that the summer day in record 7 has clearer sky conditions at solar noon than the winter day in record 9. For

the day in record 9, the direct irradiance far exceeds the global, which is not atypical for Norwegian clear winter days.

The days represented by the records 1, 8, 14 and 15 have clear sky conditions for the first part of the day, and then an almost sudden build-up of cloud and hence diffuse solar irradiation. The day in record 14 shows the increased contribution to the diffuse irradiance by the obscured sun after $11h50$. The diffuse at $13h48$ is about $40Wm^{-2}$ higher than the level of diffuse at $10h12$.

The spring days represented by the records 13 and 16 both show a large dip in the direct irradiance around solar noon and a corresponding increase in the diffuse. It is noted that the total irradiance at these times for the day in record 13 is mostly diffuse, with a high of about $382Wm^{-2}$. The cloudy day in the early spring day of record 10 shows higher levels of global irradiances than the clear day in record 9. The increase in the solar noon horizontal component of the extraterrestrial irradiance for the time between records 9 and 10 is 47% and explains the increase in the observed ground irradiance.

The influence of distinct seasons can be seen in all the day records. The times corresponding to the sharp irradiance cutoffs at sunrise and sunset show the effect of the horizon. The time span in each record show the impact of the site's high latitude.

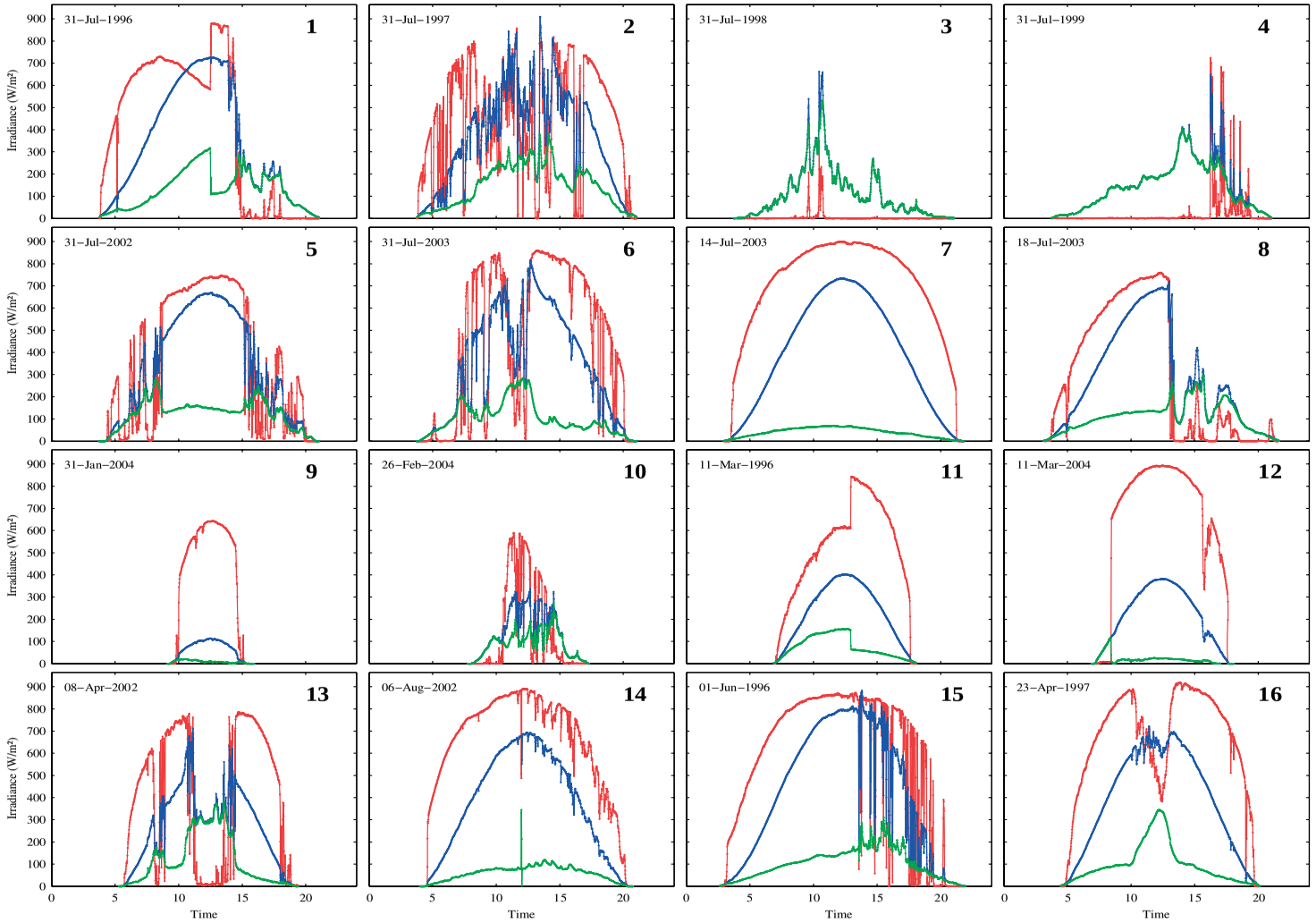

FIGURE 4.6
Sixteen records of direct normal (plotted in red) and global (plotted in blue) solar irradiance as a function of time of day for NTNU. The calculated horizontal diffuse (plotted in green) is also indicated.

4.3. Month Synopsis of Data

This section gives a summary of the data from the sites at UKZN and NTNU. The summary is in the form of tabulated energy densities per month, monthly average daily energy densities and transmission factors.

4.3.1. Energy Density

Table 4A and Table 4B gives the energy density per month for the sites at UKZN and NTNU, respectively. The tables also include the monthly average daily energy densities. The numbers are for direct, global and diffuse irradiances. According to the status of data from UKZN (see bar plots in FIGURE 2.10(a) to FIGURE 2.10(f)) there can be a number of missing data points within a day.

The results in Table 4A are taken with the missing points set to zero. This can be misleading if the status of data are not considered. The energies given for September 2001, for instance, is taken as the sum of data from just two days instead of 30 days. Filling in 1-minute data for the other 28 days is not viable. The missing points for the data from the NTNU site are also taken as zero, although there are fewer missing points in comparison to the data records from the site at UKZN. The results for UKZN may also be misleading due to omission of data quality control. Checks on the reliability of the data at UKZN is a challenge due to infrequent maintenance of the instruments and poor registration of the maintenance.

Observed irradiances, such as those in Table 4A and Table 4B can be used in applications where seasonal trends are required. For instance, the efficiency of photovoltaic systems may be tested by:

$$\eta_m = \frac{E_m}{H_m \cdot A} \tag{26}$$

where: η_m is the monthly module efficiency, E_m is the total energy produced (Wh) in the given month, H_m is the total incident radiation ($Wh\ m^{-2}$) in the given month, and A is the module area (m^2). As an example Carr et al. in [2., 2004] has carried out work on comparing the performance of different photovoltaic module types in temperate climates.

Table 4A : Month Totals and the Monthly Average of Daily Solar Irradiance from raw data at UKZN.

Year	Type	Units	Jan	Feb	Mar	Apr	May	Jun	Jul	Aug	Sep	Oct	Nov	Dec
1998	Direct Normal	kWh / m^2	-	-	-	-	-	-	-	43.99	86.39	97.18	52.08	99.91
	Direct Horizontal	kWh / m^2	-	-	-	-	-	-	-	25.54	56.35	70.49	38.00	75.86
	Global	kWh / m^2	-	-	-	-	-	-	-	35.23	100.18	141.17	91.51	145.11
	Diffuse	kWh / m^2	-	-	-	-	-	-	-	9.08	41.27	67.49	49.07	66.06
1999	Direct Normal	kWh / m^2	39.81	5.66	79.70	-	-	-	-	79.45	128.40	123.54	44.55	84.35
	Direct Horizontal	kWh / m^2	32.38	3.93	54.75	-	-	-	-	44.54	82.72	88.74	32.46	63.65
	Global	kWh / m^2	56.69	6.37	75.40	-	-	-	-	63.09	124.07	128.96	105.06	134.13
	Diffuse	kWh / m^2	24.08	2.45	19.65	-	-	-	-	18.26	41.00	40.34	62.54	66.50
2000	Direct Normal	kWh / m^2	75.55	76.16	104.46	116.75	105.44	137.92	148.28	133.05	70.73	27.25	58.94	53.16
	Direct Horizontal	kWh / m^2	56.40	56.25	68.50	65.02	52.52	62.42	71.29	73.85	46.55	20.73	40.03	40.49
	Global	kWh / m^2	115.73	122.87	115.94	110.09	83.32	81.15	92.10	105.37	114.71	101.83	104.12	118.47
	Diffuse	kWh / m^2	54.74	67.56	47.16	38.92	28.62	10.57	15.67	30.91	49.94	47.85	53.28	66.35
2001	Direct Normal	kWh / m^2	97.77	33.85	94.59	90.65	97.44	116.36	126.96	89.61	13.74	-	-	-
	Direct Horizontal	kWh / m^2	75.79	25.53	63.18	52.73	47.24	53.59	61.74	48.55	8.39	-	-	-
	Global	kWh / m^2	144.30	70.20	101.17	90.37	85.91	72.54	79.57	93.62	9.59	-	-	-
	Diffuse	kWh / m^2	52.89	40.58	36.09	37.77	26.31	18.58	14.73	33.48	1.20	-	-	-
2002	Direct Normal	kWh / m^2	-	-	73.64	140.42	130.96	136.09	136.79	102.00	116.29	103.17	132.29	101.94
	Direct Horizontal	kWh / m^2	-	-	47.57	81.89	65.24	62.12	66.03	56.76	74.27	75.37	99.37	79.44
	Global	kWh / m^2	-	-	70.70	107.44	85.17	75.37	78.51	81.82	106.39	126.84	155.94	142.77
	Diffuse	kWh / m^2	-	-	20.31	24.91	18.46	13.23	12.07	22.61	27.11	45.19	55.31	66.43
Means	Direct Normal	kWh / m^2 /day	2.29	1.38	2.84	3.86	3.59	4.34	4.43	2.89	2.77	2.83	2.40	2.74
	Direct Horizontal	kWh / m^2 /day	1.77	1.02	1.89	2.22	1.77	1.98	2.14	1.61	1.79	2.06	1.75	2.09
	Global	kWh / m^2 /day	3.41	2.37	2.93	3.42	2.74	2.55	2.69	2.45	3.03	4.02	3.81	4.36
	Diffuse	kWh / m^2 /day	1.42	1.32	0.99	1.13	0.79	0.47	0.46	0.74	1.07	1.62	1.83	2.14

Table 4B : Month Totals and the Monthly Average of Daily Solar Irradiance from raw data at NTNU.

Year	Type	Units	Jan	Feb	Mar	Apr	May	Jun	Jul	Aug	Sep	Oct	Nov	Dec
1991	Direct Normal	kWh / m^2	-	-	-	-	-	-	37.81	63.86	38.53	32.99	6.79	1.30
	Direct Horizontal	kWh / m^2	-	-	-	-	-	-	20.65	30.14	13.89	7.56	0.80	0.07
	Global	kWh / m^2	-	-	-	-	-	-	96.39	99.91	50.80	26.74	6.44	1.66
	Diffuse	kWh / m^2	-	-	-	-	-	-	32.61	64.36	35.61	19.23	5.64	1.16
1992	Direct Normal	kWh / m^2	2.48	11.82	25.80	88.56	105.91	161.20	54.89	40.34	51.14	36.79	4.69	1.34
	Direct Horizontal	kWh / m^2	0.25	2.67	9.87	42.17	59.69	91.60	31.53	19.59	19.19	8.23	0.57	0.08
	Global	kWh / m^2	2.80	16.13	48.16	109.14	149.29	174.79	123.08	85.36	63.19	27.22	5.11	1.50
	Diffuse	kWh / m^2	2.51	12.68	38.49	67.27	90.05	83.99	92.45	66.10	44.28	19.09	4.54	0.96
1993	Direct Normal	kWh / m^2	2.28	10.59	50.29	72.49	121.49	127.31	78.39	57.72	86.04	38.79	35.71	1.80
	Direct Horizontal	kWh / m^2	0.27	2.40	18.37	32.86	65.86	65.05	44.43	28.77	30.93	10.05	4.42	0.10
	Global	kWh / m^2	4.50	14.81	54.78	121.06	136.60	154.26	137.04	101.21	62.01	26.28	10.43	2.15
	Diffuse	kWh / m^2	1.37	12.45	36.48	87.52	70.92	67.37	93.04	72.61	31.14	16.40	6.01	1.26
1994	Direct Normal	kWh / m^2	2.91	58.60	64.44	97.41	155.75	41.57	165.79	82.86	110.76	22.07	11.76	4.51
	Direct Horizontal	kWh / m^2	0.33	11.16	21.21	45.34	82.48	23.17	89.57	40.02	42.92	5.31	1.36	0.26
	Global	kWh / m^2	3.53	24.81	57.73	100.00	159.74	97.61	167.65	100.59	74.95	25.55	6.81	2.26
	Diffuse	kWh / m^2	1.64	13.67	36.77	55.03	77.98	75.67	78.54	60.90	32.21	20.67	5.33	2.00
1995	Direct Normal	kWh / m^2	6.94	0.60	26.84	98.35	131.05	107.83	106.67	53.52	107.03	33.54	18.66	4.62
	Direct Horizontal	kWh / m^2	0.64	0.08	10.00	43.54	67.23	58.71	57.29	25.27	41.30	8.53	2.51	0.26
	Global	kWh / m^2	4.76	1.31	34.14	96.16	140.16	127.50	141.57	83.08	77.02	21.74	7.61	1.84
	Diffuse	kWh / m^2	4.14	1.22	24.38	35.30	73.69	68.22	84.93	58.49	35.97	13.32	5.15	1.59
1996	Direct Normal	kWh / m^2	27.10	32.86	115.37	88.47	130.80	54.97	79.97	122.87	102.95	30.52	16.37	5.22
	Direct Horizontal	kWh / m^2	2.63	6.32	39.43	40.16	66.21	32.56	44.59	57.81	37.68	7.36	1.83	0.29
	Global	kWh / m^2	6.31	18.42	69.69	88.07	144.11	107.94	129.01	114.03	72.03	24.63	7.16	1.64
	Diffuse	kWh / m^2	3.56	12.18	30.40	48.19	78.64	76.28	85.11	56.51	34.51	17.42	5.36	1.35
1997	Direct Normal	kWh / m^2	0.38	30.20	48.01	73.44	94.94	131.58	193.15	122.34	44.38	27.69	20.82	6.31
	Direct Horizontal	kWh / m^2	0.03	5.71	16.56	34.27	48.18	72.13	101.42	59.36	17.95	6.48	2.28	0.34
	Global	kWh / m^2	3.50	16.31	46.74	89.19	135.13	150.09	172.74	109.84	57.78	25.17	7.34	2.05
	Diffuse	kWh / m^2	3.51	10.71	30.90	56.39	86.92	78.69	71.60	50.61	34.29	16.21	5.07	1.70

Table 4B(continued): Month Totals and the Monthly Average of Daily Solar Irradiance from raw data at NTNU.

Year	Type	Units	Jan	Feb	Mar	Apr	May	Jun	Jul	Aug	Sep	Oct	Nov	Dec
1998	Direct Normal	kWh / m^2	6.73	14.45	45.00	150.90	138.85	93.51	78.07	76.27	99.57	47.64	17.51	5.31
	Direct Horizontal	kWh / m^2	0.47	2.84	15.19	65.98	75.54	52.52	40.26	36.22	37.53	11.61	2.28	0.24
	Global	kWh / m^2	3.99	13.33	47.90	109.82	155.45	135.28	117.76	96.67	72.04	29.09	7.18	1.65
	Diffuse	kWh / m^2	3.53	10.62	33.28	43.94	80.92	83.40	78.11	61.30	34.59	17.68	4.90	1.27
1999	Direct Normal	kWh / m^2	10.07	15.07	69.55	78.98	179.13	116.69	76.25	139.66	94.34	43.83	9.09	4.00
	Direct Horizontal	kWh / m^2	0.78	3.32	23.65	35.83	93.40	62.73	41.59	64.82	34.70	11.30	1.11	0.23
	Global	kWh / m^2	3.87	15.33	57.45	91.36	164.09	132.46	119.06	122.27	71.14	27.05	5.39	1.39
	Diffuse	kWh / m^2	2.93	11.05	34.01	56.00	71.21	70.37	78.35	57.59	36.53	15.95	4.13	1.16
2000	Direct Normal	kWh / m^2	2.39	5.46	-	0.15	-	-	42.70	47.99	31.05	6.97	18.85	-
	Direct Horizontal	kWh / m^2	0.16	1.01	-	0.06	-	-	21.16	22.24	11.93	1.25	2.47	-
	Global	kWh / m^2	2.13	6.35	-	93.98	132.77	91.35	98.21	79.25	68.32	19.36	5.45	-
	Diffuse	kWh / m^2	2.02	5.51	-	0.48	-	-	7.97	57.20	19.86	2.39	2.99	-
2001	Direct Normal	kWh / m^2	19.54	36.76	89.07	94.31	-	104.74	72.63	58.09	63.18	34.96	5.18	-
	Direct Horizontal	kWh / m^2	1.97	6.68	30.68	43.73	-	57.41	41.11	26.41	22.35	8.00	0.63	-
	Global	kWh / m^2	4.16	17.48	62.76	86.71	-	113.52	118.24	84.82	62.06	22.84	4.25	-
	Diffuse	kWh / m^2	1.85	10.98	32.19	43.07	-	51.05	77.62	50.15	25.70	14.92	3.68	-
2002	Direct Normal	kWh / m^2	4.37	6.79	7.52	70.03	56.96	17.15	76.51	158.09	25.42	47.18	15.49	3.64
	Direct Horizontal	kWh / m^2	0.35	1.67	2.53	34.55	29.31	10.04	40.57	76.31	9.56	11.12	1.73	0.21
	Global	kWh / m^2	2.50	15.12	32.66	97.05	100.54	53.51	133.23	132.26	49.67	27.86	7.81	1.26
	Diffuse	kWh / m^2	1.82	8.81	24.89	25.70	50.60	17.75	42.14	45.44	10.21	8.03	1.61	0.14
2003	Direct Normal	kWh / m^2	0.17	-	-	7.65	83.59	37.26	164.08	-	13.31	23.22	19.92	3.08
	Direct Horizontal	kWh / m^2	0.01	-	-	4.02	43.92	20.43	86.30	-	4.71	6.66	2.32	0.17
	Global	kWh / m^2	2.40	19.86	43.57	107.01	125.24	90.05	-	-	62.46	29.40	7.08	0.73
	Diffuse	kWh / m^2	0.04	-	-	9.98	43.49	19.18	-	-	10.51	19.53	1.69	0.48
Means	Direct Normal	kWh / m^2 /day	0.23	0.72	1.75	2.56	3.87	3.01	3.04	2.75	2.22	1.06	0.51	0.12
	Direct Horizontal	kWh / m^2 /day	0.02	0.14	0.60	1.17	2.04	1.66	1.64	1.31	0.83	0.26	0.06	0.01
	Global	kWh / m^2 /day	0.12	0.53	1.63	3.30	4.53	3.97	4.18	3.25	2.16	0.83	0.23	0.05
	Diffuse	kWh / m^2 /day	0.08	0.36	1.04	1.47	2.34	2.10	2.21	1.89	0.99	0.50	0.14	0.038

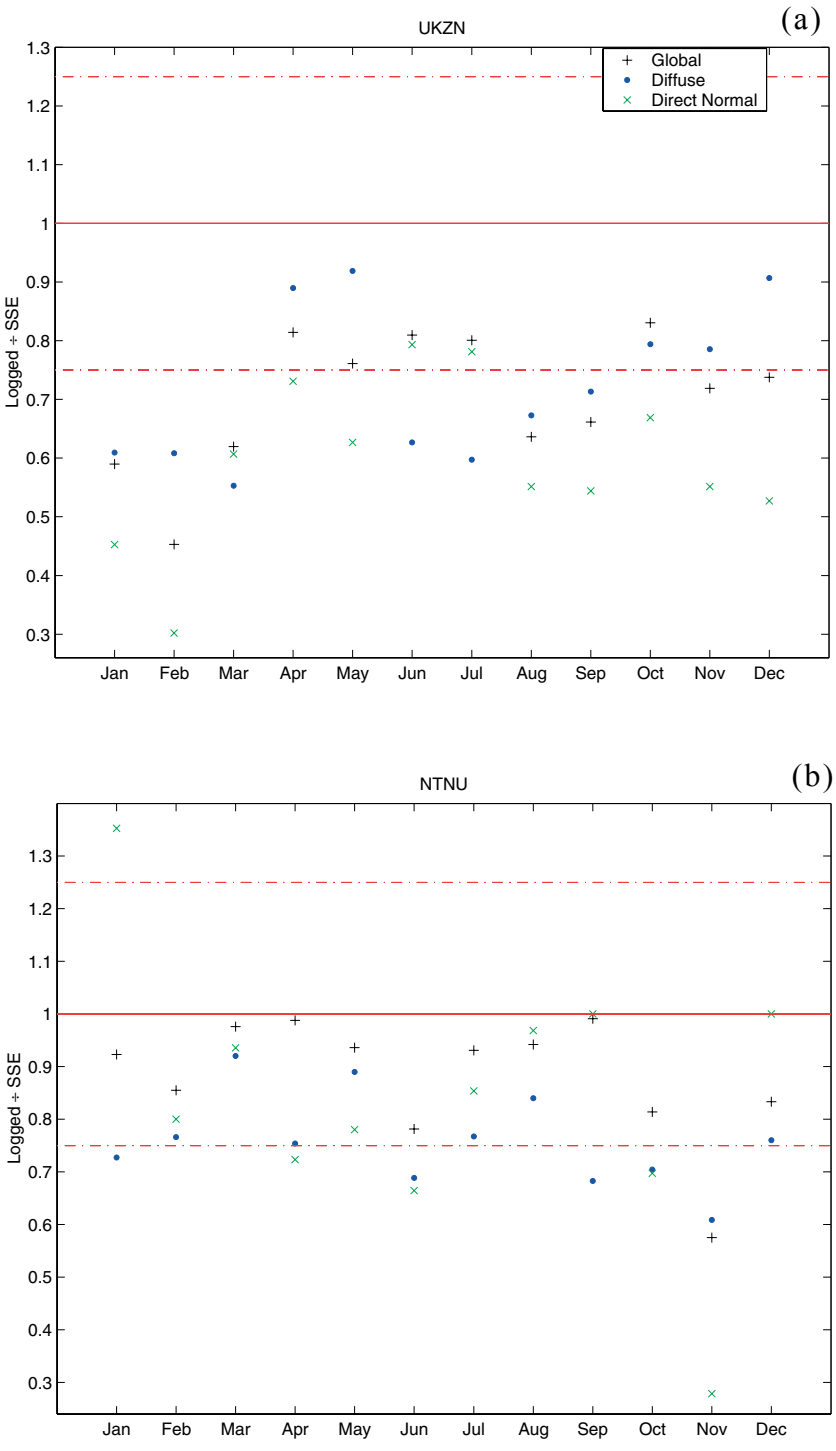

FIGURE 4.7
Ratios between collected data and SSE projections at:
(a) UKZN and (b) NTNU.

It is possible to compare the monthly averaged irradiances given in the Table 4A and Table 4B to data sets generated by physical models. For instance the solar energy data supplied by NASA in [10., 2005] with references to Stackhouse et al. in [15., 2000] and Stackhouse et al. in [16., 2003] (see Part B, section 6.2 on page 186). These data are referred to as the Surface Meteorology and Solar Energy (SSE) data. Results from comparisons between the SSE and UKZN and NTNU, respectively, are given by the ratio plots in FIGURE 4.7. The SSE data sets have an uncertainty of below 25%. It is seen that the majority of ratios for NTNU in FIGURE 4.7(b) are within the ±25% band. This is not the case for the ratios for UKZN in FIGURE 4.7(a). The main reason for a larger deviation from unity in the UKZN-to-SSE comparison would be the status of the logged data at UKZN. On the other hand, valid data logs would give the advantage of assessing data sets such as from the SSE. As an example, FIGURE 4.7(b) shows that the SSE data set for NTNU consists mainly of irradiance overestimates.

4.3.2. Transmission Factors

Table 4C and Table 4D give the mean month variations of transmission factors for the sites at UKZN and NTNU, respectively.

The transmission factors are:

* the direct transmission $T = (T_m)^m = \frac{S_m}{S_o}$, and follows from equation (7) on page 8.
* the clearness parameter (also called the clearness index) as given by equation (10) on page 9, $\left(K_T = \frac{F^H_{Global}}{S_o \cdot \cos\theta_z} \right)$, and
* the diffuse fraction:

$$K_d = \frac{F^H_{diffuse}}{F^H_{Global}}, \tag{27}$$

where $F^H_{diffuse}$ and F^H_{Global} are respectively the diffuse and global irradiances on a horizontal surface (see section 1.2.3 on page 9).

The transmission means are calculated as follows:

- the transmission factor for each 1-minute irradiance is calculated,
- the day average is calculated for all factors within the solar day,
- the month average is calculated from the day averages.

The direct normal transmission factor, or the atmospheric transparency factor as given by T_m in equation (7) on page 8 can be used to assess diurnal and seasonal variations of the direct solar irradiance. Since, as shown by Kondratyev in [9., 1969], either factor is dependent on the solar height, it would be more suitable to use turbidity factors in quantifying atmospheric pollution. The turbidity factor is a relative transparency characteristic. It indicates the degree to which the real atmospheric transparency differs from the ideal and is less dependent on atmospheric mass than the former factors. An investigation into the transparency coefficient and turbidity for the site at NTNU based on the work by Ohvril et al. in [11., 1999], is being carried out. This would allow conclusions with regard to multi-annual trends of atmospheric transparency and turbidity.

It is typical to see both diurnal and seasonal variations in the clearness index. Table 4C shows that the clearness index for UKZN in the year 2000 reaches its lowest values during the summer months (for example December). The highest values are in the winter months (for example June). This is due to variation in the condition of the air between the seasons. During the summer months the level of fine dust particles in the air as well as the relative humidity are higher than that during the winter months. Table 4D shows that the clearness index for NTNU is generally lower in the winter months. This is attributed to the climate associated with areas at high latitudes.

Table 4C : Transmission Factors from irradiance data at UKZN.

Year		Jan	Feb	Mar	Apr	May	Jun	Jul	Aug	Sep	Oct	Nov	Dec
1998	T	-	-	-	-	-	-	-	0.36	0.26	0.23	0.22	0.25
	K_T	-	-	-	-	-	-	-	0.49	0.42	0.41	0.39	0.39
	K_d	-	-	-	-	-	-	-	0.26	0.41	0.48	0.54	0.46
1999	T	0.34	0.36	0.41	-	-	-	-	0.37	0.32	0.35	0.14	0.24
	K_T	0.48	0.58	0.54	-	-	-	-	0.49	0.46	0.46	0.39	0.40
	K_d	0.42	0.38	0.26	-	-	-	-	0.29	0.33	0.31	0.60	0.50
2000	T	0.21	0.20	0.29	0.32	0.33	0.43	0.42	0.34	0.23	0.12	0.21	0.17
	K_T	0.37	0.40	0.45	0.46	0.46	0.49	0.50	0.46	0.41	0.30	0.34	0.33
	K_d	0.47	0.55	0.41	0.35	0.34	0.13	0.17	0.29	0.44	0.47	0.51	0.56
2001	T	0.28	0.17	0.29	0.25	0.31	0.34	0.37	0.26	0.49	-	-	-
	K_T	0.37	0.35	0.42	0.38	0.47	0.44	0.44	0.42	0.57	-	-	-
	K_d	0.37	0.58	0.36	0.42	0.31	0.26	0.19	0.36	0.13	-	-	-
2002	T	-	-	0.35	0.37	0.38	0.40	0.39	0.32	0.32	0.25	0.31	0.26
	K_T	-	-	0.45	0.47	0.44	0.46	0.43	0.36	0.39	0.37	0.41	0.36
	K_d	-	-	0.29	0.23	0.22	0.18	0.15	0.28	0.25	0.36	0.35	0.47
Means	T	0.28	0.24	0.33	0.31	0.34	0.39	0.39	0.33	0.32	0.19	0.22	0.23
	K_T	0.41	0.45	0.47	0.44	0.46	0.46	0.45	0.44	0.45	0.31	0.38	0.37
	K_d	0.42	0.50	0.33	0.33	0.29	0.19	0.17	0.29	0.31	0.32	0.50	0.49

T is the direct normal transmission factor with respect to extraterrestrial

K_T is the global horizontal transmission factor (clearness parameter) with respect to extraterrestrial horizontal

K_d is the ratio of diffuse horizontal with respect to global horizontal

Table 4D : Transmission Factors from irradiance data at NTNU.

Year		Jan	Feb	Mar	Apr	May	Jun	Jul	Aug	Sep	Oct	Nov	Dec
1991	T	-	-	-	-	-	-	0.15	0.11	0.09	0.09	0.03	0.01
	K_T	-	-	-	-	-	-	0.41	0.38	0.33	0.37	0.30	0.34
	K_d	-	-	-	-	-	-	0.34	0.64	0.70	0.72	0.88	0.70
1992	T	0.01	0.04	0.05	0.15	0.14	0.22	0.08	0.07	0.11	0.11	0.03	0.01
	K_T	0.25	0.30	0.32	0.44	0.43	0.49	0.36	0.35	0.41	0.42	0.32	0.38
	K_d	0.89	0.79	0.80	0.62	0.60	0.48	0.75	0.77	0.70	0.70	0.89	0.64
1993	T	0.04	0.03	0.10	0.12	0.18	0.22	0.11	0.09	0.21	0.11	0.13	0.02
	K_T	0.34	0.31	0.35	0.50	0.41	0.43	0.39	0.39	0.47	0.34	0.47	0.47
	K_d	0.30	0.84	0.67	0.72	0.52	0.44	0.68	0.72	0.50	0.62	0.58	0.58
1994	T	0.04	0.18	0.15	0.18	0.22	0.08	0.24	0.13	0.22	0.06	0.05	0.02
	K_T	0.36	0.50	0.39	0.43	0.45	0.31	0.51	0.39	0.42	0.33	0.30	0.41
	K_d	0.47	0.55	0.64	0.55	0.49	0.78	0.47	0.61	0.43	0.81	0.78	0.89
1995	T	0.03	0.02	0.09	0.19	0.19	0.12	0.15	0.10	0.24	0.11	0.07	0.03
	K_T	0.35	0.27	0.31	0.39	0.41	0.38	0.42	0.35	0.49	0.31	0.34	0.39
	K_d	0.87	0.94	0.71	0.37	0.53	0.54	0.60	0.70	0.47	0.61	0.68	0.86
1996	T	0.12	0.11	0.23	0.21	0.19	0.08	0.12	0.19	0.22	0.08	0.07	0.04
	K_T	0.45	0.38	0.45	0.46	0.43	0.30	0.38	0.42	0.44	0.31	0.33	0.36
	K_d	0.56	0.66	0.44	0.55	0.55	0.71	0.66	0.50	0.48	0.71	0.75	0.82
1997	T	0.00	0.11	0.12	0.14	0.15	0.18	0.27	0.24	0.09	0.08	0.08	0.04
	K_T	0.27	0.38	0.33	0.36	0.39	0.40	0.50	0.47	0.34	0.32	0.34	0.39
	K_d	1.00	0.66	0.66	0.63	0.64	0.52	0.41	0.46	0.59	0.64	0.69	0.83

Table 4D(continued): Transmission Factors from irradiance data at NTNU.

Year		Jan	Feb	Mar	Apr	May	Jun	Jul	Aug	Sep	Oct	Nov	Dec
1998	T	0.03	0.05	0.11	0.26	0.21	0.13	0.11	0.13	0.20	0.13	0.07	0.04
	K_T	0.31	0.27	0.32	0.45	0.44	0.35	0.36	0.36	0.42	0.38	0.30	0.40
	K_d	0.88	0.80	0.69	0.40	0.52	0.62	0.66	0.63	0.48	0.61	0.68	0.77
1999	T	0.05	0.05	0.15	0.14	0.27	0.17	0.12	0.23	0.20	0.12	0.04	0.02
	K_T	0.37	0.30	0.38	0.37	0.46	0.35	0.32	0.43	0.41	0.30	0.21	0.23
	K_d	0.76	0.72	0.59	0.61	0.43	0.53	0.66	0.47	0.51	0.59	0.77	0.84
2000	T	0.02	0.03	-	0.03	-	-	0.35	0.08	0.15	0.08	0.13	-
	K_T	0.14	0.24	-	0.37	0.41	0.30	0.45	0.31	0.39	0.33	0.29	-
	K_d	0.95	0.87	-	0.01	-	-	0.08	0.72	0.29	0.12	0.55	-
2001	T	0.13	0.12	0.19	0.19	-	0.20	0.10	0.12	0.14	0.09	0.02	-
	K_T	0.29	0.33	0.39	0.40	-	0.42	0.33	0.35	0.37	0.28	0.18	-
	K_d	0.44	0.63	0.51	0.50	-	0.45	0.66	0.59	0.41	0.65	0.86	-
2002	T	0.02	0.03	0.03	0.23	0.18	0.18	0.22	0.28	0.14	0.19	0.11	0.08
	K_T	0.16	0.27	0.35	0.40	0.44	0.35	0.37	0.46	0.29	0.34	0.26	0.18
	K_d	0.73	0.58	0.76	0.26	0.50	0.33	0.32	0.34	0.21	0.29	0.21	0.11
2003	T	0.03	-	-	0.09	0.21	0.27	0.26	-	0.14	0.07	0.13	0.03
	K_T	0.16	0.33	0.29	0.42	0.36	0.44	-	-	0.36	0.33	0.25	0.15
	K_d	0.02	-	-	0.09	0.35	0.21	-	-	0.17	0.66	0.24	0.66
Means	T	0.04	0.07	0.12	0.16	0.19	0.17	0.17	0.15	0.17	0.10	0.07	0.03
	K_T	0.29	0.32	0.35	0.41	0.42	0.38	0.40	0.39	0.40	0.34	0.30	0.34
	K_d	0.66	0.73	0.65	0.44	0.51	0.51	0.52	0.60	0.46	0.60	0.66	0.70

T is the direct normal transmission factor with respect to extraterrestrial

K_T is the global horizontal transmission factor (clearness parameter) with respect to extraterrestrial horizontal

K_d is the ratio of diffuse horizontal with respect to global horizontal

Knowledge of the clearness index can be used in models to predict diffuse radiation. Coppolino, in [4., 1989], gives the diffuse radiation as linear and cubic expressions in K_T as derived by Page and Klein respectively. On the other hand, knowledge of the diffuse fraction K_d defined by equation (27) can be used to develop correlations between the diffuse fraction and the clearness index. Examples of such models are Collares-Pereira/Rabl and Ruth/Chant given by Duffie et al. in [5., 1980] and Skartveit/Olseth given by Skartveit et. al in [13., 1987]. A model for the diffuse fraction, tuned for locality, can provide means to estimate direct solar irradiance and insolation on inclined planes. It is found that the Skartveit/Olseth model best fits the data at both UKZN and NTNU. This is shown by the plots in FIGURE 4.8 and FIGURE 4.10. The data points in each of the plots are based on the following sequence:

* A selection of observed irradiances are taken. The selection represents clear, partly cloudy and very cloudy days.
* the 1-minute clearness indices and diffuse fractions are calculated from the data.
* the corresponding 1-minute diffuse fractions are calculated from the respective models.
* the 1-minute clearness indices and diffuse fractions are averaged over the solar day and plotted against each other.

The Skartveit/Olseth model differs from the previous models by including a dependence on solar elevation, not just the clearness index. The model does appear to overestimate the diffuse fraction under clear skies, for both UKZN and NTNU. According to Skartveit et al. in [14., 1998], this may be since the model does not account for climatic parameters such as surface albedo and atmospheric content. An improved model described by Skartveit et al. in [14., 1998], though not implemented in this work, considers corrections for variable/inhomogeneous clouds and surface albedo.

Another approach to estimate diffuse radiation is by finding correlation between the diffuse fraction of extraterrestrial irradiance[1] and the clearness

1. The diffuse fraction of extraterrestrial irradiance is given as $K_d = \frac{F_{diffuse}}{S_o}$.

index. Selected days of data from UKZN and NTNU are used for generation of plots given in FIGURE 4.9 and FIGURE 4.11. It is clear that correlations do exist for the specific sites and allows further investigation.

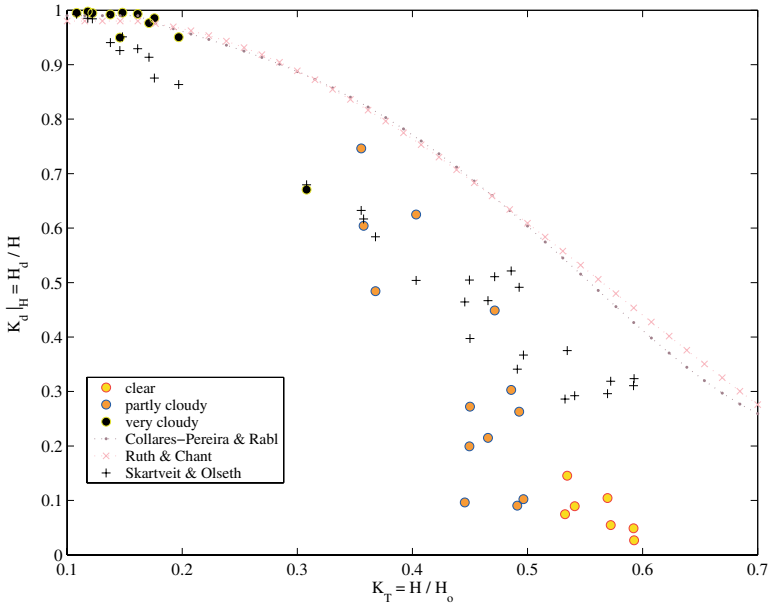

FIGURE 4.8
Variation of the diffuse fraction of daily global irradiance as a function of the clearness parameter for selected days at UKZN.

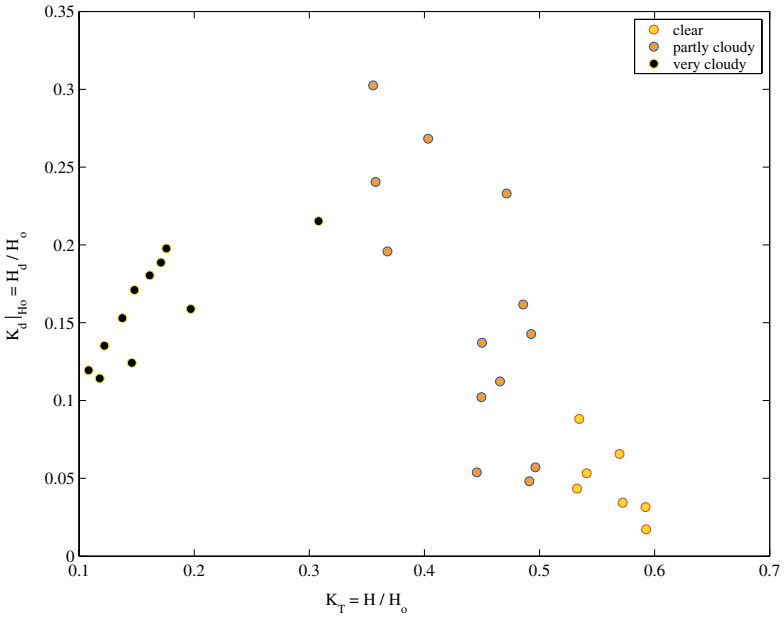

FIGURE 4.9
Variation of the diffuse fraction of daily extraterrestrial irradiance as a function of the clearness parameter for selected days at UKZN.

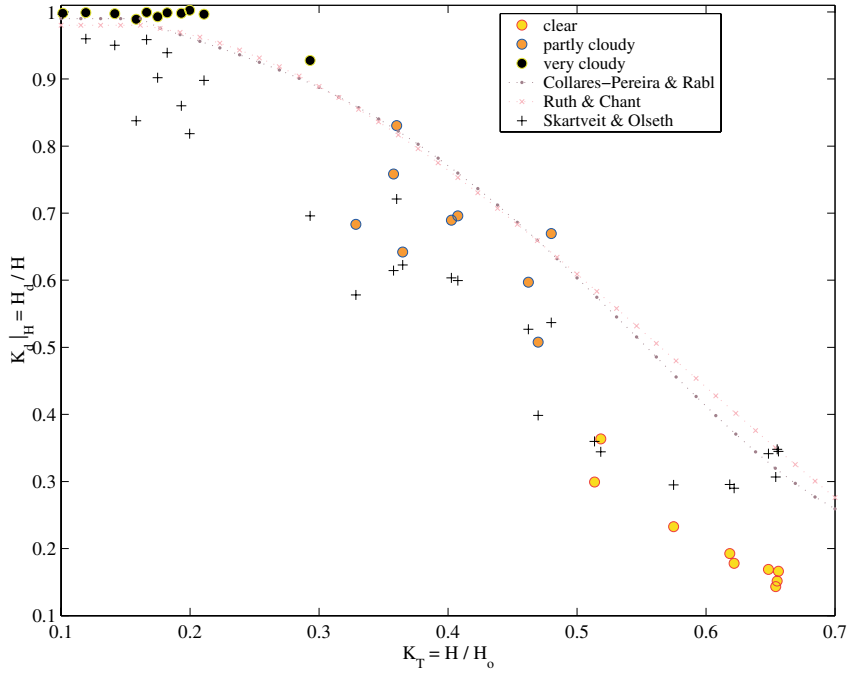

FIGURE 4.10
Variation of the diffuse fraction of daily global irradiance as a function of the clearness parameter for selected days at NTNU.

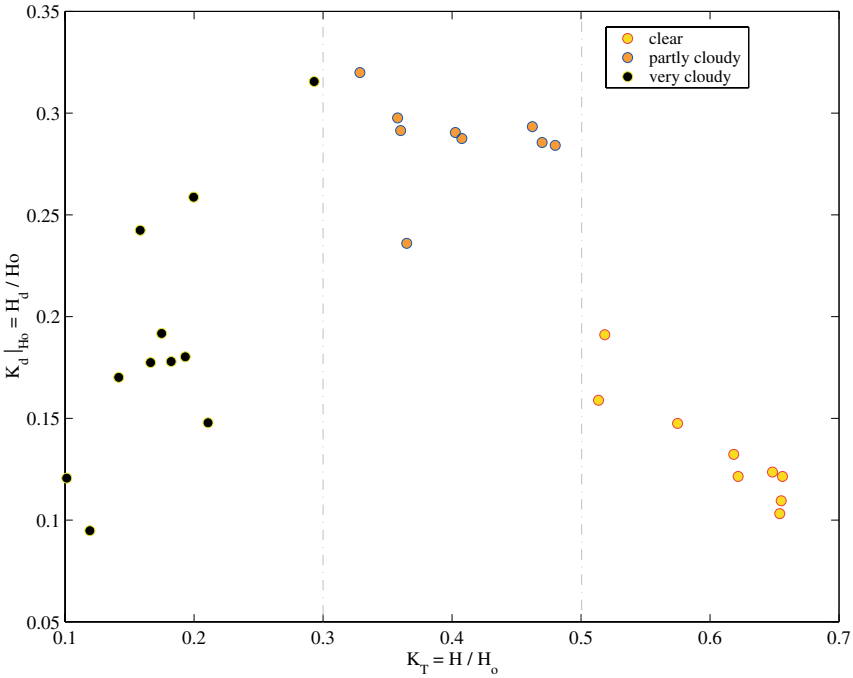

FIGURE 4.11
Variation of the diffuse fraction of daily extraterrestrial irradiance as a function of the clearness parameter for selected days at NTNU.

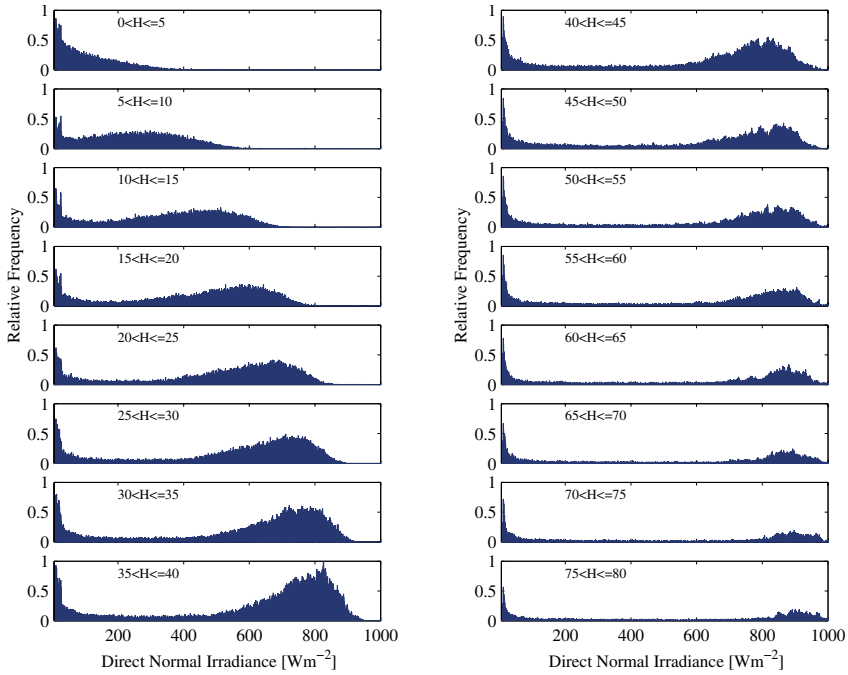

FIGURE 4.12
Relative frequency distributions of all measurements of the direct normal solar irradiance at UKZN in 16 intervals of solar height. The bin size is $1 Wm^{-2}$. The distributions are normalised to 1.

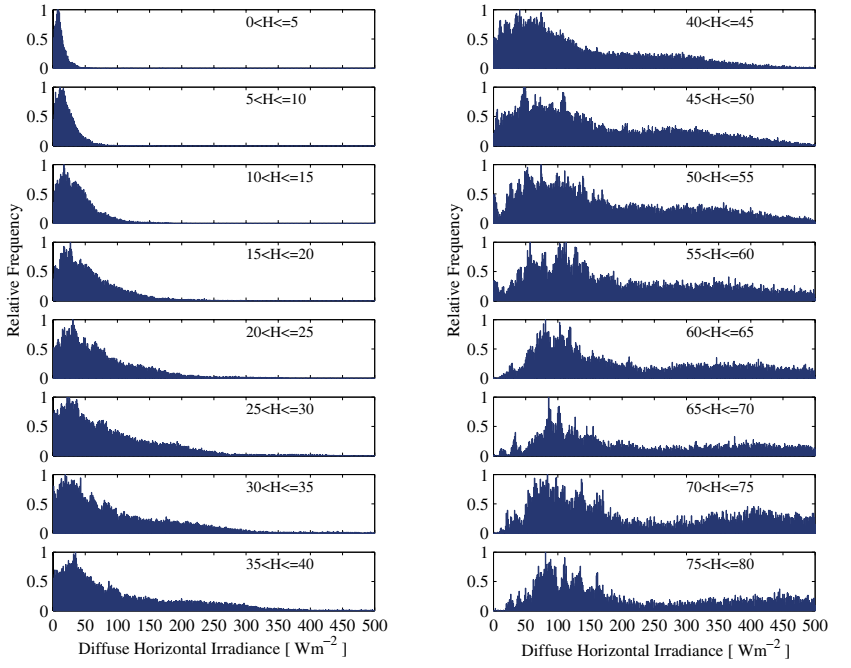

FIGURE 4.13
Relative frequency distributions of all derived measurements of the diffuse horizontal solar irradiance at UKZN in 16 intervals of solar height. The distributions are normalised to 1 in each plot.

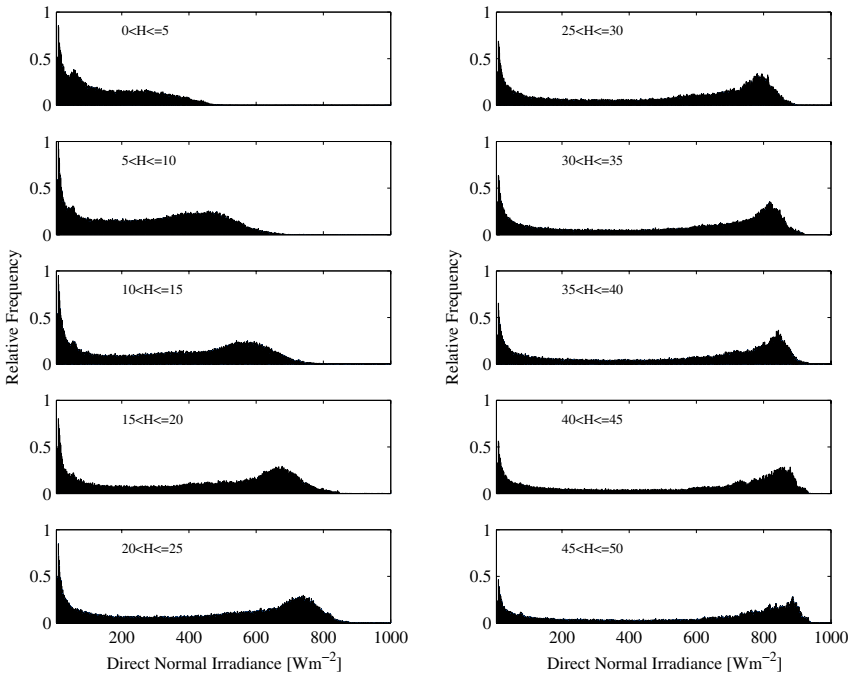

FIGURE 4.14
Relative frequency distributions of all measurements of the direct normal solar irradiance at NTNU in 10 intervals of solar height. The bin size is $1 Wm^{-2}$. The distributions are normalised to 1.

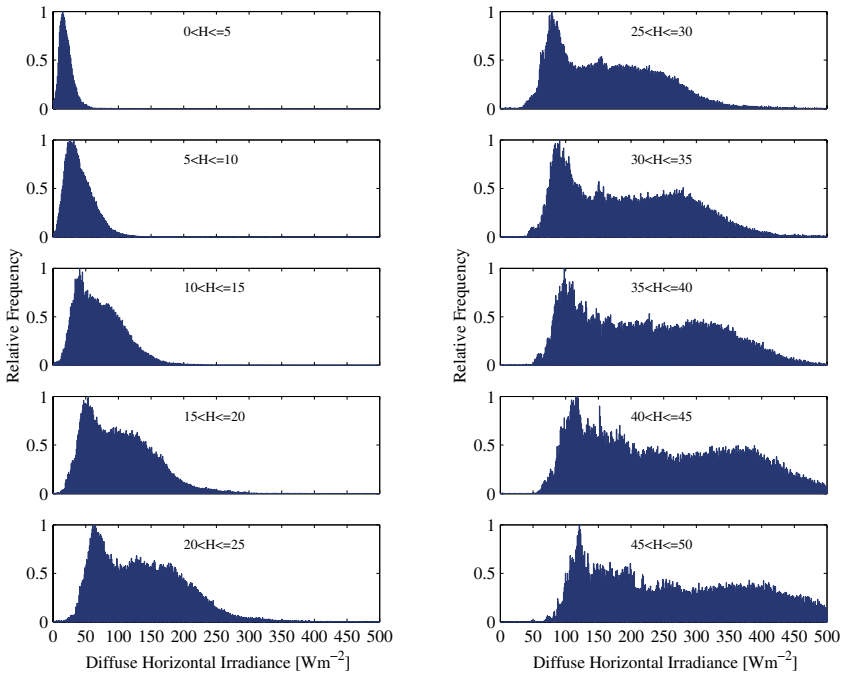

FIGURE 4.15
Relative frequency distributions of all derived measurements of the diffuse horizontal solar irradiance at NTNU in 10 intervals of solar height. The distributions are normalised to 1 in every interval.

4.4. Frequency Distributions

Frequency distributions of all measurements of direct normal and measurement related diffuse horizontal irradiances for the observation sites at UKZN and NTNU can be used to characterise the radiation data in terms of solar height dependency. The histograms in the figures FIGURE 4.12 to FIGURE 4.15 display the direct and diffuse frequency distributions, from all measurements, for each site. The data are divided into 16 intervals of solar height (from 0^o to 80^o in steps of 5^o). The bin size for each histogram is $1 Wm^{-2}$.

As expected, there is a dependence on solar height. The relative frequencies of direct irradiances above $600 Wm^{-2}$ from UKZN are most pronounced for solar heights between 35^o and 40^o (FIGURE 4.12). It appears that this would be an optimum inclination for a stationary solar collector. This also confirms the report by Duffie et al. in [5., 1980]. That is, a system designed with a receiving slope equal to latitude is best for maximum annual energy availability. NTNU is at a much higher latitude, and the optimum inclination on site would be between 25^o and 30^o (FIGURE 4.14).

The diffuse frequency distributions (FIGURE 4.13, FIGURE 4.15) suggest an increase of the irradiance with increasing solar height. Brevik, in [1., 1984] has shown that diffuse data from NTNU reflects different distributions for clear, partly cloudy and overcast days.

4.5. Chapter Summary and Conclusions

This chapter has presented the data collected at UKZN and NTNU. It has been shown, by comparison to an empirical model, that the data from UKZN is unreliable due to lack of cleaning of sensor windows. It has been shown that site maps of solar irradiance can be used to describe cloud structures. In addition, the correlation between transmission factors confirm claims as being useful in estimating direct solar irradiances and insolation on inclined planes. The various frequency distributions of irradiances at different intervals of solar height can be used in, for example, solar collector technology and building design.

4.6. References

1. Brevik I., *Models of the Direct and Diffuse Solar Radiation*, Department of Physics, University of Tondheim, 1984.
2. Carr A.J., Pryor T.L., *A Comparison of the Performance of Different PV Module Types in Temperate Climates*, Solar Energy, Vol. 76, pp. 285-294, 2004.
3. CEROI (Cities Environmental Report on the Internet), http://www.ceroi.net/reports/durban/drivers/Climate/temperat.htm, 1999.
4. Coppolino S., *A Simple Model for Computing Diffuse Solar Radiation*, Solar Energy, Vol. 43, No. 6, pp. 385-389, 1989.
5. Duffie J. A., Beckman W. A., *Solar Engineering of Thermal Processes*, John Wiley & Sons, Inc., USA, 1980.
6. Fröhlich C., Lean J., 1998, *The Suns Total Irradiance: Cycles, Trends and Related Climate Change Uncertainties since 1978*, Geophys.Res.Let., 25, pp. 4377-4380, 1998 (up to version 8).
7. Fröhlich C., *Solar Irradiance Variability*, in: Chapter 2 of Geophysical Monograph Series, 111, American Geophysical Union, in press 2003.
8. Hveem C., Eksperimentelt Studuim av Forskjellige tidsserier for solstråling og analyse av variasjonsmønsteret, Fysisk institutt, NTNU, 1998
9. Kondratyev K.YA., Radiation in the Atmosphere, International Geophysics series, Vol. 12, 1969.
10. NASA, '*Surface Meteorology and Solar Energy (release 5)*', URL: http://eosweb.larc.nasa.gov/sse/, January 2005.
11. Ohvril H., Okulov O., Teral H., Teral K., T*he Atmospheric Integral Transparency Coefficient and the Forbes Effect*, Solar Energy, Vol. 66, No. 4, pp. 305-317, 1999.
12. Rapti A.S., Atmospheric Transparency, Atmospheric Turbidity and Climatic Parameters, Solar Energy, Vol. 69, No. 2, pp. 99-111, 2000.
13. Skartveit A., Olseth J. A., *A Model for the Diffuse Fraction of Hourly Global Radiation*, Solar Energy, Vol. 38, No. 4, pp. 271-274, 1987.
14. Skartveit A., Olseth J. A., Tuft M. E., *An Hourly Diffuse Fraction Model with Correction for Variability and Surface Albedo*, Solar Energy, Vol. 63, No. 3, pp. 173-183, 1998.
15. Stackhouse, P. W., S. K. Gupta, S. J. Cox, M. Chiacchio, and J. C. Mikovitz, 2000: *The WCRP/GEWEX Surface Radiation Budget Project Release 2: An assessment of surface fluxes at 1 degree resolution*. In IRS 2000: Current Problems in Atmospheric Radiation, W. L. Smith and Y. M. Timofeyev, Eds., International Radiation Symposium, St. Petersburg, Russia, July 24-29, 2000.
16. Stackhouse, P.W., Jr., S. J. Cox, S. K. Gupta, J.C. Mikovitz, M. Chiacchio, 2003: *The WCRP/GEWEX Surface Radiation Budget Data Set: A 1 degree resolution, 12 year flux climatology*. (in preparation)

Chapter 5
Direct-Diffuse Solar Radiometer-1B

The Direct-Diffuse Solar Radiometer-1B (DDSR-1B) is an on the field, ground based instrument which is mounted on a remotely controlled solar tracker/sky positioner. DDSR-1B thereby measures direct/diffuse solar irradiance. The sensing element is a pyroelectric detector, 'triggered' by a modulator at 5Hz. The modulator and surrounding electronics with a second order bandpass pass filter minimises noise in the system. This noise elimination extends the limit on the lower irradiance level. Operation of the instrument is controlled by a miniature, modular PC unit.

5.1. Introduction

A dual mode radiometer has been developed at NTNU. This radiometer is called the Direct-Diffuse Solar Radiometer-1B (DDSR-1B). Motivations for a dual mode radiometer, such as the DDSR-1B, has been given in Chapter 1, section 1.3.4 on page 17. To recap, quantification of the angular distribution of sky radiance from localised sites are not readily available. This is due mainly to the lack of instrumentation. Development of the DDSR-1B is with the intent to fill this gap. DDSR-1B can be mounted onto a remotely controlled positioner for scanning the sky (to integrate sky radiances into diffuse measurements) and for pointing to the sun (for direct measurements).

It is advantageous to have a built-in positioner/radiometer system. However the development of a solar tracker has not been considered for the prototype DDSR-1B. Focus has been on the development of a sensing mechanism for the radiometer. This includes an optical design for the two modes of operation. In addition, a pyroelectric detector is selected for use in complement with a mechanical chopper. It is hoped that the chopper not only sources the pyroelectric detector but also facilitates elimination of thermal drift and signal noise. Necessary electronics have been considered for signal conditioning. Finally, custom engineered software is developed for remotely controlling the radiometer. Sections 5.2. to 5.5.3. give the mechanical, optical, electrical and control overview of the DDSR-1B. Section 5.6. describes the procedure for signal extraction. Sections 5.7. to 5.9. present the laboratory and on field test results together with an assessment of the system.

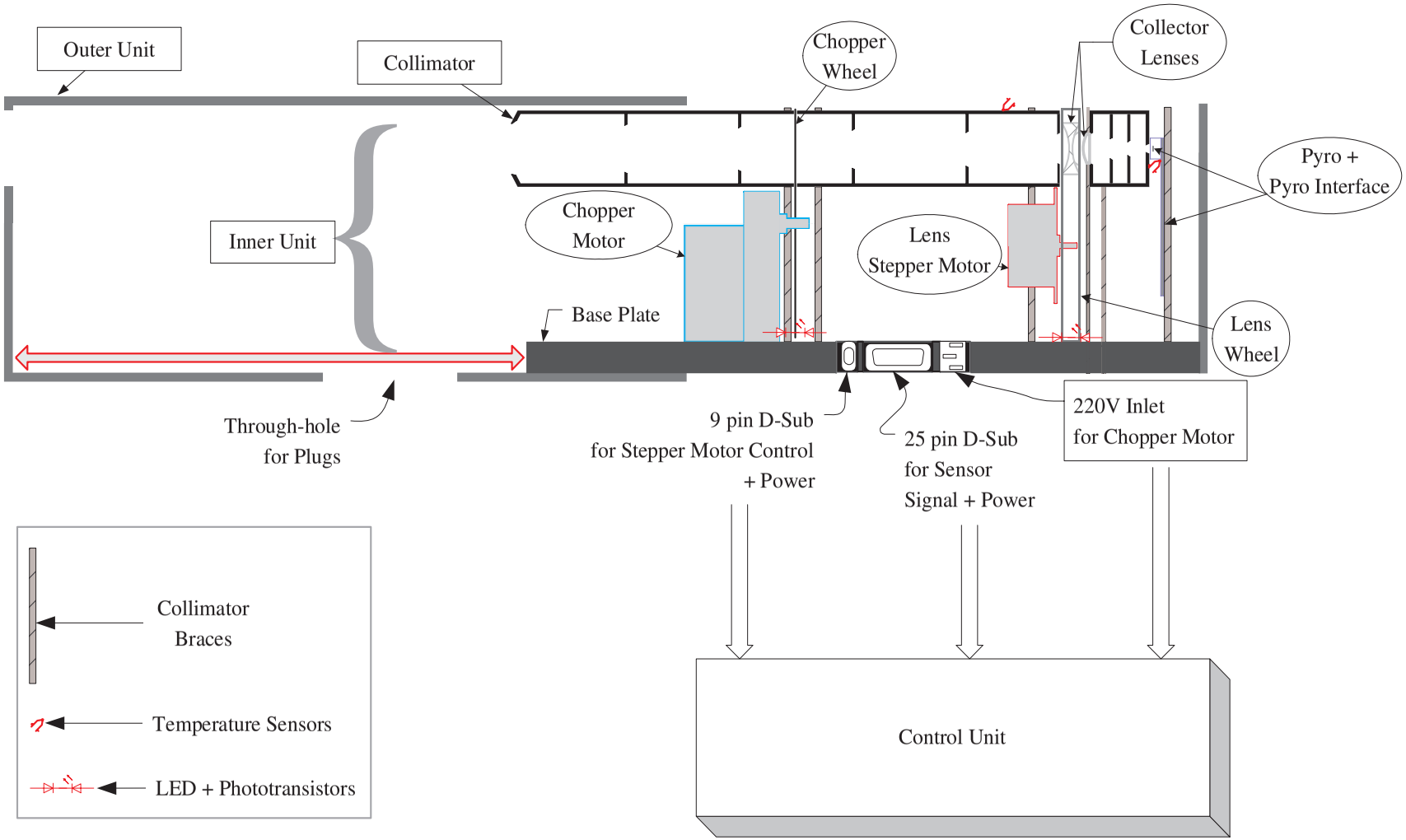

FIGURE 5.1
DDSR-1B system layout. The base plate provides a platform for the collimator braces, denoted motors and necessary cables. The system is held together by sliding the base plate through the outer unit (denoted by ⟺), and by fixing the two pieces by throughputs at the rear. The throughputs provide a mechanism for aligning the components of the collimator along its optic axis.

5.2. System Layout

DDSR-1B has a compact, modular design. Its system layout is given in FIGURE 5.1. The radiometer consists of two assembled units namely an outer unit and an inner unit. The outer unit, an aluminuim tube, is an encasement for the inner unit. It has an opening, at the base, for plug access. The inner unit consists of five sub-modules. These are a connector module, a chopper module, a lens module, a sensing module and a collimator module. The connector module is a base plate. It provides a mounting platform for the remaining sub-modules. Two throughputs at the rear of the inner and outer units allow for the units to be fastened together. The throughputs also provide a mechanism to align optical components and to keep the sub-modules fixed.

The collimator module is made up of fragmented tubes. Diffraction vanes are fastened at the fragment ends for optical limitations. The collimator module has three collimator sections as indicated in FIGURE 5.2. Sectioning of the collimator gives mounting ease and leeway for a chopper wheel and a lens wheel.

The chopper wheel, with 5 identical apertures, is used for beam modulation. The wheel is made from brass, is 1mm thick and oxidised for a black finish. The apertures are sized for a 100% beam transmission. The chopper wheel is spun with a synchronous motor, at 60 revolutions per minute. Power to the motor, and thus rotation of the wheel, is controlled remotely via software. An infra-red light emitting diode (LED) and phototransistor pair is used as a reference pick-up. The chopper wheel, synchronous motor and reference pick-up makes up the chopper module.

The lens module consists of two collector lenses, a stepper motor with a lens wheel, and a lens wheel position feedback. The collector lenses give the options for beam spreading or focussing, which are critical for the system. Beam spreading by a defocusing (concave) lens reduces the level of direct radiation on the sensor. Beam focussing by a convex lens can increase a diffuse signal. The defocusing lens is mounted on the lens wheel. The lens wheel has three view posts namely defocus lens, closed and open. The orientation of the lens wheel defines the mode of operation. DDSR-1B is in '*focus*' or '$Mode_{Diffuse}$' (measuring sky radiance) if the open post is along the optic axis. DDSR-1B is in '*dark measure*' mode if the closed post

is along the optic axis. DDSR-1B is in '*spread*' or '$Mode_{Direct}$' (measuring direct solar radiance) if the defocus lens post is along the optic axis. The stepper motor is used to position the view posts of the lens wheel. A LED/ phototransistor pair is used as the lens wheel position feedback for orienting the lens wheel in the required direction.

The sensor module consists of a pyroelectric detector, preliminary signal conditioning by a pyro-interface and two temperature sensors. A detector with high enough sensitivity to low intensities has been a major criterion in the choice of the pyroelectric detector as the sensing element in this system. It is expected that the combination of the beam focussing lens and the sensitive detector with a modulator would provide a viable probe for sky radiances. The two temperature sensors, one mounted close to the pyroelectric detector and the other on the outside of the collimator, serve to monitor the thermal state of the system.

Signals, power and relay to/from the radiometer is taken by cables connecting the radiometer to a control unit.

5.3. Optics

FIGURE 5.2 gives a scaled longitudinal section of the collimator. It shows the position of the diaphragms, chopper wheel, lenses and detector. Special attention has been given to the design of a light, compact and modular collimating tube for the DDSR-1B. The limitation on size and weight has been the chopper wheel and motor as well as the lens wheel and motor systems. Dimensions for the tube (with the above factors in mind) was derived based on WMO specifications for the view limiting geometry with respect to direct solar irradiance measurements.

Ideally the inner tube (collimator) should have a matt black coating so as to maximise stray light absorption. However, in this version of the DDSR the collimator has not been coated with a matt finish. Instead, the collimator, chopper wheel, housing tube and all frames have been oxidised. The process of oxidisation results in a black surface finish and this is presumed to suffice since the effect of reflections off the now less reflective collimator surface can be 'calibrated off'.

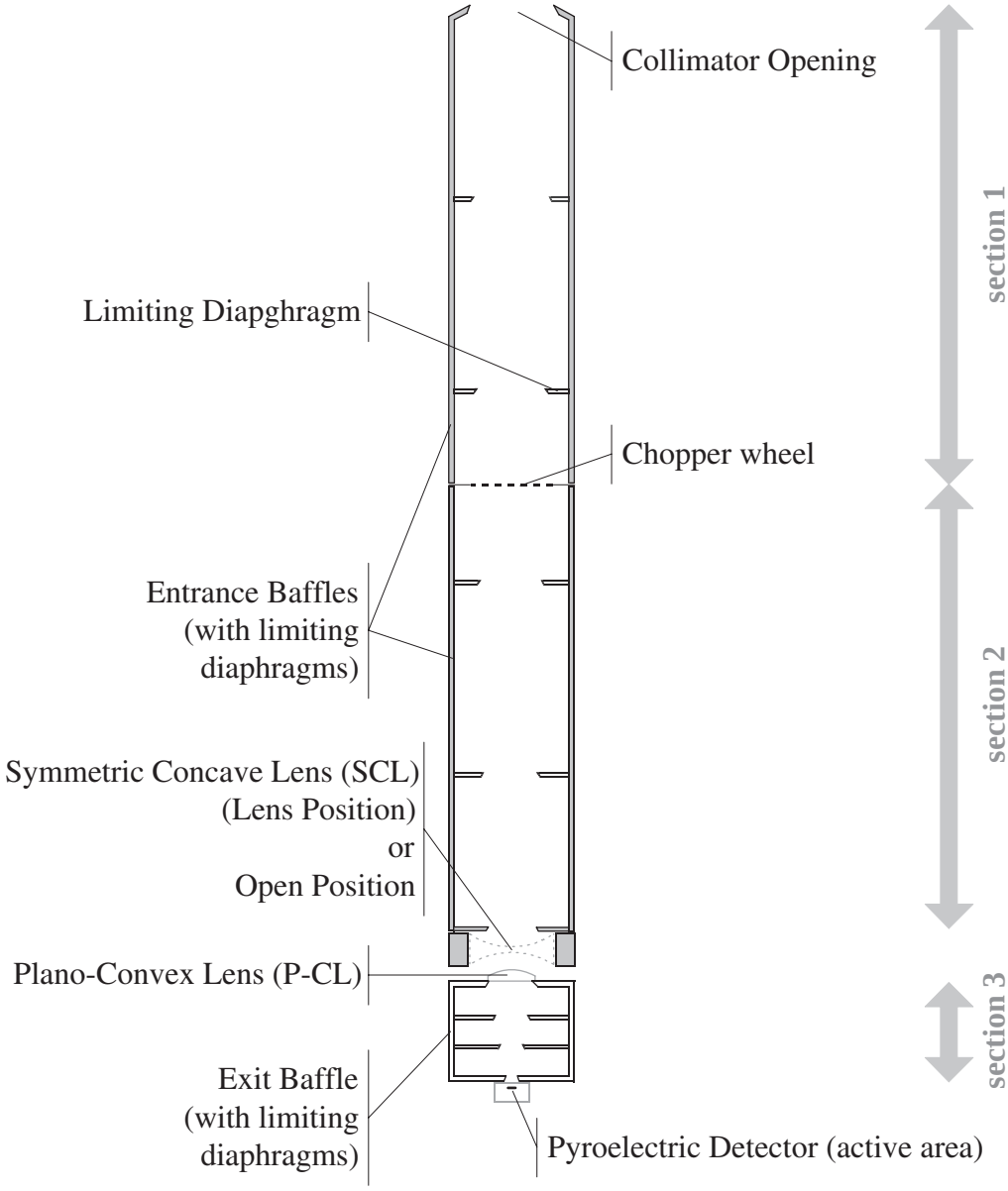

FIGURE 5.2
Longitudinal section of DDSR-1B's fragmented collimator.

5.3.1. View Limits

Instruments at normal incidence to the sun (for direct solar measurements) require a view limit so as to minimize the registration of circumsolar radiation. The view limit is defined by the diameters of the front aperture and the receiver. FIGURE 5.3 gives a sketch to illustrate the limiting angles.

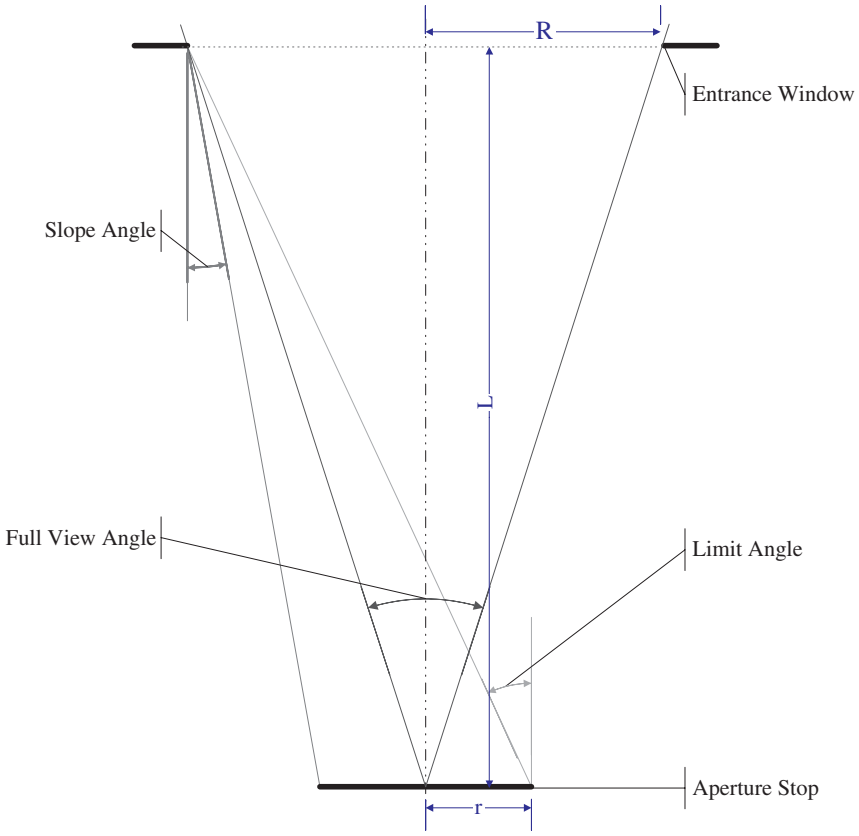

FIGURE 5.3
Definition of the view limiting angles for DDSR-1B.

From the geometry in FIGURE 5.3, the limiting angles are:

$$a_f \equiv \text{Full View Angle} \;=\; 2 \cdot \text{atan}\left(\frac{R}{L}\right) \tag{28}$$

$$a_s \equiv \text{Slope Angle} \;=\; \text{atan}\left(\frac{R-r}{L}\right) \tag{29}$$

$$a_l \equiv \text{Limit Angle} \;=\; \text{atan}\left(\frac{R+r}{L}\right) \tag{30}$$

Although the average subtended angle of the Sun as viewed from Earth is approximately 0.5^o, WMO suggests the use of a 5^o full field of view, a 1^o slope angle and a 4^o limit angle. The reason for this is the tracking tolerance of most solar trackers.

Limitations on the slope and limit angles are required due to the finite area of the aperture stop. The following relation is derived from the equations (28), (29) and (30):

$$2\tan\left(\frac{a_f}{2}\right) = \tan a_s + \tan a_l \tag{31}$$

which is:

$$a_f = a_s + a_l \tag{32}$$

for a_f, a_s and a_l sufficiently small.

Equation (32) shows that an increase in the Limit Angle (by moving along and away from the centre of the aperture stop) shifts the field of view such that the area of view is larger than that defined by the centre of the stop. Thus a larger limit angle would imply the registration of a larger disc about the sun. However, the 1^o Slope Angle (defined by the area of the aperture stop) keeps the Full View Angle within the maximum permissible view.

For the direct mode operation of the DDSR-1b, the aperture stop as shown in FIGURE 5.3 refers to the diaphragm behind the defocusing lens and which holds the defocusing lens to the lens wheel. The distance between the entrance window and aperture stop is $L = 256.00 \pm 0.01\text{mm}$. The radius of the entrance window is $R = 11.20 \pm 0.01\text{mm}$ and the radius of the aperture stop is $r = 6.00 \pm 0.01\text{mm}$. The viewing angles are thus:

$$a_f = \text{Full view Angle} = 5.01^o \pm 0.03\% \tag{33}$$

$$a_s = \text{Slope Angle} = 1.16^o \pm 0.03\% \tag{34}$$

$$a_l = \text{Limit Angle} = 3.78^o \pm 0.03\% \tag{35}$$

which are within the WMO specifications.

A test of DDSR-1B's opening angles has been made against the sun. The instrument is mounted on Eppley's ST-3 solar tracker and aligned to the sun. The tracker's equation of time adjustment is then altered such that the sun can glide over the instrument's entrance window on removal of power

to the tracker. The result is as shown in FIGURE 5.4. It is noted from the figure that a complete response is within 2^o. A 50% drop in response is observed for an alignment offset of 2.5^o. The response drops to zero by 3^o.

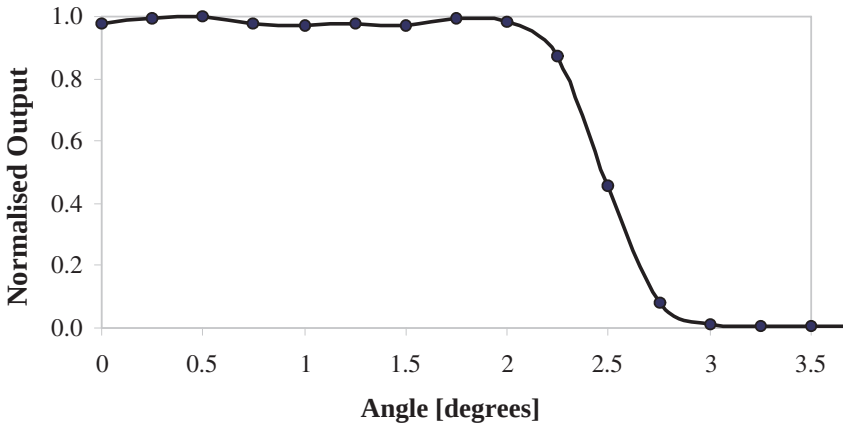

FIGURE 5.4
DDSR-1B's angular response. The instrument is mounted on the Eppley ST-3 tracker and offset from the sun using the tracker's equation of time adjustment. Power to the tracker is removed to allow the movement of the sun over the opening. The angles are scaled from the time records using the fact that the sun moves 15^o in one hour.

The view limiting angles are not too different for the instrument when in the diffuse mode of operation. This is because the aperture stop is now the focussing lens, with the same radius as the diaphragm stop for the direct mode and with a distance $L' = 0.98L$mm from the entrance window. The angles for the diffuse mode are:

$$\text{Full view Angle} = 4.92^o \pm 0.03\% \tag{36}$$

$$\text{Slope Angle} = 1.14^o \pm 0.03\% \tag{37}$$

$$\text{Limit Angle} = 3.78^o \pm 0.03\% \tag{38}$$

An approximation of the diffuse irradiance at a particular point in the sky would, ideally, require a narrow viewing angle. However, the narrower the viewing angle, the more scan points would be required to map the entire hemisphere. This would greatly increase the scan time and so the integrated diffuse value would have a greater deviation from the 'true' instantaneous total diffuse irradiance.

5.3.2. The Chopper Wheel

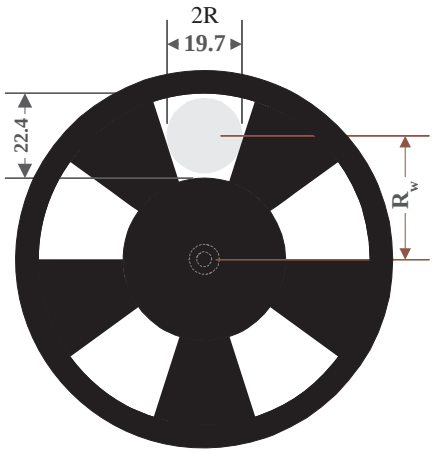

FIGURE 5.5
Front view of the chopper wheel.

The chopper wheel has five apertures and five screens. The screens and apertures have the same dimensions. Each screen completely veils the incident flux when in-line with the optic axis. The aperture fill ratio (taken as the width of wheel aperture divided by the width of the diaphragm in front of the chopper wheel) is 1.2. Thus, each on-axis wheel aperture allows full passage of the incident flux. Further, the collector's (defocusing lens) FOV of 5^o is maintained.

Faulhaber, in [4., 1977], suggests that contributions from higher harmonic frequencies can be suppressed by considering the geometry of the chopper wheel. For the case of DDSR-1B's current chopper wheel design, the ratio of the aperture radius to the distance between the centre of aperture and centre of the wheel is 0.318. According to a solution to Faulhaber's numerical approximation for a five notch/tooth wheel, the above ratio would imply a 6% contribution from the 3rd harmonic and a less than 2% contribution from the 5th harmonic. This can be seen by the plots given in FIGURE 5.6. The data for the curves in these plots are calculated from the absolute value of the ratio of the corresponding harmonic coefficient to the fundamental one:

$$\left|\frac{C_i}{C_1}\right| = \frac{1}{i} \cdot \frac{F\left[-\frac{i \cdot n}{2}, \frac{i \cdot n}{2}, 2, z^2\right]}{F\left[-\frac{n}{2}, \frac{n}{2}, 2, z^2\right]}, \tag{39}$$

where i is the corresponding harmonic, C is the Fourier coefficient of the modulated radiation, F is the hypergeometrical function, n is the number of notch-tooth (aperture-screen) pairs, and z is the ratio of the aperture radius to distance of the centre of the aperture from the centre of the wheel (i.e. R/R_w as illustrated in FIGURE 5.5.).

In light of the above, a total harmonic contribution of 9% is considered in the derivation of a system response factor for the DDSR-1B.

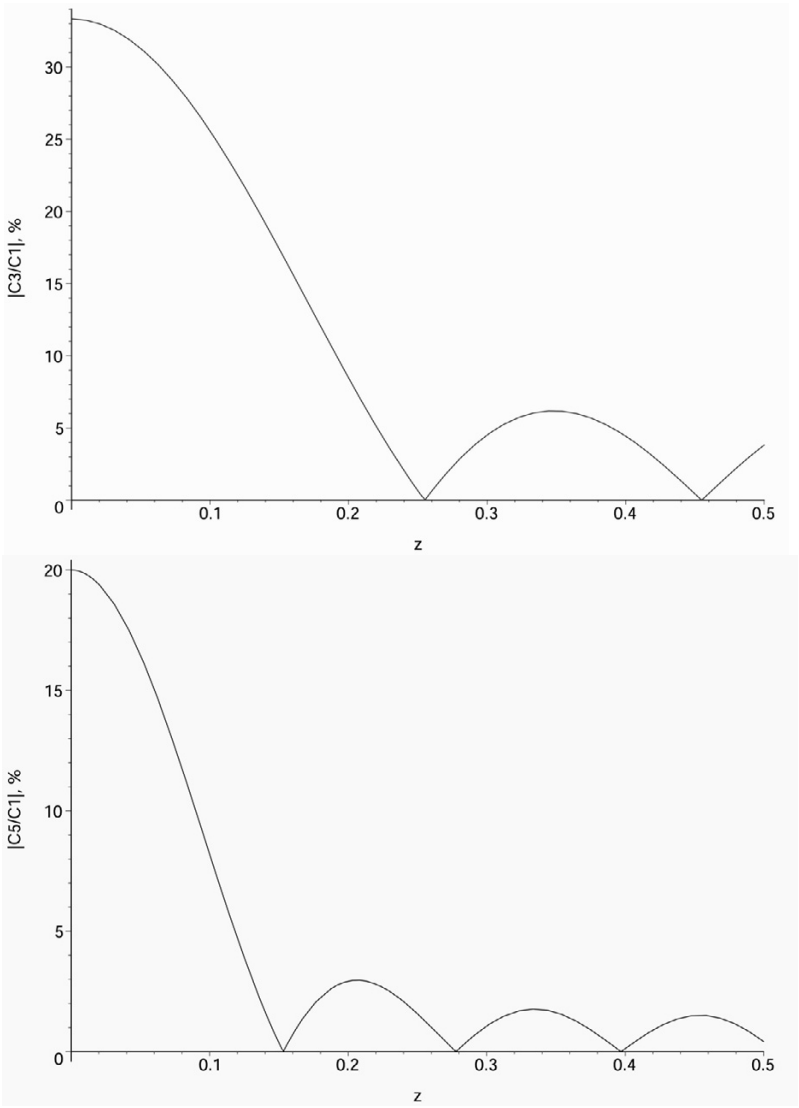

FIGURE 5.6
Contribution of the third and fifth harmonic frequency relative to the base frequency for $n = 5$ notch-tooth pairs. Calculation based on *[4., 1977]*.

5.3.3. The Lenses

Optical lenses are used as collectors in the DDSR-1B system. The lenses are used as a solution to dynamic range limitations of the system. DDSR-1B is intended to operate over a wide irradiance span brought on due to the attempt to measure at the low level diffuse (0 to ~150Wm^{-2}) and at the high level direct (<1200Wm^{-2}) solar irradiances. Two lenses are used in the system, a plano-convex (focussing) lens and a symmetric concave (defocusing) lens. The focussing lens condenses the incident flux (of the low level diffuse irradiance) onto the detector, thereby increasing the signal pick-up. On the other hand, the focussing lens and defocusing lens, in combination, spreads the incident beam (of the high level direct irradiance) and thus reduces the signal level for the detector. It is evident that beam reshaping results in loss of radiant power, but as mentioned above, beam shaping is necessary to avoid saturation effects at the upper limit and to avoid low signal to noise ratio (SNR) at the lower limit.

The lenses, serial numbers 313330 (for the defocusing lens) and 312258 (for the focussing lens), have been purchased from Linos Photonics. The choice of lens' has been based on stability with material type, coating, thickness, diameters and focal lengths.

5.3.3.1. Stability of Properties

Stability of the optical properties of any lens is dependant on the lens' response to variations in incident power and ambient temperture. These variations could result in changes to a lens' absorption, thermal conductivity, and thermal expansion. Such changes may alter the lens' optical properties (in particular, shifts in specified aberrations and focal lengths) and thus alter the system's responsivity. It is noted that the defining factor in lens stability is its material type.

In DDSR-1B, the lenses used are from fused silica substrates. The fused silica substrate has been selected for its transparency over a wide spectrum, its low thermal coefficient of expansion and high thermal conductivity.

A lens from material having poor thermal conductivity could result in the lens having a large difference in temperature profile between edge and centre. This could alter the shape of the lens by the uneven thermal

expansion across the profile. Alteration of the shape of the lens indubitably alters its optical properties. Fused silica is specified to have a coefficient of thermal conductivity of $1.4 Wm^{-1}K^{-1}$. This high thermal conductivity is responsible for the relative measure of uniformity in thermal expansion across a lens of this material.

Variations in temperature could result in the volumetric expansion of a material. For a lens, the change in temperature could alter its thickness, radius of curvature and density. Such alterations modify the lens' accuracy by corrupting its refractive index and focal length.

A model, developed by Noecker et al. in [20., 1994], is considered for analysing the changes in focal length of the focussing lens and defocusing lens with respect to changes in temperature. According Noecker et al. the focal length f of a lens changes with temperature T at the rate:

$$\frac{1}{f}\frac{df}{dT} = \alpha - \left(\frac{1}{n-1}\right)\frac{dn}{dT} \tag{40}$$

where n is the refractive index and α is the coefficient of thermal expansion for fused silica. A simplified approximation of equation (40) is given by:

$$\log\left(\frac{f_2}{f_1}\right) = (T_2 - T_1)\left[\alpha - \left(\frac{1}{n-1}\right)\frac{dn}{dT}\right] \tag{41}$$

where the subscripts *1* and *2* refer to the initial and final values respectively, for f and T.

Equation (41) has been used to find the approximate shifts in focal lengths with changes in temperature in the focussing lens and defocusing lens for the following wavelengths and refractive indices from [14.]:

* $(f_{400nm} = 26.78mm, n_{400nm} \approx 1.4700)$,
* $(f_{588nm} = 27.46mm, n_{588nm} \approx 1.4587)$, and
* $(f_{2325nm} = 29.07mm, n_{2325nm} \approx 1.4330)$.

Fused silica is specified to have a thermal coefficient of expansion of $\alpha = 5.5 \times 10^{-7} K^{-1}$ and a change in index of refraction with temperature

$\frac{dn}{dT} \approx 10^{-5}/^{o}K$. With the above inputs to equation (41), the resulting focal shifts $f_2 - f_1$ with change in temperature are as shown in FIGURE 5.7. An extreme temperature change of 70°C would imply a focal shift of about 0.04mm. This contributes to a radiance uncertainty of less than 1% (see section 5.7.3).

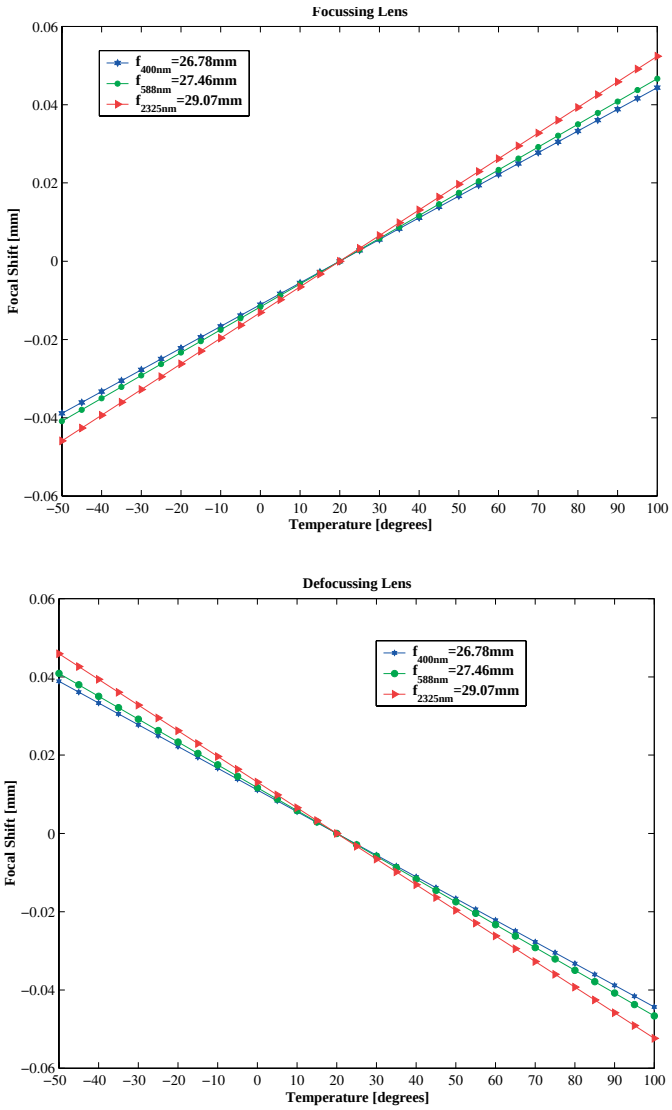

FIGURE 5.7
Changes in focal length with temperature for 3 wavelengths. The initial temperture is $T_1 = 20^{o}C$. (a) focal shifts due to thermal expansion of the focussing lens. (b) focal shifts due to thermal expansion of the defocusing lens.

5.3.3.2. Coating

Both lenses are uncoated; an anti-reflection coating would distort the spectral transmission. The external transmission range for fused silica is approximately 175 to 2400nm. This is shown graphical by the external transmission curves given in FIGURE 5.8 for Optical Quality and UV Grade synthetic fused silica, as taken from [17.] for 10mm thick samples. The curves show insignificance in variation over the visible spectrum i.e 400 to approximately 1300nm.

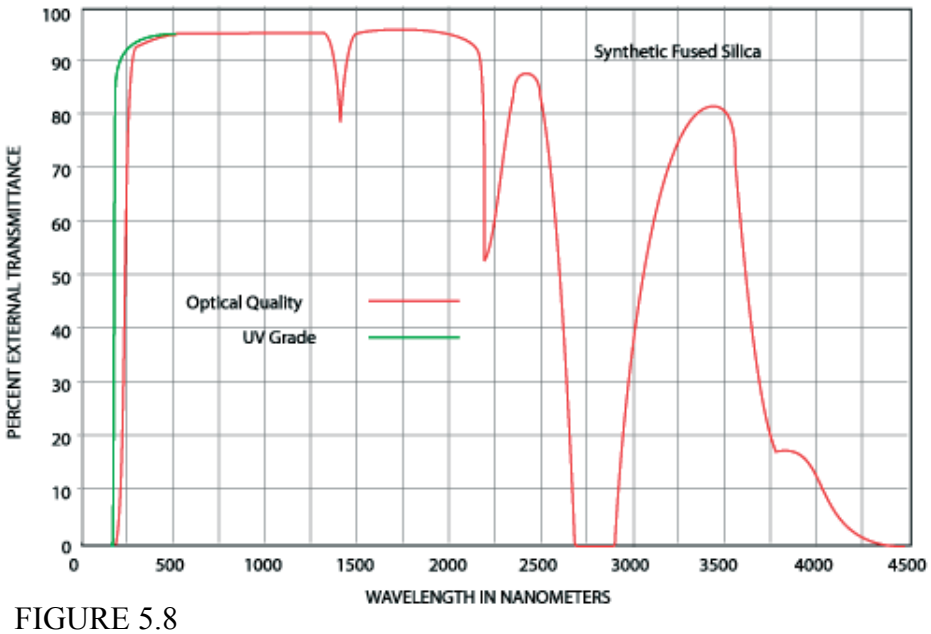

FIGURE 5.8
External transmittances for UV-grade and optical grade fused silica. [17.].

5.3.3.3. Lens Thickness

The percentage of transmittance depends mainly on a lens' thickness. Centre thicknesses for the defocusing lens and focussing lens are 1.5mm and 3mm, respectively. It is therefore expected that the defocusing lens has a higher transmittance than the focussing lens. This is verified using the optics analysis software, WinLens. FIGURE 5.9 shows three transmittance curves. The curves correspond to transmission data for the defocusing lens, the focussing lens and the analysed total transmission of the lens pair. It is noted that the total internal transmission loss within the visible spectrum is less than 0.09%.

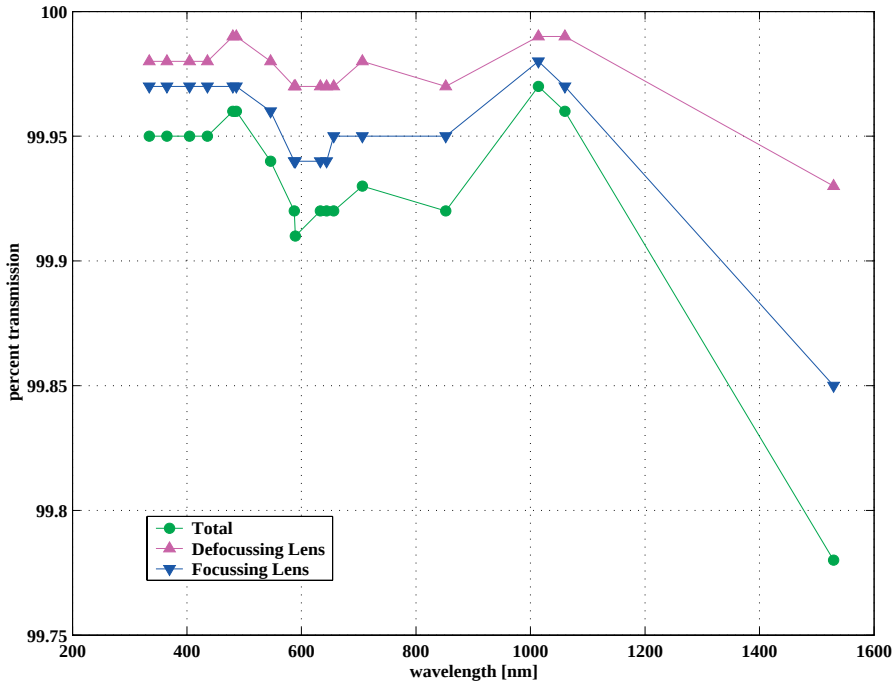

FIGURE 5.9
Internal transmission curves as a function of wavelength for the defocusing lens, focussing lens and their combination.

5.3.3.4. Diameter

The diameter of the defocusing lens is 22.4mm, and the diameter of the focussing lens is 12.5mm. These diameters have been selected as they fit closest to the geometrical dimensions of the instrument.

5.3.3.5. Focal Length

A significant factor when choosing the lenses has been their focal lengths. The defocusing lens has a focal length of $f_{258nm} = -20mm$ and the focussing lens a focal length of $f_{258nm} = 25mm$. These foci, together with the calculated placement of the lenses within the collimator, enable the construction of a shorter collimator and hence a less bulky system. DDSR-1B requires that the defocusing lens be placed at the focal point of the focussing lens for a spreaded beam and hence signal transmission for high

solar irradiances. At the time of the optical design of the DDSR-1B, the shortest available focal length for a suitable defocusing lens was $-20mm$. Thus, the focal length of the focussing lens has been restricted to no less than $20mm$. In light of the latter, the optimum choice for the focussing lens is the $25mm$ focal length.

More importantly, the focal distance and collector field of view for the unitary focussing lens should (and does) yield an image size in comparison with the system's detector sensitive area. This follows from two factors, viz.:

i. According to Elizarov et al. i [3.], the pyroelectric detector threshold sensitivity deteriorates as $A^{1/2}$, where A is the area of the sensitive element.

ii. According to Yakushenkova in [37.], the size $2h'$ of the image grows as the full angle of view a_f increases according to the law:

$$2h' = F \cdot 2\tan\left(\frac{a_f}{2}\right), \tag{42}$$

where F is the focal distance of the system.

Thus, with the systems' full angle of view $a_f = 5^o$ and the focussing lens focal length $F_{588} = 27.46mm$, the size of the sensitive element of the detector should, for an optimum threshold sensitivity, not exceed the size of the image $2h' = 2.4mm$. Actually, for $\lambda \in [400, 2400]$ $2h'$ is less than $2.6mm$. The size of the sensitive element of the detector is $2mm$, which does not exceed $2h'$.

In summary, the Linos Photonics specifications for both lenses are given in Table 5A with parameters as illustrated by the geometries in FIGURE 5.10.

f	focal length	**s'**	image distance	**e**	distance, primary principal point-primary vertex
ø	lens diameter	**dm**	centre thickness	**e'**	distance, secondary principal point-secondary vertex
dr	edge thickness	**h**	primary vertex	**h'**	sagittal height secondary vertex
F,F'	focal points	**H,H'**	primary points	**Tolerances**: focal length f: ±2% image distance s': ±2%	

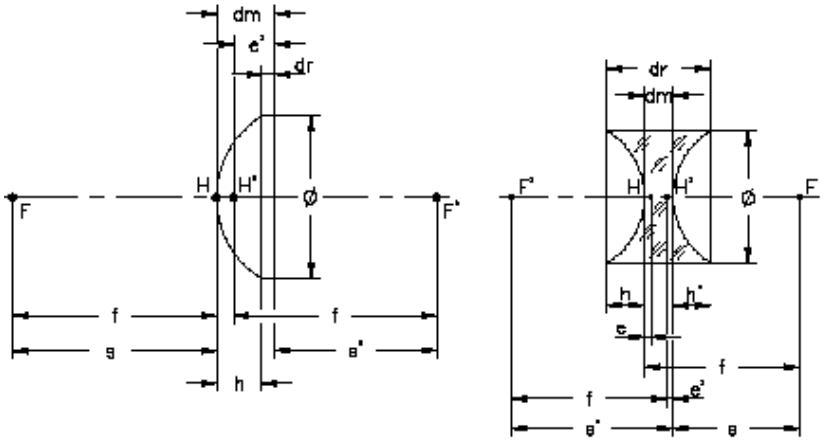

FIGURE 5.10
Geometrical description of the parameters for the focussing lens and defocusing lens.

Table 5A: Parameter values for the focussing and the defocusing lens.

	Symmetric Concave (# 313330)	**Plano-Convex (# 312258)**
focal length, f (mm)	-20	25
diameter, ø (mm)	22.4	12.5
centre thickness, dm (mm)	1.5	3.0
edge thickness, dr (mm)	8.1	1.3
primary vertex, h (mm)	3.3	1.7
e' (mm)	0.49	1.99
material	synthetic fused silica	
Abbé Constant	67.8±0.5	
Change of refractive index with temperature	$1.28\times10^{-5}/^{o}C$	
continuous operating temperature	$900^{o}C$ (maximum)	
coefficient of thermal expansion	$5.5\times10^{-7o}K^{-1}$	

5.3.4. Object-Image Relation

DDSR-1B can operate in either of two modes:

A. $Mode_{Diffuse}$, and

B. $Mode_{Direct}$.

$Mode_{diffuse}$ and $Mode_{direct}$ differ because of their difference in optic systems. The optic system in $Mode_{diffuse}$ has a single lens component whilst that in $Mode_{direct}$ is a dual lens system. Each mode therefore has its own characteristic object-image relation.

The discussions in this section are on the object-image relation for each mode. It includes a description of the image plane, aberration effects and irradiance transfer.

Discussions on the image plane and aberration effects are based on results obtained from the optical design simulations and calculations using the lens design programs, Winlens (version 4.3).

5.3.4.1. Mode Diffuse

Measurements of diffuse solar irradiance are taken with only the focussing lens in the path of the incoming irradiance beam. Without this lens in the optical path of the incoming flux, the recovery and measurement of the low level diffuse radiance would be difficult. This is because the irradiance levels approach the level of system noise and hence may require special techniques to reflect measurements accurately and precisely.

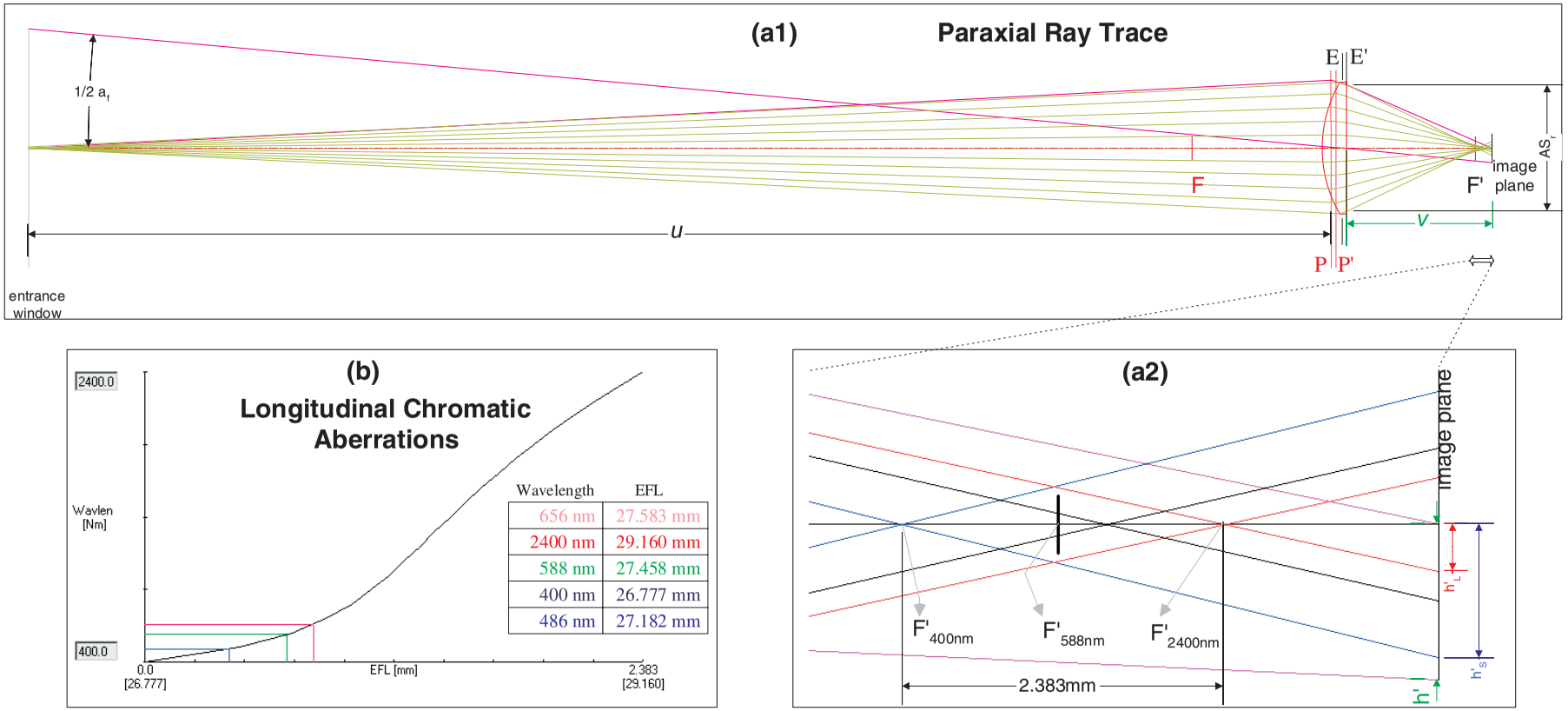

FIGURE 5.11
Winlens simulation for $Mode_{diffuse}$. (a1) Ray trace with marginal rays shown in magenta. (a2) Magnification of region in image space to show aberration effects. (b) Shifts in focal length due to longitudinal chromatic aberrations.

5.3.4.1.1. Ray Trace and Aberrations for Mode$_{diffuse}$

A simulation in Winlens has been made for investigating the effects of the focussing lens with the following input parameters (with reference to FIGURE 5.11(a)):

- Object distance: $u = -257mm$,
- Aperture Stop (radius) $AS_r = 6mm$,
- Object Angle (1/2 FOV) $\frac{1}{2}a_f = 2.5^o$, and
- Wavelengths (λ):
  - λ(middle) = $587.6nm$,
  - λ(short) = $400nm$, and
  - λ(long) = $2400nm$.

Results from the simulation include a paraxial ray trace, Seidal aberrations and transmission calculations. The transmission results have been discussed in sections (5.3.3.2.) and (5.3.3.3.). FIGURE 5.11 gives the paraxial ray trace for the optical system, and a plot for the longitudinal chromatic aberrations.

5.3.4.1.1.1. Paraxial Ray Trace

Referring to FIGURE 5.11(a), it is noted that a single component analysis has been run. That is, only the focussing lens is along the optical axis. The influence of baffles have been not been considered. The edge (marginal) ray (with an object view angle of 2.5^o and distance $u = 257mm$) is imaged as illustrated by the magenta ray trace on the figure. The image height and distance is found to be $h' = 1.4mm$ and $v = 28.7mm$, respectively. The above ray trace analysis results are specified for the images' circle of least confusion[1] (see FIGURE 5.14).

1. Circle of least confusion is a best placement approximation for a 'focused' image after consideration of the effect of ray aberrations.

5.3.4.1.1.2. Seidal Aberrations

In an ideal system, the spherical wavefronts emitted from an object point would emerge in image space as spherical waves converging on the gaussian image point. In practice, the wavefront is perturbed to some extent. Deviations from the ideal case are called aberrations. The greater the angle of incidence on a refracting surface, the greater is the deviation. The theory, based on a third order approximation has been developed by Ludwig von Seidal and the aberrations are referred to as Seidal aberrations. In general there are five Seidal aberrations: spherical aberration, coma, astigmatism, curvature of field and distortion. It is common to include the chromatic aberration as a Seidal aberration.

Chromatic Aberrations:

All refracting systems would generate a splitting of incident polychromatic light into a set of rays, each of which is associated with a different wavelength. Consequently, the image will not be sharp. This phenomena (illustrated in FIGURE 5.12) is referred to as chromatic aberration. It is evident both longitudinally and laterally.

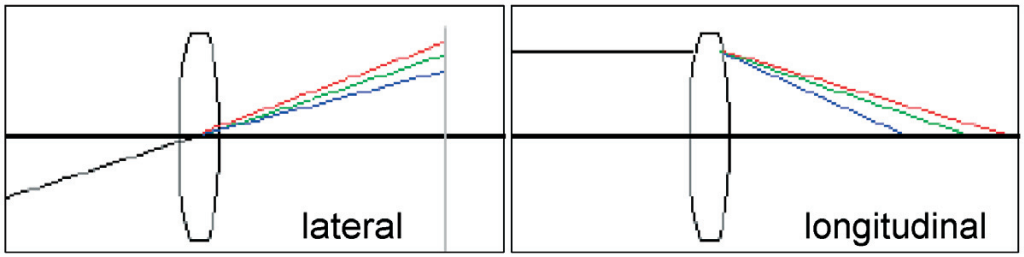

FIGURE 5.12
Pictorial definition of lateral and longitudinal chromatic aberration.

Winlens obtains the data for the lateral chromatic aberrations by tracing 10 chief rays at equal angle increments starting with an axial object and incrementing up to the specified field size (i.e an object field size of 2.5^{o} for the current case). The data for the long wavelength $2400nm$ and the short wavelength $400nm$ has been plotted as shown in FIGURE 5.13, depicted by the curves in red and blue respectively. The solid dots in the plot are the data points taken from the Table Summary of Field Aberrations generated by Winlens. The solid lines in the plot correspond to a best linear

fit through the data points. It may be concluded from these curves that lateral chromatic aberration is at most $0.0046mm$ for the spectral range $400nm$ to $2400nm$.

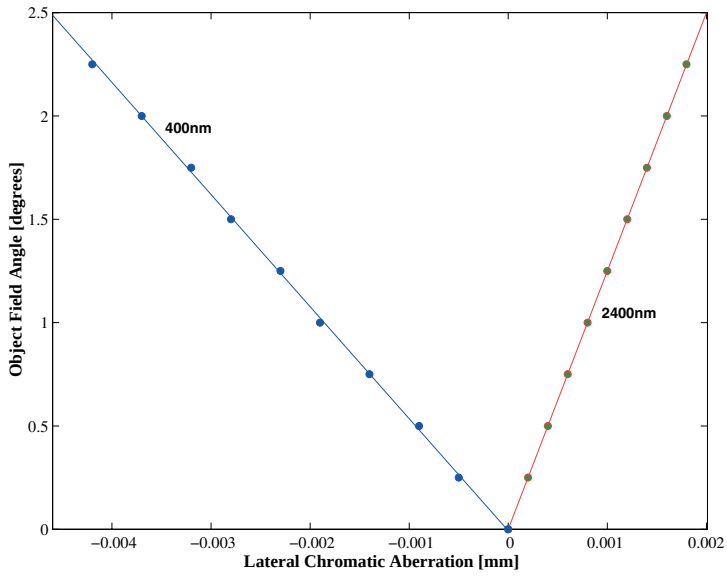

FIGURE 5.13
Measure of lateral chromatic aberration across the focussing lens in $\text{Mode}_{\text{diffuse}}$.

Winlens generates a graph for the longitudinal chromatic aberrations. This is shown in FIGURE 5.11(b), for the spectral range of $400nm$ to $2400nm$, as a variation of the end focal length (EFL). The zero point in the figure corresponds to the ray with the lower limit wavelength of $400nm$ and having an EFL of $26.777mm$. All chromatic shifts in the figure are relative to this extremum. The maximum focal shift is thus $2.383mm$ and corresponds to the ray with the upper limit wavelength of $2400nm$. The above shifts are shown in FIGURE 5.11(a2), which is a magnification of the *Rear Focus to Image Plane* region of FIGURE 5.11(a1).

Longitudinal chromatic aberration results in monochromatic images with correspondingly different heights at the image plane. For the above numbers, a paraxial incident ray at full view (i.e. 2.5^{o}) would undergo chromatic splitting such that the refracted ray with the shortest wavelength

($400nm$) would fall on the image plane at a point which is $h'_S = 0.8mm$ (see FIGURE 5.11(a2)) from the optic axis. Likewise, the refracted ray with the longest wavelength ($2400nm$) would fall on the image plane at a point which is $h'_L = -0.12mm$ from the optic axis.

Spherical Aberrations:

Spherical aberrations occur for widely spread beams originating *from an object point on the optical axis*. With reference to FIGURE 5.14, they appear as follows: The outer circular lens zones allow image points to develop on the optic axis, which do not coincide with the paraxial image point. What results is a rotationally symmetric diversion around the paraxial image point.

Winlens reports a tranverse spherical aberration of $0.2568mm$ and a longitudinal spherical aberration of $2.2011mm$.

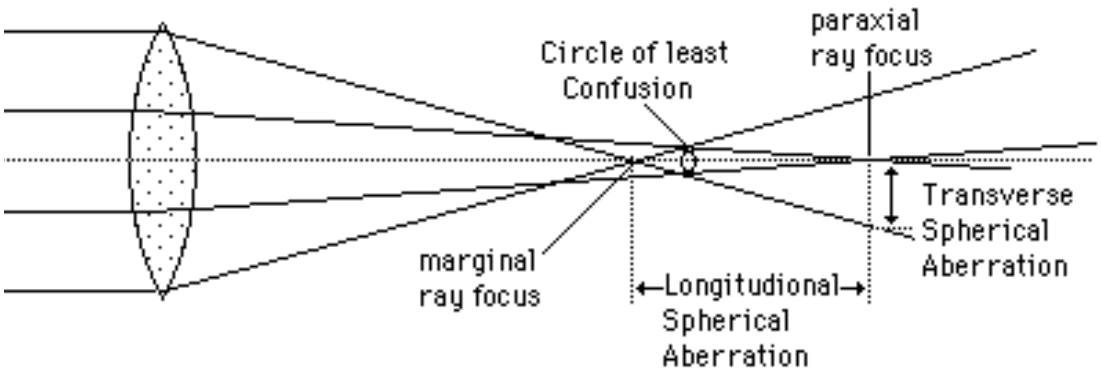

FIGURE 5.14
Spherical aberration produced by refraction at the lens' surfaces. The marginal rays meet the axis at points nearer to the lens as compared to the paraxial rays.

Coma:

Seidal coma is an aberration which varies linearly with the field angle. The sagittal and tangential comas for the system (as calculated in Winlens) are $-0.0208mm$ and $-0.0625mm$ respectively. It is noted that coma can also arise from a misalignment of the optical elements.

5.3.4.1.1.3. Discussion on Ray Trace and Aberrations

An optical system has been simulated to analyse its feasibility of use in the measurements of diffuse solar irradiance.

The analysis further enables the determination of the optimum placement of the detector. The image plane's optimum position, corresponding to the *circle of least confusion,* is at $28.7mm$ from the back of the plano-convex lens. To keep the detector within this vicinity, it has therefore been fixed on the optic axis, at a distance of $28mm$ from the rear of the lens.

It is noted that the effects of spherical aberrations have been minimized by using the plano-convex lens instead of a bi-convex lens. The curvature of the focussing lens is towards the incoming rays, and according to literature such as [22.], this orientation reduces spherical aberrations.

Magnitudes of the Seidal aberrations would give an indication of the detection performance. Critical to the sensor's performance is the 'thinning' of the beam when the transverse aberrations fall outside the detector's view. The detector has an active radius of $1mm$, whilst all of the transverse Seidal aberration components are evaluated to be less than $1mm$.

5.3.4.1.2. Irradiance Transfer in $Mode_{diffuse}$

Calculations are made to find the radiation transfer from the object plane to the image plane for $Mode_{diffuse}$.

5.3.4.1.2.1. Calculations

For a system with fractional losses (that is by reflection, absorption and scattering) amounting to α, the flux $d\Phi_o$ incident over the entrance pupil indicated by *EP* in the FIGURE 5.11(a1) and the flux $d\Phi_i$ leaving the exit pupil *E'P'* in the direction of the image is given by:

$$d\Phi_i = (1-\alpha)\cdot d\Phi_o \tag{43}$$

A relation for the image irradiance E_i in terms of the object irradiance E_o is found with the aid of equation (43), with the assumption of Lambertian surfaces at the respective planes. FIGURE 5.15 illustrates the imaging in $\text{Mode}_{\text{Diffuse}}$ for an object of elemental area dA_o, with the entrance and exit pupils as shown in the FIGURE 5.11(a1). If dA_o is irradiated by E_o in Wm^{-2} then the radiant flux reflected in any direction θ to the surface normal is given by definition as:

$$d^2\Phi_o = L_o dA_o \cos\theta d\Omega \tag{44}$$

where L_o is the surface radiance and $d\Omega = 2\pi\sin\theta d\theta$ is the elemental solid angle.

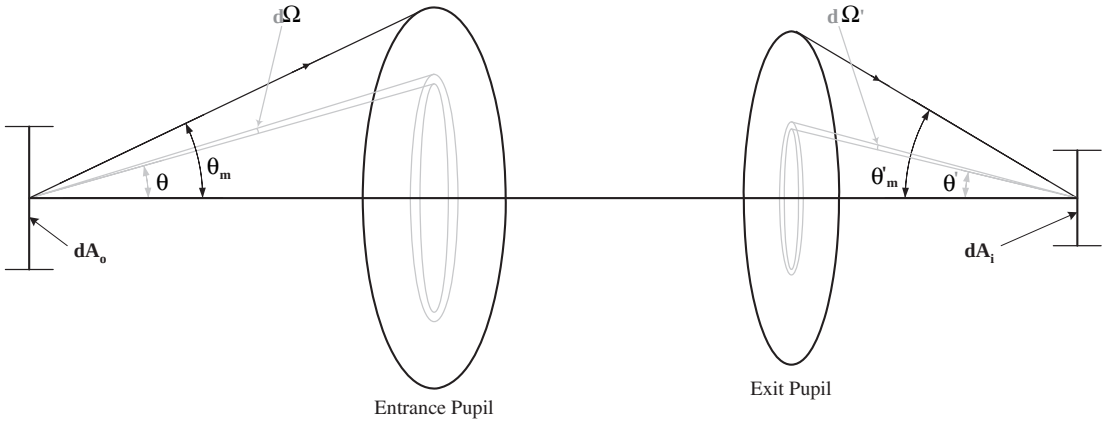

FIGURE 5.15
Geometry for the radiometry of the optical system for $\text{Mode}_{\text{Diffuse}}$.

For $\theta_m = \frac{a_f}{2} = 2.5^o$, that is the marginal ray passing through the entrance pupil, the flux incident over the entrance pupil *EP*, by integration of equation (44), is:

$$d\Phi_o = \pi L_o dA_o \sin^2\theta_m \tag{45}$$

A similar expression can be given for the flux $d\Phi_i$ incident over the exit pupil from a fictitious Lambertian source L_i in the plane of the image.

Then, by the principle of the reversibility of light, this flux $d\Phi_i$ leaving the exit pupil *E'P'* in the direction of the image, gives rise to an image plane radiance L_i according to:

$$d\Phi_i = \pi L_i dA_i \sin^2\theta'_m \tag{46}$$

where dA_i is the image area and θ'_m is the inclination of the marginal ray in image space.

It follows from equations (43), (45) and (46), with system transmission given by:

$$\tau = (1-\alpha), \tag{47}$$

that:

$$L_i \sin^2\theta'_m dA_i = \tau L_o \sin^2\theta_m dA_o \tag{48}$$

The ratio of the elemental areas, which is equivalent to the square of the lateral magnification m, i.e.

$$\frac{dA_i}{dA_o} = m^2 \tag{49}$$

and the Abbe sine condition[1]

$$\frac{\sin\theta_m}{\sin\theta'_m} = m \tag{50}$$

reduces equation (48) to:

$$L_i = \tau L_o \tag{51}$$

Replacing L_i in equation (46) for equation (51) and rearranging factors gives:

$$E_i = \frac{d\Phi_i}{dA_i} = \tau\pi L_o \sin^2\theta'_m \tag{52}$$

1. For simplification it is presumed that the lens exhibits zero spherical aberration and coma for objects near the axis.

With the approximation:

$$\sin\theta'_m \approx \tan\theta'_m = \frac{D_i}{2v}, \tag{53}$$

where D_i is the diameter of the exit pupil and v is the image distance, the image irradiance becomes:

$$E_i = c \cdot (\pi L_o) \tag{54}$$

where the factor $c = \tau \cdot \left(\frac{D_i}{2v}\right)^2$. For the presumption of a Lambertian surface in the object plane the irradiance E_o is:

$$E_o = \pi L_o \tag{55}$$

Thus equation (54) reduces to:

$$E_i = c \cdot E_o. \tag{56}$$

For system constants given in Table 5B, the image irradiance in $\text{Mode}_{\text{Diffuse}}$ is:

$$E_i = 0.0425 \cdot E_o \tag{57}$$

Table 5B: Optic system parameters for $\text{Mode}_{\text{Diffuse}}$

Parameter	Value
object height, h_o	11.2mm
image height, h'	1.4mm
object distance, u	257mm
image distance, v	28.7mm
diameter of exit pupil, D_i	12mm
lateral magnification, m	-0.12
transmission, τ	0.9
refractive index	1.45

5.3.4.1.2.2. Discussion on Irradiance Transfer

Irradiance transfer in $Mode_{diffuse}$ has been derived and is given by equation (54). The equation implies that a perfect lossless system would have an irradiance transfer coefficient of 0.0425.

In practice, losses are expected. The contribution to interference are reflections, absorptions and scattering within the transfer section. The use of a lens contributes to losses due to aberration effects and internal absorption.

5.3.4.2. Mode Direct

Measurements of direct solar irradiance are taken with both the defocusing lens and focussing lens in the path of the incoming irradiance beam. The defocusing lens is a negative diverging lens and is placed in front of the positive collimating focussing lens. The lenses are placed with their focal points nominally coincident. This arrangement of the lens pair makes a Galilean type beam expander, and helps to attenuate the detector's pick-up of the transferred direct solar irradiance.

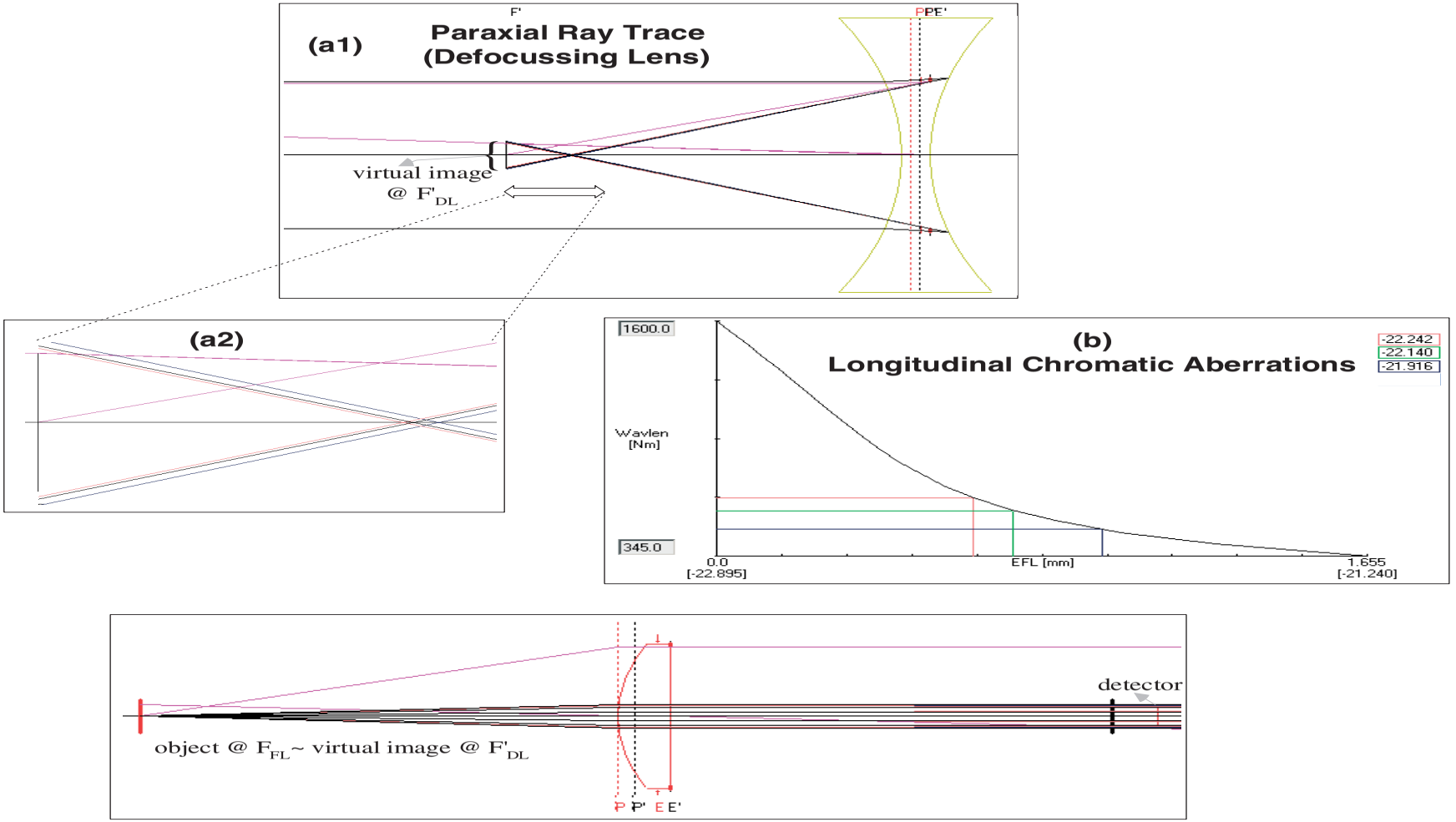

FIGURE 5.16
Winlens simulation of $Mode_{direct}$. (a1) Ray trace for the first lens, the defocusing lens. (a2) Magnification of the region about the virtual image plane. (b) Shifts in focal length due to longitudinal chromatic aberrations off the defocusing lens (DL). (c) Beam broadening of the virtual image by the focussing lens (FL).

5.3.4.2.1. Ray Trace and Aberrations for Mode$_{direct}$

Simulations in Winlens have been made for investigating the effects of the defocusing lens/focussing lens combination. The first simulation has been made to assess the image formation by the defocusing lens alone. The second simulation takes the resulting image properties as input parameters for the trace through the focussing lens. A single trace analysis could have been made, but the dual simulation has been used so as to find consequences of aberration from the defocusing lens to the focussing lens.

5.3.4.2.1.1. Paraxial Ray Trace

The source (from infinity) incident on the defocusing lens is restricted to an object angle of 2.5^{o}. As shown in FIGURE 5.16(a1), the defocusing lens focuses the incident beam onto its front focus plane. Since the position of this virtual image coincides with the position of the back focus plane of the focussing lens, the beam emerges collimated from the focussing lens. The collimation, as viewed by the detector, is as shown in FIGURE 5.16(c). The detector is positioned $28mm$ from the plane surface of the focussing lens.

5.3.4.2.1.2. Aberrations

It is expected that the influence of aberrations on the system responsivity for Mode$_{direct}$ is scaled down compared to the Mode$_{diffuse}$. This is due to the beam collimation in Mode$_{direct}$ instead of beam focusing in the Mode$_{diffuse}$.

Longitudinal chromatic aberrations from the defocusing lens imply that the chromatic images off the defocusing lens does not coincide at one focus. The consequence would be chromatic separations in the collimated beam. But with the level of shift as shown in FIGURE 5.16(b), beam power across the detector would remain unchanged.

Longitudinal spherical aberrations would mean multiple image points for the defocusing lens. Multiple on-axis image points for the defocusing lens would mean multiple object points for the focussing lens. Some of these object points fall between the focussing lens front focus and the focussing lens. These points would form virtual images but it is the area of the beam emergent from the focussing lens that is required. The area covered by the

beam emergent from the focussing lens for the case of virtual imaging is comparable to the non-virtual image case.

5.3.4.2.2. Irradiance Transfer in Mode$_{direct}$

Calculations are made to find the radiation transfer from the object plane to the image plane for Mode$_{direct}$.

5.3.4.2.2.1. Calculations

Equation (52) may be used to find the irradiance transfer for Mode$_{direct}$. In this mode the rays emerge parallel to the optic axis so that the inclination $\theta'_m = 90^o$. It follows that:

$$E_i = \tau E_o \tag{58}$$

5.3.4.2.2.2. Discussion on Irradiance Transfer

The system transmission factors τ in equations (57) and (58) differ for the respective modes of operation. With the dual lens system in Mode$_{direct}$ and the single lens in Mode$_{diffuse}$, system transmission is expected to be lesser in the former. The dual lens system introduces larger losses by the amplification of absorption, reflections and scattering. Aberration effects would account for differences in transmission as well.

In Mode$_{Diffuse}$ the energy is incident on the focussing lens of diameter 12mm and focused into a spot diameter of about $2.8mm$. Hence the energy per unit area is increased by a factor of about 18. In Mode$_{Direct}$ the energy incident at the exit pupil of the lens pair emerges parallel to the optic axis, and with a beam size of 12mm. The energy density amplification ratio between the two modes is $\frac{A_{diffuse}}{A_{direct}} = 18$. Only a fraction, $\sin^2\theta_m$, of diffuse irradiance is admitted, whereas the full direct irradiance shines on the sensor. So the signal ratio for the two cases is:

$$\frac{Signal_{diffuse}}{Signal_{direct}} \approx 18 \cdot \sin^2\theta_m = 0.034. \tag{59}$$

5.4. The Transducer and Associated Electronics

The sensing element of the DDSR-1B system is a P2613-06 pyroelectric sensor. The pyroelectric type detector has been considered because of its high sensitivity to thermal radiation of low intensity, and its spectral insensitivity.

The electrical signal off the detector is conditioned with appropriate electronics for signal amplification, and the minimisation of DC offset and noise.

5.4.1. The Pyroelectric P2613-06 Transducer

P2613-06 is a lead zirconate titanate (PZT) type sensor. PZT is an electroceramic that exhibits pyroelectricity. This implies that a change in incident temperature can result in the PZT generating electric dipole moments, which in turn generates current in proportion to the rate of the change in temperature.

5.4.1.1. The Pyroelectric Effect

The chemical formulation for PZT is $Pb(Zr_xTi_{1-x})O_3$ and its unit cell in the cubic phase is as shown in FIGURE 5.17. In this structure, a Ti^{4+} ion is at the body centre with Pb^{2+} ions at the cube corners, and O^{2-} ions at the face centres.

Below the Curie temperature[1] the structure is slightly deformed, with the Pb^{2+} and Ti^{4+} ions displaced relative to the O^{2-} ions, thereby developing a dipole moment. When the crystal is electrically polarized, the dipoles are oriented in such a manner as to make one side of the material positive and the opposite side negative.

1. ***Curie Temperature*** is the temperature above which the spontaneous magnetization vanishes and the material becomes paraelectric i.e the crystal has no dipole moment and thus zero polarization.

FIGURE 5.17
$PbTiO_3$ has a Perovskite crystal structure. At temperatures below the Curie point the structure is a non-centrosymmetric tetragonal and is ferroelectric. Application of external stress (for example thermal) can cause switching in the direction of polarization. Above the Curie temperature the structure has a cubic symmetry, and is paraelectric. *Courtesy of Tadmor in [32., 2002].*

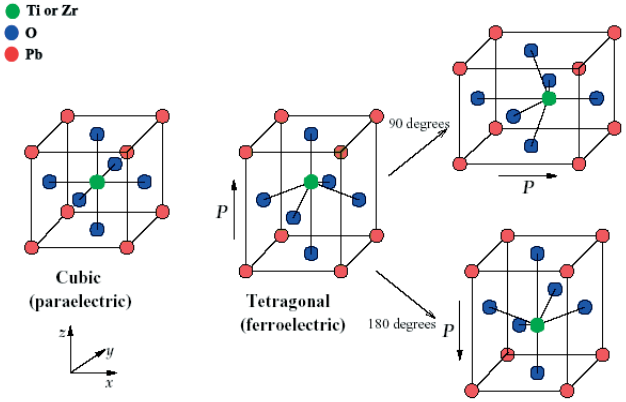

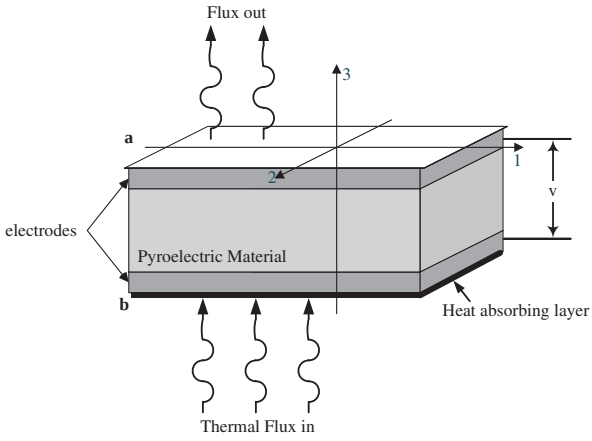

FIGURE 5.18
A pyroelectric detector is made up of a pyroelectric material and electrodes. The combination behaves as a variable capacitor when subject to temperature changes. *Courtesy of Fraden in [5.,1996].*

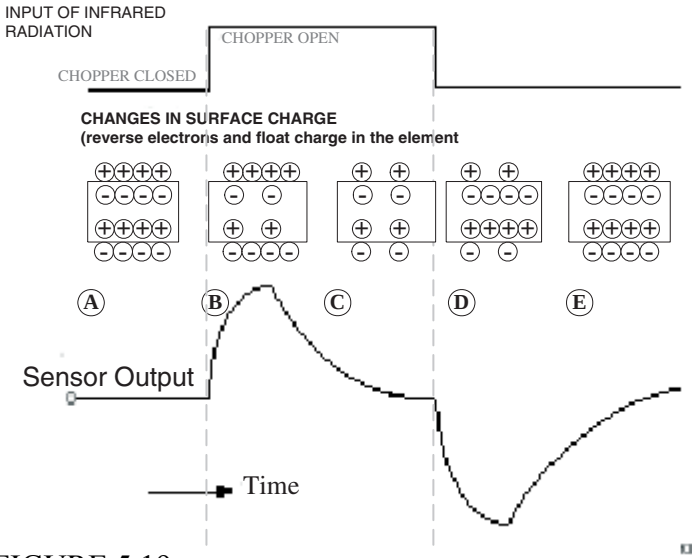

FIGURE 5.19
Schematic representation of the pyroelectric effect. Phases A to E are the detector's response to a thermal step function.

A slice of a pyroelectric material can be a pyroelectric detector if metal electrodes are plated onto the opposite faces of the material. FIGURE 5.18 shows such a detector. When the detector is heated by incident radiation, the polarization P of the pyroelectric changes by an amount determined by the temperature change ΔT and the pyroelectric coefficient

$$p = \left.\frac{dP}{dT}\right|_T \tag{60}$$

of the material. This change in polarization can be logged as a capacitive charge Q that is formed by the pyroelectric material with its two surface electrodes. The generated charge is thereby given as:

$$Q = pA\Delta T \tag{61}$$

where A is the electrode area of the detector.

However, there is no observable potential difference v between the electrode plates under steady state conditions. This is because free charge carriers neutralize the net polarization charge. In order to fold the influence from the electrical leakage (by the free charge carriers), the detector can only be used in a.c. mode at a high enough frequency.

FIGURE 5.19 gives a schematic representation of the pyroelectric effect with the sensor output as a voltage response. Phase A corresponds to the initial state, that is when the chopper is closed. In this phase, although the element surface is electrified, the output across the plates is neutralised due to the electrical leakage. The sensor appears to have no response. With exposure to heat (by the open chopper), the response moves into phases B and C. Phase B corresponds to when the chopper opens and the sensor reaches its peak response. It is seen that the electric charge reaches its peak value with a characteristic rise time of τ_E and then starts to decay with a thermal time constant τ_T. This time constant defines the thermal loss (by convection, conduction and thermal radiation) from the sensing element to its surroundings. In Phase D the chopper is closed and the polarity is reversed. The sensor output decays to a negative extrema with the time constant τ_E and then starts to approach its initial state, again with the thermal time τ_T.

It is noted that the pyroelectric sensor is sensitive to mechanical stress. A thermally induced stress (by heat absorption), for example, would generate an electrical charge. This is because the pyroelectric crystal is, to some degree, piezoelectric as well.

5.4.1.2. Detector Responsivity

It has been noted that radiation incident on the pyroelectric detector should be modulated. This then modulates the temperature of the detector at the same frequency ω as the radiation modulation. The level of change in temperature ΔT depends on the fraction η of incident radiation E_i absorbed, the heat capacity c of the detector, and the thermal conductance σ_T which couples the detector to its housing. Porter in [25., 1981], has defined the following relation for the temperature difference between the detector and its heat sink:

$$\eta E_i = c\frac{d\Delta T}{dt} + \sigma_T \Delta T \tag{62}$$

With the incident irradiance expressed in the form:

$$E_i = E_{io} e^{j\omega t}, \tag{63}$$

equation (62) has the solution:

$$\Delta T = \frac{\eta E_{io}}{\sigma_T + j\omega c} e^{j\omega t} \tag{64}$$

The primary aim is to find the voltage responsivity

$$R_v = \left|\frac{v}{E_i}\right| \tag{65}$$

of the detector.

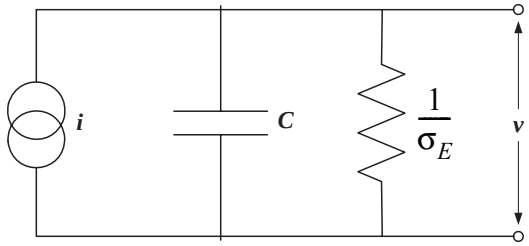

FIGURE 5.20
Equivalent circuit of a pyroelectric detector connected to a high impedance amplifier.

.The equivalent circuit of a pyroelectric detector with a high impedance field-effect transistor (FET) amplifier may be as shown in FIGURE 5.20. The high impedance amplifier makes it possible to observe a signal which is equal to the voltage v produced by the charge Q. Thus the detector is represented as a capacitor, a current generator with

$$i = \frac{dQ}{dt}, \tag{66}$$

and a shunt conductance. The voltage v generated is given (with reference to the circuit in FIGURE 5.10) by:

$$v = \frac{i}{\sigma_E + j\omega C} \tag{67}$$

It follows from equations (61) to (67) that the voltage responsivity can be expressed as:

$$R_v = \frac{\eta \cdot p \cdot A \cdot \omega}{(\sigma_T \cdot \sigma_E)(1 + \omega^2\tau_T^2)^{1/2}(1 + \omega^2\tau_E^2)^{1/2}} \cong \frac{\eta \cdot p \cdot A}{(\sigma_T \cdot \sigma_E) \cdot \tau_T} \tag{68}$$

where $\tau_T = \frac{c}{\sigma_T}$ is the thermal time constant and $\tau_E = \frac{C}{\sigma_E}$ is the electrical time constant.

Numerical values for the parameters in equation (68), for the P2613-06 pyroelectric detector, are listed in Table 5C and have been used to plot the frequency dependence of the voltage responsivity R_v. The plot is given in FIGURE 5.21. A load resistance of $10M\Omega$ is used in parallel to the pyroelectric element so as to widen the frequency characteristic, but at the same time limit the voltage output so as to avoid saturation at high power

inputs. It is noted that the voltage responsivity is relatively flat over the frequency range 0.2 to 210Hz. A modulation frequency of 5Hz is in the middle of the flat region and can be regarded as being a stable modulation frequency with respect to voltage responsivity. The second curve in FIGURE 5.21 gives the derivative of the voltage responsivity with respect to frequency. It is noted that a 5% shift in the 5Hz modulation frequency could result in a 0.00023% change in voltage responsivity.

Finally, a pyroelectric detector has no wavelength dependence. However, an encased detector with a window would restrict the pyroelectric's spectral response. A TO-5[1] detector assembly is used for Hamamatsu's P2613-06 detector in the DDSR-1B instead of a customised assembly. The housing, with a sapphire window, shields the detector. The transmission performance for the sapphire window is shown in FIGURE 5.22. The average sapphire transmittance of light over the wavelength range spanning from 400 to 2400 nanometers is about 87%.

Table 5C: Numerical Parameters for the P2613-06 detector.

Symbol	Parameter	Value	Source
η	detection efficiency (radiation absorption fraction)	0.87	sapphire transmission
T	absolute temperature	-20 to 60°C	[29.]
A	area of detecting element	$3.14\times10^{-6}m^2$*	[29.]
d	thickness of detecting element	$10^{-4}m$	[7.]
σ_T	thermal conductivity	$11Wm^{-1}K^{-1}$	[8.]
ε'	relative dielectric constant	from 250 to 300	[7.]
p	pyroelectric coefficient	$3\times10^{-4}Cm^{-1}K^{-1}$	[8.]
τ_T	thermal time constant	$1.59s$	[29.]
τ_E	electrical time constant	$568\mu s$	[29.]

1. ***T0-5*** is a standard metal can with a window used for housing detectors.

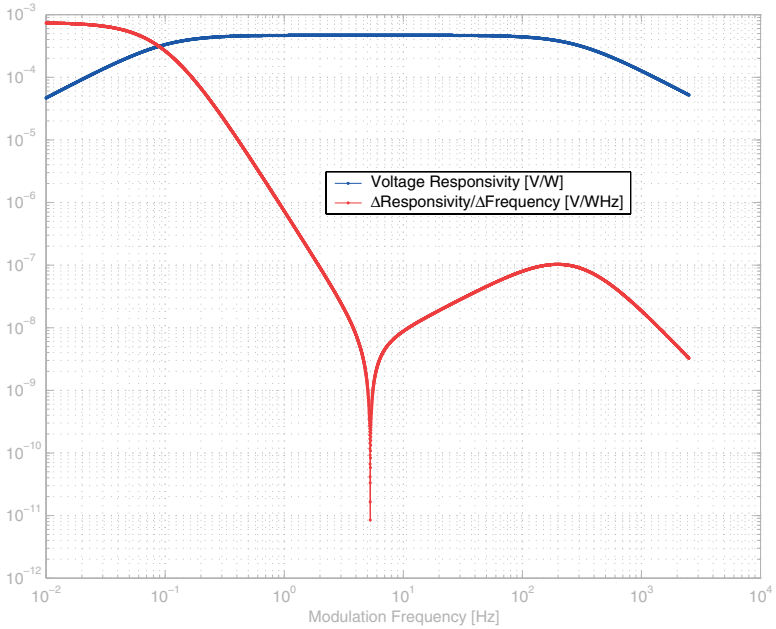

FIGURE 5.21
P2613-06 pyroelectric detector voltage responsivity to modulating frequencies for a load resistance of $10M\Omega$, and the derivative of responsivity w.r.t. frequency.

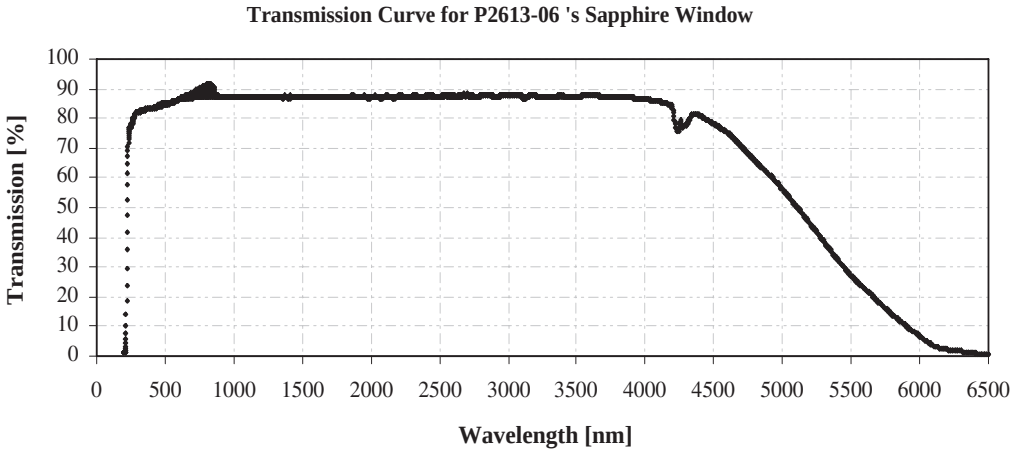

FIGURE 5.22
Transmission performance of the pyro-detector's sapphire window. *Courtesy of Layertec GmbH in [12., 2003].*

5.4.1.3. Noise Equivalent Power

The detector has a specified minimum detectable incident power (or NEP for noise equivalent power) of $1nWHz^{-1/2}$ at a reference temperature of 500K, a modulation frequency of $1Hz$ and a unity frequency bandwidth. DDSR-1B's current application of the P2613-06 involves a modulation frequency of $5Hz$ and a bandwidth of $0.5Hz$. In this case $NEP = 0.225mWm^{-2}$. It follows from equations (57) and (58), that:

$$NEP(Mode_{Diffuse}) = 0.014mWm^{-2}, \text{ and} \tag{69}$$

$$NEP(Mode_{Direct}) = 0.25mWm^{-2} \tag{70}$$

The values in equations (69) and (70) do not include noise contributions from the conditioning electronics nor from the data-acquisitioning system. It also excludes the resolution of the analog to digital converter.

5.4.1.4. Temperature Characteristic

P2613-06 is not a self-compensating detector. Changes in ambient temperature would alter the detector responsivity due to the detectors piezoelectric property. To illustrate, the temperature sensitivity plot is for a P7178 Hamamatsu pyro-series is shown in FIGURE 5.23. Here, the temperature coefficient is about 0.2%/^{o}C at $1Hz$. This implies that the sensitivity of the detector could differ by as much as 3% over an ambient temperature range of 15^{o}C.

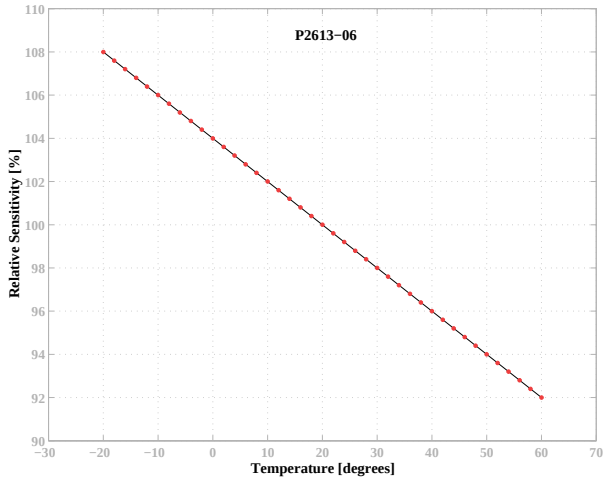

FIGURE 5.23
Sensitivity of the P2613-06 versus element temperature.

5.4.2. Detector Signal Conditioning

Two interfaces are used to condition the detector signal. The first interface, referred to as the ***pyro-interface***, is in the radiometer. The pyro-interface is a preliminary conditioning block to adjust for DC-offset and to amplify the sensor signal. The second interface, referred to as the ***filter-interface***, is in the control unit. The signal off the pyro-interface is transmitted to the filter-interface where it is filtered from interfering signals.

5.4.2.1. Pyro-Interface

The pyro-interface is on the same printed board as the pyroelectric detector so as to minimise fundamental signal transmission losses. The operating circuit/interface for the P2613-06 is as shown in FIGURE 5.22. The 10$M\Omega$ resistor, connected in parallel to the sensor element, defines the sensor response level (see Section 5.4.1.2, “Detector Responsivity,” on page 130). The unity gain amplifier serves as a high-to-low impedance transformer. It provides a high input impedance which is necessary for interfacing the high-impedance sensor output. A 10x gain amplifier is used to amplify the sensor signal before transmission to the filter.

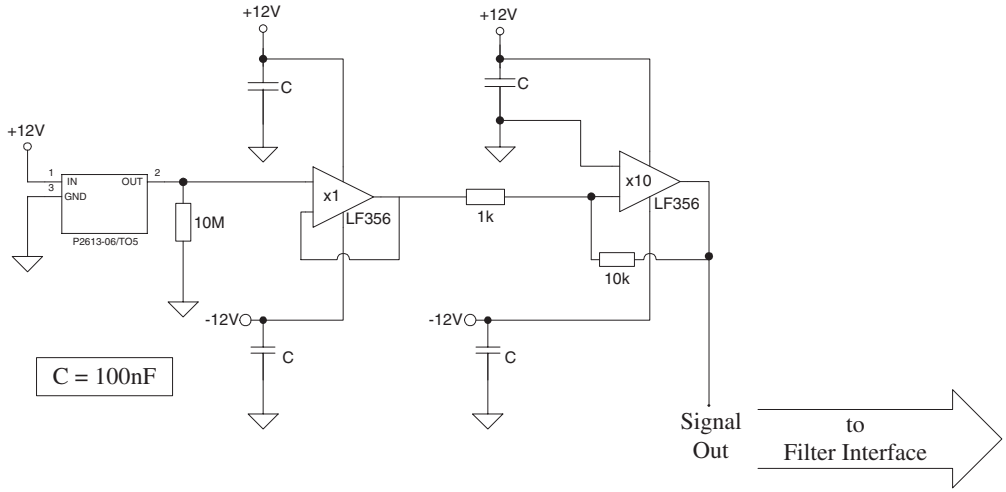

FIGURE 5.24
P2613-06 interface (referred to in the text as the pyro-interface)

5.4.2.2. Filter-Interface

The amplified signal from the pyro-interface is passed through an analogue filter-interface to select the 5*Hz* modulation component. A schematic of the interface is shown in FIGURE 5.25 and the filter's response for circuit theory versus measurements is given by the plots in FIGURE 5.26.

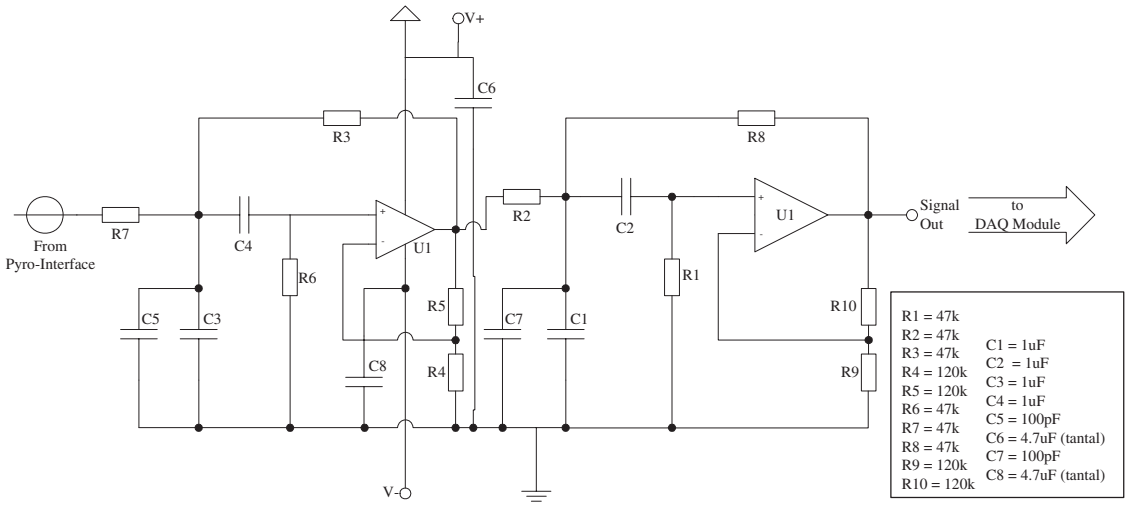

FIGURE 5.25
Schematic of the filter-interface for the DDSR-1B. The interface consists of 2 bandpass Sallen-Key filters in series connection.

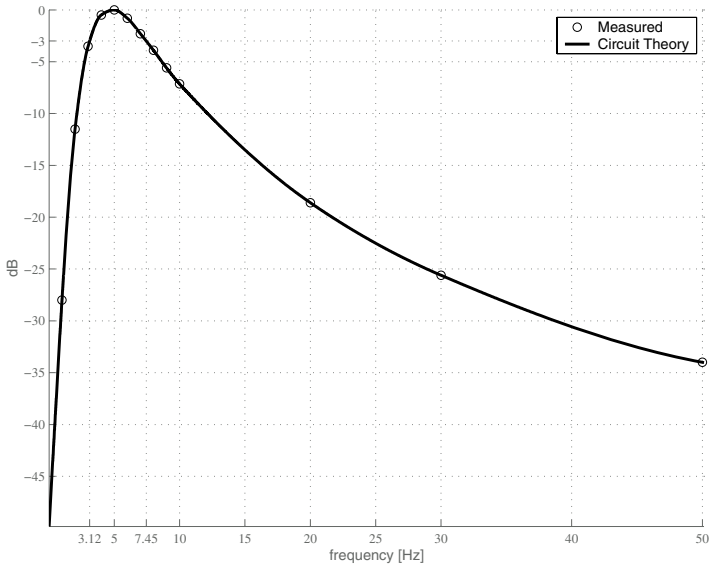

FIGURE 5.26
Response for the second order Sallen-Key filter. The plot shows a 0dB peak at 5*Hz* and the -3dB points at 3.12*Hz* and 7.45*Hz*.

The filter-interface consists of two Sallen-Key bandpass filters in series. With component values as given in FIGURE 5.25, the filter gives a peak of unity gain at $5Hz$. The filter's bandwidth, defined at $-3dB$, is $4.33Hz$.

5.4.2.3. Total Analog Transfer

DDSR-1B's system transfer function is the product of the analog and digital transfer functions. Contributions from digitization is discussed in section 5.5.2 on page 139.

The analog factors are: chopper modulation *(see "The Chopper Wheel" on page 104.)*, imaging *(see "Object-Image Relation" on page 113.)*, signal detection *(see "Detector Responsivity" on page 130.)*, amplification *(see "Pyro-Interface" on page 135.)*, and filtering *(see "Filter-Interface" on page 136.)*. The total analog transfer is given by the responsivity vs frequency plot in FIGURE 5.27.

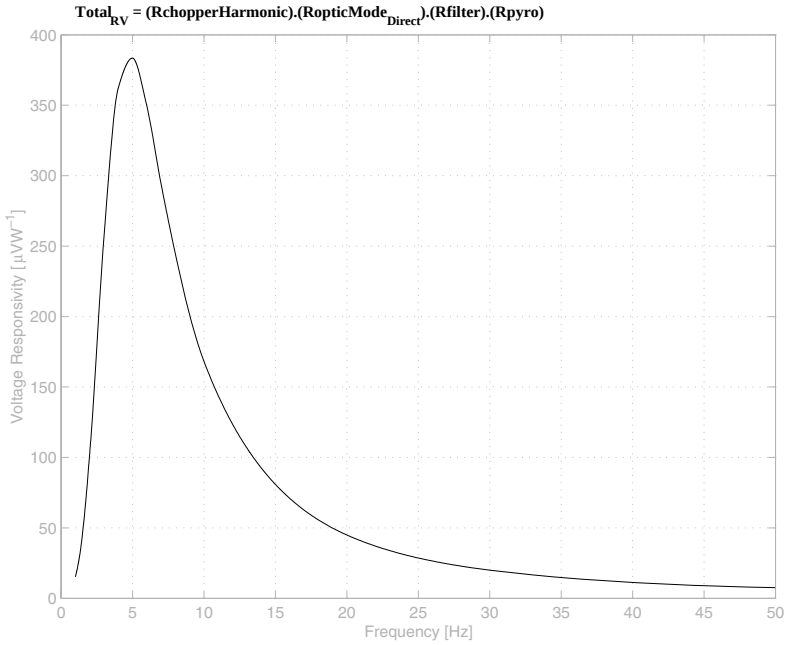

FIGURE 5.27
Total voltage responsivity of the DDSR-1B system.

The transfer factor at the modulation frequency of $5Hz$ for $\text{Mode}_{\text{Direct}}$ is:

$$K_{theoretical} \cong 383 \frac{\mu V}{Wm^{-2}} \tag{71}$$

5.5. The Control System

The radiometer of the DDSR-1B is remote from the control unit so as to locate the control unit in an indoor, stable environment. A block diagram of the control unit and its functionality is given in FIGURE 5.28. The core of the control unit is a central processing unit (CPU) module, a DAQ module and developed software in the Labview environment.

5.5.1. The Central Processing Module

The control unit for the radiometer has an embedded microcomputer based on the PC/104 standard, with the functions of an AT-compatible PC. The main module is a PCM3350 CPU module with the following:

- a 300*MHz* CPU,
- 128*MB* system memory,
- a Video Graphics Array (VGA)/Liquid Crystal Display (LCD) interface,
- an IDE(AT bus) hard-disk drive interface,
- a PS/2 keyboard/mouse connector,
- 2 serial ports (RS-232 and optional RS-233/422/485),
- a parallel port,
- 2 USB ports, and
- an Ethernet interface.

The hard-disk drive interface has been used for an IDE hard disk (with a capacity of 10 gigabytes) with a Windows 2000 operating system. Device interaction is via LCD and mouse/keyboard. The Ethernet provides an optional inter-access mode.

The PCM3350 CPU module is a plug compatible mainframe; with a PC/ 104 connector for upgrades.

5.5.2. The Data Acquisition Module

The Data Acquisition Module (DAQ), type AXIOM AX10410A, is a PC/104 standard expansion module. It is installed in line to the PC/104 CPU board.

5.5.2.1. Analog Input Subsystem

The DAQ module has a 16 channel analog multiplexer when used in the single-end mode. Currently 6 of the 16 channels are used for analog input. These are, as shown in FIGURE 5.28, for the signals from the:

1. pyro-interface,
2. filter-interface,
3. chopper modulation reference (sync),
4. photo-transistor for the orientation of the lens wheel,
5. body temperature transducer, and
6. detector temperature transducer.

The analog signals are converted to digital by a 12-bit analog- to-digital (A/D) converter (ADC). A/D conversion is initiated by Direct Memory Access (DMA) in order to use the high speed conversion. The gain on the analog inputs is programmable to 1, 2, 4 or 8, with high impedance input (bipolar) ranges of $\pm 10V$, $\pm 5V$, $\pm 2.5V$ or $\pm 1.25V$ depending on the respective gain setting. The full-scale resolutions of conversions for the respective gains are $4.88mV$, $2.44mV$, $1.22mV$ and $0.61mV$. It follows from equation (71) and the signal ratio given in section 5.3.4.2.2.2, that these full-scale resolutions would allow measurements down to about $2Wm^{-2}$ in $\text{Mode}_{\text{Direct}}$ and about $0.1Wm^{-2}$ in $\text{Mode}_{\text{Diffuse}}$.

5.5.2.2. Digital Input/Output Subsystem

The DAQ module has 8 digital input/output (I/O) lines. Four of these digital lines are used (with reference to FIGURE 5.28) for the following:

- chopper motor power on/off,
- stepper motor power on/off,
- stepper motor clock, and
- stepper motor direction.

Power to the chopper motor and the stepper motor are controlled so as to reduce heating within the radiometer. Logic levels are required for the clock setting (which sets the number of steps to be taken by the stepper motor) and the direction specification of the stepper motor. This, together with holding magnets and feedback from the position sensor at the lens wheel, gives the mechanism for controlled positioning of the open, closed and lens ports on the lens wheel.

5.5.3. Control Software

The radiometer and associated modules are controlled automatically, under Windows, with software in the Labview version 6.1 environment. The AXIOM DAQ module uses an AXIOM DAQ card driver for use under Windows and a Labview Interface Driver for interfacing between the DAQ card driver and the Labview software. The driver transition to Labview is illustrated in FIGURE 5.29. Flowcharts for the Virtual Intruments (VI) that control the acquisition of data are given in FIGURE 5.30 and FIGURE 5.31. The VI 'Scan.vi' has the option to either:

- run a 'scan' to get the radiation, modulation synchronous and temperature signals, or
- rotate the lens wheel.

On the Scan option, the chopper motor is programmatically powered up and a time delay is allowed for transient settling. The VI 'DMAmeas3.vi' is then called to start the multiple A/D conversions from the conditioned analog synchronous and pyroelectric signals. The raw data from the DMA buffer is copied to a user-specified array and converted to a floating point data array (real voltage) by considering the DAC's bipolar range, resolution and DAQ module gain. The chopper motor is programmatically powered down at the end of data retrieval.

On the option to rotate the lens wheel, the first step is to find if the reference 'closed' post is along the optic axis. In the advent of a positive return the lens wheel is then set to rotate in the direction so as to position the desired post (open or lens) along the optic axis. In the advent of a negative return the closed post is first centred along the optic axis and the above procedure is then repeated. Knowledge of the position of the reference 'closed' post is via the LED/phototransitor signal.

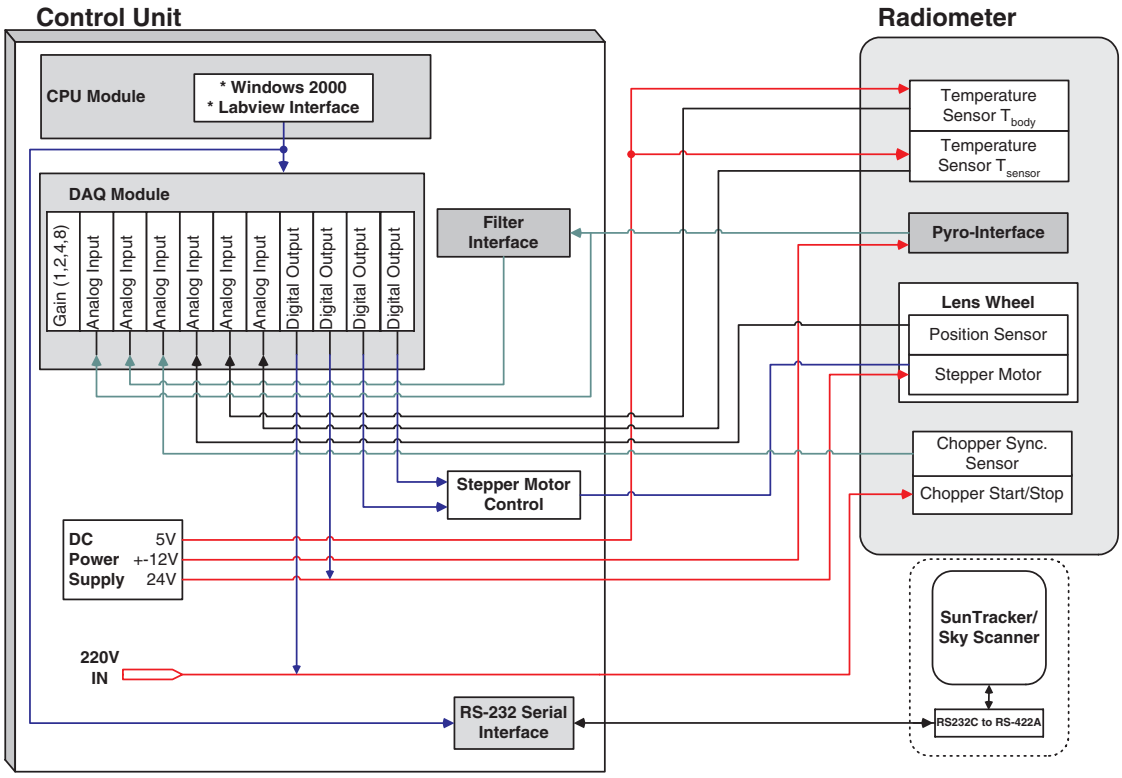

FIGURE 5.28
Block Diagram of the control structure for the DDSR-1B.

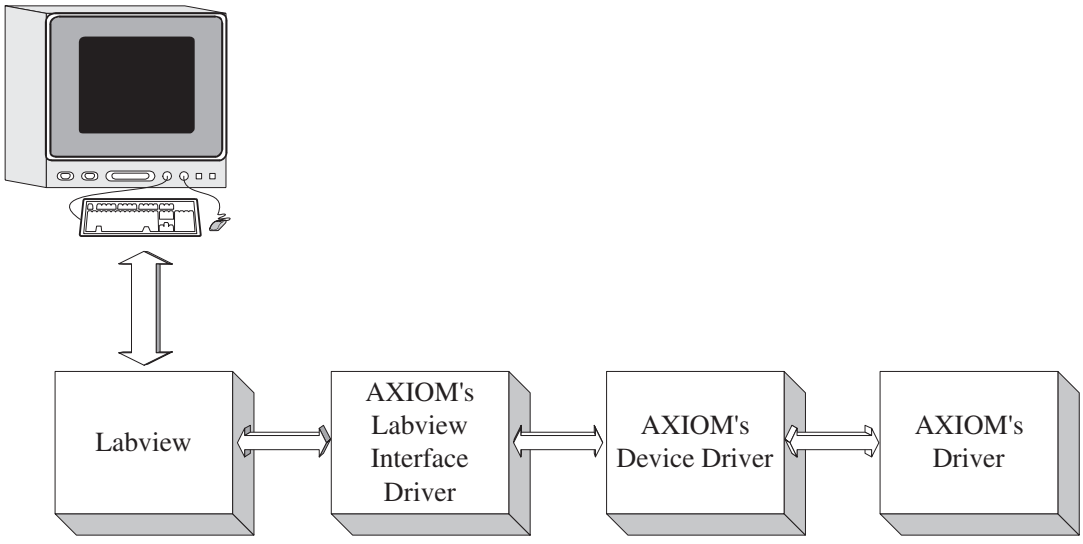

FIGURE 5.29
AXIOM's DAQ Driver transition from the device driver to Labview.

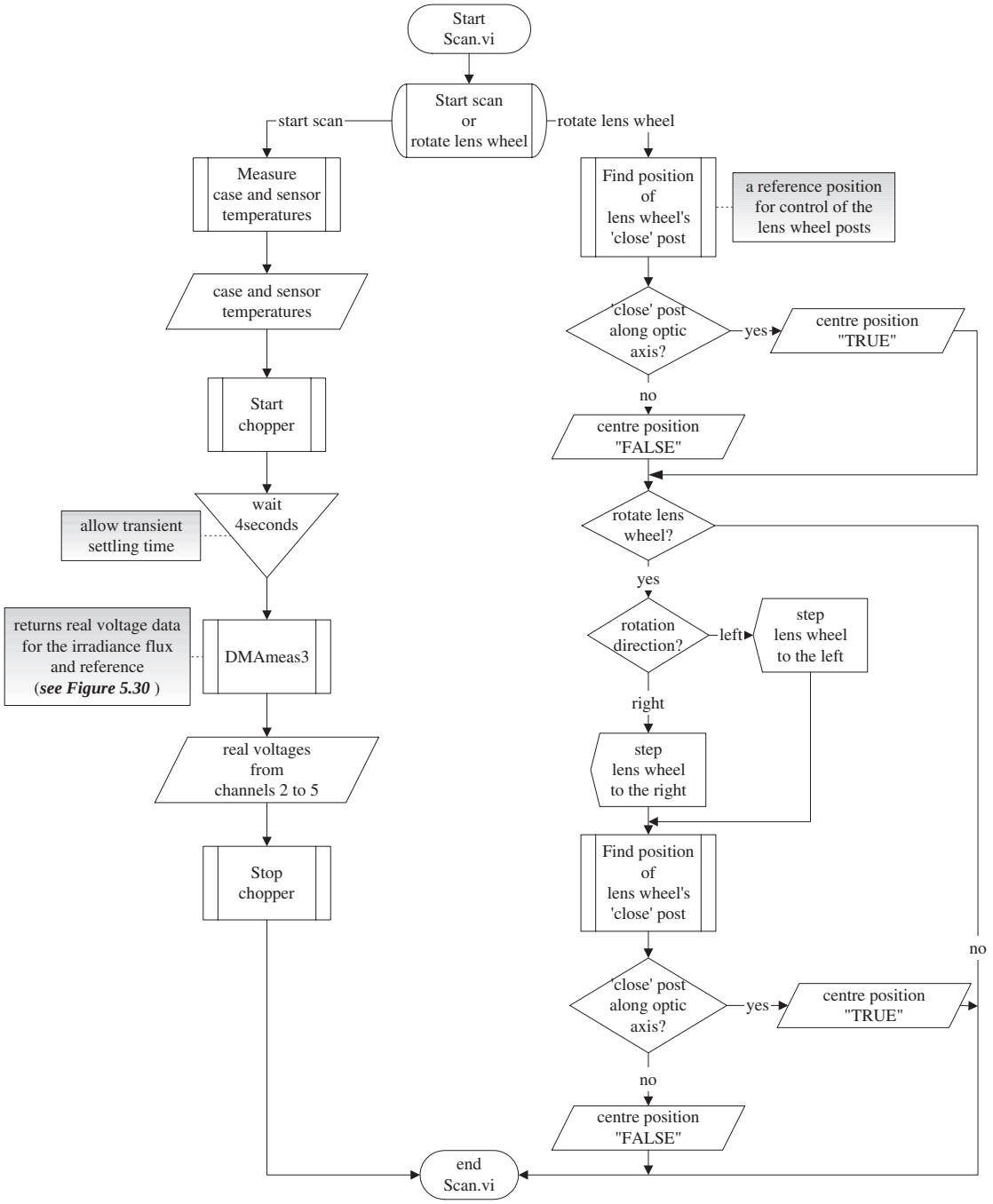

FIGURE 5.30
Flowchart of the VI *Scan* which, together with the *DMAmeas3* VI acquires the radiation and temperature data. The VI gives the option to step the lens wheel into the required position.

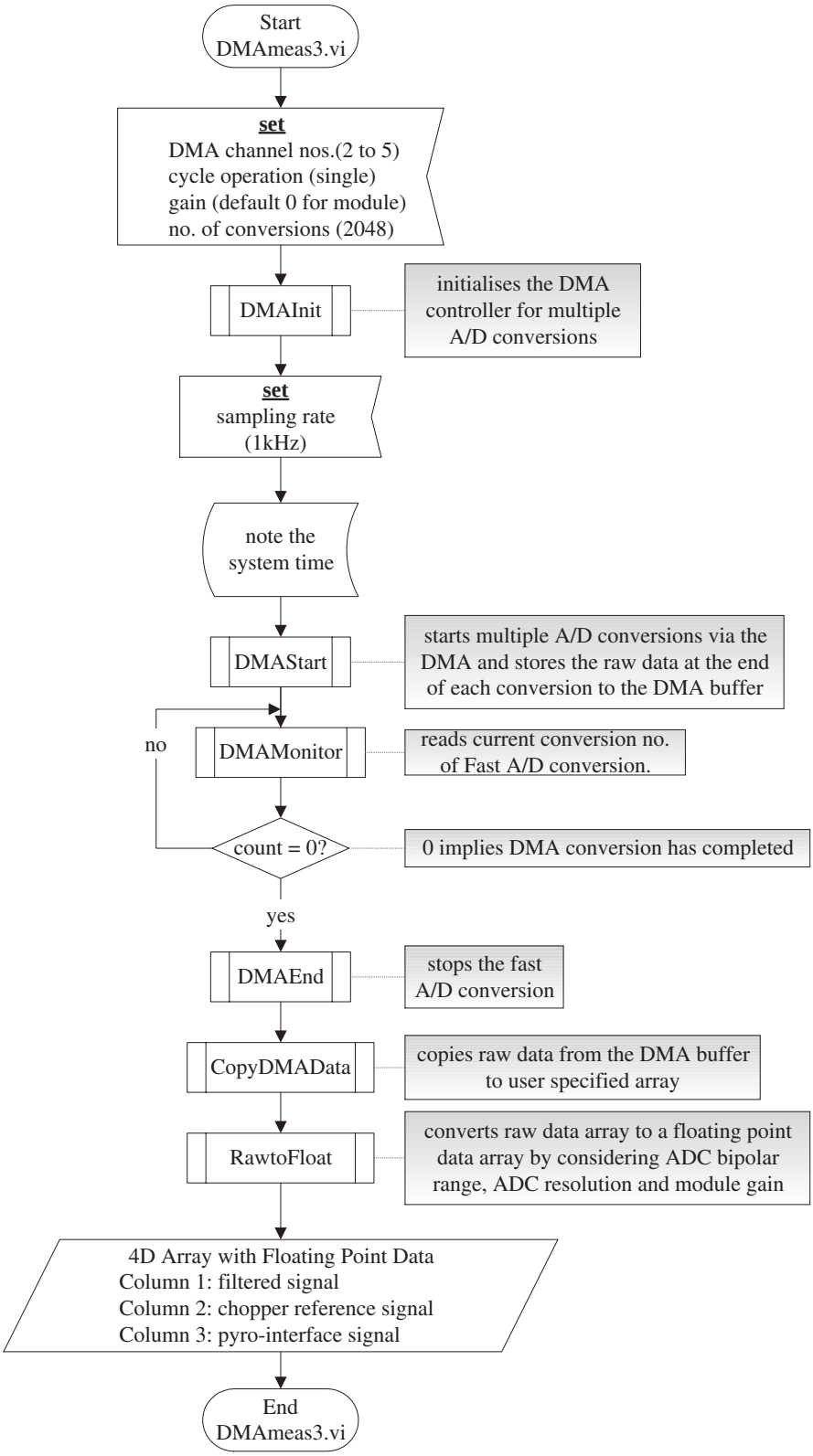

FIGURE 5.31
Flowchart of the VI *DMAmeas3*. The VI starts a fixed number (2048) of A/D conversions via DMA and copies the raw data to a specified array.

5.5.4. Discussion on the Control System

The main criteria in the development of the control unit has been simplification of the system by maximum usage of standard components. This has allowed ease of system testing and system modifications.

The following is a list of features gained:

* The PC compatibilty of the CPU module has allowed the use of the familiar Windows environment.

* The Ethernet interface has allowed:
  - access to the collected data through the network,
  - the possibility to remotely control the system, and
  - system time correction via a time server.

* The serial and USB ports give the possibility to:
  - control the automatic sun-tracker/sky-scanner,
  - connect a GPS-based time corrector (instead of using a time server),
  - integrate several DAQ systems, and
  - have a single system for on-field calibrations of the radiometer.

  (The latter two are feasible as communication with an external data logger would be made possible by appropriate software in the DDSR-1B control environment.)

* The plug compatible mainframe of the CPU module has allowed the choice of the DAQ *expansion* module.

* All measurement-related functions (multiple analog I/O and digital I/O) are on the single PC/104 form factor DAQ module.

* The CPU/DAQ module stacking and associated producer provided drivers reduces the system software development time.

* Development of software in the Labview environment has allowed for:

- direct integration with the measurement hardware, and
- incorporation of previously developed VIs, for calibration and DAQ (for the NIPs and PSPs), into the control software.

It is understood that the potential of the system may be tapped with a higher resolution ADC. The use of stackable standard PC/104 modules ensures that any future upgrade would be possible without having to disintegrate or modify the system core.

5.6. Signal Analysis

The required signal amplitude is extracted using the theory of Fourier analysis, within the discrete time domain. The discrete-time Fourier series (DTFS) is considered since the signals are periodic (being modulated by the chopper) and their spectrum is limited by the hardware analog filter prior to the A/D conversion. The spectrum satisfies the sampling theorem[1] and, together with the periodicity of the signals, leads to the spectrum being unaliased within the finite set of N numbers.

5.6.1. Definitions in Fourier Representation

A DTFS representation of a periodic signal $x[n]$, with fundamental period N and fundamental frequency $\Omega_o = \frac{2\pi}{N}$ is given by,

$$x[n] = \sum_{k=0}^{N-1} X[k] e^{jk\Omega_o n} \tag{72}$$

where

1. **Sampling Theorem**: If the highest frequency component in a signal is f_{max}, then the signal should be sampled at the rate $F_s \geq 2f_{max}$ for the samples to describe the signal completely.

$$X[k] = \frac{1}{N}\sum_{n=0}^{N-1} x[n]\mathrm{e}^{-jk\Omega_o n} \tag{73}$$

are the DTFS coefficients of the signal $x[n]$. The DTFS coefficients $X[k]$ are termed a frequency-domain representation for $x[n]$. This is because each coefficient is associated with a complex sinusoid of a different frequency. The variable k determines the frequency of the sinusoid associated with $X[k]$.

From N values of $x[n]$, $X[k]$ may be determined by using equation (73). The magnitude of $X[k]$, which is the absolute value of $X[k]$ denoted $|X[k]|$, is the magnitude spectrum of $x[n]$.

$$|X[k]| = \sqrt{\mathrm{real}(X[k])^2 + \mathrm{imag}(X[k])^2} \tag{74}$$

By definition, the frequency domain representation $X[k]$ is the DTFS and the time domain signal $x[n]$ is the inverse DTFS (IDTFS). For both the DTFS and the IDTFS it is assumed that the signal is deterministic, not stochastic. Before complete characterisation of the flux responsivity of the DDSR-1B, the output signal from the ADC has been treated as stochastic. According to [Beyon, 1., 2001, p.264] the same transformations as equation (72) and equation (73) apply for a stochastic signal, but the correlation function of the signal is used instead of the original signal. [Newland, 19., pp. 122-123, 1993] derives the relation for the discrete series of auto correlations

$$S_{XX}[k] = X^*[k] \cdot X[k] \tag{75}$$

and cross correlations

$$S_{XY}[k] = X^*[k] \cdot Y[k] \tag{76}$$

where * denotes the complex conjugate and $X[k]$, $Y[k]$ are the DTFS of time-domain signals $x[n]$ and $y[n]$ respectively.

The equations (73) to (76) indicate that the signals are viewed in the frequency domain. The obvious advantages of digital signal processing (DSP) in the frequency domain are the ability to observe the frequencies that make up the signal and the distribution of noise. The standard Fast Fourier Transform (FFT) or Discrete Fourier Transform (DFT) function in any DSP software environment can be used to realise equation (73).

Finally, the magnitude of the required signal in the DDSR-1B system is estimated from DSP in the Labview environment. The estimate is denoted by $|V[k]|$ in FIGURE 5.32, and is derived by a cross-correlation process involving discrete signals $v[n]$ (which represents the transferred solar irradiance signal) and $c[n]$ (which represents the reference signal from the chopper). The estimate of $|V[k]|$ is calculated as

$$|V[k]| = \frac{|S_{VC}[k]|}{\sqrt{|S_{CC}[k]|}} \tag{77}$$

which is derived as follows:

$$\begin{aligned} |V[k]|^2 &= \left(\frac{|V[k]| \cdot |C[k]|}{|C[k]|}\right)^2 \\ &= \frac{(|V^*[k]| \cdot |C[k]|)^2}{|C[k]| \cdot |C[k]|} \\ &= \frac{|V^*[k] \cdot C[k]|^2}{|C^*[k] \cdot C[k]|} \\ &= \frac{|S_{VC}[k]|^2}{|S_{CC}[k]|} \end{aligned} \tag{78}$$

It is intended that the cross-correlation process as given in equation (77) reduces inaccuracy in amplitude extraction. The signal $v(t)$ is repetitive and holds random noise. Due to its repetitiveness, the multiplication process builds the signal up. Since the noise is random, the multiplication process should not increase its magnitude. Thus a higher signal to noise ratio is achieved.

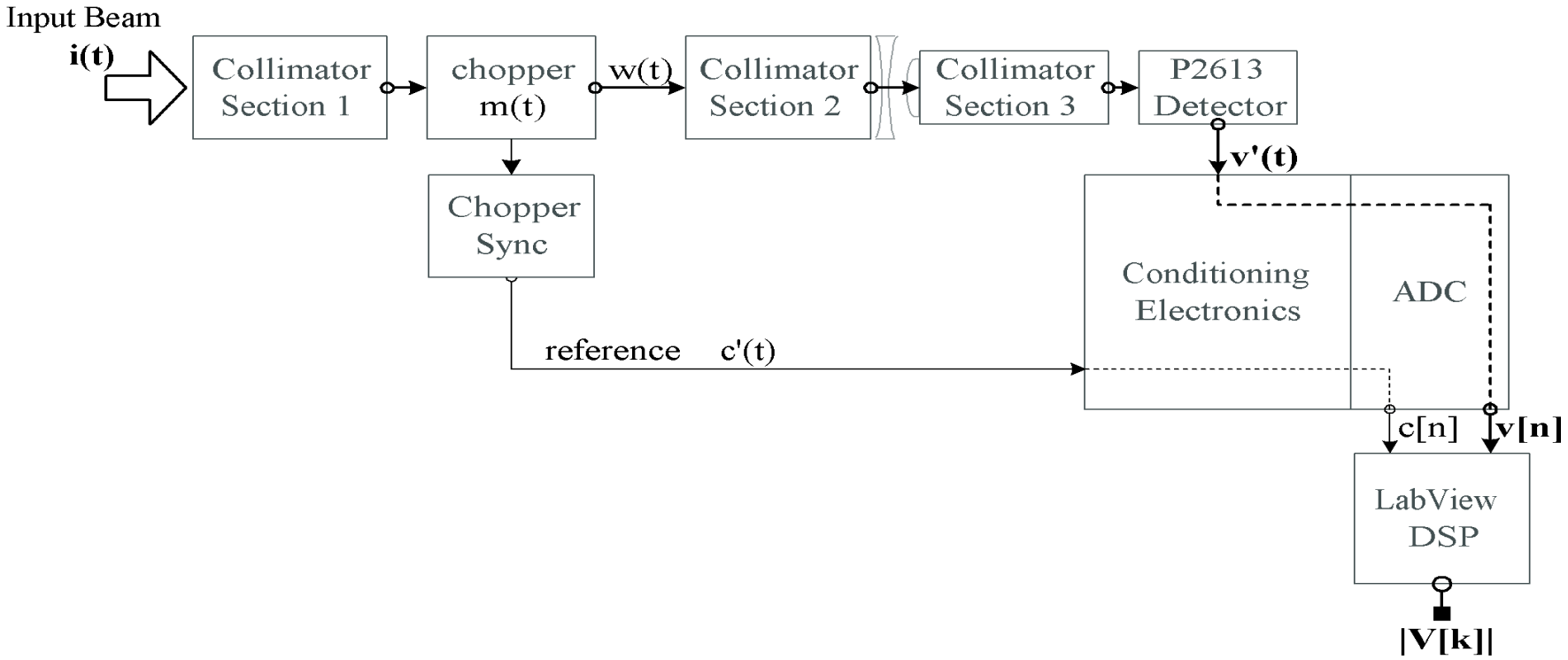

FIGURE 5.32
Illustration of the paths and transformations of the signals for DDSR-1B.

5.6.2. Signal Sampling Overview

An illustration of the paths and transformations of the signals for DDSR-1B are given in FIGURE 5.31. The incoming radiant flux is denoted by $i(t)$. Different notations should have been given to the beam on exit from the collimator sections 1 through to 3, but these have been omitted in this text. However, the total system response to the incident flux does take into consideration effects within the collimator sections.

The chopper modulation is shown by $m(t)$. The result of modulating the input flux $i(t)$ by the chopper is indicated as $w(t)$. The modulated signal $w(t)$ is picked up by the pyroelectric detector and converted to a voltage signal $v'(t)$. The signal $v'(t)$ is routed through a network of conditioning elements (i.e the pyro-interface and the filter-interface) and finally is sampled by the ADC. The sampled output is denoted by $v[n]$.

The alternating of the chopper wheel window and frame gives rise to a square-wave response picked up by the photodiode from the LED. This sensing pair is positioned such that the emitter is 'seen' by the receiver only at the same instance as when the oncoming irradiance passes through the wheel slits. The square-wave response is termed the reference signal $c'(t)$. The reference signal is sampled by the ADC. The sampled output is denoted by $c[n]$.

The following numerical quantities are used during sampling:

- total number of samples per scan per channel = 512 samples. A total of 500 samples are actually used. This is to ensure that the number of samples are an integer multiple of the chopper period as well as the mains frequency (this is discussed by Løvseth et al. in [16., 1992]).
- sampling frequency = 250Hz
- chopper modulation frequency = 5Hz

5.6.3. System Noise Reduction

Some steps have been taken in order to increase the signal to noise ratio (SNR) in the DDSR-1B system. Hardware and software methods have been used.

The co-implementation of modulation and analogue filtering eliminates noise outside the required signal frequency range.

Aside from the purpose of chopping the incident flux for the pyroelectric detector, signal modulation also:

> Moves the bandwidth of information of the signal to a portion of the frequency spectrum where it is less subject to interference. In the case of the DDSR-1B system, modulation at $5Hz$ moves the signal to the $5Hz$ region which is fairly 'free' of environment noise.

The low pass of the filter ensures satisfaction of the Kotelnikoff (Sampling) theorem so as to avoid aliasing in the estimated spectrum of the detector signal. It is noted however, that the amplifiers (necessary for amplifying the otherwise small signal) in both the pyro-interface and filter-interface not only generates amplifier noise that gets superimposed to the amplified signal but also amplifies the level of noise already incumbent on the signal. Such noise, with matching spectral content as a signal, constrains the extraction of weak signals.

It has been stated in Section 5.6.2, "Signal Sampling Overview," on page 149 that the total number of samples per scan is 512 samples at a sampling frequency of $250Hz$. But the signal is post processed with 500 samples to achieve minimum error. To confirm this, the amplitudes of a pure sinusoidal test signal with unit amplitude have been retrieved by the method of cross-correlation as described in section 5.6.3. for a variable number of samples. The curve of error as a function of the total number of samples is shown in FIGURE 5.33. It is clear from the figure that post processing with 500 samples give the least error in amplitude retrieval.

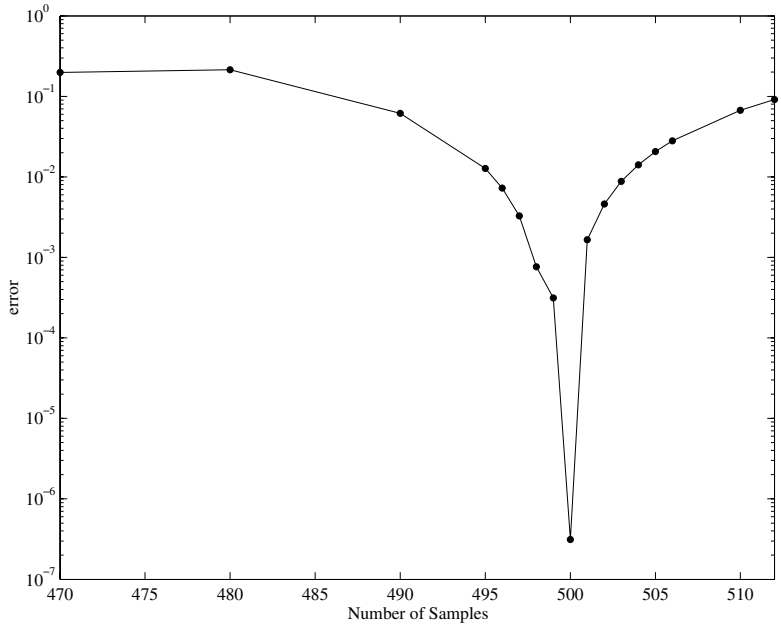

FIGURE 5.33
Error estimate as a function of the number of samples per ADC scan. The error is taken as the deviation from a unit amplitude test signal.

The above results follow since, in the domain of the DTFS, the ratio of modulation frequency $f_m = 5Hz$ to frequency step Δf should be an integer so as to avoid spreading of energy into side-lobes. The frequency step for a data set of 512 samples is $\Delta f = \frac{0.25kHz}{512 \text{ samples}}$, giving:

$$\frac{f_m}{\Delta f} = 10.24 \notin \text{integers} \tag{79}$$

On the other hand, the ratio for a data set of 500 samples is:

$$\frac{f_m}{\Delta f} = 10 \in \text{integers} \tag{80}$$

The initial intention had been to use $2^9 = 512$ samples so as to utilise the fast fourier transform (FFT). Nonetheless the computation power of the CPU compensates for the necessity of using the discrete fourier transform instead of the much faster FFT.

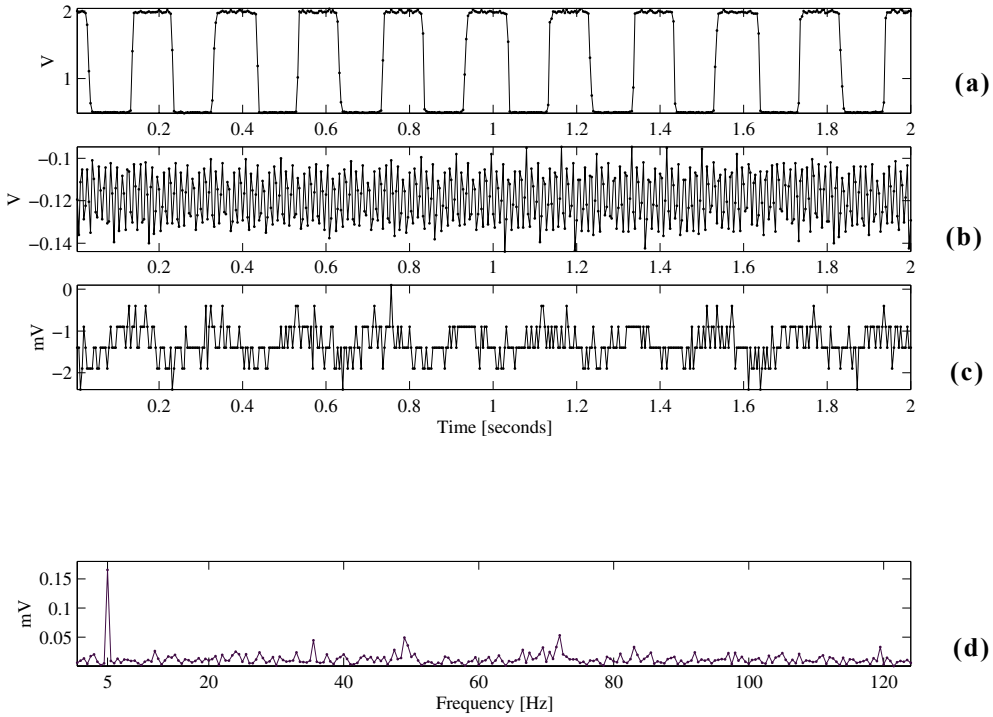

FIGURE 5.34
Illustration of recovery of a weak signal embedded in noise from $\text{Mode}_{\text{Direct}}$. (a) gives the signal from the chopper, (b) the pyro-interface signal-out, (c) the filter-interface signal-out and (d) the signal spectrum calculated using equation (77).

The spectral analysis approach in the DSP provides a mechanism to detect a signal embedded in noise. As an illustration a weak signal recovery from $\text{Mode}_{\text{Direct}}$, with the radiometer directed away from the sun, is shown in the FIGURE 5.34. The signal should correspond to an irradiance of about $0.5 Wm^{-2}$, which is below the threshold of the ADC and quantisation errors are expected. The effect of quantisation is clearly visible in FIGURE 5.34(c). The 500 point data shown in part (c) represents the filter-interface signal out and contains the required periodic signal buried in noise. The transform, calculated using the cross-correlation approach given in equation (77), is shown in part (d). There is a more-or-less even distribution across the spectrum, plus a pronounced peak at $5Hz$. It is seen that modulation, analogue filtering and the observation of almost steady incident fluxes over the sampling time keeps the signal's spectral energy well concentrated. So long as the signal and noise have different spectral distributions, a weak signal can be detected by the DSP approach as described in section 5.6.2 and illustrated in the FIGURE 5.34.

5.7. Absolute Calibration

It is understood that for solar instruments, solar standards would be better. A preliminary calibration of DDSR-1B had been an absolute calibration. Absolute calibration refers to calibration undertaken in a steady state environment using a standard lamp source.

The calibration procedure had been carried out in the dark room facility at NTNU with a 1000 watt lamp (an Eppley EN-60) source. The lamp is traceable to the National Institute of Standards and Technology (NIST).

5.7.1. Calibration Procedure

The optical set-up for the absolute calibration was as illustrated by the sketch in FIGURE 5.35

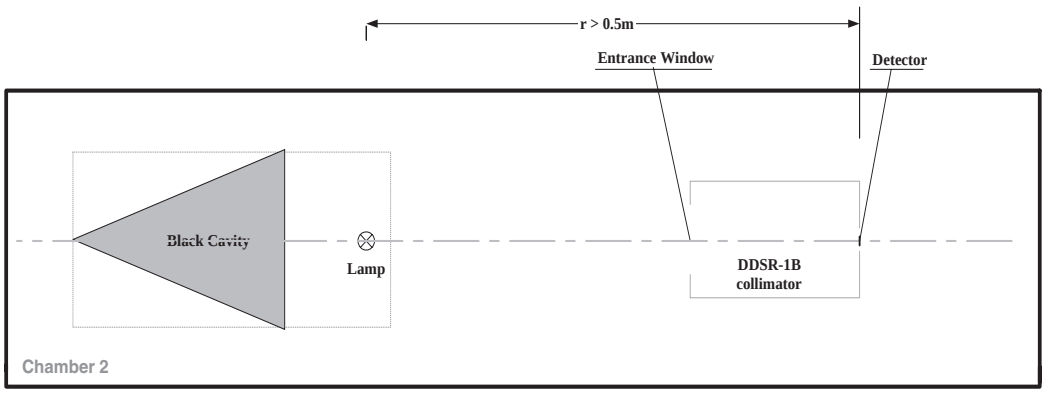

FIGURE 5.35
Optical bench set-up for an absolute calibration of the DDSR-1B.

The coned black cavity, lamp and radiometer were mounted on the same optical plane. A laser positioning system was used to setup the horizontal alignment of the above mentioned components.

Surfaces of the calibration chamber (walls, doors and optical benches) are painted matt black so as to avoid disturbances by stray light.

The EN-60 lamp generates a total (spectrally integrated) irradiance of $298 Wm^{-2}$ at a distance of $0.5m$ from the filament centre. Different levels of

reference irradiances could be imposed onto the radiometer by sliding the lamp towards or away from the radiometer. That is, by altering the distance r between the lamp and receiver. The ideal reference irradiance E_R at the aperture stop for varying distances r is given by:

$$E_R = \left(\frac{r_o}{r}\right)^2 \cdot E_o \tag{81}$$

where $r_o = 0.5m$ is the reference distance between the lamp and the detector, and E_o is the total irradiance at distance r_o.

The black cavity shown in FIGURE 5.35 is a hollow cone, painted matt black. Background reflections could be controlled by maintaining a constant cavity-to-lamp distance.

The power supply for the lamp is a Power Ten Inc. model 3400B-1502. This power source has a $5-7\ mA$ per hour drift if not regulated. It has been possible to automatically control the lamp current drift by using a computer controlled feedback system as described by Thorseth in [33., 2000]. The regulating system maintained stability of current to the lamp to within $1mA$ during the calibration process.

Except for the manual adjustment of the cone-lamp-receiver distance, the calibration processes had been automated. Details of the calibration automation are shown by the flowchart in FIGURE 5.36.

A set of 5 reference intensities are selected for $\text{Mode}_{\text{Direct}}$. Ten measurements were taken at each reference intensity. For each measurement an estimate of the voltage was made and saved to file. The calibration procedure had been repeated, but now by manually increasing the distance between the lamp and source. A measure of the instrument's hysteresis had thus been made by comparing the results from the increasing intensities and the decreasing intensities.

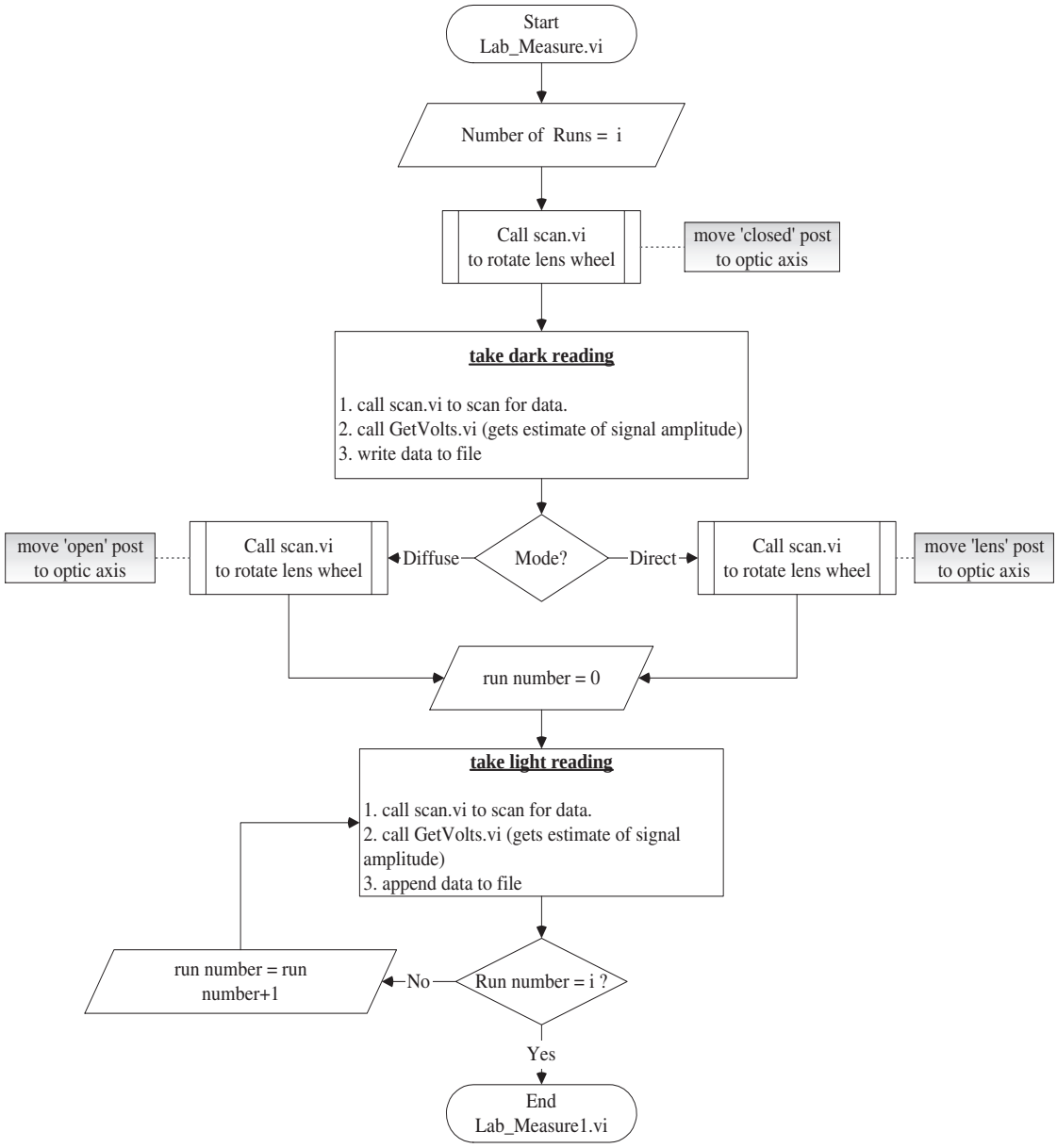

FIGURE 5.36
Program procedure for automated measurements for absolute and field calibrations.

5.7.2. Absolute Calibration Results

The lamp intensities and corresponding DDSR-1B voltage outputs are listed in the Table 5D. The errors for the lamp intensities are the result of errors in distance approximation, power supply and lamp tolerance. These errors are discussed in section 5.7.3.1 on page 161. The standard deviations listed in Table 5D for $Mode_{Direct}$ are the deviations from the average of 20 measurements i.e. 10 forward and 10 backward measurements.

Table 5D: Results for the absolute calibration of DDSR-1B.

$Mode_{Direct}$				
Reference Lamp Intensity	**DDSR-1B Response**		**Function Estimate**	
	Average	**Standard Deviation**	**Estimate**	**deviation from Reference**
Wm^{-2}	mV	mV	Wm^{-2}	Wm^{-2}
16.44	4.32	0.03	11.83	4.61
26.12	8.35	0.10	22.83	3.29
33.60	11.49	0.05	31.71	1.90
63.99	22.49	0.13	62.31	1.68
140.18	50.08	0.60	139.23	0.95
$Mode_{Diffuse}$				
Reference Lamp Intensity	**DDSR-1B Response**			
	Average		**standard deviation**	
Wm^{-2}	mV		mV	
26.12	137.38		0.52	
33.60	183.38		0.52	

5.7.2.1. Response Function

A first degree polynomial fit had been made through the points of the intensity versus voltage output (average of the 10 forward and 10 backward runs) for each mode so as to best approximate the system response to lamp intensity.

The fitted function is of the form:

$$E_{mode} = a \cdot V_R \tag{82}$$

where $E_{mode} \equiv$ Incident Irradiance, subscript *mode* is *Direct* or *Diffuse* and $V_R \equiv$ Average Response from DDSR-1B.

The fit is made using Matlab's 'polyfit' function which fits the data in a least-squares sense.

The results from the approximations are given numerically in Table 5D and graphically by the plots in FIGURE 5.37 for $\text{Mode}_{\text{Direct}}$.

The coefficient a in equation (82) for $\text{Mode}_{\text{Direct}}$ is found to be:

$$a = 2.757 \times 10^{3} Wm^{-2}/V. \tag{83}$$

Equations (71) and (83) suggest a disagreement of less than 5% between the calibrated and calculated system transfer factors.

Calibration in $\text{Mode}_{\text{Diffuse}}$ is a challenge. A preliminary test in the laboratory has been made to compare the outputs from $\text{Mode}_{\text{Diffuse}}$ against those from $\text{Mode}_{\text{Direct}}$. The voltage estimates from $\text{Mode}_{\text{Diffuse}}$ for two reference intensities are shown in Table 5D. The ratios of output voltage in $\text{Mode}_{\text{Diffuse}}$ to output voltage in $\text{Mode}_{\text{Direct}}$ for each intensity is:

$$\left.\frac{V_{out}(Diffuse)}{V_{out}(Direct)}\right|_{I_1} = \frac{137.38mV}{8.35mV} = 16.46 \tag{84}$$

$$\left.\frac{V_{out}(Diffuse)}{V_{out}(Direct)}\right|_{I_2} = \frac{183.38mV}{11.49mV} = 15.96 \tag{85}$$

However, the lamp filament is the object in this case. The image is smaller than the theoretical image and the "object-image" relations are irrelevant.

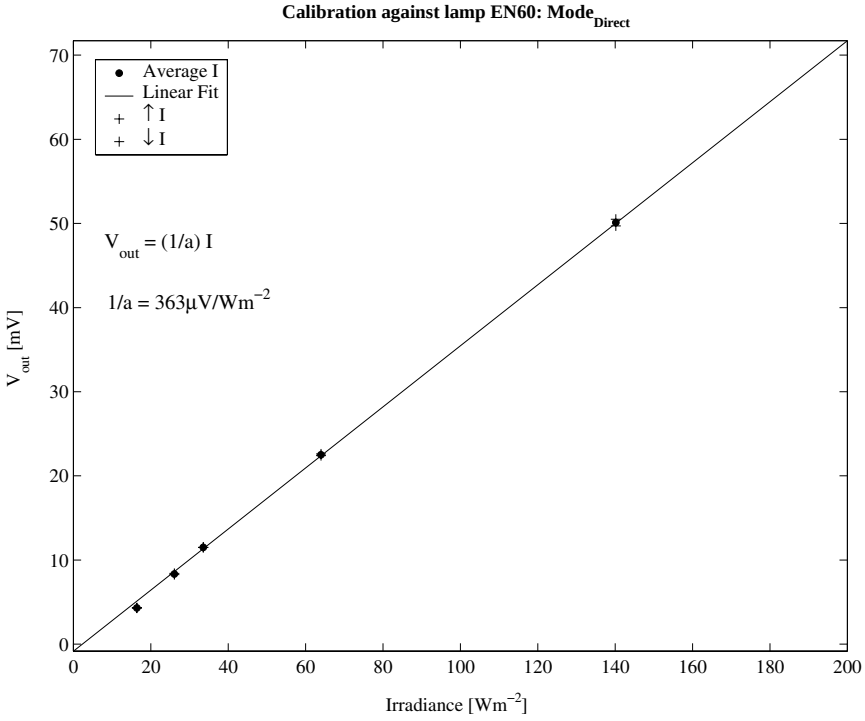

FIGURE 5.37
DDSR-1B voltage response in $Mode_{Direct}$ to lamp irradiance *I*.

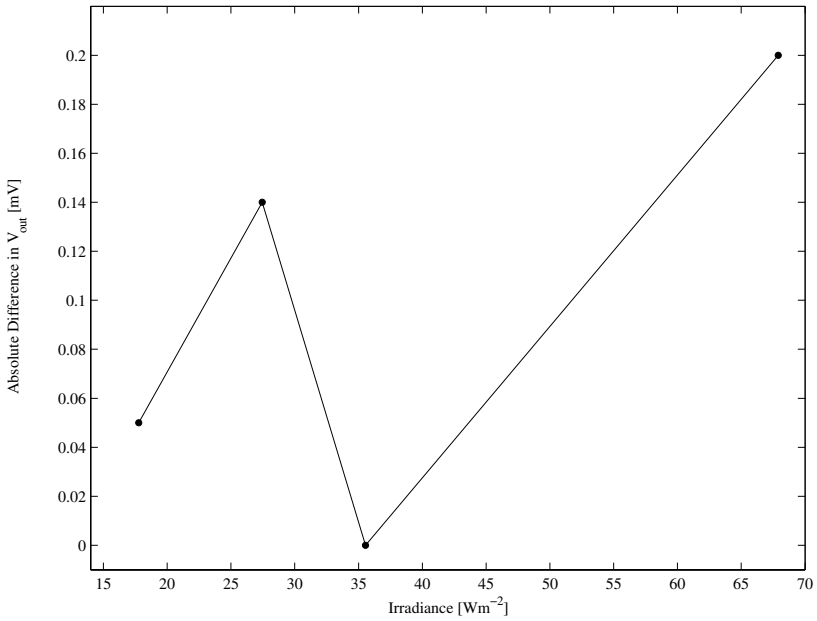

FIGURE 5.38
Measure of hysteresis in $Mode_{Direct}$.

5.7.2.2. Hysteresis

A hysteresis test, in absolute mode, can give a measure of the calibration uncertainty. The absolute difference in voltage output from the forward measured (increasing) and backward measured (decreasing) intensities for $\text{Mode}_{\text{Direct}}$ is shown in FIGURE 5.38. The maximum absolute difference is shown to be $0.2mV$. This implies, using equation (71), that the uncertainty in lamp irradiance measure for $\text{Mode}_{\text{Direct}}$ is:

$$\delta E_{S_{Direct}} = 0.52 Wm^{-2}. \tag{86}$$

5.7.2.3. Repeatabilty: Temperature Variation

Results from the voltage response to changes in ambient temperature (for a constant intensity reference) are shown graphically, for both modes, in the FIGURE 5.39. The maximum change in responsivity over the observed temperatures is below 1% in either mode.

Ideally, one should test the responsivity of the detector and pyro-interface (which is in the radiometer). Under field applications the control unit can be kept at a stable temperature within a room. In this test the radiometer is unavoidably in the same environment as the control unit.

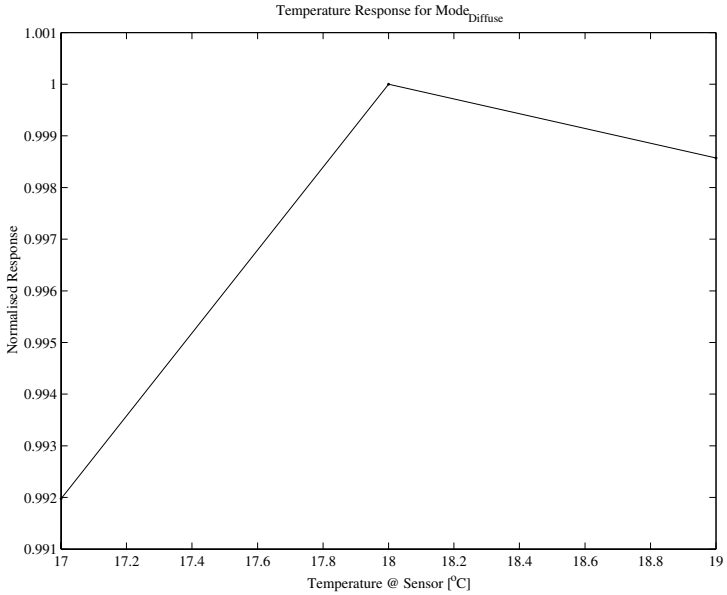

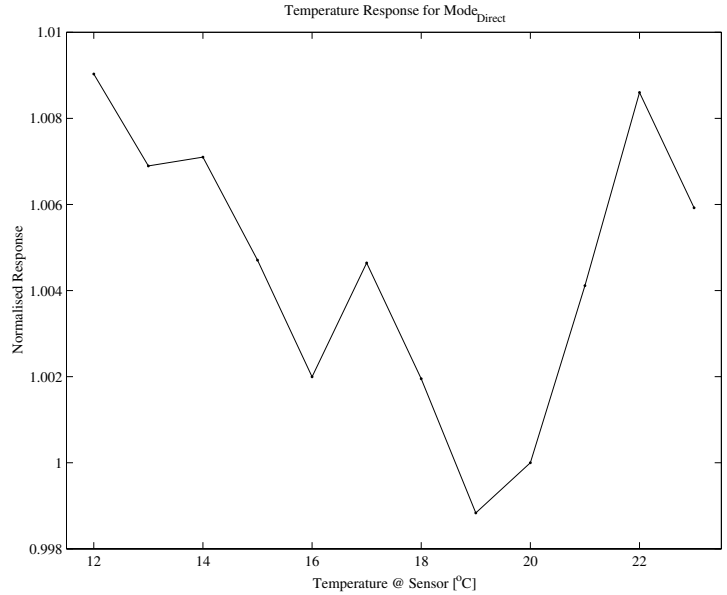

FIGURE 5.39
DDSR-1B response to temperature for $Mode_{Direct}$ and $Mode_{Diffuse}$. It is noted that the control unit is under the influence of the changes in ambient temperature during these measurements.

5.7.3. Absolute Calibration Uncertainties

The uncertainty in the observed irradiance is a cumulation of the following uncertainties:

- uncertainty in the reference radiance,
- uncertainty in the radiance transfer, and
- uncertainty in the measurement of signals.

5.7.3.1. Uncertainty in the Absolute Reference

The reference radiance E_R is given by equation (81). With reference to equation (81), the uncertainty of E_R (denoted by δE_R) is approximated by the manufacturer specified tolerance of the reference lamp δE_{Ro}, the uncertainty in the distance between the lamp and radiometer's aperture stop δE_{Rr}, and the uncertainty in regulation of constant current for the lamp δE_{RI}. Mathematically, the relative uncertainty is given by:

$$\frac{\delta E_R}{E_R} = \sqrt{\left(\frac{\delta E_{Ro}}{E_R}\right)^2 + \left(\frac{\delta E_{Rr}}{E_R}\right)^2 + \left(\frac{\delta E_{RI}}{E_R}\right)^2} \tag{87}$$

where:

$$\delta E_{Ro} = \frac{\partial E_R}{\partial E_o} \cdot \delta E_o \tag{88}$$

$$\delta E_{Rr} = \frac{\partial E_R}{\partial r} \cdot \delta r \tag{89}$$

A test lamp's irradiance transfer (to the NIST scale) uncertainty is about 0.22% at 350nm and 2.6% at 2400nm according to Walker et al. in [35., 1987]. The NIST spectral irradiance scale itself has an uncertainty of 1% in the visible and 3% in the infrared at 2400nm, from [35.]. It has been found that the EN-60 lamp has a total intensity uncertainty (integrated over the spectral range $350nm$ to $2400nm$) of:

$$\delta E_o = 11.92 Wm^{-2}. \tag{90}$$

Equations (81), (88) and (90) imply that:

$$\frac{\delta E_{Ro}}{E_R} < 4\% \tag{91}$$

The distances between the lamp and radiometer's aperture stop could be resolved with an uncertainty of:

$$\delta r = 3mm \tag{92}$$

Equations (81), (89) and (92) imply that:

$$\frac{\delta E_{Rr}}{E_R} < 2\% \tag{93}$$

The lamp power regulating system (see Section 5.7.1, "Calibration Procedure," on page 153) compensates for variations in the lamp current and maintains current stability to within

$$\delta I = 1mA. \tag{94}$$

According to Grandum in [6., 1997], the above mentioned uncertainty in lamp current results in a relative change in irradiance:

$$\frac{\delta E_{RI}}{E_R} < 0.1\%, \quad \lambda > 400nm \tag{95}$$

The equations (91), (93) and (95) imply, from (87), that the total relative uncertainty in the reference radiance is:

$$\frac{\delta E_R}{E_R} \cong 5\% \tag{96}$$

5.7.3.2. Uncertainty in Irradiance Transfer

An estimate of the uncertainty in radiance transfer from the reference lamp to the pyroelectric detector follows from the equation (56):

$$\frac{\delta E_i}{E_R} = \sqrt{\left(\frac{\delta E_{i\tau}}{E_R}\right)^2 + \left(\frac{\delta E_{iv}}{E_R}\right)^2 + \left(\frac{\delta E_{iE_R}}{E_R}\right)^2} \tag{97}$$

where:

* $\delta E_{i\tau}$ is the uncertainty contribution from the system transmission τ:

$$\delta E_{i\tau} = \frac{\partial E_i}{\partial \tau} \cdot \delta\tau \tag{98}$$

One may consider uncertainty in transmission as a combination of uncertainty in transmission:

- between the reference lamp and radiometer opening, and
- in the collimator sections of the radiometer.

The sapphire window of the pyroelectric detector has a transmission factor of 0.87 ± 0.01 over the required spectral range (see Section 5.4.1.2, "Detector Responsivity," on page 130). Together with transmission losses along the collimator it is feasible to approximate:

$$\delta\tau = 0.02 \tag{99}$$

The uncertainty in transmission relative to the reference irradiance is then, from equations (57), (98) and (99):

$$\frac{\delta E_{i\tau}}{E_R} = c \cdot \delta_\tau < 0.1\% \tag{100}$$

* δE_{iv} is the uncertainty contribution from the image distance v in $\text{Mode}_{\text{Diffuse}}$:

$$\delta E_{iv} = \frac{\partial E_i}{\partial v} \cdot \delta v \tag{101}$$

The uncertainty in the image distance is the same as the uncertainty in the focal length. The uncertainty in focal lengths is a combination of:

(1) tolerance in the focal lengths of the individual lenses. This is specified to be ±2%.

(2) focal shifts with temperature change. An extreme temperature change of 70°C would imply a focal shift of

about $0.04mm$. This is according to the focal shift versus temperature plots in FIGURE 5.7.

(3) seidal aberrations. The maximum shift in focal length is due to chromatic longitudinal chromatic aberration. This is shown to be less than $3mm$ (see "Aberrations" on page 125.).

The above three factors suggest a total uncertainty in image distance of:

$$\delta v \approx 3.06mm \tag{102}$$

The uncertainty contribution from v is then:

$$\frac{\delta E_{iv}}{E_R} = \left(\frac{2\tau D_i^2}{4v^3}\right) \cdot \delta v < 1\ \% \tag{103}$$

* δE_{iE_R} is the uncertainty contribution from the reference irradiance E_R itself:

$$\delta E_{iE_R} = \frac{\partial E_i}{\partial E_R} \cdot \delta E_R \tag{104}$$

It follows from equation (96) that the maximum absolute error in the reference is:

$$\delta E_R = 7.9 Wm^{-2} \tag{105}$$

The uncertainty contribution from the reference source is then:

$$\frac{\delta E_{iE_R}}{E_R} = \frac{c}{E_R} \cdot \delta E_R < 2\% \tag{106}$$

The equations (100), (103), and (106) imply, from equation (97), that the total uncertainty in radiance transfer relative to the reference radiance is:

$$\frac{\delta E_i}{E_R} \cong 2\% \tag{107}$$

5.7.3.3. Uncertainty in the Measurement of Signals

The uncertainties associated with a signal generation by the pyroelectric detector, signal conditioning by the pyro-interface, signal carry over a cable length of 20 meters, signal conditioning by the filter-interface, digitization by the 12-bit ADC, and associated electronics are sources for the uncertainty in measurement of a signal.

The uncertainty in measurement of a signal for $\text{Mode}_{\text{Direct}}$ is given in Section 5.7.2.2, “Hysteresis,” on page 159. The relative uncertainties in the measurement of the signals are:

$$\frac{\delta E_{S_{Direct}}}{E_R} < 3.2\% \tag{108}$$

5.7.3.4. Total Uncertainty in Absolute Calibration

The total uncertainty in calibration is taken as:

$$U = \sqrt{\left(\frac{\delta E_R}{E_R}\right)^2 + \left(\frac{\delta E_i}{E_R}\right)^2 + \left(\frac{\delta E_S}{E_R}\right)^2} \tag{109}$$

Substitution of equations (96), (107) and (108), or (108), into equation (109) gives:

$$U < 6.2\% \tag{110}$$

5.8. Field Calibration

DDSR-1B had been mounted on the Eppley ST-3 solar tracker for a trial calibration of the instrument with the sun as the source. The software used is the same as described in FIGURE 5.36. The trial was taken during the Norwegian winter, on the 2nd of December 2004, a period with subzero temperatures, day lengths of about 4 hours and solar altitudes below 5°.

5.8.1. $Mode_{Direct}$

The above conditions do not satisfy the calibration protocol given in section 3.3.1 on page 51. To avoid possible harm to the absolute cavity AHF31117 the Eppley NIP #21132E6 had been used as the reference for the trial calibration of $Mode_{Direct}$. With the of the automatic control 4 measurements were taken by the DDSR-1B every minute. These were averaged and converted to solar irradiance by the system transfer factor. These one-minute irradiances could then be compared with the corresponding irradiances from the NIP.

The ratio between the NIP and DDSR-1B direct solar irradiances was calculated and averaged. The result is a correction factor which is traced to the WRR:

$$C_{Direct} = 0.6854 \pm 0.0009 \quad (111)$$

The plots in FIGURE 5.40 give the NIP irradiances and the corrected $Mode_{Direct}$ irradiances. The deviations of the corrected irradiances from the NIP are less than 0.5%. This is well within the expected uncertainty given by equation (110).

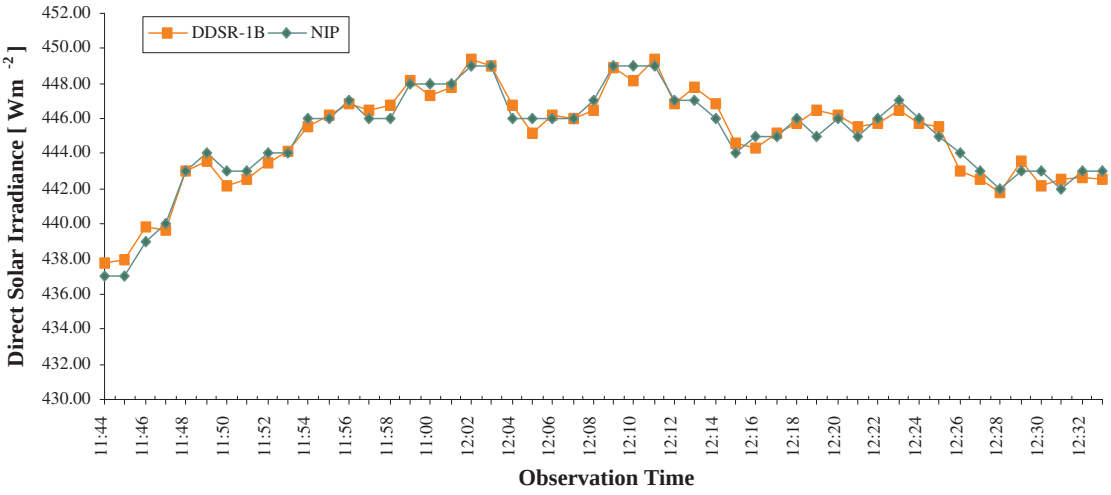

FIGURE 5.40
Results from a trial calibration of DDSR-1B, with the sun as the source. The irradiance points for the DDSR-1B includes the system transfer factor and correction to the WRR.

5.8.2. $Mode_{Diffuse}$

Field calibration of $Mode_{Diffuse}$ could not be performed due to an incomplete test on the scanning software for INTRA. The intention is to integrate measurements taken from sectors of the hemisphere for comparison with the global irradiances recorded by a pyranometer, during a day with a 'homogeneously' overcast sky. Still, the on-field response in $Mode_{Diffuse}$ could be observed by considering the relation between the signals in $Mode_{Diffuse}$ and $Mode_{Direct}$ (see section 5.3.4.2.2.2).

The radiometer had been fixed to view a fixed section in a cloudless sky by cutting power to the ST-3 tracker at a known time. The time is used to calculate the centre position of the observed sector. The central point of the observed sector is 187.5^{o} azimuth and 4.3^{o} altitude. The sun was at 190.4^{o} azimuth and 4.0^{o} altitude at the start of measurements. Measurements were taken continuously. The resulting voltage response versus the time of observation are given by the plots in FIGURE 5.41.

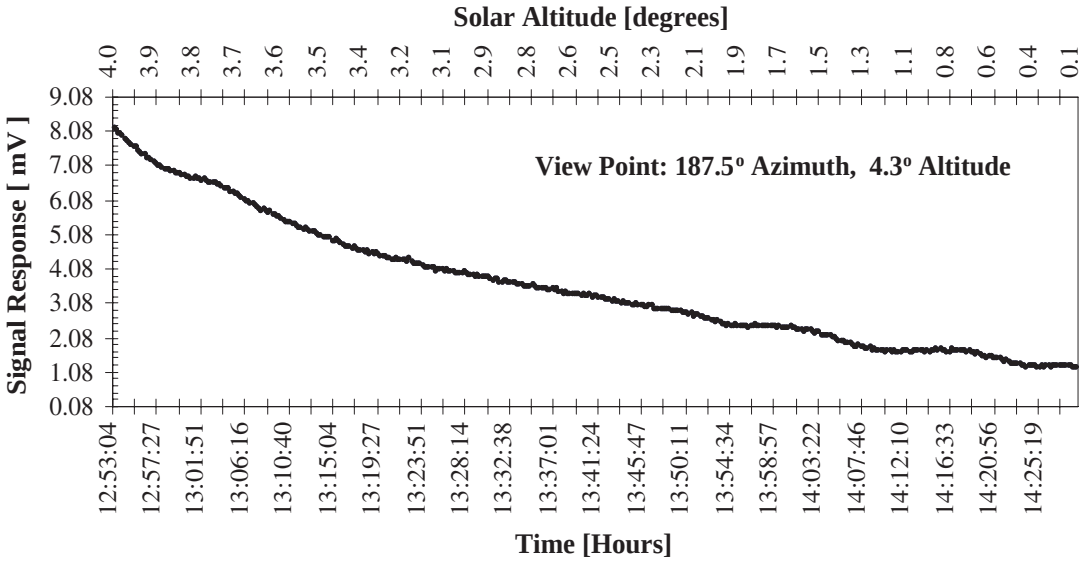

FIGURE 5.41
Measurements of sky irradiance at a point using $Mode_{Diffuse}$.

The point distribution in the FIGURE 5.41 gives an exponential related decay that can be related to the level of irradiance within the considered solid angle for increasing distances from the sun.

The measurement conditions as described on page 166 may be considered extreme. These factors imply that DDSR-1B, in $Mode_{Diffuse}$, is sufficiently sensitive for finding the angular distribution of diffuse solar radiation.

5.8.3. Discussion: Calibration

With the conventional source-based calibration method as discussed in Section 5.7.1, “Calibration Procedure,” on page 153, the irradiance calibration rely on the radiance of the reference lamp, the inverse square law, and accurate measurements of distance between the source and receiver. Alignment of the reference lamp is critical. The reproducibility of the lamp itself and the departure from the inverse-square law at short distances are major uncertainty components. These factors are a major contribution in the absolute calibration of DDSR-1B. Calibration against the lamp source also limits maximum and minimum attainable reference irradiances.

The next phase of calibration for $Mode_{Direct}$ is in the field with the sun as the source and AHF31117 as the absolute reference, at normal incidence to the sun. It should be possible to calibrate for $Mode_{Direct}$ with a reference relative uncertainty of less than 0.06%, according to the report [24., 2001] by PMOD/WRC.

Calibration for $Mode_{Diffuse}$ in the field is challenging. One option is to calibrate against a pyranometer on a homogeneously overcast sky by integrating the directional response of DDSR-1B for comparison with the reference pyranometer. A high quality pyranometer, however, has an hourly uncertainty (95% confidence level) of 3% or more according to the WMO in [36.]. Problems such as pyranometer zero offset need also to be addressed.

Measurement uncertainty is associated with temperature fluctuations and signal digitization. It is understood that greater resolution is achievable by a higher bit ADC.

The system's sensitivity to temperature may be attributed to interferences due to the piezoceramic nature of the pyroelectric detector. Moulson et al. in [18.] suggest that the interference can be compensated for by the provision of a duplicate of the detecting element that is protected from the radiation by reflecting electrodes or masking, but which is equally exposed to the mount surroundings. The duplicate is connected in series with the detector and with its polarity opposed so that the piezoelectric outputs cancel.

Further, the temperature associated with the incident flux is measured relative to the chopper surface. Instability in the surface temperature of the chopper and/or fluctuations in the ambient or background temperature would produce unwanted 'noise' signals, verified by Porter in [25., 1981]. Porter refers to the use of compensated detector configurations in order to overcome the problem. An example of a compensated pyroelectric detector configuration is given by Shie et al. in [31., 1989] and by Phelan et al. in [23., 1993]. A further example is given by Pradhan et al. in their report [26., 1982], on their Electrically Balanced Pyroelectric Radiometer (EBPR). The principle of operation in the EBPR is the matching of electrical power with radiation power by use of a triglycine sulfate (TGS) pyroelectric detector. The front electrode of the detector is used as a radiation absorption film and as an electric heater for producing heating

pulses. The electrical heating signal is provided by the chopper reference signal which is first phase regulated and then passed through the front electrode of the detector. Pulses due to the radiation and electrical heating are balanced by a null detection method in a lock-in amplifier. The principle of operation of an electrically calibrated pyroelectric null radiometer is outlined by the National Bureau of Standards in [38., 1978].

In practice, a pyroelectric detector's transfer function is the result of a composite process of integration and differentiation involving solutions to equations for heat flow, pyroelectric and charge flow. Sources of error are therefore multi-fold. Phelan et al., in [23.], show that non-uniformity of the detector responsivity across the receiving aperture is a great source of error. Phelan et al. suggest that two causes of this error are variations in the reflectance off the front face and variations in the thickness of the pyroelectric material. It is therefore critical to minimise spatial variance of the image over the detector. The main cause of the spatial variance in the DDSR-1B system would be aberrations due to the focusing and defocusing lenses and reflections within the detector housing. The detector is housed in a silver T0-5 can. Additionally, the active area is uncoated. It has been found that several designs of electrically calibrated detectors involve a gold-black deposit onto the absorbing face of the detector to achieve higher absorptance over a broad spectral range. A few citations for the latter are [13., 1999], [23., 1993], [26., 1982], and [31., 1989].

5.9. On Field Operation

The quantities to be measured by DDSR-1B, with solar radiation as the source, are direct, circumsolar and sky diffuse irradiances. Software has been developed for integration of DDSR-1B with BRUSAG's INTRA (acronym for INTelligent solar TRAcker) for acquisition of the above quantities.

INTRA is an 'embedded' solar tracking unit for autonomous operation and can be controlled remotely to scan the sky. Details of the integration development software are given by the flowcharts in FIGURE 5.41 to FIGURE 5.45.

5.9.1. Developed Software for on Field Operation

The main virtual instrument (vi) is *DDSR-1B_Main.vi* (see flowchart in FIGURE 5.43). The preliminary process in *DDSR-1B_Main.vi* is to define the:

* site parameters,
* computer serial communication port allocation for INTRA,
* file paths for storage of the acquired data, and
* total number of scans.

For each scan number, *DDSR-1B_main.vi* executes sub-vis *Direct.vi*, *Circumsolar.vi* and *SkyScan.vi*. The sequence of events is thus:

i. The position of the sun is calculated in sub-vi *Direct.vi* (see program flowchart in FIGURE 5.46). Sub-VI *MoveMeasureWrite.vi* (see flowchart in FIGURE 5.44) is called to set the radiometer for $Mode_{Direct}$:
   * The 'lens' post is moved to the optic axis,
   * INTRA is instructed to align the radiometer to the sun using the calculated sun coordinate,
   * *Measure.vi* (see FIGURE 5.45) is executed to get an estimated voltage reading from the direct radiation, and

* Data is written to file.

ii. Sub-VI *Circumsolar.vi* is called (see FIGURE 5.47). The position of the sun is calculated. Circumsolar coordinates at $\pm(5^o, 10^o, 15^o)$ from the sun position in both azimuth and zenith are calculated. In total, 12 circumsolar coordinates are stored. Sub-VI *MoveMeasureWrite.vi* is called:

* The 'lens' post is moved to the optic axis,
* INTRA is sent to one of the 12 circumsolar coordinates,
* *Measure.vi* is gets an estimated voltage reading,
* Data is written to file,
* The latter 3 steps are repeated for each of the remaining 11 circumsolar coordinates.

iii. Sub-VI *SkyScan.vi* is called (see FIGURE 5.48). The position of the sun is calculated. An array of sky points is generated using Labview's random number generator. The generation is divided into 3 parts so as to have a uniformly distributed scan in 3 hemisphere bands with 4 sectors in the top band, 10 sectors in the middle band and 12 sectors in the bottom band (see FIGURE 5.42).

The bands are:

- Top band with $\text{zenith} \leq 30^o$,
- Middle band with $30^o < \text{zenith} \leq 60^o$, and
- Bottom band with $60^o < \text{zenith} \leq 90^o$.

Scan points in the above array that are within 15^o off the sun's position are removed so as to prevent focusing of a direct-sun or circumsolar beam onto the detector (as a precautionary measure). The remainder of the 26 scan points are sorted to optimise INTRA's speed to points. Sub-VI *MoveMeasureWrite.vi* is called:

* The 'open' post is moved to the optic axis,
* INTRA is sent to one of the scan points,

* Measure.vi is executed to get an estimated voltage reading,
* Data is written to file,
* The latter 3 steps are repeated for each of the scan points.

Top Band: **Sectors 1 to 4**
***Middle Band*: Sectors 5 to 14**
***Bottom Band*: Sectors 15 to 26**

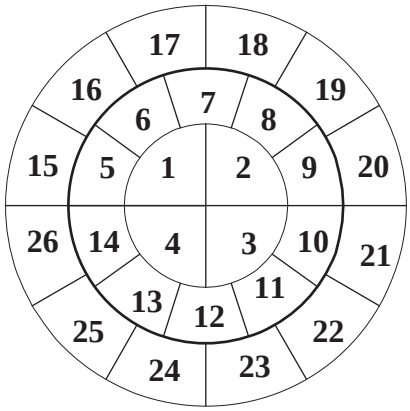

FIGURE 5.42
A top view of the sky dome showing its division into 3 bands with a total of 26 sectors.

5.9.2. Description of Data

A complete measurement cycle consists of a single direct sun irradiance measure, 12 solid angle views for circumsolar measurements (evenly distributed in steps of 5degrees for azimuth and zenith about the sun) and a maximum of 26 solid angle views that are uniformly distributed about the hemisphere for angular diffuse measurements.

A complete measurement cycle is expected to take about 10 minutes with optimised software for INTRA and DDSR-1B. This run time should reduce temporal effects of cloud cover, pollution build-up, tropospheric temperature changes, etc. on the angular distribution of sky radiance. The acquired data for the uniform pseudo-random distribution of angular diffuse views and the direct and circumsolar views give the possibility to develop atmospheric irradiance models based on the raw data sets.

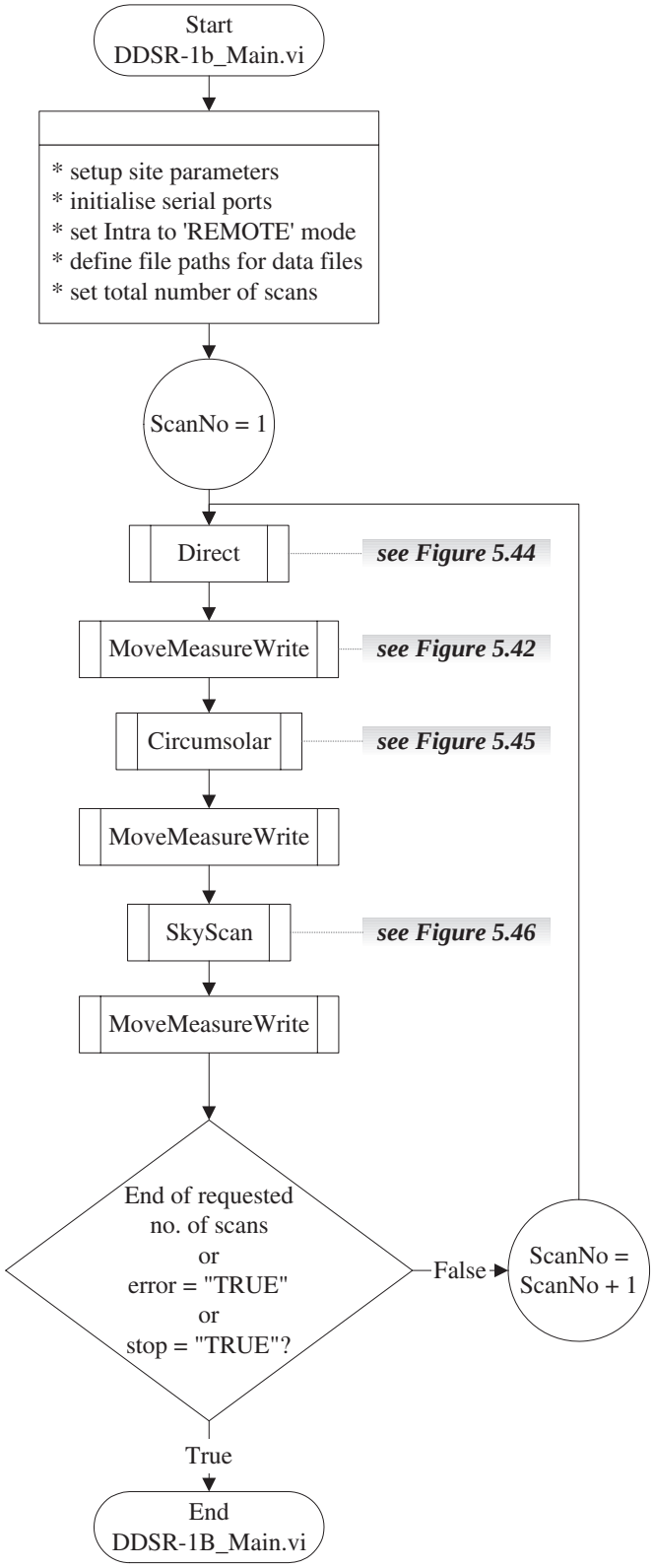

FIGURE 5.43
Flowchart description the main program for control of DDSR-1B during routine operation.

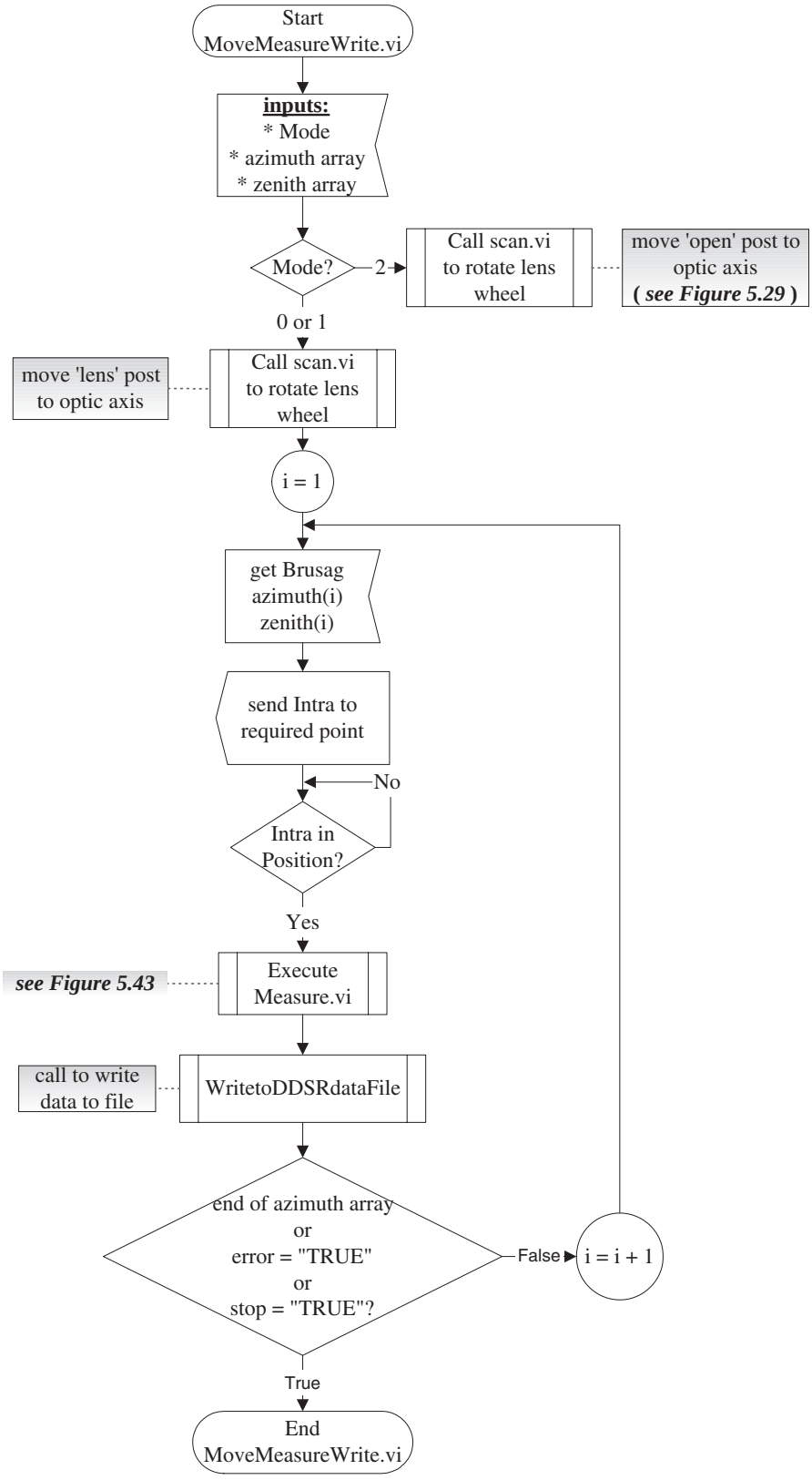

FIGURE 5.44
Flowchart describing structure of sub-vi *MoveMeasureWrite*.

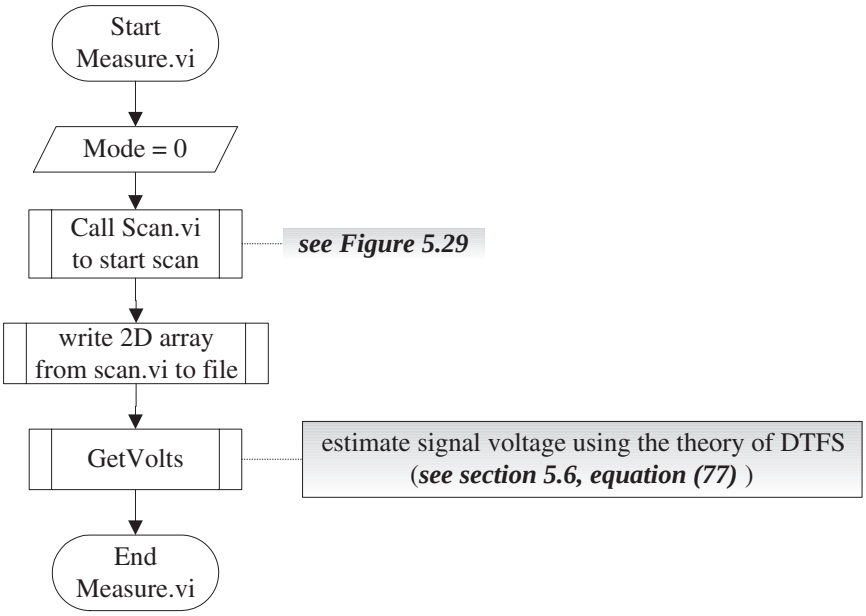

FIGURE 5.45
Flowchart describing structure of sub-vi *Measure*

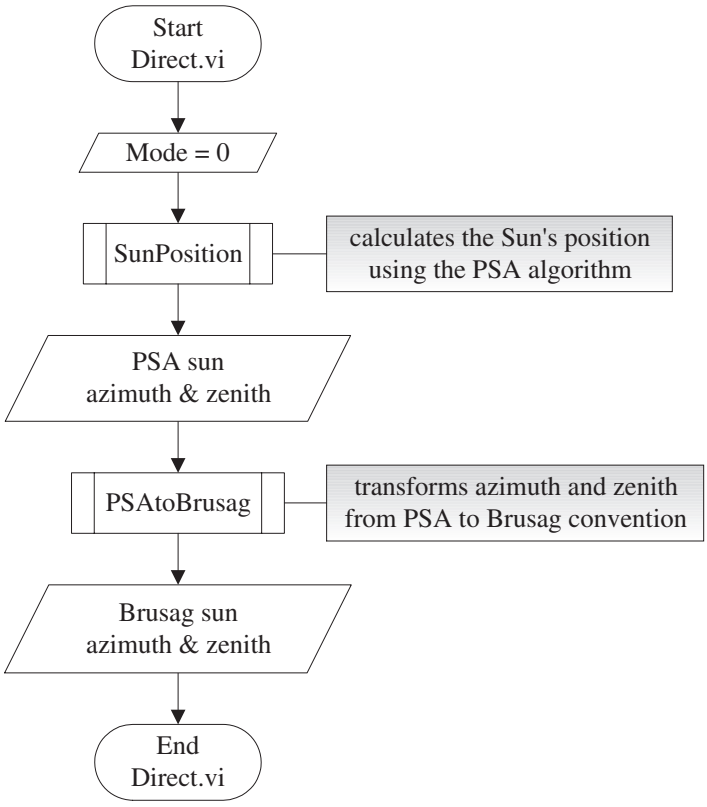

FIGURE 5.46
Flowchart describing structure of sub-vi *Direct*.

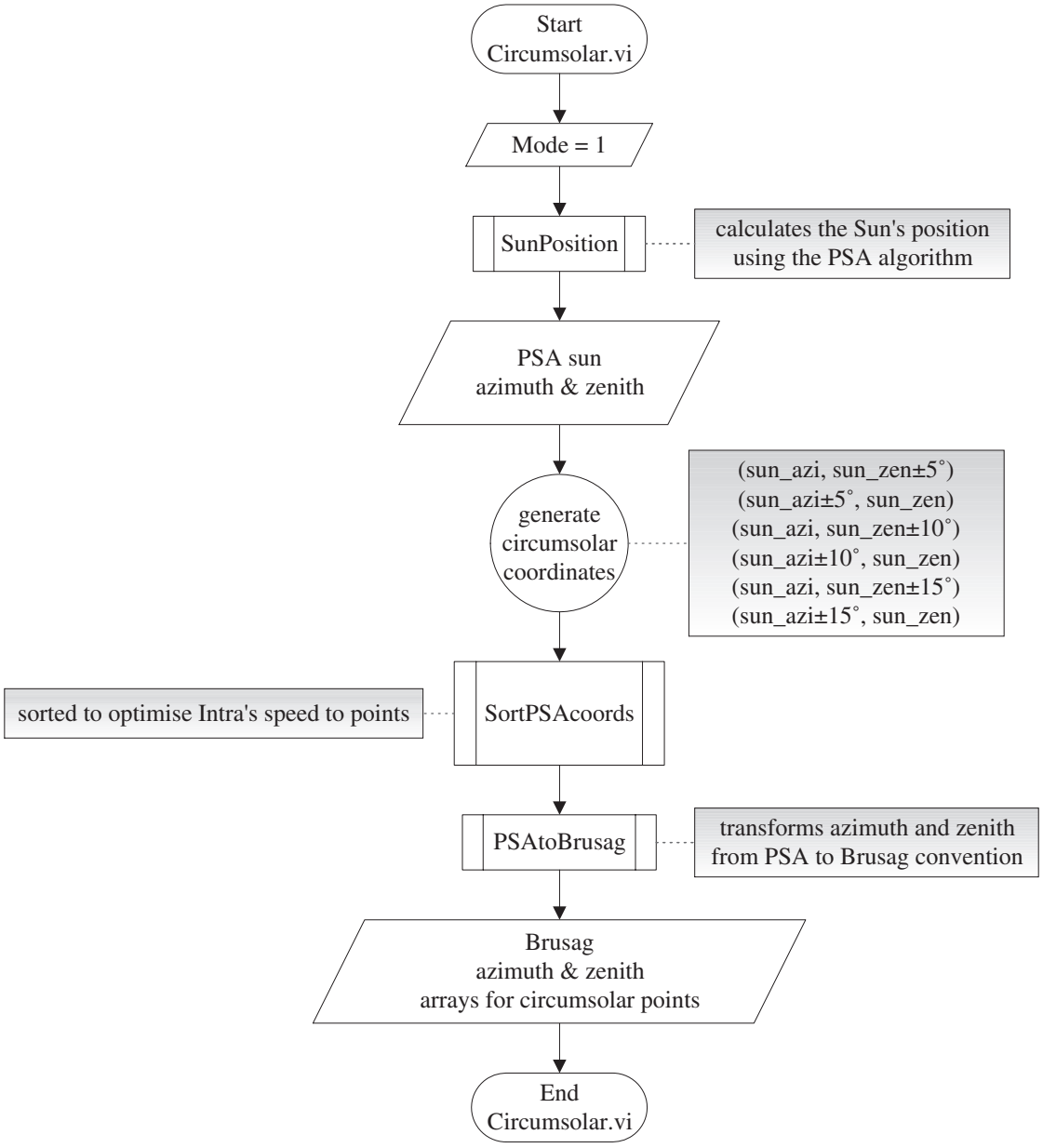

FIGURE 5.47
Flowchart describing structure of sub-vi *Circumsolar*.

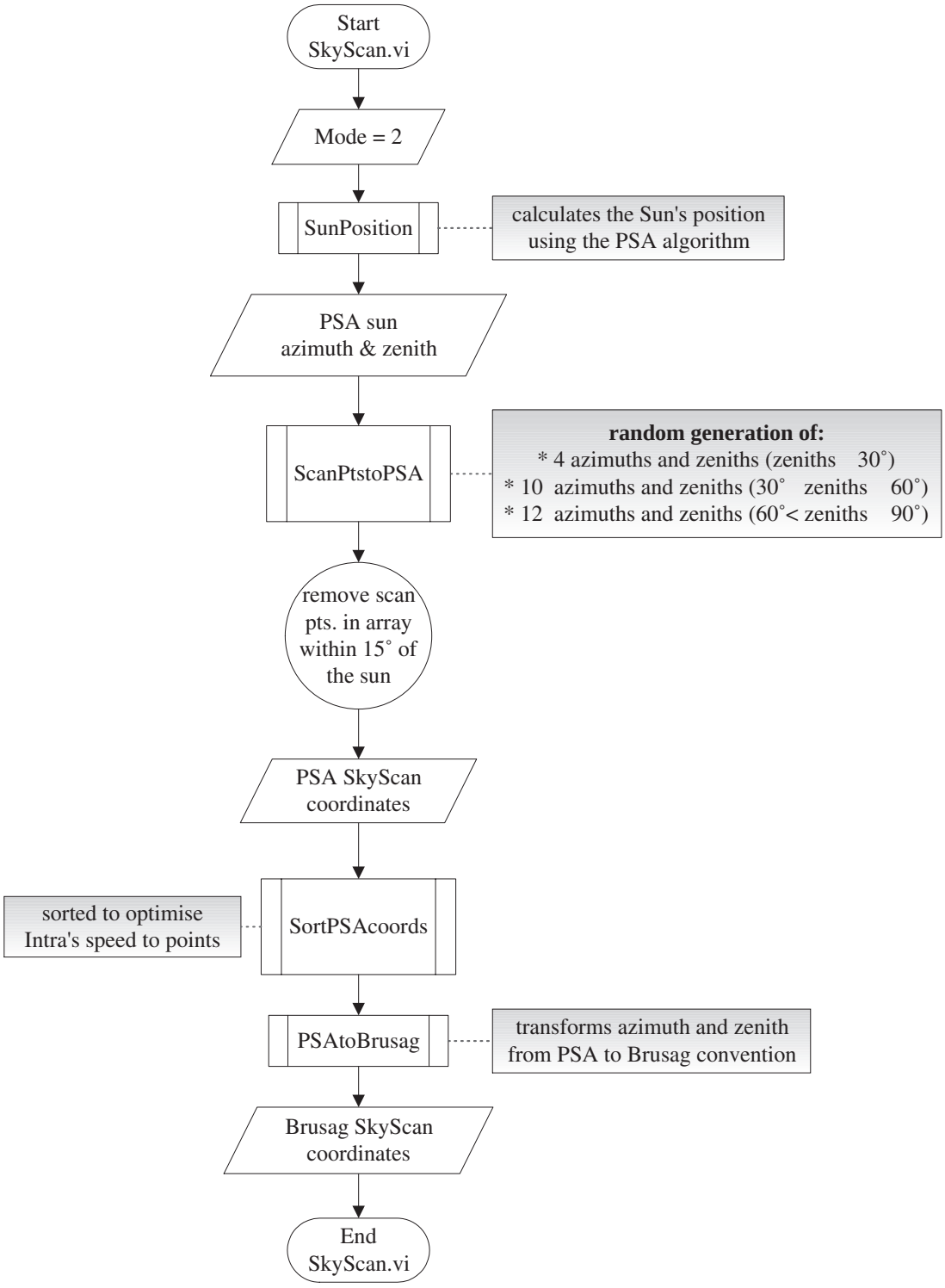

FIGURE 5.48
Flowchart describing structure of sub-vi *SkyScan*.

5.10. Chapter Summary and Conclusions

This chapter has described the design, trial calibrations and intended operation of the dual mode radiometer, the DDSR-1B. Typical sky scan radiometers must omit direct solar irradiance measurements so as to avoid a dynamic irradiance range. For instance, the Molectron PR200 pyroelectric radiometer as cited in [28., 1989] uses a shadow ball to shade off the aperture from direct beam solar radiation. Instead, the direct normal solar irradiance is taken with a supplementary pyrheliometer. The DDSR-1B works around the issue by its mode duality.

The main challenge in development of the instrument has been the dynamic irradiance range associated with measuring both direct and diffuse solar irradiances. It has been shown that the challenge is overcome by the use of a fixed and a deployable collector lens pair in combination with a sensitive transducer. In $\text{Mode}_{\text{Diffuse}}$ the fixed focussing lens condenses the weak incident flux onto the transducer. In $\text{Mode}_{\text{Direct}}$ the deployed defocusing lens in combination with the fixed lens spreads the intense flux over the transducer to decrease the signal level. Implementation of the imaging system does generate an uncertainty related to a change in system focus. It has been shown that this contribution is less than 1%.

There is no absolute reference for the calibration of global and diffuse solar irradiance measurements. It has been shown that direct solar irradiance measurements in $\text{Mode}_{\text{Direct}}$ gives a way to calibrate for sky radiance measurements in $\text{Mode}_{\text{Diffuse}}$. The direct measurements can be traced to the WRR. With the linear correlation in image irradiance between the two modes, sky irradiances may also be linked to the WRR.

The intention of the design of the electrical network coupled to the pyroelectric detector and the flux modulator was to suppress the influence of interference and noise voltages on the measurement voltage. It has been shown that movement of the bandwidth of information of the signal to the $5Hz$ region by the mechanical chopper, exclusion of signals with frequencies outside the frequency response of the second order Sallen-Key bandpass filter, and post-processing of the signal in the frequency domain allows for the extraction of weak signals that are embedded in noise. Post-processing by the cross-correlation process of equation (77) extracts the wanted signal thereby giving a higher signal to noise ratio.

It is noted that a significant source of uncertainty is related to the pyroelectric detector and digitization by the 12-bit ADC. The contribution can be reduced by a higher resolution ADC. The detector is sensitive to temperature fluctuations. The normalised responses to a narrow temperature range given by the plots in FIGURE 5.39 can be up to 1%. An alternative would be to use a temperature compensated pyroelectric detector.

Overall, it can be concluded that the DDSR-1B can be used for the measurements of direct solar irradiance. In addition, the instrument will be amongst the very few sky radiometers used for mapping the much needed angular distribution of shortwave sky radiances.

5.11. References

1. Beyon J.Y., *Labview Programming, Data Acquisition and Analysis*, Prentice Hall, 2001.
2. Chirtoc M., Candea R.M., Mercea V., *Operation Theory of Pyroelectric Detectors 1. A New Physical Model and the Resulting Operation Modes*, Ferroelectrics, Vol. 56, pp. 283-291, 1984.
3. Elizarov A.S. et al., *Compact Pyroelectric Detector*, UDC 621.317.78:537.227, 1985
4. Faulhaber R., *Suppression of the Third Harmonic Frequency of Radiation Modulated by a Chopper Wheel*, Infrared Physics, Vol. 17, pp.315-317, 1977.
5. Fraden J., *Handbook of Modern Sensors: Physics, Designs and Applications*, 2nd ed., Springer-Verlag New York, 1996.
6. Grandum O., *Et Automatisk Målesystem for Kartlegging av Vinkel- og Spektralfordeling av Direkte og Diffus Solstråling*, Dr. scient avhandling, FIM, NTNU, February 1997.
7. Hamamatsu, *personal communication with Björn Eriksson*, HAMAMATSU PHOTONICS NORDEN AB, Nov. 2003.
8. Hamamatsu, *Characteristics and Use of Infrared Detectors*, Technical Information SD-12, Hamamatsu Photonics K.K., Solid State Division, Cat. No. KIRD9001E03, Nov. 2004
9. Harrison A.W., Coombes C.A., Angular Distribution of Clear Sky Short Wavelength Radiance, Solar Energy, Vol. 40, No. 1, pp. 57-63, 1988.
10. Haykin S., Van Veen B., *Signals and Systems*, John Wiley and Sons, 2003.
11. Keyes R.J., *Topics in Applied Physics*, vol.19, Springer-Verlag Germany, 1980
12. Layertec GmbH, *Sapphire Window Transmission Data by Personal Communication with Alexander Ancsin*, 2003.
13. Lehman J., Eppeldauer G., Aust J.A., Racz M., *Domain-Engineered Pyroelectric Radiometer*, Applied Optics, Vol. 38, No. 34, Dec. 1999.
14. Linos Photonics, *The Catalog*, GE5, Germany, BE BA 120/1099.

15. Lucat C., Menil F., Von Der Mühll R., Thick-Film Densification for Pyroelectric Sensors, Meas. Sci. Technol. 8, pp. 38–41, 1997.
16. Løvseth J., Grandum O., *An Automatic Scanning Spectroradiometer*, North Sun '92, Conference Proceedings, SINTEF, Trondheim, pp. 427-432, 1992.
17. Melles Griot, *The Practical Application Light*, 1999
18. Moulson A.J., Herbert J.M., *Electroceramics: Materials, Properties, Applications*, John Wiley and Sons Ltd, England, 2nd ed., 2003
19. Newland, D.E., *An Introduction to Random Vibrations, Spectral and Wavelet Analysis*, 3rd ed., Pearson Education Ltd., 1993.
20. Noecker M.C., Phillips J.D., *Guoy and Curvature Phase Errors in POINTS Michelson Gauges: Requirements on the Fibre-Objective Assembly*, Centre for Astrophysics, Harvard College Observatory, TM94-06, 1994.
21. Optronic Laboratories, Inc., *OL FEL High-Accuracy Irradiance Standard*, Bulletin 53, Ref.3/02.
22. Pedrotti F.L, Pedrotti L.S., *Introduction to Optics*, Prentice Hall, 1996.
23. Phelan R.J., Lehman J.H., Larson D.R., *Electrically Calibrated Pyroelectric Detector - Refinements for improved Optical Power Measurements*, SPIE, Vol. 2022, Photodetectors and Power Meters, 1993.
24. PMOD/WRC, *International Pyrheliometer Comparison IPC-IX Results and Symposium,* Working Report No. 197, MeteoSwiss, May 2001.
25. Porter S.G., *A Brief Guide to Pyroelectric Detectors*, Ferroelectrics, 33, 193-206, 1981.
26. Pradhan M.M., Garg R.K., Bhide V.G., *Electrically Balanced Pyroelectric Radiometer*, Infrared Physics, Vol. 22, pp. 113-116, 1982.
27. Rosen M.A., *Investigation of the Validity of the TDRC Model for the Distribution of Diffuse Sky Radiance*, Solar Energy, Vol. 48, No. 2, pp. 123-131, 1992.
28. Rosen M.A., Hooper F.C., Brunber A.P., *The Characterization and Modelling of the Diffuse Radiance Distribution Under Partly Cloudy Skies*, Solar Energy, Vol. 43, No. 5, pp. 281-290, 1989.
29. Scitec Instruments Ltd, *Pyro-Electric Detector P2613*.
30. SGS-Thomson Microelectronics, *Wide Bandwidth Single J-FET Operational Amplifiers*, November 1995
31. Shie J-S., Hong J-C, Yu G-H., *Design Electrically Calibrated Pyroelectric Radiometer*, Journal of the Chinese Institute of Engineers, Vol. 12, No. 2, pp. 239-247, 1989.
32. Tadmor E.B., *Polarization Switching in PbTiO3: an **Ab Initio** Finite Element Simulation*, Acta Materialia, 50, 2989-3002, 2002.
33. Thorseth T.M., *Solar Ultraviolet Irradiance Measurements, Instrumentation, Intercomparisons and Interpretations*, Dr. Scientiarum Thesis, NTNU, Trondheim, 2000.
34. Valasek J., *The Early History of Ferroelectricity*. Ferroelectrics, 2:239-244, 1971
35. Walker J.H., Saunders R.D., Jackson J.K., McSparron D.A., *NBS Measurement Services: Spectral Irradiance Calibrations*, SP250-20, U.S. Government Printing Office, Washington, DC 20402-9325, 1987.

36. WMO-No.8, *Guide to Meteological Instruments and Methods of Obseravtion*, Secretariat of the World Meteor. Org., Geneva, Switzerland, 1997.
37. Yakushenkova T.I., *Design of Mirror and Mirror-Lens Systems*, Institute of Engineers of Geodesy, Aerial Photography, and Cartography, Moscow, Part 1, 1972.
38. Zalewski E., *A Modern Approach to Accurate Radiometry, National Bureau Of Standards*, Washington, DC 20234, 1978.
39. Zang Q., Whatmore R.W., *Sol–gel PZT and Mn-doped PZT Thin Films for Pyroelectric Applications*, J. Phys. D: Appl. Phys. 34, pp. 2296–2301, 2001.

Part B: Data Modelling

Generating synthetic radiation values is often the only practical way to obtain radiation data... This is so because measured sequences of radiation values are available only for a small number of locations in each country or region.

Aguiar and Collares-Pereira

Chapter 6

Meteonorm and SSE

*This chapter compares ground observations of direct normal solar irradiance to corresponding site data sets that are generated by two software programs. The two software programs are the NASA **S**urface meteorology and **S**olar **E**nergy (SSE) and Meteonorm. The ground reference observations are by courtesy of the World Radiation Data Centre.*

6.1. Introduction

Ground-based solar irradiances vary spatially. There are many reasons for the spatial variations. The distribution of land and sea, land topography, variation of insolation as a function of latitude, and time create different climatic zones. Predominant cloud cover and cloud types may be different from one region to another, atmospheric aerosols may differ, and there may be large differences in albedo. A region's climate and/or climate changes can only be inferred from extended observations, yet long term data records are not available in most places. Ground measurement stations are scattered throughout the world, but are not sufficient to represent all regions given the vast differences in climate.

Physical models of surface solar irradiance, based on radiative transfer theory, have the potential to produce reliable results once all the requisite input parameters are available. The input parameters are generated from a region's climate. Long term data on a global scale are necessary to determine parameters and calibrate the models. Another option is the synthesis of net data. For instance, observed data from neighbouring locations can be interpolated or inferred from cloud cover or satellite data. Also this approach requires knowledge of the local climate variability to estimate the reliability of the interpolation procedure.

Researchers such as Laszlo et al. in [10., 1991], have used global satellite datasets for the synthesis of horizontal surface insolation values. Global estimates of ground based diffuse horizontal and direct normal solar irradiances can be calculated with the knowledge of the horizontal surface insolations. Programs such as Meteonorm and the NASA Surface meteorology and Solar Energy (SSE) compute components of solar

irradiances at any ground site based on satellite data such as broadband clear and cloudy top of the atmosphere albedos and columnar amounts of water vapour.

This work compares the direct solar irradiances derived by Meteonorm and SSE to references of true ground observations for selected sites in an attempt to assess the utilizabilty of the derived data. The reference data are by courtesy of the World Radiation Data Centre (WRDC). The following sections gives a review of the SSE, Meteonorm and the WRDC, proceeded by a presentation of the results and discussions of the comparisons.

6.2. SSE

The NASA Surface meteorology and Solar Energy (SSE) resource is a convenient calculator for solar data applications as it is freely available through the world wide web by courtesy of the NASA Langley Atmospheric Sciences Data Center (see [15., 2005]). A review of SSE's methodology is given by Witlock et al. in [16., 2004]. SSE implements the extended Page method [4., 1964] to calculate the monthly direct normal solar radiation component. The approach is to take the difference between the monthly horizontal values of total and diffuse radiation (see equation (13) and below). The monthly diffuse radiation is calculated by the extended Page method and the monthly horizontal insolation is SSE's release 5 set of basis data. These basis data, which corresponds to a 1^o x 1^o latitude/longitude resolved grid over the globe, are compiled from a reference set of synthesised data for cells. The data for the reference cells are synthesised using the model by Laszlo et al., described in [10., 1991]. Laszlo et al. estimates the downwelling surface solar irradiance by relating the broadband transmissivity[1] to the broadband top of the atmosphere reflectivity[2] according to a radiative transfer algorithm. Inputs to the algorithm are the total cloud amount data from the International Satellite Cloud Climatology Project (ISCCP) for the period July 1983 through June 1993 (see [13.]), water vapor from the NASA Data Assimilation Office's

1. **Broadband transmissivity** is the ratio of the irradiance at the surface to that at the top of the atmosphere.
2. **Broadband top of the atmosphere reflectivity** is the ratio of the reflected flux at the top of the atmosphere to the top of the atmosphere irradiance.

Version 1 Goddard Earth Observation System (GEOS-1) (see [9.]) and ozone from the Total Ozone Mapping Spectrometer (see [3.]).

SSE's monthly diffuse component H_d of the direct normal irradiance is estimated by the Extended Page Method as:

$$H_d = (a + bk)H \tag{112}$$

where a and b for a particular cell[1] are determined by linear regression with 12 months of data from a group of reference sites. H is the monthly horizontal insolation and k the clearness index. There is a total of 12960 cells whilst the reference group consists of 74 sites in 12 climate regions. The reference sites are indicated by the blue/(blue with yellow) dots on the globe map in FIGURE 6.1. The distribution of dots are visibly biased and the climates at these sites may not be representative for all the cells. The coefficients a and b are approximate, and are confirmed in [16., 2004]. The lack of detailed input data would account for significant inaccuracies in the estimated direct normal irradiances. South Africa, for instance, has at least 9 distinct climate regions whilst only 3 sites/climates are represented by the reference group. SSE used observed data from 23 ground sites for a statistical comparison of the Extended Page Method. The sites are indicated by the yellow/(blue with yellow) dots on the globe map in FIGURE 6.1. The ratio of Page to ground site direct normal irradiance (each in kWh/m^2/day) is about 2 for a single data point from Burlington in 1999. Witlock et al. in [16.] reports a root mean square error of 24% with a 1.7% bias for 276 data points.

Comparisons between a selection of WRDC reference observations and corresponding SSE direct normal estimates are given in section 6.5. The choice of reference sites is shown by the red/yellow dots on the globe map in FIGURE 6.1.

1. A data cell is a 2^o x 2.5^o latitude/longitude section over the globe.

6.3. Meteonorm

A review of Meteonorm's software and theoretical background is given by Remund et al. in [11., 2003]. Meteonorm is a commercial computer program for climate calculations. Its basis data for the globe is a coupling of databases such as the Swiss database and the Global Energy Balance Archive. In total, Meteonorm's database consists of global radiation data from 1000 ground stations. The worldwide distribution of the stations is given in Table 6A. Meteonorm's version 5.0 include satellite data for radiation interpolation in remote areas in addition to data from ground sites, like with SSE. The final set of basis data is based on 10-year measurement periods (mainly from 1981 to 1990).

Table 6A: World-wide distribution of the ground stations contributing to Meteonorm's basis of mean global radiation data.

Location	*Number of Stations*
Europe	335
North America	277
Asia (with Russia)	150
Africa	123
South/Central America	76
Australia/Pacific	39
World	***1000***

This work uses Meteonorm as a tool to get estimates of monthly average direct normal solar radiation at arbitrary sites on the earth's surface. Meteonorm resolves generated mean hourly global horizontal radiation data stocastically into diffuse and direct normal components using the model by Perez et al. (see [6., 1991]). The components are then transformed into monthly average data. Meteonorm's generation of hourly global insolation at any desired location is by look-up to a set of 9x10x10 Markov transition matrices based on the methodology by Aguiar et al. (see [1., 1988]). The Perez et al. model was derived for a few selected climatic regions in Europe and America. Meteonorm's transition matrices were calculated using stations from the USA, Europe, North Africa and Saudi Arabia with the intention to cover 31 major climatic zones. A total of 121 stations were used to set up the transition matrices. Meteonorm used 14 stations distributed between Europe and North America, indicated by the green points on FIGURE 6.1, in testing the calculations of the average diffuse and direct radiation. These stations represent just 4 out of Meteonorm's set of

31 climatic zones. The test results are given in by Remund et al. in [11., 2003]. On average, the monthly values of diffuse radiation are overestimated by 4 W/m^2 (6%). The root mean square error of the monthly values is 11 W/m^2 (15%). Remund et al. also report that the error distribution shows a distinct yearly pattern. Larger root mean square errors are registered in winter. According to Remund in [12., 2005] the January average for diffuse radiation for Sydney is overestimated by 19% for the period 1985-1994. In July it is overestimated by 25%. Remund claims that errors seem to be bigger in dry areas.

Comparisons between the selected WRDC reference observations and corresponding Meteonorm direct normal estimates are given in section 6.5.

6.4. WRDC

The World Radiation Data Centre (WRDC) at the Voeikov Main Geophysical Observatory in St. Petersburg, Russia, quality-controls, processes and archives observational data that are received from over 500 ground stations in over 30 countries of the world. The processed data are published periodically in bulletins of the “Solar Radiation and Radiation Balance. The World Network”. The WRDC adheres to a strict protocol with regards to data handling. A description of the protocol is given in each bulletin, for example [14.]. The WRDC also publishes data through the internet. The web site’s URL is given in [17.]. The WRDC’s internet publication provides a convenient source for site observations of monthly mean horizontal beam solar irradiance for this work. Monthly mean horizontal beam irradiance are taken from a total 21 stations, distributed about the globe. The distribution of the stations are shown by the red dots on the world map in FIGURE 6.1. The required direct normal component is got by dividing the respective horizontal beam components by a localised month estimate of the cosine of the solar zenith angle. The basis data in both SSE and Meteonorm are prior to the year 1995 whilst the data from the WRDC are for the years 2000 to 2002. This period is taken with deliberation. The point being to assess temporal variations in the monthly means, if any, between the generated estimates from each program and the true observations. The choice of locations is also deliberate. The point being to assess spatial variations, if any, between the generated monthly mean estimates from each program and the true observations.

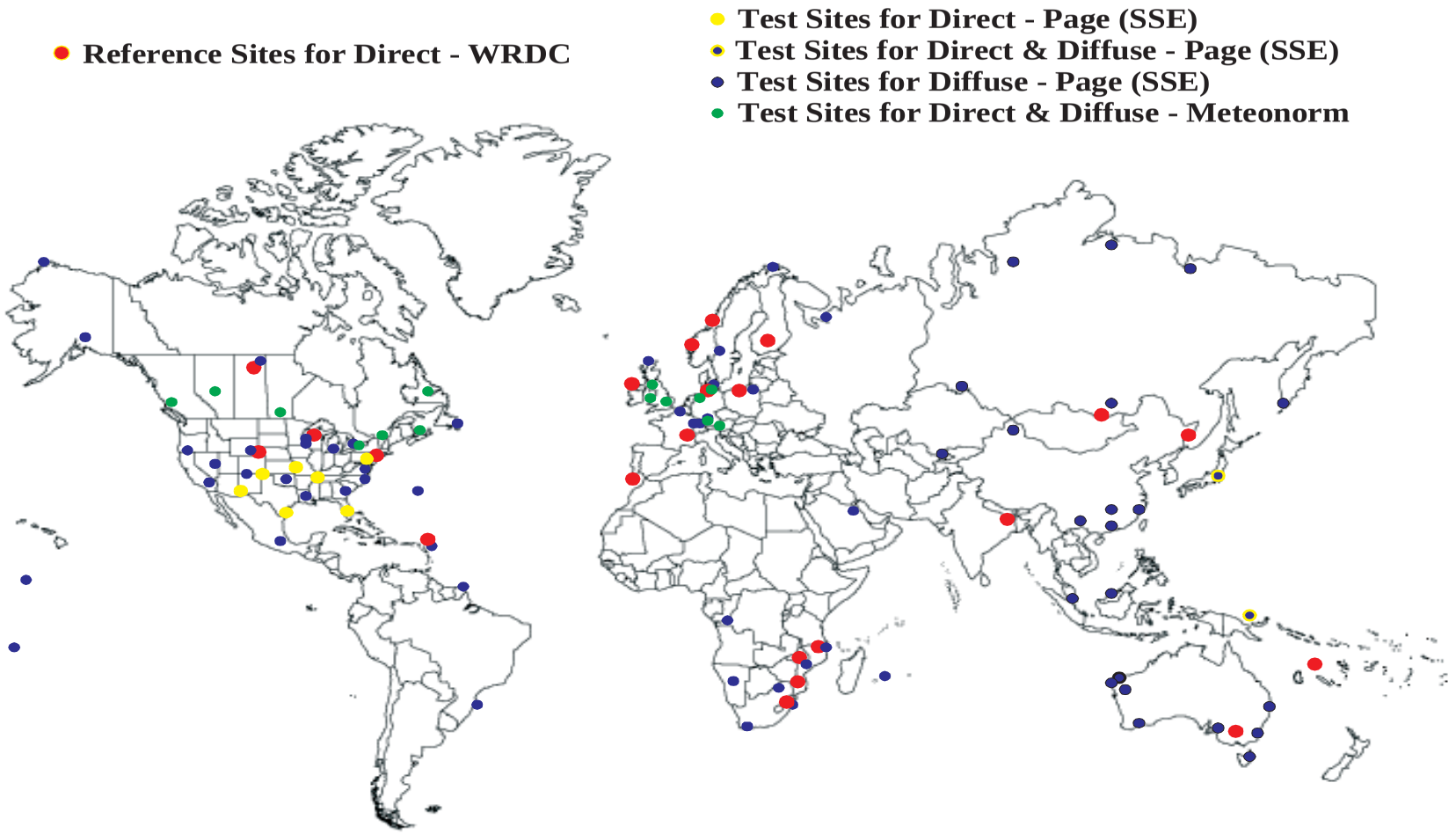

FIGURE 6.1
Test and reference sites for the assessment of direct normal solar irradiances. Observed surface radiation data is by courtesy of the World Radiation Data Centre (WRDC) [17., 2004].

6.5. Comparisons

The respective comparisons of estimates from SSE and Meteonorm to true direct irradiance data are made qualitatively.

The data estimates as well the reference data are taken in the form of monthly averages $\overline{H}_d(i)$, where i represents the month. This is the monthly average amount of direct solar radiation on a surface oriented normal to the solar beam. The units are in kWh/m^2/day. Two sets of ratios are generated: $\frac{\overline{H_d}(i)|_{SSE}}{\overline{H_d}(i)|_{WRDC}}$ and $\frac{\overline{H_d}(i)|_{Meteonorm}}{\overline{H_d}(i)|_{WRDC}}$, i = 1 to 12 months.

The sets of ratios are plotted in the FIGURE 6.2 and FIGURE 6.3. Data from SSE or Meteonorm are referred to as ‘model’ and that from the WRDC as ‘observed’. FIGURE 6.2 gives the model to the observed ratios for sites in the Southern Hemisphere. The ratios for the sites in the Northern Hemisphere are given in FIGURE 6.3.

The high monthly ratios on most of the plots suggest significant deviations between each of the model estimates and ‘true’ observations at the various sites. Deviations can be expected.

One possible source for deviations is the validity of the reference data. The WRDC direct normal component is inferred from observations of global and diffuse irradiances. The diffuse components are got with measurements from pyranometers equipped with a shadow band to shade out the direct component. Such measurements require correction for the diffuse radiation obstructed by the shadow band. The corrections can be derived theoretically, using the assumption of uniform sky radiance, or experimentally. In either case, as discussed by Iqbal in [2.], further corrections are necessary for heterogeneous skies. These corrections could vary by as much as 9% or more.

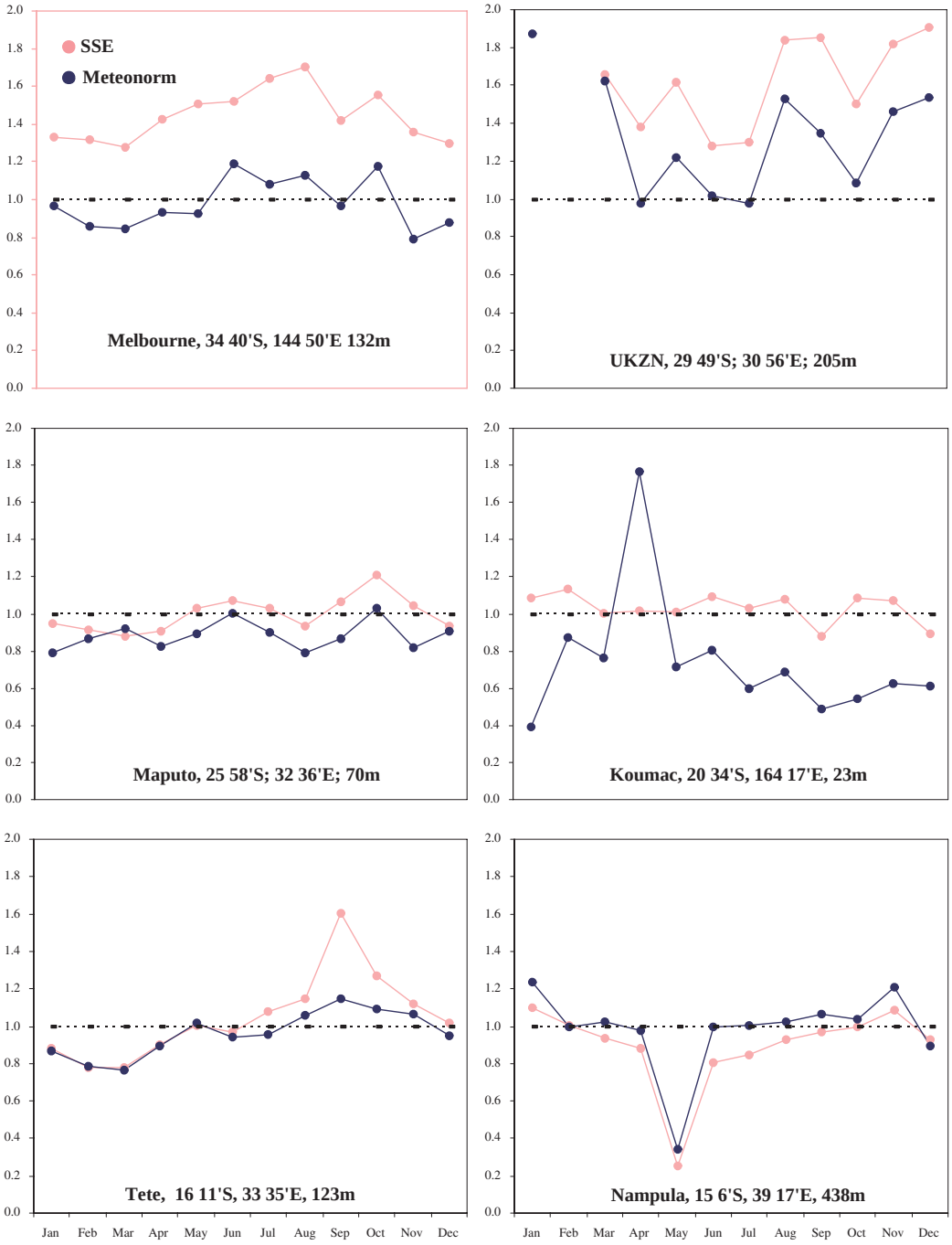

FIGURE 6.2
The ratio of SSE to WRDC data and the ratio of Meteonorm to WRDC data for sites in the southern hemisphere. The curves with pink dots represent the SSE to WRDC ratios and the curves with blue dots represent the Meteonorm to WRDC ratios.

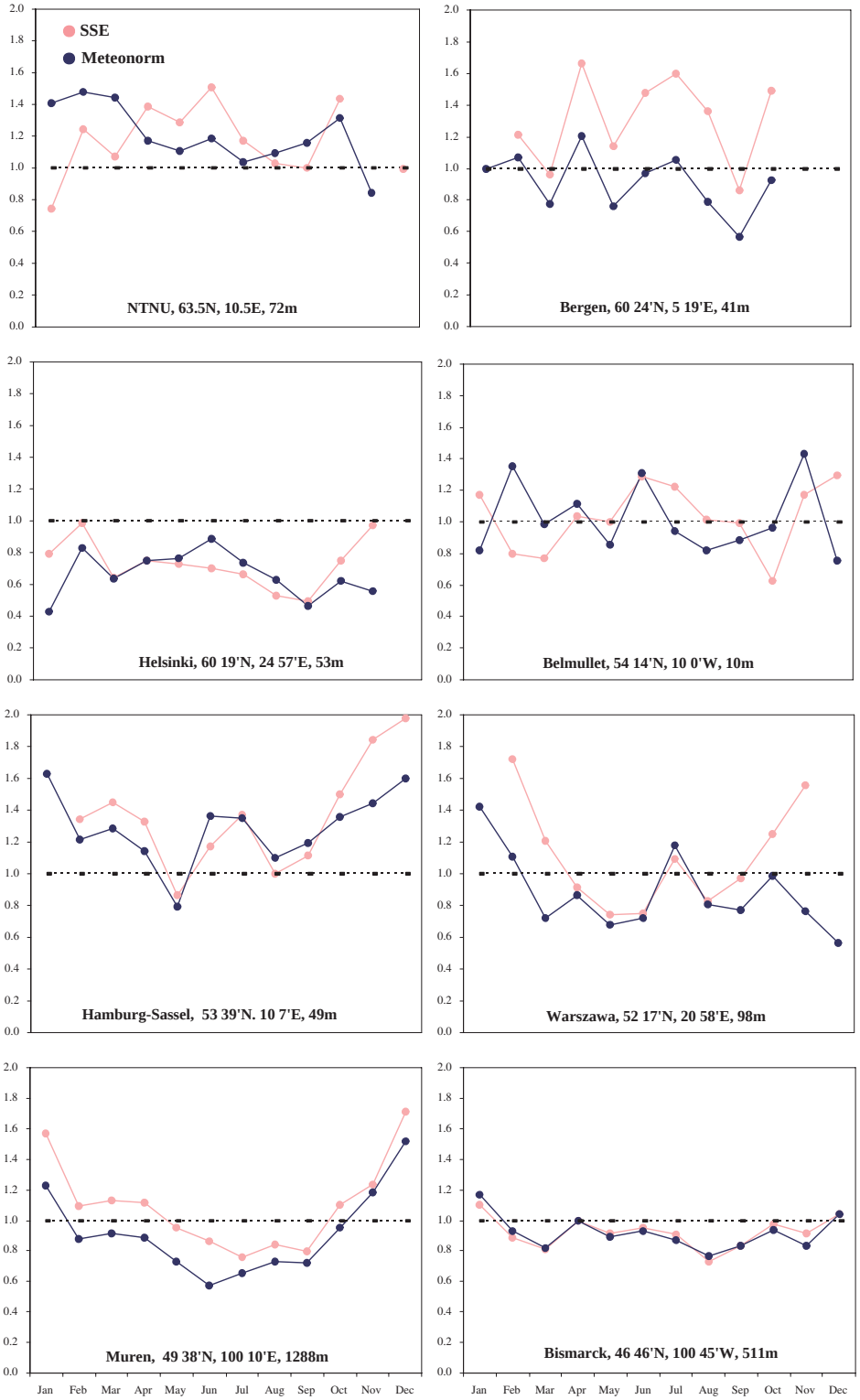

FIGURE 6.3
The ratio of SSE to WRDC data (with pink dots) and the ratio of Meteonorm to WRDC data (with blue dots) for sites in the northern hemisphere.

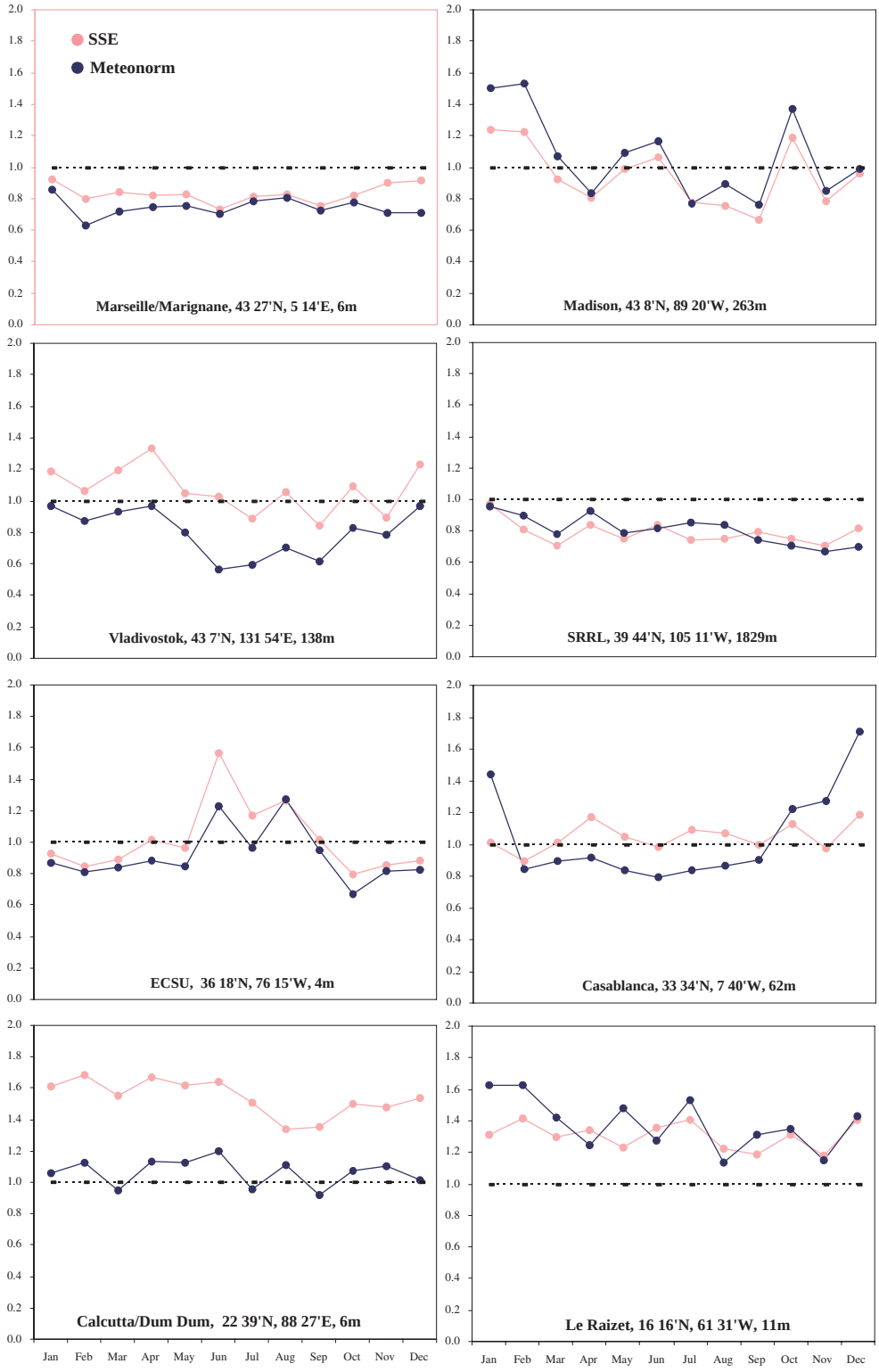

Figure 6.3 continued
The ratio of SSE to WRDC data (pink dots) and the ratio of Meteonorm to WRDC data (blue dots) for sites in the northern hemisphere.

Some of the points in FIGURE 6.2 and FIGURE 6.3 show ratios greater than 50%. These high values suggest significant deviations between each of the model estimates and 'true' observations at the respective sites. Such deviations can be expected, as is illustrated by the ground-truth versus satellite-estimated irradiances found by Perez et al. in [5.] and by others. FIGURE 6.4 is taken from [5.]. The ground-truth versus satellite derived irradiance plots in FIGURE 6.4 show that there can be good correlation between ground-truth measurements and satellite estimated global irradiances. The modelled values of direct irradiance show less correlation. The derived direct irradiances are widely scattered about the 1-1 line, with better correlation at higher irradiances. Both SSE and Meteonorm depend on the satellite estimated global irradiances in deriving their respective direct component. The global estimates, needed as model inputs for estimates of the direct component, can be considered reliable. The inaccuracies in direct irradiance estimates stem from each programs' model to decompose the global into direct and diffuse. The measurements in FIGURE 6.4 are for Desert Rock, Nevada (36.63^{o}N, 116.02^{o}W), a climatically distinct location in the sense that it is located in an arid valley with high albedo. Perez et al. in [5.] have identified that a climate dependent clear sky calibration brings direct irradiance modelled values closer to the 1-1 line. A climatic evaluation of three global-to-direct conversion models is given by Perez et al. in [8., 1990]. The modelled beam irradiances are compared to measured data from 3 sites with markedly distinct climatic environments. Their evaluation shows that the performance of each model depends on the handling of the sky conditions. Based on the difference in climate classification in SSE and Meteonorm, it should be expected that the implementations of the models (Page in SSE and Perez et al. in Meteonorm) for global-to-direct conversion, behave differently. Meteonorm uses a larger number of climate zones and does perform slightly better than SSE.

The curves for some of the plots in FIGURE 6.2 and FIGURE 6.3 reflect the trend suggested by Remund et al. in [11., 2003]. That is, there is a yearly pattern. Both SSE and Meteonorm register larger model to observation ratios in the winter, with higher winter ratios for latitudes above 50^{o}. This may be due to each models' handling of the influence of larger daily air mass in the winter period.

Omission of raised skylines from the sites would have a strong influence on data projection. The observed data from NTNU are included in the set of reference sites. NTNU has a defined skyline profile. Meteonorm can include the influence of skyline profiles in radiation calculations. The Meteonorm-to-observed ratios for NTNU are closer to unity, but only in the summer months. SSE does not include skyline profiles in calculations of the direct and diffuse estimates.

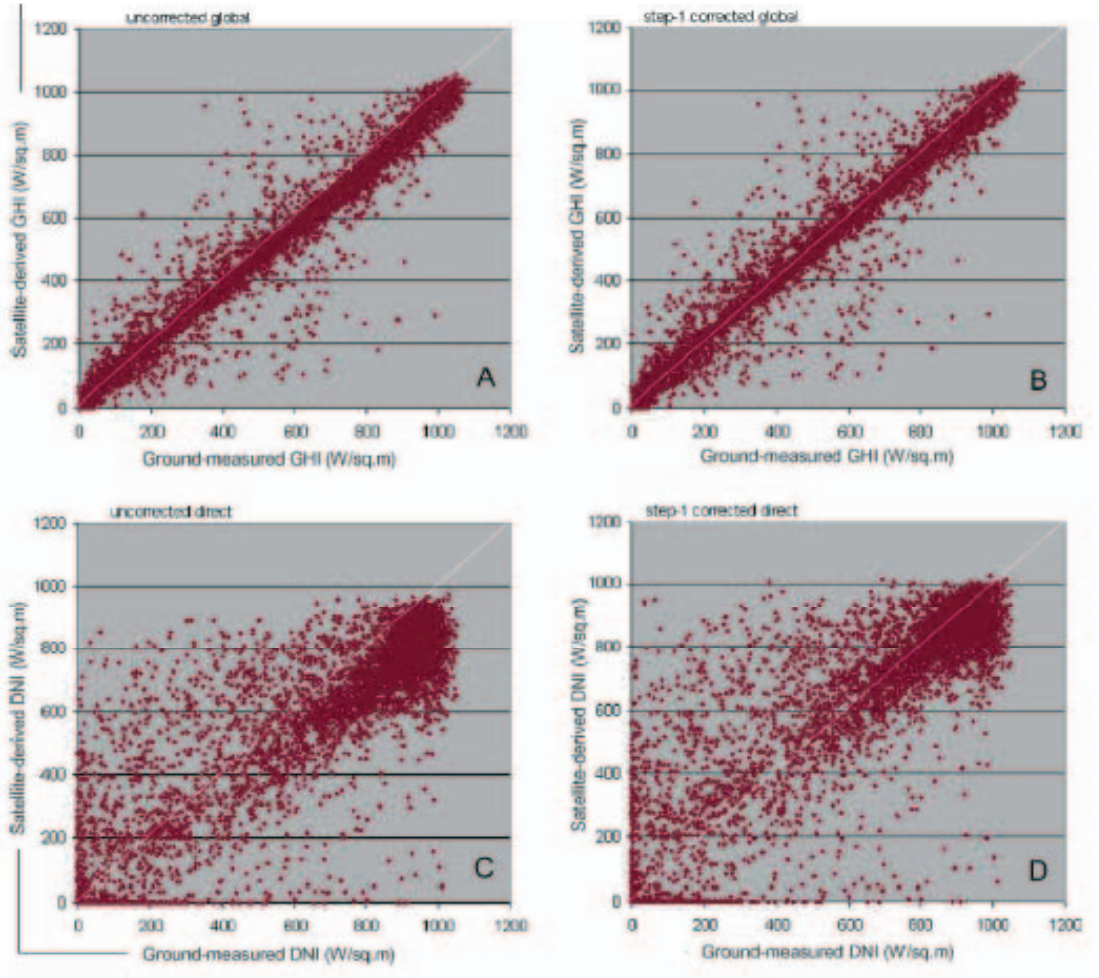

FIGURE 6.4
Satellite estimated vs. ground-truth measurements at Desert Rock, NV, for global irradiance before and after correction (respectively A and B) and direct irradiance before and after correction (respectively C and D). Figure by courtesy of Perez et al. in [5., 2004].

The accuracy of the derived data does depend on spatial variability. In this work, the selected reference sites with true data from the WRDC are well distributed about the globe. Meteonorm does not necessarily use the true global data at these stations but synthesises the data by inference from a non-strategic (remote-to-site) network of stations. In such a case satellite estimated irradiance data for a remote site becomes more accurate than local ground station extrapolation/interpolation, if the distance from the station exceeds 34 km. This follows from Perez et al. in [7., 1997].

Observation of ground records of surface solar irradiance indicate definite alterations in the levels of solar irradiance over temporal scales. The observed deviations in FIGURE 6.2 and FIGURE 6.3 from the unity line are also influenced by temporal variations. The basis data for both SSE and Meteonorm are gathered from between 1980 and 1995. The reference data from WRDC is selected for the years 2000 to 2002.

6.6. Chapter Summary and Conclusions

The intent of the qualitative comparisons of SSE's and Meteonorm's direct irradiance estimates to a set of ground-truth data is not to assess the performance of the programs. Interest is on the models used to synthesise the direct component, and on instrumentation for measured data. The measured data are questionable because of the uncertainty in corrections for instrument shading. The models are challenged with temporal and spatial variations, as well as a complex multitude of climates.

Meteonorm uses a larger multi-climatic database and results in a better approximation to ground-truth values than SSE. SSE's direct solar irradiance data are derived from satellite data which, as acknowledged by Witlock et al. in [16., 2004], is not intended to replace quality ground measurement data. It does provide the much needed data where ground measurements are missing. The model's parameters a and b given in equation (112) on page 187, depends on atmospheric conditions, cloud cover conditions/types, as well as latitude. A better knowledge of the parameters a and b may improve SSE's adopted model.

Presently, few ground measurement stations record the direct normal irradiance. It is typical to calculate the direct component from observation

of the global and diffuse components. The accuracy of the diffuse record and the calculated direct component is influenced by the pyranometer blockage effect under real-skies. At the same time, a direct record requires two pyranometers. Single instruments such as the DDSR-1B can provide records of all three components (that is direct, diffuse and global) inexpensively. Such records are a vital source of ground-truth data, both for model generation and validation, as well as for solar system designing.

All ground measurements stations are scattered throughout the world and, with the differences in climate, are not sufficient to represent all regions. It is not surprising that on a global scale, there is poor correlation between model estimates and ground-truth direct irradiance data. A larger set of reference sites are needed to tune the existing models to better accuracy. This would also provide a base to develop new irradiance models. The ultimate aim being to have a wonder model that would give close to true approximations for the direct and diffuse solar irradiance components.

6.7. References

1. Aguiar R.J., Collare-Pereira M., Conde J.P., *Simple Procedure for Generating Sequences of Daily Radiation Values using a Library of Markov Transition Matrices*, Solar Energy, Vol. 40, No. 3, pp. 269-279, 1988.
2. Iqbal M., An Introduction to Solar Radiation, Academic Press, Canada, 1983.
3. McPeters R.D, Krueger A.J., Bhartia P.K., Herman, J.R. et al., *Earth Probe Total Ozone Mapping Spectrometer (TOMS) Data Products User's Guide*, NASA Reference Publication 1998-206895, 1998. Online: http:// toms.gsfc.nasa.gov/index_v8.html, maintained by the NASA Ozone Processing Team, 2005.
4. Page J.K., The Estimation of Monthly Mean Values of Daily Total Shortwave Radiation on Vertical and Inclined Surfaces from Sunshine Records for Latitudes 40^{o}N-40^{o}S, Proceedings of the United Nations Conference on New Sources of Energy; Solar Energy, Wind Power and Geothermal Energy, 1964.
5. Perez R., Ineichen P., Kmiecik M., Moore K., Reene D., George R., *Producing Satellite-Derived Irradiances in Complex Arid Terrain*, Solar Energy, Vol 77, pp. 367-371, 2004.
6. Perez R., Ineichen P., Maxwell E., Seals R., Zelenka A., *Dynamic Models for Hourly Global-to-Direct Irradiance Conversion*. Edited in: Solar World Congress 1991, Vol. 1, Part II, Proceedings of the Biennial Congress of the International Solar Energy Society, Denver, Colorado, USA, 19-23 August 1991.

7. Perez R., Seals R., Zelenka A., *Comparing Satellite Remote Sensing and Ground Network Measurements for the production of Site/Time Specific Irradiance Data*, Solar Energy, Vol. 60, No. 2, pp. 89-96, 1997.
8. Perez R., Seals R., Zelenka A., Ineichen P., *Climatic Evaluation of Models that Predict Hourly Direct Irradiance from Hourly Global Irradiance: Prospects for Performance Improvements*, Solar Energy, Vol. 44, No. 2, pp. 99-108, 1990.
9. Pfaendtner J., Bloom S., Lamich D., Seablom M., Sienkiewicz M., Stobie J., da Silva A., *Documentation of the Goddard Earth Observing System (GEOS) Data Assimilation System-Version 1*, NASA Tech. Memo. No. 104606, vol. 4, Data Assimilation Office, Goddard Space Flight Center Greenbelt, MD 20771, pp. 44., 1995. Online: http://gmao.gsfc.nasa.gov/, maintained by the NASA Goddard Space Flight Center Global Assimilation Office, 2003.
10. Pinker R.T., Laszlo I., *Modelling Surface Solar Irradiance for Satellite Application on a Global Scale*, Journal of Applied Meteorology, Vol. 31, pp. 194-211, 1992.
11. Remund J., Kunz S., *Meteonorm Handbook*, Meteotest, Switzerland, 2003.
12. Remund J., *Personal Communication on the question of error in radiation splitting for Australia*, Meteotest, March 2005.
13. Schiffer R.A., Rossow W.B., *The International Satellite Cloud Climatology Project (ISCCP): The First Project of the World Climate Research Programme*, Bull. Amer. Meteor. Soc., 64, 779-784, 1983. Online: http:// isccp.giss.nasa.gov, maintained by the ISCCP research group at the NASA Goddard Institute for Space Studies, New York, NY. on January, 2005.
14. *Solar Radiation and Radiation Balance Data (The World Network) July - September 1997*, Russian Federal Service for Hydrometeorology and Environmental Monitoring, Voeikov Main Geophysical Observatory, WMO World Radiation Data Centre, ISSN 0235-4519.
15. Stackhouse P. W., Witlock C.H., Barkstrom B. R., *Surface meteorology and Solar Energy (release 5.1)*, URL: http://eosweb.larc.nasa.gov/sse/, 2005.
16. Witlock C.H. et. al., '*NASA Surface Meteorology and Solar Energy: Methodology*', URL: http://eosweb.larc.nasa.gov/cgi-bin/sse print.cgi?methodology.
17. WRDC, internet address http://wrdc.mgo.rssi.ru

Chapter 7

Conclusions

At the time of writing, the accurate generation of synthetic solar radiation data for an arbitrary location by existing models is difficult due to spatial, temporal and angular variability. The best remedy is in the dependence on localised solar observations.

Data mapping for the sites at UKZN and NTNU are described in detail, including calibration of the radiometers to ensure renewed traceability to the World Radiometric Reference. It is shown that system automation increases the reliability of data.

The development of the dual mode Direct-Diffuse Solar Radiometer (DDSR-1B) is with the intent to quantify irradiance at normal solar incidence and the angular distribution of sky radiance, at localised sites. Overall, it can be concluded that the DDSR-1B can be used for the measurements of direct solar irradiance. In addition, the instrument will be amongst the very few sky radiometers used for mapping the much needed angular distribution of shortwave sky radiances. From this work the following conclusions can be drawn:

* the physics of DDSR-1B's optical system is well understood;
* sensitivity is mainly limited by the conditioning electronics and can thus be easily improved;
* the preliminary calibration in $\text{Mode}_{\text{Direct}}$ is traceable to the World Radiometric Reference with a correction factor of 0.6854 ± 0.0009;
* calibration for $\text{Mode}_{\text{Diffuse}}$ in the field is challenging. One solution is to use a homogeneously overcast sky and integrate the directional response of DDSR-1B for comparison with a reference pyranometer.

As a final remark: There is need for measuring the angular dependence of solar radiation over the hemisphere. There is also need for a larger set of reference sites. Accurate, yet low cost instrumentation are the solutions.